Monte Carlo simulations of 250 keV photons effects on a 3D realistic mitochondria phantom and evaluation of radiation enhancement using gold nanoparticles

Sara Zein

ED SF n° d'ordre : 917

UNIVERSITE CLERMONT AUVERGNE

ECOLE DOCTORALE DES SCIENCES FONDAMENTALES

N° 917

THESE

présentée pour obtenir le grade de

DOCTEUR D'UNIVERSITE

Spécialité : Physique

Par **ZEIN Sara**
Master

Simulations Monte Carlo des effets des photons de 250 keV sur un fantôme 3D réaliste de mitochondrie et évaluation des effets des nanoparticules d'or sur les caractéristiques des irradiations

Soutenue publiquement le 29/09/2017, devant la commission d'examen.

Président:	M. Patrick VERNET
Rapporteurs:	Mme Marie-Claude BORDAGE
	M. Ziad El BITAR
Examinateurs:	Mme Lydia MAIGNE
	M. Wehbeh FARAH
	M. Haitham ZARAKET
Invité:	M. Arnaud CHEVROLIER
Directeurs de thèse:	M. Gérard MONTAROU
	M. Ziad FRANCIS

Simulations Monte Carlo des effets des photons de 250 keV sur un fantôme 3D réaliste de mitochondrie et évaluation des effets des nanoparticules d'or sur les caractéristiques des irradiations

Résumé

Dans le domaine de la radiobiologie, les dommages causés à l'ADN nucléaire sont largement étudiés puisque l'ADN est considéré la cible la plus sensible dans la cellule. En plus de l'ADN, les mitochondries commencent à attirer l'attention comme des cibles sensibles, car elles contrôlent de nombreuses fonctions importantes pour la survie de la cellule. Ce sont des organites à double membranes principalement chargées de la production d'énergie ainsi que la régulation réactive des espèces d'oxygène, la signalisation cellulaire et le contrôle de l'apoptose. Certaines expériences ont montré qu'après exposition aux rayonnements ionisants, les teneurs mitochondriales sont modifiées et leurs fonctions sont affectées. C'est pourquoi nous sommes intéressés par l'étude des effets des rayonnements ionisants sur les mitochondries.

À l'échelle microscopique, les simulations Monte-Carlo sont utiles pour reproduire les traces de particules ionisantes pour une étude approfondie. Par conséquent, nous avons produit des fantômes 3D de mitochondries à partir d'images microscopiques de cellules fibroblastiques. Ces fantômes ont été transformés de façon à être téléchargés dans Geant4 sous forme de mailles tessélisées et tétraédriques remplies d'eau représentant la géométrie réaliste de ces organites. Les simulations numériques ont été effectuées afin de calculer les dépôts d'énergie induits par des photons de 250 keV à l'intérieur de ces fantômes. Les processus électromagnétiques Geant4-DNA sont utilisés pour simuler les traces des électrons secondaires produits. Étant donné que les dommages groupés sont plus difficiles à réparer par les cellules, un algorithme spécifique est utilisé pour étudier le regroupement spatial des dégâts potentiels des rayonnements.

En radiothérapie, il est difficile de donner une dose efficace aux sites de la tumeur sans affecter les tissus environnants sains. L'utilisation de nanoparticules d'or comme radio-sensibilisateurs semble être prometteuse. Leur coefficient d'absorption élevé augmente la probabilité d'interaction des photons et induit une dose tumorale plus importante lorsque ces particules sont absorbés de manière préférentielle dans les tumeurs. Puisque l'or a un nombre atomique élevé, les électrons Auger sont produits en abondance. Ces électrons ont une portée plus faible que les photoélectrons, ce qui leur permet de déposer la majeure partie de leur énergie près de la nanoparticule, ce qui augmente la dose locale. Nous avons étudié l'effet radio-sensibilisant des nanoparticules d'or sur le fantôme des mitochondries. L'efficacité de cette méthode dépend du nombre, de la taille et de la répartition spatiale des nanoparticules d'or.

Après exposition aux rayonnements ionisants, des espèces réactives d'oxygène sont produites dans le milieu biologique qui contient une quantité d'eau abondante. Dans cette étude, nous simulons les espèces chimiques produites à l'intérieur du fantôme des mitochondries et leur regroupement est estimé. La distribution spatiale des produits chimiques et leur évolution avec le temps et par la suite analysée au moyen d'algorithme spécifique de traitement de données.

Monte Carlo simulations of 250 keV photons effects on a 3D realistic mitochondria phantom and evaluation of radiation enhancement using gold nanoparticles

Abstract

In the field of radiobiology, damage to nuclear DNA is extensively studied since it is considered as a sensitive target inside cells. Mitochondria are starting to get some attention as sensitive targets as well since they control many functions important to the cell's survival. They are double membraned organelles mainly in charge of energy production as well as reactive oxygen species regulation, cell signaling and apoptosis control. Some experiments have shown that after exposure to ionizing radiation the mitochondrial contents are altered and their functions are affected. That is why we are interested in studying the effects of ionizing radiation on mitochondria.

At the microscopic scale, Monte Carlo simulations are helpful in reproducing the tracks of ionizing particles for a close study. Therefore, we produced 3D phantoms of mitochondria starting from microscopic images of fibroblast cells. These phantoms are easily uploaded into Geant4 as tessellated and tetrahedral meshes filled with water representing the realistic geometry of these organelles. Microdosimetric analysis is performed to deposited energy by 250 keV photons inside these phantoms. The Geant4-DNA electromagnetic processes are used to simulate the tracking of the produced secondary electrons. Since clustered damages are harder to repair by cells, a clustering algorithm is used to study the spatial clustering of potential radiation damages.

In radiotherapy, it is a challenge to deliver an efficient dose to the tumor sites without affecting healthy surrounding tissues. The use of gold nanoparticles as radio-sensitizers seems to be promising. Their high photon absorption coefficient compared to tissues deposit a larger dose when they are preferentially absorbed in tumors. Since gold has a high atomic number, Auger electrons are produced abundantly. These electrons have lower range than photoelectrons enabling them to deposit most of their energy near the nanoparticle and thus increasing the local dose. We studied the radio-sensitizing effect of gold nanoparticles on the mitochondria phantom. The effectiveness of this method is dependent on the number, size and spatial distribution of gold nanoparticles.

After exposure to ionizing radiation, reactive oxygen species are produced in the biological material that contains abundant amount of water. In this study, we simulate the chemical species produced inside the mitochondria phantom and their clustering is estimated. We take advantage of the Geant4-DNA chemistry processes libraries that is recently included in the Geant4.10.1 release to simulate the spatial distribution of the chemicals and their evolution with time.

Acknowledgements

I would like to thank every person who helped me to produce this work.

My advisors M. Gérard Montarou and M. Ziad Franics you have both been very supportive in many ways. Thank you for everything.

Special thanks to M. Arnaud Chevrollier who provided us with the microscopic images of the mitochondria and to M. Frédéric Chandez who did all the Imaris analysis. I also want to thank M. Sebastian Incerti for his advice with Geant4-DNA simulations.

Concerning the biology of cells, mitochondria, and gold nanoparticles the advice and opinions of M. Serge Alziari and M. Patrick Vernet were indispensable. Thank you for your enlightening information.

I would also want to thank each and everyone of the jury members for reading and reviewing my manuscript.

And of course I have to thank the Institut des Recherche pour les Developpement for granting the cotutelle scholarship under the ARTS program.

A big thanks to the members of the AVIRM group for supporting me and accepting me as one of them.

The true sign of intelligence is not knowledge but imagination.

~ Albert Einstein

Table of Contents

List of Symbols and Abbreviations

Abbreviations

DNA	Deoxyribonucleic acid
ATP	Adenosine triphosphate
ROS	Reactive oxygen species
GNRT	Gold nanoparticle-aided radiation therapy
GNP	Gold nanoparticles
mtDNA	Mitochondrial DNA
TFAM	Mitochondrial transcription factor A
mtSSBP	Mitochondria single-strand binding protein
8-OHdG	8- hydroxydeoxy guanosine
GSH	Glutathione in reduced state
SSB	Single strand break
DSB	Double strand break
DBSCAN	Density Based Spatial Clustering of Applications with Noise
RMSR	Root mean square radius
STL	Stereo-lethograpy format
PLY	Stanford polygon file format
GDML	Geometry description markup language
LET	Linear energy transfer

Symbols

Z	Atomic number
A	Mass number
h	Planck's constant
c	Speed of light in vacuum
σ	Cross-section
N_A	Avogadro's number
ρ	Density
D	Absorbed dose
ϵ	Imparted energy
z	Specific energy
y	Lineal energy
$\overline{l}$	Mean chord length
$\overline{y}_F$	Frequency mean lineal energy
$\overline{y}_D$	Dose mean lineal energy

Chemicals

H^+	Proton
$O_2^{-\bullet}$	Superoxide anion
H_2O_2	Hydrogen peroxide

$OH^{\bullet}$	Hydroxyl radical
$H^{\bullet}$	Hydrogen atom
O_2	Oxygen molecule
e_{aq}^{-}	Aqueous electron or solvated electron
H_3O^+	Hydronium ion
OH^-	Hydroxide anion
H_2O	Water molecule
H_2O^*	Excited water molecule
H_2O^-	Negatively charged water ion
H_2O^+	Positively charged water ion
H_2	Dihydrogen

1 Introduction

Radiation damage to nuclear DNA is a major research subject in radiobiology since damage to the genome affects the viability of a cell. However, recent studies have shown that mitochondria are susceptible to damages as well when subjected to radiation [1, 2].

Mitochondria are small double membraned organelles inside eukaryotic cells mainly in charge of energy production in the form of adenosine triphosphate (ATP) via oxidative phosphorylation [3, 4]. They are also responsible for other functions such as cell signaling, apoptosis control and reactive oxygen species production [5]. They contain their own distinct genome in the form of circular DNA [6] which is present in multiple copies per mitochondrion [7].

Mitochondria are dynamic organelles performing fission to multiply in number in response to the cell's energy needs [8]. In some cells, such as lymphocytes, mitochondria can account up to approximately 30% of the total cell volume [9]. This makes them highly probable candidates for radiation exposure putting them and the whole cell at risk of molecular damage and eventually carcinogenesis and death.

In mammalian cells, mitochondria take on a wide variety of shapes ranging from long interconnected tubules to individual small spheres [10]. In cultured fibroblasts the mitochondrial population consists mostly of short and long tubules which constantly migrate along their axes along the microtubule tracks [11].

Reactive oxygen species are normally produced inside mitochondria as byproducts of oxidative phosphorylation. These chemicals when kept under control are used by the immune system to attack pathogens. When out of control they act as free radicals attacking the sensitive structures of the cell. When subjected to radiation, these chemicals are produced abundantly inside the cells by the process of radiolysis.

An approach known as gold nanoparticle-aided radiation therapy (GNRT) is a recent development in radiation therapy which seeks to make a tumor more susceptible to radiation damage by modifying its photon interaction properties with an infusion of gold nanoparticles (GNPs).

Because of their high energy absorption coefficient, high density and bio-compatibility, gold nanoparticles (GNP) have been studied as radio-sensitizing agents [12] in pre-clinical studies of a wide variety of cell lines irradiated with different photon beams [13-19]. Compared to water, which is the main compound of biological material, gold has a relatively higher photoelectric cross-section which enhances the local dose especially for photons in the kilovoltage energy range [20]. As a high Z element, gold usually produces

Auger electrons when irradiated with photons of energy ranging between 10-500 keV [21]. So in addition to the photo-electrons, Auger electrons contribute to local dose in the vicinity of the GNP [22, 23].

GNP enter the cell by the process of endocytosis where they are mostly confined in lysosomes. However this depends on their size and their coating properties [24, 25]. In the work of Wang *et al*. [26] gold nanorods were selectively taken up by the mitochondria of lung carcinoma cells (A549). The lysosomes membranes of the cancerous cells are permeable to the nanorods such that they were released into the cytoplasm and eventually collected on the mitochondria.

The goal of this work is to produce a phantom modelling the mitochondria of a fibroblast cell from a microscopic 3D image and study how ionizing radiation affects it in the physical and the chemical phases.

The insertion of GNP is included in the simulation where irradiation with x-rays is performed and the energy deposits are measured to see what difference the presence of GNP makes.

Chapter 2 is a brief introduction to the biology of eukaryotic cells showing the different parts of the cell and some of the important processes going on inside.

Chapter 3 demonstrates the interaction processes of ionizing radiation with biological matter and the theoretical background behind the use of gold nanoparticles in radiotherapy.

The microdosimetry formalism and the DBSCAN clustering analysis are described in chapter 4.

Chapter 5 summarizes the physical processes implemented in the Geant4 Monte Carlo code and how to use CADMesh Libraries to import complex geometries like the tessellated and tetrahedral meshes.

In chapter 6 the detailed process of creating the realistic 3D phantom of the fibroblast mitochondria from a microscopic image is described.

Three phantoms of three different mitochondria are created in chapter 7. They are imported successfully into Geant4 and are irradiated with 250 keV photons. The lineal energies are calculated and the clustered damages are analyzed.

Chapter 8 investigates the use of gold nanoparticles and their effect on mitochondria after irradiation. In the last chapter, chemical species are produced and their effects on the mitochondria are analyzed.

1. Kam, W.W.-Y. and R.B. Banati, *Effects of ionizing radiation on mitochondria.* Free Radical Biology and Medicine, 2013. **65**: p. 607-619.
2. Yamamori, T., et al., *Ionizing radiation induces mitochondrial reactive oxygen species production accompanied by upregulation of mitochondrial electron transport chain function and mitochondrial content under control of the cell cycle checkpoint.* Free Radical Biology and Medicine, 2012. **53**: p. 260-270.
3. Pfeiffer, T., S. Schuster, and S. Bonhoeffer, *Cooperation and competition in the evolution of ATP-producing pathways.* Science, 2001. **292**(5516): p. 504-507.
4. Attardi, G. and G. Schatz, *Biogenesis of mitochondria.* Annual Review of Cell and Developmental Biology, 1988. **4**: p. 289-333.
5. Fang, F., et al., *Mitochondrial modulation of apoptosis induced by low-dose radiation in mouse testicular cells.* Biomedical and Environmental Scineces, 2013. **26**: p. 820-830.
6. Cooper, G.M., *The Cell: A Molecular Approach*. 1997, Washington DC: ASM Press.
7. Satoh, M. and T. Kuroiwa, *Organization of Multiple Nucleoids and DNA Molecules in Mitochondria of a Human Cell.* Experimental Cell Research, 1991. **196**: p. 137-140.
8. Chan, D.C., *Mitochondrial fusion and fission in mammals.* Annual Review of Cell and Developmental Biology, 2006. **22**: p. 79-99.
9. Kam, W.W.Y., et al., *Predicted ionization in mitochondria and observed acute changes in the mitochondrial transcriptome after gamma irradiation: a Monte Carlo simulation and quantitative PCR study.* Mitochondrion, 2013. **13**(6): p. 736-742.
10. Bereiter-Hahn, J. and M. Voth, *Dynamics of mitochondria in living cells: shape changes, dislocations, fusion, and fission of mitochondria.* Microscopy Research and Technique, 1994. **27**: p. 198–219.
11. Chen, H. and D.C. Chan, *Mitochondrial dynamics in mammals.* Current Topics in Developmental Biology, 2004. **59**: p. 119–44.
12. Hainfeld, J.F., D.N. Slatkin, and H.M. Smilowitz, *The use of gold nanoparticles to enhance radiotherapy in mice.* Physics in Medicine and Biology, 2004. **49**(18): p. 309-315.
13. Berbeco, R.I., et al., *DNA damage enhancement from gold nanoparticles for clinical MV photon beams.* Radiation Research, 2012. **178**(6): p. 604-608.
14. Butterworth, K.T., et al., *Evaluation of cytotoxicity and radiation enhancement using 1.9 nm gold particles: potential application for cancer therapy.* Nanotechnology, 2010. **21**(29).
15. Chang, M.Y., et al., *Increased apoptotic potential and dose-enhancing effect of gold nanoparticles in combination with single-dose clinical electron beams on tumor-bearing mice.* Cancer Science, 2008. **99**(7): p. 1479-1484.
16. Chithrani, D., et al., *Gold nanoparticles as radiation sensitizers in cancer therapy.* Radiation Research, 2010. **173**: p. 719-728.
17. Jain, S., et al., *Cell-specific radiosensitization by gold nanoparticles at megavoltage radiation energies.* International Journal of Radiation Oncology Biology Physics, 2011. **79**(2): p. 531-539.
18. Kong, T., et al., *Enhancement of radiation cytotoxicity in breast-cancer cells by localized attachment of gold nanoparticles.* Small, 2008. **4**(9): p. 1537-1543.

19. Rahman, W.N., et al., *Enhancement of radiation effects by gold nanoparticles for superficial radiation therapy.* Nanomedicine: Nanotechnology, Biology, and Medicine, 2009. **5**: p. 136-142.
20. McMahon, S.J., et al., *Nanodosimetric effects of gold nanoparticles in megavoltage radiation therapy.* Radiotherapy and Oncology, 2011. **100**(3): p. 412-416.
21. Mesbahi, A., *A review on gold nanoparticles radiosensitization effects in radiation therapy of cancer.* Reports of Practical Oncology and Radiotherapy, 2010. **15**: p. 176-180.
22. McMahon, S.J., et al., *Biological consequences of nanoscale energy deposition near irradiated heavy atom nanoparticles.* Scientific Reports, 2011. **1**(18).
23. Cho, S.H., B.L. Jones, and S. Krishnan, *The dosimetric feasibility of gold nanoparticle-aided radiation therapy (GNRT) via brachytherapy using low-energy gamma-/x-ray sources.* Physics in Medicine and Biology, 2009. **54**(16): p. 4889-4905.
24. Chithrani, D., *Intracellular uptake, transport, and processing of gold nanostructures.* Molecular Membrane Biology, 2010. **27**: p. 299-311.
25. Shukla, R., et al., *Biocompatibility of gold nanoparticles and their endocytotic fate inside the cellular compartment: a microscopic overview.* Langmuir, 2005. **21**(23): p. 10644-10654.
26. Wang, L., et al., *Selective targeting of gold nanorods at the mitochondria of cancer cells: implications for cancer therapy.* Nano Letters, 2010. **11**(2): p. 772-780.

2 Biology of Cells

Cells are the basic structural, functional, and biological units of all organisms. They are the smallest units of life that can replicate independently and are often called the building blocks of life. They are small compartments holding the biological equipment necessary to keep an organism alive. Living organisms can be single-cell such as bacteria or protists or they can be multicellular such as a human being. Cells are classified into two types:

- **Prokaryotic cells**: They do not contain a nucleus. Prokaryotic organisms are single-cell such as bacteria.
- **Eukaryotic cells**: They contain a nucleus. Eukaryotic organisms can be either single-cell such as fungi or multicellular such as plants, animals and humans.

2.1 Cell Structure

The cell is made up of an organization of sub-cellular compartments that regulate cell's functions. A detailed figure of the cell structure is shown in figure (2-1). The different parts of the cell are [27]:

- **Nucleus**: Is a membrane-enclosed organelle found in the eukaryotic cells. Its diameter varies between 10 to 20 microns, so it is the largest organelle. It contains most of the cell's genetic material, organized as multiple long linear DNA molecules in complex with proteins such as histones to form chromosomes. The chromosomes contain the genes which form the human genome. The nucleus maintains the integrity of the genes and controls the activities of the cell by regulating gene expression. The genetic material is stored in the form of chromatin inside the nucleus.
- **Cytoplasm**: This compartment is constituted by a solution (cytosol) where all the cell organelles and many molecules such amino acids, ions and glucose are present.
- **Cell membrane**: Also called plasma membrane is the membrane surrounding the whole cell and separates its interior from the outside environment. It plays the role of a selectively permeable boundary of nutrients and waste by controlling the movement of substances in and out of the cell. It is involved in a variety of cellular processes such as cell adhesion, ion conductivity and cell signaling.
- **Mitochondria**: are double-membraned organelles mainly responsible for energy production for the cell, but also involved in key metabolisms (fatty acids oxidation, amino-acids metabolism…).
- **Endoplasmic Reticulum**: There are two types of endoplasmic reticulum, rough and smooth. The outer face of the rough endoplasmic reticulum is stubbed with ribosomes that are sites of protein synthesis. The smooth endoplasmic reticulum lacks ribosomes and functions in lipid and carbohydrate metabolism.

- **Golgi apparatus**: Also called Golgi body is a major collection and dispatch station of proteins received from endoplasmic reticulum. These proteins are modified and destined for use in different parts of the cell or to the extracellular space.

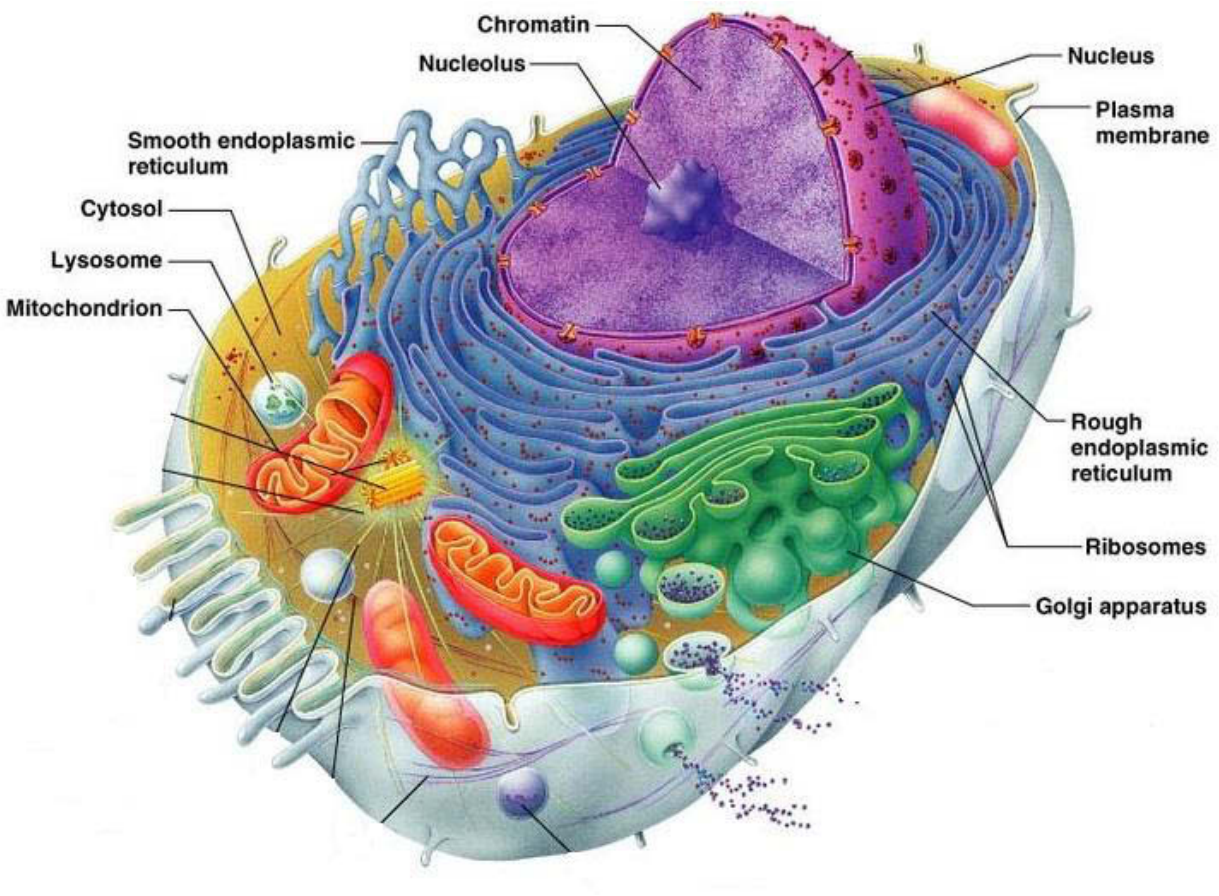

Figure (2-1) A typical eukaryotic cell Structure from reference [28]

2.2 Mitochondria

The mitochondria are double membrane-bound organelles found in most eukaryotic cells. They are famously known as the power houses of the cell. They produce energy in the form of adenosine triphosphate (ATP) needed by the cells to survive and to perform many functions.

They are also responsible for many processes such as cell signaling, cell cycle control, apoptosis regulation, and reactive oxygen species production [5].

They range in size from 0.5 μm to 10 μm when isolated. However, they can be also organized as a complex dynamic network. They contain their own DNA. The number of mitochondria in a cell can vary by cell type. For instance, red blood cells have no mitochondria, while liver cells can have more than 2000 [29]. In some cells, such as

lymphocytes, mitochondria accounts for up to approximately 30% of the total cell volume [9]. Figure (2-2) shows an example of how mitochondria are dispersed in the cytoplasm of the cell.

Mitochondria divide by binary fission similar to bacterial division [30]. They may replicate their DNA and divide mainly in response to energy needs of the cells.

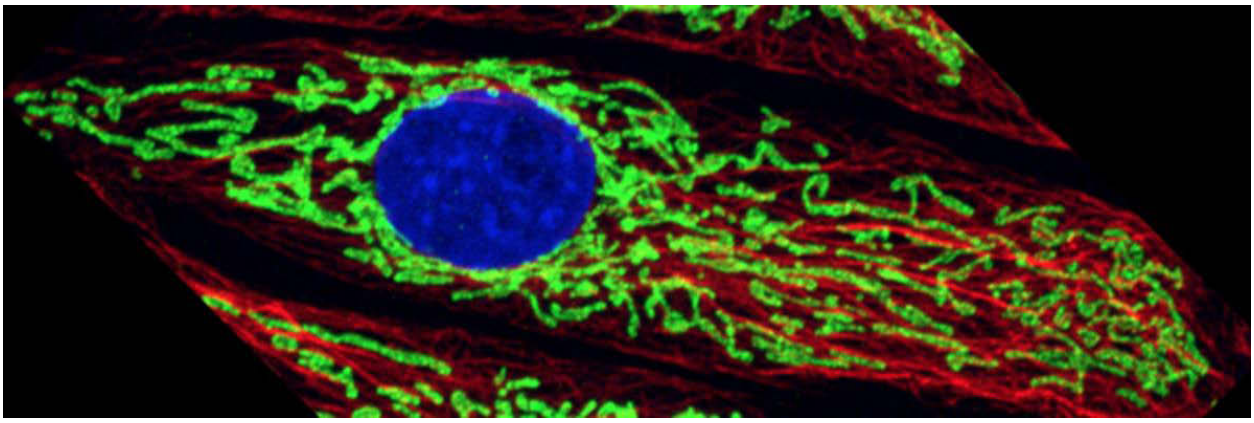

Figure (2-2) Mitochondrial network (green) within a cell. Nucleus in blue. Image from reference [31]

Figure (2-3) shows a single mitochondrion with all its components.

The mitochondrion consists of:

1. **Outer membrane**: It is a highly permeable membrane allowing water, minerals, proteins and other molecules to pass through it.
2. **Inner membrane**: It is less permeable than the outer membrane. It consists of many complexes that perform the electron transport chain responsible for ATP production. It has many folds (cristae) providing a large surface area for reactions to take place.
3. **Matrix**: is the space enclosed by the inner membrane. It contains a highly concentrated mixture of hundreds of enzymes, mitochondrial ribosomes, transfer RNA and several copies of the mitochondrial DNA genome.

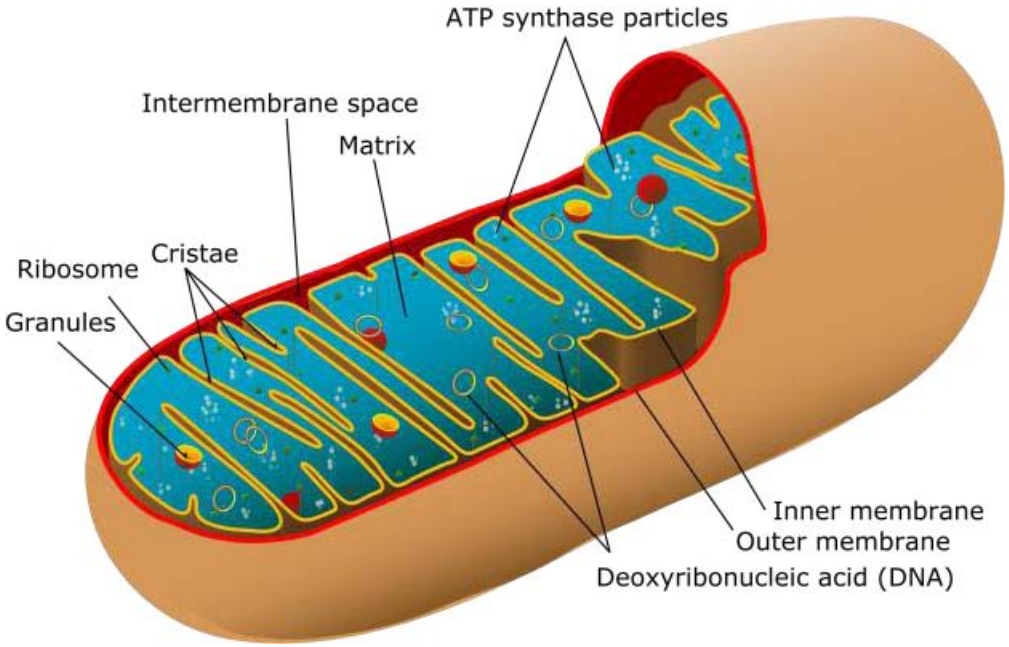

Figure (2-3) Mitochondrion structure from reference [32]

2.3 DNA

Deoxyribonucleic acid (DNA) is a molecule that carries most of the genetic instructions used in the development, functioning and reproduction of the cell. It is made up of a series of nucleotides arranged in two strands that resemble a ladder and twist to form a double helix [33]. Each nucleotide is composed of a nitrogen-containing nucleobase, a deoxyribose sugar and a phosphate group. DNA has 4 nucleobases, adenine (A), guanine (G), cytosine (C) and thymine (T) that pair with each other by hydrogen bonds. Adenine always pairs with thymine and guanine always pairs with cytosine. Figure (2-4) shows a representation of the structure of the DNA and its nucleobase pairing. Parts of the DNA encoding information are named genes. These messages are converted into ribonucleic acids (RNA), then possibly translated into proteins needed for instance for the growth and development of the organism and act like a set of instructions for the cells. In animal eukaryotic cells, DNA is found in the nucleus as well as in the mitochondria.

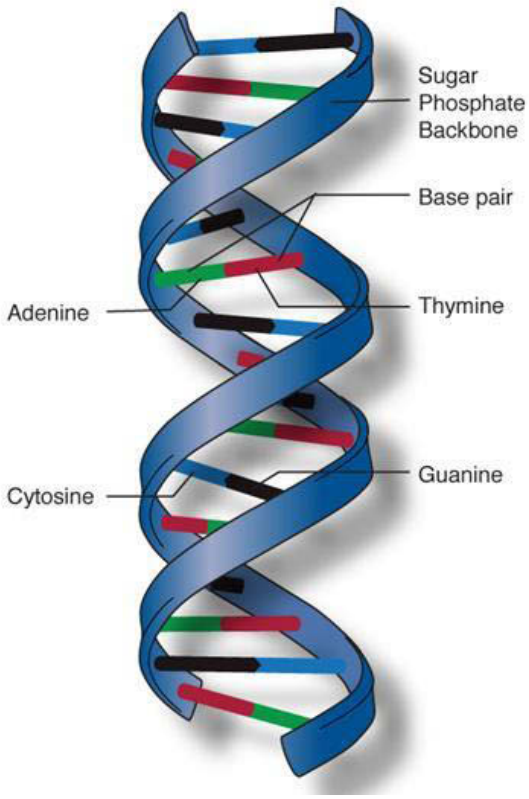

Figure (2-4) DNA Structure: Double helix from reference [34]

2.3.1 **Nuclear DNA**

The nucleus contains most of the cell's DNA. DNA is a very large molecule having the form of a double helix of diameter 2 nm. The double helix is then packed and coiled over proteins mainly histones. These histones form a spindle that the DNA is wrapped around to form nucleosomes that are 11 nm in diameter. The nucleosomes are then grouped together in structures called chromatin that is about 30 nm in diameter. The condensed chromatin forms the chromosomes. Figure (2-5) shows how the long macromolecule of nuclear DNA is packed progressively around histones, then as nucleosomes and finally as chromosomes.

The unique structure of chromosomes keeps DNA tightly wrapped to fit inside cells. They also play a key part in insuring the accuracy of DNA copying during cell division. A chromosome consists of two chromatids (half a chromosome) joined together at a protein junction called a centromere. The diploid human genome (set of parents chromosomes) is made up of 46 chromosomes [29].

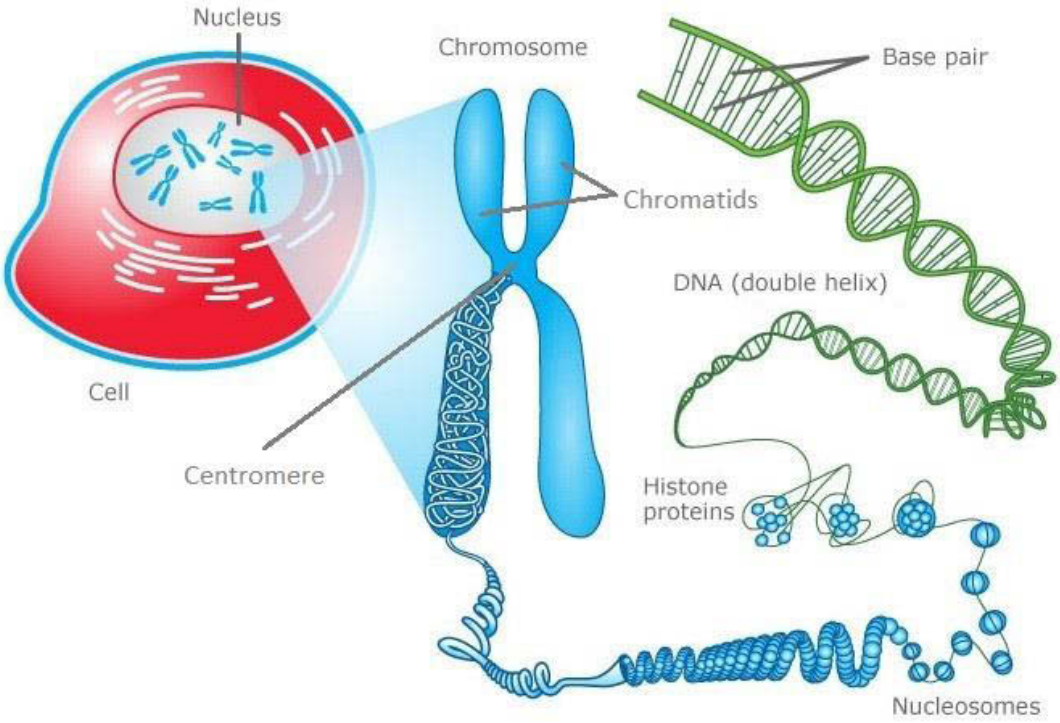

Figure (2-5) DNA packaging in chromosomes from reference [35]

2.3.2 **Mitochondrial DNA**

Mitochondrial DNA (mtDNA) is a small portion of the cell's DNA located inside the mitochondria and is inherited solely from the mother. In humans, mtDNA encode for only 37 genes specifically related to the functions of the mitochondria. Not all proteins necessary for mitochondrial function are encoded by the mitochondrial genome. Most of them are coded by genes in the cell nucleus and the corresponding proteins are imported into the mitochondria [36].

The mitochondrial DNA is made up of a circular covalently closed double-stranded DNA. A single mitochondrion contains several copies of the mtDNA. Mitochondrial DNA is organized in structures called nucleoids. A mitochondrial nucleoid is an aggregate of mtDNA genome and a group of protein factors such as mitochondrial transcription factor A (TFAM), mitochondria single-strand binding protein (mtSSBP), and the helicase Twinkle [37]. These protein factors maintain the replication, repair and transcription of mtDNA. The number of nucleoids per mitochondrion varies depending on tissue type. Figure (2-6) shows an example of a nucleoid formed by circular mtDNA molecules packed together by protein factors.

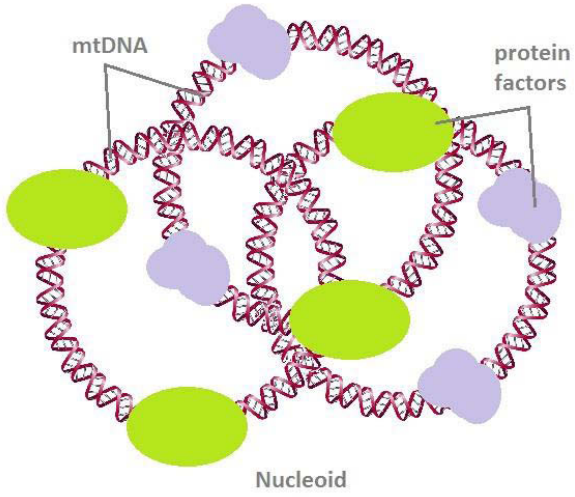

Figure (2-6) Nucleoid

Any damage to the mitochondrial DNA results in mitochondrial dysfunction that is related to many diseases such as cardiac dysfunction, optical atrophy, neurodegenerative diseases and autism[38]. Such damages to the mitochondria and their DNA would ultimately trigger the cell death.

2.4 Cell Cycle

Cells undergo a process called the cell cycle to divide and duplicate. The eukaryotic cells perform the mitotic cell division or simply mitosis. The cell cycle is divided into two phases: interphase (I) and the mitotic (M) phase as shown in figure (2-7). During the interphase, the cell grows, prepares itself for division and duplicates its DNA. During the mitotic phase, the cell splits into two daughter cells each having their own nucleus and DNA.

Before a cell can enter cell division (the mitotic phase), it needs to take in nutrients and perform all the preparations for division. So the interphase is a period of growth for the cell. During this phase, DNA replication occurs and its integrity is checked before and after it is replicated. Moreover, chromatin is usually dispersed within the nucleus and individual chromosomes cannot be distinguished.

The interphase consists of three main stages:

- **Gap1 (G_1)**: The cell increases in size. At this point the G_1 checkpoint ensures that everything is ready for DNA synthesis.
- **Synthesis (S)**: DNA replication occurs during this stage.
- **Gap2 (G_2)**: During the gap between DNA synthesis and mitosis, the cell continues to grow. G_2 checkpoint ensures that everything is ready to enter the M phase and

divide. Any errors in DNA duplication will be corrected. This is a preparatory phase for mitosis.

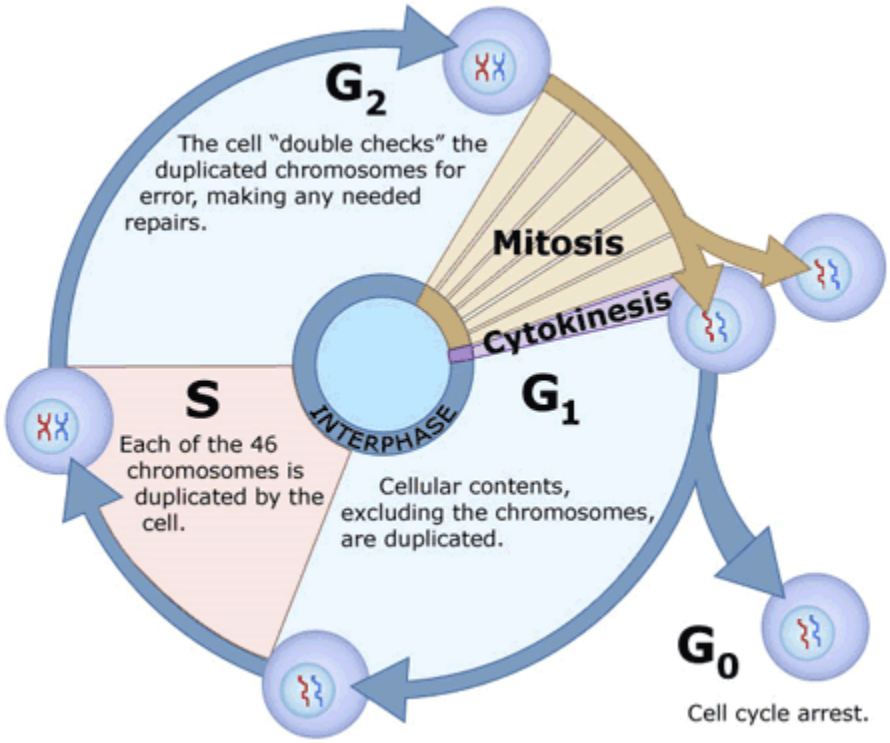

Figure (2-7) The cell cycle from reference [39]

During interphase, the cell might enter into G_0 phase, a quiescent or senescent phase. Non-proliferative cells or fully differentiated cells enter the quiescent state from G_1 and may remain quiescent for long periods of time, possibly indefinitely as in the case of neurons. Cells enter the senescent phase when their DNA is damaged. They are not able to divide any longer so their cell cycle stops until they die. Some cells enter the G_0 phase semi-permanently such as liver, kidney and stomach cells. Many cells do not enter G_0 and continue to divide throughout an organism's life such as epithelial cells.

At the end of G_2 phase the cell is ready to divide, so mitosis begins. During mitosis the chromosomes will divide into two chromatids.

When mitosis is completed, the cell will have divided into two identical daughter cells each having its own nucleus and cytoplasm. The M phase is considered the shortest phase of the cell cycle and accounts for approximately 10% of the cell cycle duration. The M phase has five consecutive steps as illustrated in figure (2-8) : prophase, prometaphase, metaphase, anaphase, and telophase, followed by cytokinesis [40].

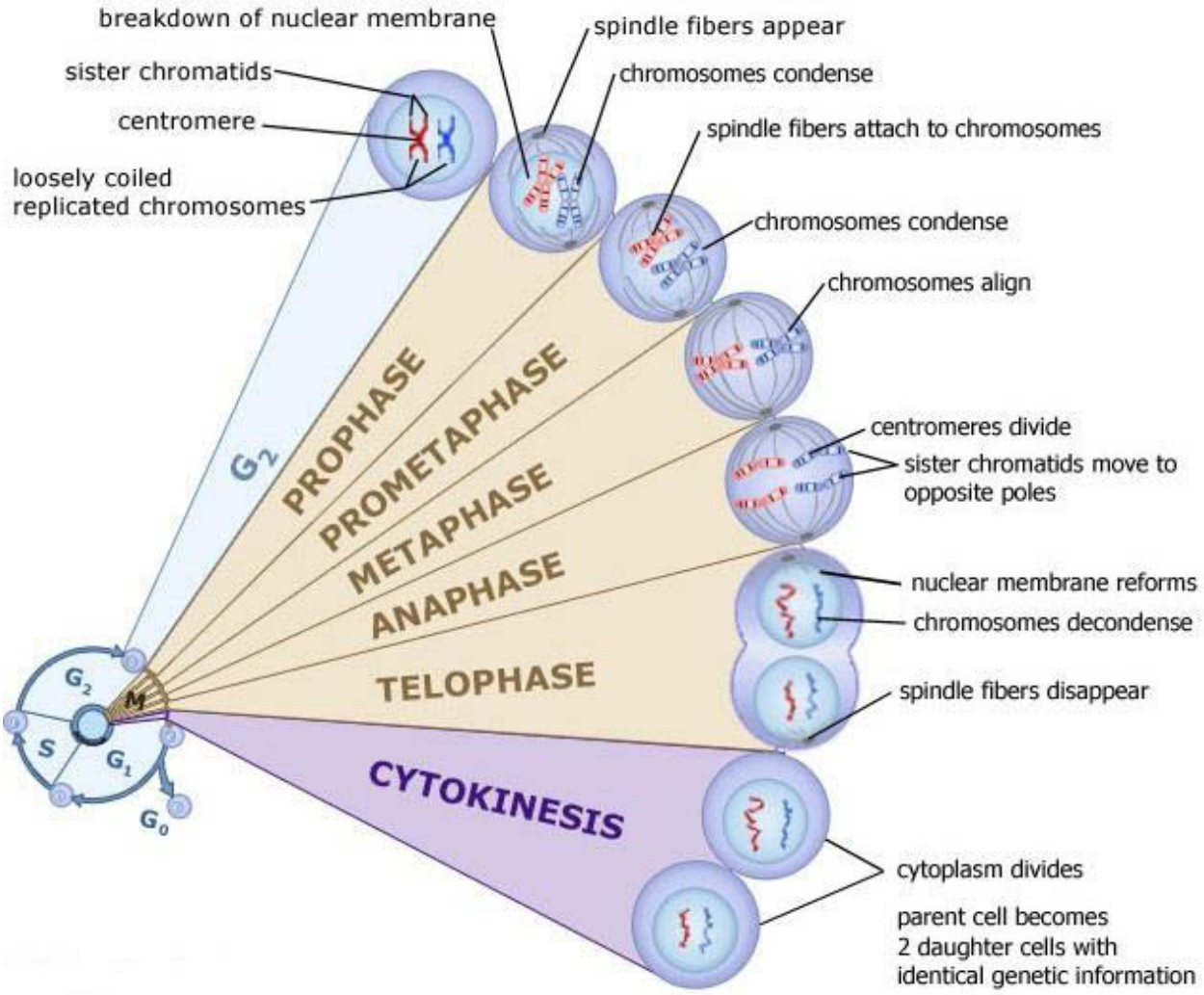

Figure (2-8) Cell Mitosis from reference [39]

The cell cycle progress is monitored and regulated by certain checkpoints to minimize the occurrence of mistakes in cell cycle events. These checkpoints stop the progress of the cell cycle to verify the DNA integrity and repair any damage. The cell cannot proceed to the next phase until checkpoint requirements have been met. Checkpoints consist of regulatory proteins that monitor and dictate the progression of the cell through different stages of the cell cycle [41]. They ensure that damaged or incomplete DNA is not passed on to daughter cells.

The three main checkpoints as illustrated in figure (2-9) are:

- **G_1/S checkpoint**: (restriction checkpoint) the cell checks whether the environment favors proliferation and whether its genome is ready for replication. Cell cycle is

stopped for checking and repairing DNA damages. If the damages can't be repaired the cell will die through apoptosis.

- **G_2/M checkpoint**: (DNA damage checkpoint) DNA replication is checked.
- **Metaphase checkpoint**: (mitotic spindle checkpoint) the cell cycle is arrested until all chromosomes are aligned on the spindles.

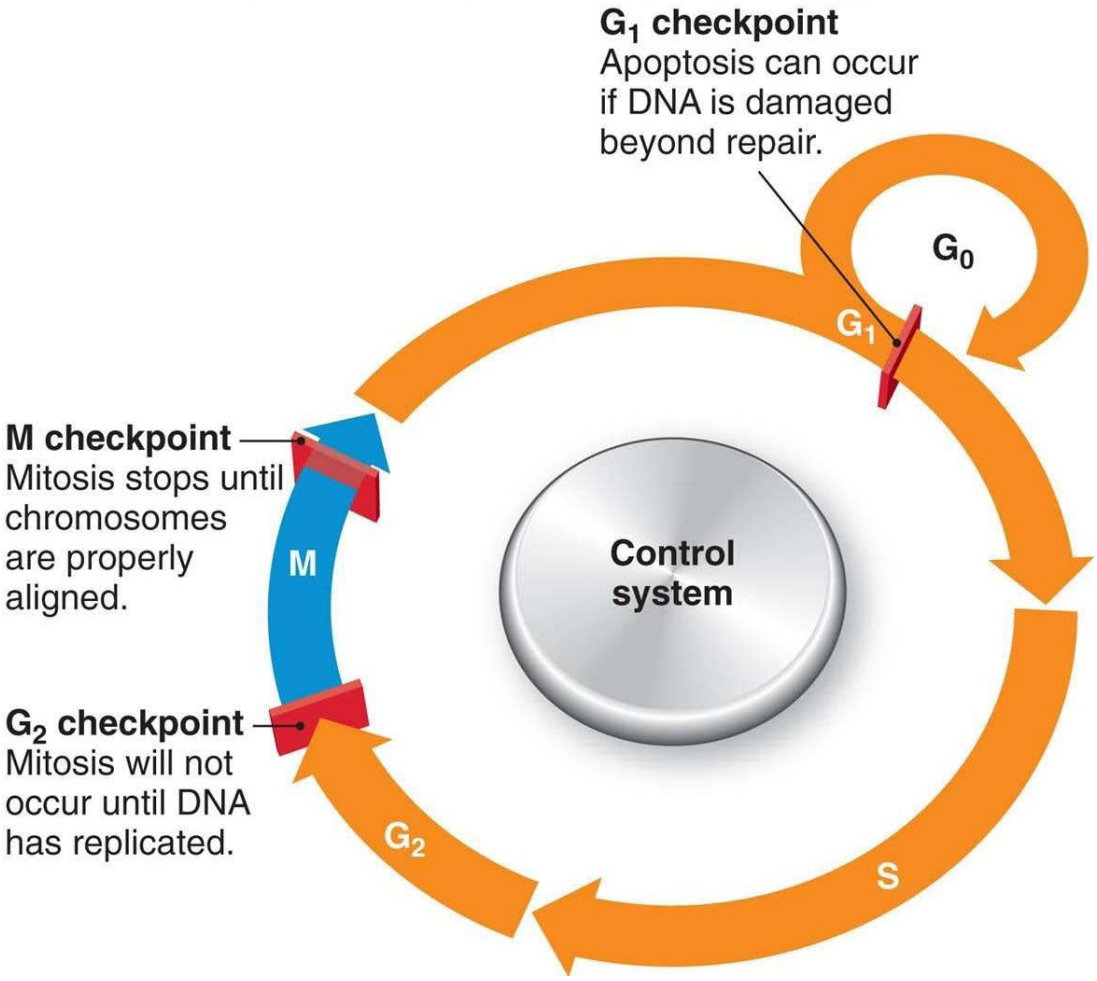

Figure (2-9) Cell Cycle Checkpoints from reference [42]

Checkpoint mechanisms arrest the cell cycle when genetic integrity is detected to prevent the transmission of genetic mutations to the subsequent cell generations. Thus mutations in any of the checkpoint genes contribute to a variety of human diseases such as cancer. It has been found that most cancers possess mutations in one or more checkpoint genes and are genetically unstable [43].

Genes that normally function to prevent malignancy such as p53 and Rb are called tumor suppressor genes. Mutant p53 proteins are found in at least 50% of all malignant tumors. Loss of p53 function could contribute to the development of cancer in several ways:

1. Cell cycle arrest in response to DNA damage would be compromised, presumably allowing a cell to accumulate additional mutations required for malignant transformation.
2. Apoptosis triggered by DNA damage and other events (such as cell-cell contact) may be compromised.
3. Telomere lengthening which regulate cell lifespan may be regulated by p53.

Loss of Rb function would allow cells to escape the growth factor requirement at the restriction point [41].

In short, cell cycle checkpoints permit the progress of cell cycle when all conditions are in favor of cellular division and restrict the progress otherwise. When checkpoint requirements are not met, the cell may die.

2.5 Cellular Death

The cell cycle is a very organized and well controlled process. Any dysfunction detected by the checkpoints will arrest the cycle and cell death is triggered. The types of cellular death are categorized as:

- **Necrosis**: Is death due to external unfavorable factors
- **Apoptosis**: Is a highly regulated process of programmed cell death.
- **Mitotic catastrophe**: Is the death caused by the inability of a cell to accomplish a normal mitosis due to unrepaired or undetected DNA damages by the control checkpoints[44].

Apoptosis is a form of programmed cell death carried out in a regulated process which is usually advantageous to the organism's life. In contrast, necrosis is an uncontrolled passive process caused by external injury to the cell and results in its premature death. Necrosis affects large fields of cells whereas apoptosis affects individual or clusters of cells.

Necrosis is caused by factors external to the cell or tissue such as infection, toxins or trauma (caused by radiation for example). Necrosis results in the swelling of the cell and dissolution of the chromatin due to enzymatic degradation by endonucleases. The cell membrane integrity is lost and cellular contents are released into the intracellular space [45]. This initiates an inflammatory response in the surrounding tissue.

However, in the case of apoptosis, phagocytosis of the cell components takes place without causing any inflammation. During apoptosis, the cell shrinks and the chromatin condenses

inside the nucleus. So the cell becomes smaller in size, the cytoplasm becomes dense and the organelles become more tightly packed. Extensive plasma membrane blebbing occurs followed by the destructive fragmentation of the nucleus. The cell fragments are then separated into apoptotic bodies during a process called "budding". The apoptotic bodies consist of cytoplasm with tightly packed organelles with or without a nuclear fragment. These bodies are subsequently phagocytosed and degraded by macrophages, parenchymal cells or neoplastic cells. Thus there is essentially no inflammatory reaction associated with apoptosis[46]. Figure (2-10) shows a graphical representation of apoptosis and necrosis.

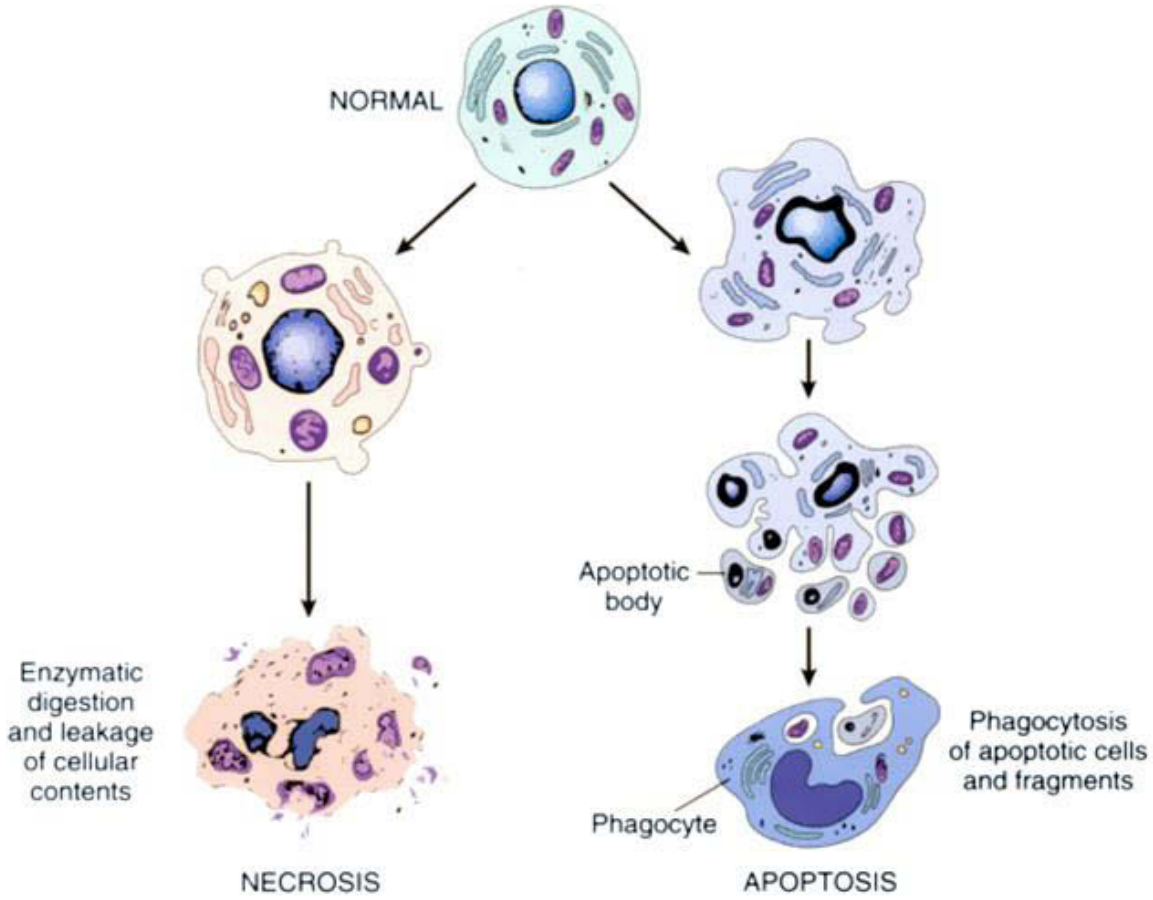

Figure (2-10) Apoptosis and Necrosis from reference [47]

Apoptosis plays a crucial role in developing and maintaining the health of the organism by eliminating old cells, unnecessary cells and unhealthy cells. When apoptosis does not work correctly, cells that should be eliminated may persist and become immortal causing cancer.

When apoptosis overworks, it kills too many cells and inflicts grave tissue damage. This is the case of strokes and neurodegenerative disorders such as Alzheimer's and Parkinson's diseases [46].

2.6 Role of Mitochondria in Apoptosis Control

Mitochondria are mainly responsible for energy production in the form of ATP through the electron transport chain process. This process takes place by transporting electrons through protein complexes found in the inner mitochondrial membrane. As part of the electron transport chain, cytochrome *c*, a protein associated with the inner mitochondrial membrane, has a well-defined and specific function in electron transfer between complex III and complex IV.

When the cell is subjected to certain stimuli such as growth factor withdrawal, absence of certain hormones, ionizing radiation, toxins, hypoxia, viral infections and free radicals, changes occur in the inner mitochondrial membrane. This results in the permeability of the inner membrane, loss of potential and the subsequent release of cytochrome *c* to the cytosol. Cytochrome *c* then activates the death protease caspase-3 that initiates apoptosis [48].

2.7 Radiation Damages

Ionizing radiation damages the structure and function of cells and tissues of the targeted biological material. It may consequently result in cancerization or death of the cells.

2.7.1 Radiation Effects: Physical, Chemical, Biological

Biological material is believed to contain 70% water[29], so it is widely accepted to consider water as viable substitute to biological matter. As the radiation beams traverse the biological material, the direct interaction occurs as ionization and excitation of atoms and molecules of the material known as the “direct action” of radiation. These physical interactions will produce a large amount of free electrons ready to interact with the surrounding medium consisting mainly of water.

Such amount of free electrons results in the production of highly reactive chemical compounds referred to as free radicals. These radicals can diffuse inside the cell and react with sensitive parts, the DNA molecule for example resulting in the “indirect action” of radiation on biological material. Consequently, the DNA integrity is compromised resulting in damages and mutations.

The damaged or mutated DNA will cause serious diseases on the long run, cancer being the most vicious. Cell death by apoptosis or necrosis may also be triggered.

Since ionizing radiation has detrimental effects on cells and tissues, it is used in the treatment of malignant tumors. In radiotherapy, ionizing radiation is directed towards the tumor targeting the cancerous cells in an attempt to kill them.

DNA damage naturally occurs all the time due to environmental agents such as ultraviolet radiation from sunlight and normal cellular metabolism products. The reactive oxygen

species derived from oxidative respiration and lipid peroxidation constitute a permanent enemy to DNA integrity from within [49].

Since DNA is subjected to a considerable amount of damage, cells have developed a repair mechanism to counteract the errors in DNA structure. After irradiation, the cell attempts to repair the damages produced by initiating the repair pathways. If the cell is successful in repairing the damages, it can reproduce and continue its lifecycle. However, if repair fails, the cell may die or may become cancerous.

The following figure (2-11) shows the radiation effects in time after the direct impact with the biological medium.

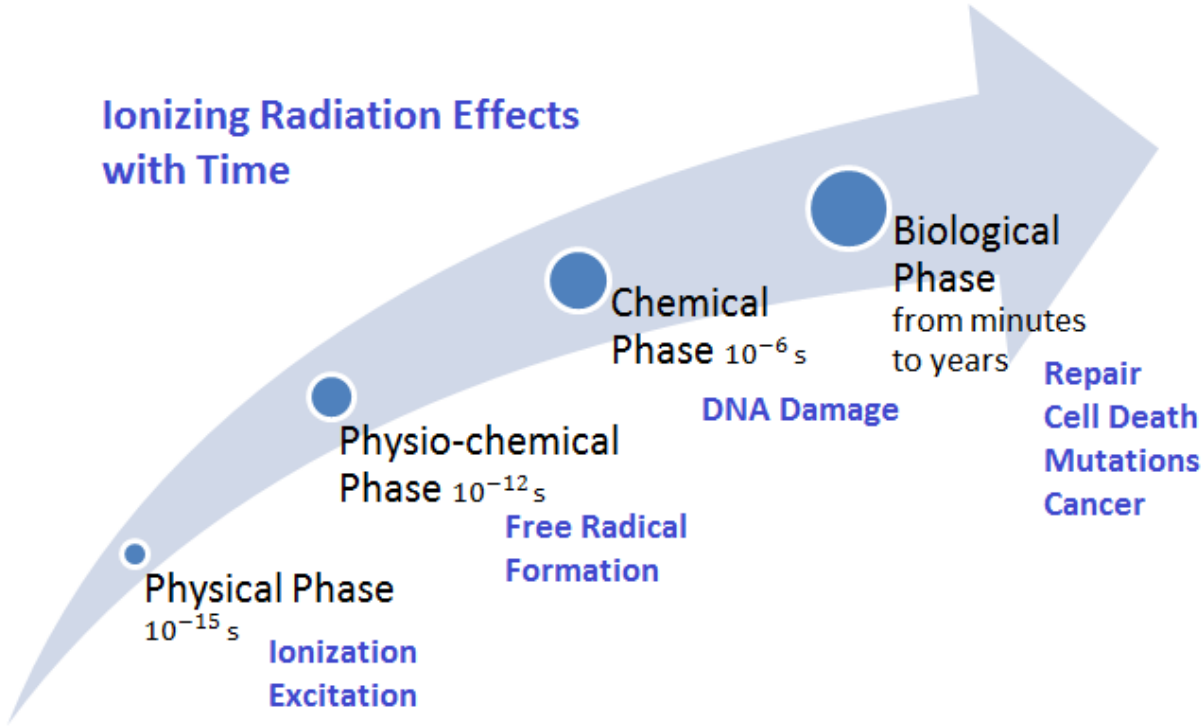

Figure (2-11) Stages of Ionizing Radiation Effects

2.7.2 **DNA damages and Mutations**

DNA damages are alterations in its chemical structure such as a break in a strand of DNA, a base missing from the backbone or a chemically changed base. DNA damage can be distinguished from mutation although both are types of error in DNA. DNA damage is an abnormal chemical structure in DNA, while a mutation is a change in the sequence of standard base pairs. However, DNA damage could lead to mutation when repair processes are not accurate.

Ionizing radiation induces damages to the DNA structure. As the radiation traverses the biological medium it induces ionization and excitation of the molecules of the medium. The DNA molecule is considered a sensitive target inside the cell, and a direct hit of the DNA by the radiation results in the alteration of its structure. The chemical bonds will be broken. An ionized DNA molecule may bind with a nearby compound. This changes the original structure of the DNA.

Ionizing radiation also affects the DNA indirectly by ionizing and exciting the biological medium surrounding the DNA consisting mainly of water. This eventually produces free radicals of the water molecules. These radicals are highly reactive and if produced in vicinity of the DNA will interact with it and produce changes in its chemical structure.

Figure (2-12) summarizes the direct and indirect damages on the DNA molecule.

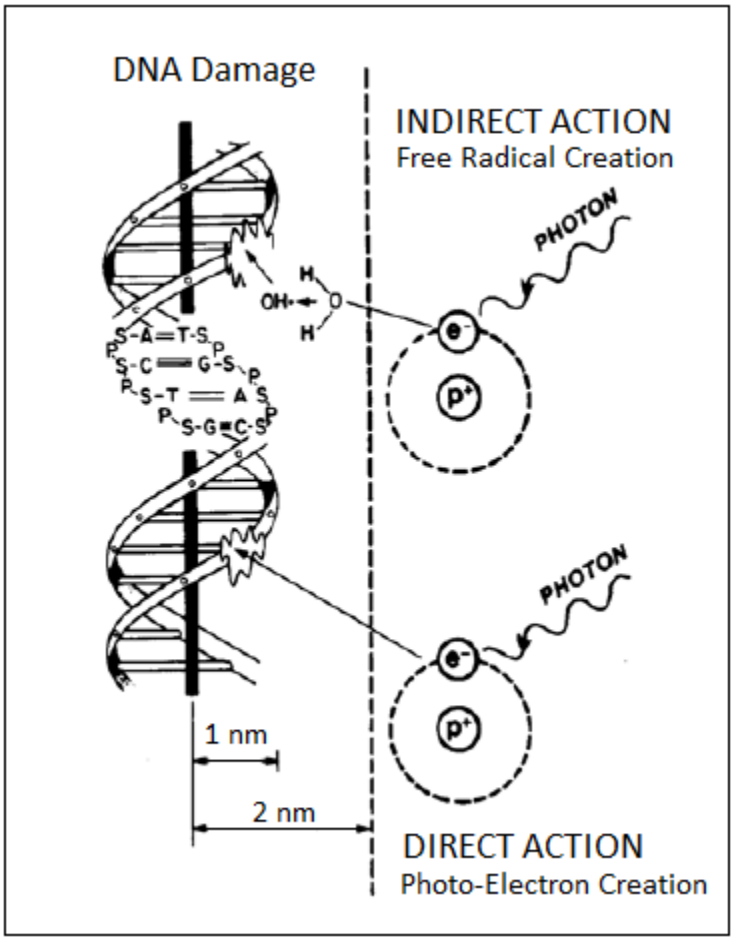

Figure (2-12) Direct and Indirect Radiation DNA Damages (figure adapted from[50])

a. Damages of the DNA Molecule

As discussed previously, after irradiation the physical and chemical changes take place inside the biological material. These changes affect the DNA structure in several ways inflicting serious damages to its unique shape. Breaks in one or both strands may result as direct effect of ionization. Indirect effects of irradiation in the form of free radical attack on the chemical bonds results in strand breaks and the deletion or alteration of the nucleobases. The most distinguished types of DNA damages [51] are listed below and illustrated in figure (2-13)

- Single and Double Strand Breaks
- DNA bases loss
- Chemical modification of DNA bases
- DNA-protein crosslinks
- Inter and Intra-strand crosslinks

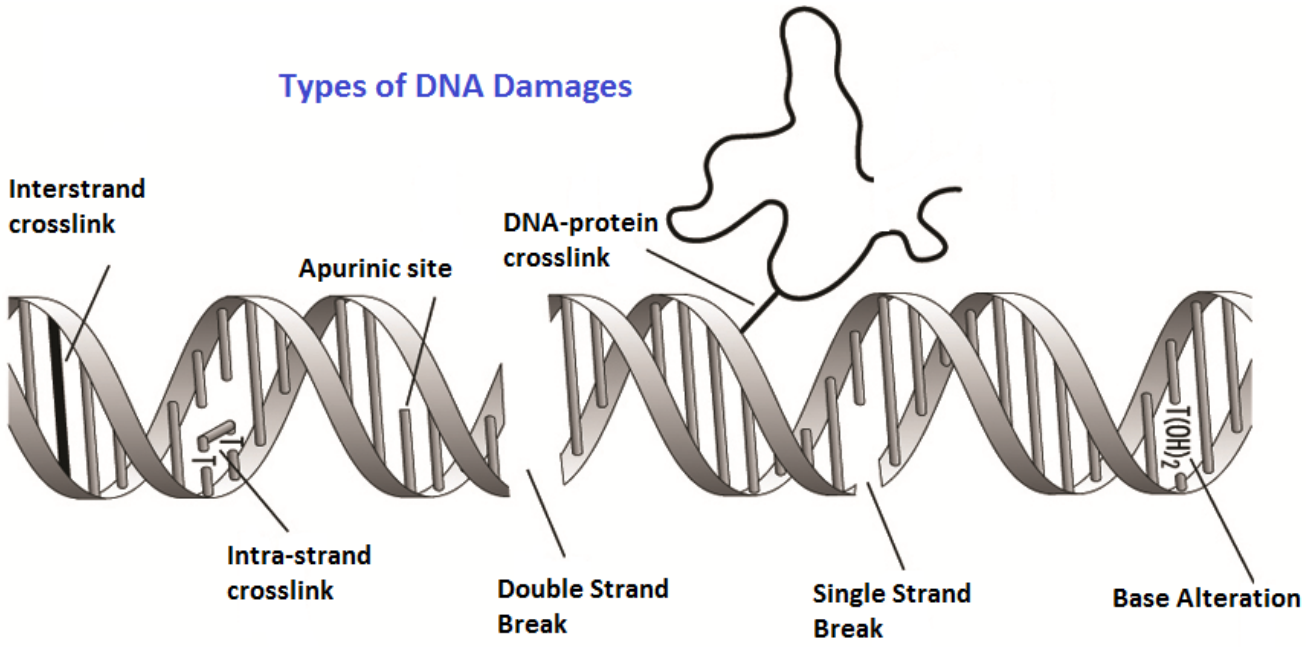

Figure (2-13) Damages of the DNA Molecule (figure adapted from[52])

b. Irradiation Induced Mutations

Mutation is a natural process that changes the DNA sequence. As a cell replicates its DNA before dividing, an error occurs. However, damage induced mutation is more likely to happen when the organism is subjected to radiation. Radiation DNA damages may result in the change of its sequence causing a mutation. There are many types of mutations listed below and illustrated in figure (2-14):

- **Deletion**: Parts of a chromosome are deleted meaning that a section of DNA is missing
- **Duplication**: Part of a chromosome is repeated meaning that there are many copies of some genes
- **Inversion**: a DNA sequence is reversed within a chromosome
- **Insertion**: a new base or section of DNA is added to a chromosome
- **Translocation**: a part of one chromosome is moved to or exchanged with a different chromosome

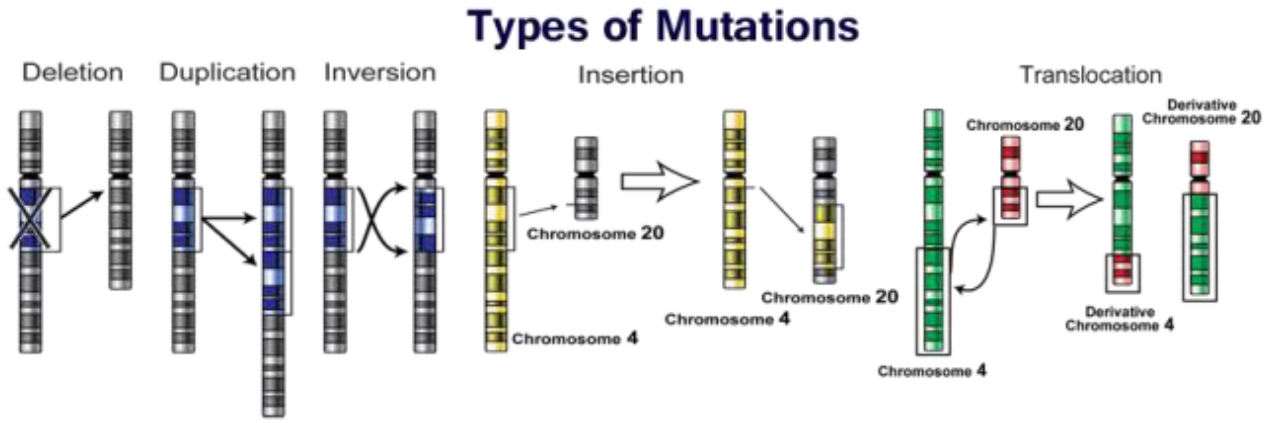

Figure (2-14) Types of Mutations from reference [27]

Mutations in genes can have no effect (silent mutations), alter the product of a gene, or prevent the gene from functioning properly or completely. The change in the DNA sequence could result in changing the sequence of the coded proteins, leading to new properties. This may be good for the organism such as inducing evolutionary traits to cope with the environmental changes. For example, a butterfly may produce offspring with mutation of color making it harder for predators to see. Over time the number of butterflies with this mutation may form a larger percentage of the population. The mutation may also be bad for the organism resulting in a poorly or non-functioning protein.

p53 is a tumor suppressor gene. It encodes a protein responsible for protecting the cell against carcinogenesis. It activates DNA repair in case of detected damage, arrests the cell cycle and consequently initiates apoptosis if damage is irreparable. The mutation or deletion of this gene will make the cell vulnerable to cancer [53].

c. Chromosomal aberration

Chromosome abnormality or aberration is a missing, extra or irregular portion of chromosomal DNA. It can be from an atypical number of chromosomes or a structural abnormality in one or more chromosomes.

Chromosomal aberrations can be numerical as in an abnormal number of chromosomes. This happens when an individual has a missing chromosome from a pair (monosomy), or has more than two chromosomes of a pair (trisomy, tetrasomy, etc.).

They can also be structural when the chromosome's structure is altered. Double strand breaks and mis-repaired double strand breaks are mostly responsible for structural chromosomal aberrations. These abnormalities include deletions, duplications, translocations, inversions and insertions. Theses abnormalities are illustrated in figure (2-14).

2.7.3 Effects on Mitochondria:

a. Mitochondrial DNA Damage

Mitochondria contain their own genome and similar to nuclear DNA, the circular mtDNA is subject to radiation induced damages in the form of single and double strand breaks, base mismatches and large deletions. In addition, mtDNA is susceptible to mutations. Since it lacks histone protection and has a limited capacity to repair the damages, that makes it prone to frequent mutations [1].

A mitochondrion contains multiple copies of its genome. The proper control of the mtDNA copy number is believed to be important for normal cell function. An increase in the mtDNA copy number after radiation stimulation, termed "mitochondrial polyploidization", is believed to be a compensatory mechanism or an adaptive response of mitochondria to maintain function in post irradiated cells. The intact or partially damaged mtDNA might then replicate to compensate for the loss and maintain mitochondrial function. This is correlated with increase in oxidative stress levels and an increase in mitochondrial mass. Although such increase in the mitochondrial content could be a transient gain that later might strain the cells as more resources are needed to support this high proliferation and to cope with the subsequent increase in reactive oxygen species [1].

b. Effects on Cellular Respiration

Mitochondria are mainly responsible for energy production for the cell in the form of Adenosine Triphosphate (ATP), a molecule that stores energy chemically in the form of highly strained bonds. This process is called oxidative phosphorylation performed by members of the electron transport chain, mainly enzymes and compounds (complexes I, II, III, and IV, ubiquinol and cytochrome *c*) found in the inner membrane of a mitochondrion that transfer electrons from electron donors via redox reactions and also transfer of protons (H^+ ions) across the inner membrane into the intermembrane space. This creates an electrochemical proton gradient that drives the synthesis of ATP through ATP synthase [27].

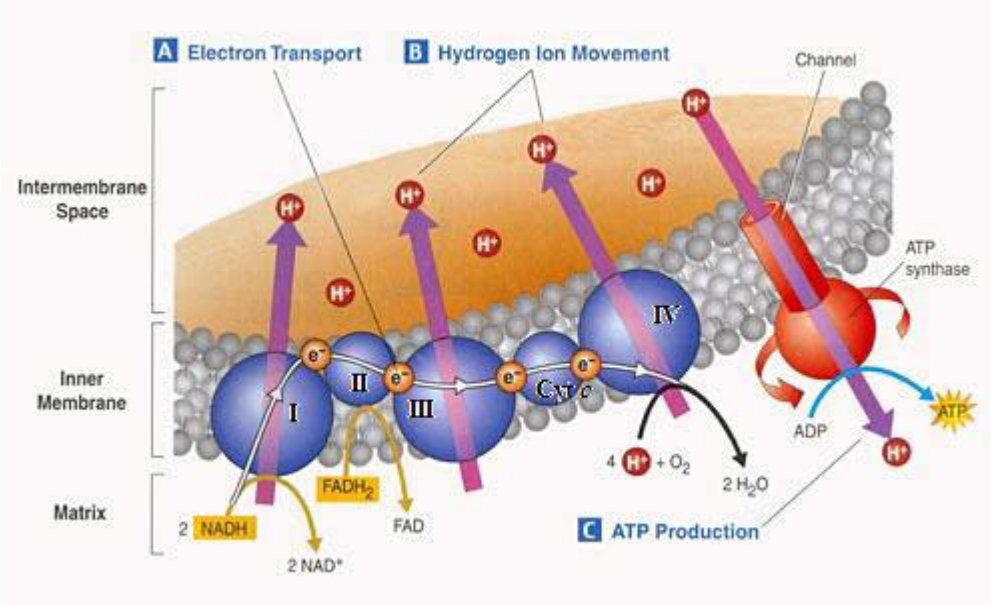

Figure (2-15) Electron Transport Chain and ATP Synthesis from reference [54]

The process of cellular respiration creates chemical energy as ATP following oxidation of carbohydrates, fatty acids or proteins. Glucose for instance is broken down in the cytosol outside the mitochondrion during glycolysis producing 2 molecules of ATP for each glucose molecule. After glycolysis, the remnants of glucose in the form of pyruvates enter into the mitochondria. The pyruvates are oxidized after which the citric acid cycle takes place in the mitochondrial matrix finally producing few ATPs, NADH and FADH2. NADH and FADH2 are then used as electron donors by the electron transport chain.

The buildup of H^+ ions in the inter-membrane space creates a proton potential leading to protons funneling through ATP synthase protein in the inner membrane by a process called chemiosmosis. Consequently, the ATP synthase spins to create ATP from ADP and

inorganic phosphate. Thus, the proton potential provides the energy for making ATP. The electron transport chain process producing ATP is summarized in figure (2-15).

Ionizing radiation affects the oxidative phosphorylation by inhibiting or partially deactivating the activity of electron transport chain members. Consequently, the whole process is slowed down resulting in ATP content reduction. Oxidative phosphorylation is altered for a while (about 12 hours) by irradiation after which this process is later recovered [1].

An experiment carried out by Daya *et al.* [55] irradiating hamster fibroblast cells with 10 Gy X-rays shows a 20-40% decrease in the mitochondrial membrane potential and an increase in mitochondrial content compared to control. The change in membrane potential indicates a mitochondrial dysfunction. This suggests that radiation exposure results in mitochondrial function injury causing the cells to increase mitochondrial mass in order to maintain adequate levels of ATP from oxidative phosphorylation.

c. Oxidative Stress

Reactive oxygen species (*ROS*) are chemically reactive molecules containing oxygen such as peroxides, superoxide and hydroxyl radical. They are formed as natural by products of the normal metabolism of oxygen in the body and have important roles in cell signaling and homeostasis. They are also generated by exogenous sources such as pollutants, tobacco, smoke, drugs and ionizing radiation. The cells usually keep a balance between the production and elimination of *ROS* by a protective mechanism of antioxidants such as glutathione in reduced state (*GSH*). However, if this imbalance is disturbed the cells suffer from over accumulation of *ROS* wreaking havoc on their structure and function. This imbalance is also known as oxidative stress [56].

Oxidative stress levels are likely to rise when mitochondria are damaged or impaired. Electrons may leak during transport within the electron transport chain [1]. The partial reduction of an oxygen molecule (O_2) by a free electron generates a superoxide anion ($O_2^{-\bullet}$), which is the precursor of most ROS.

$$O_2 + e^- \longrightarrow O_2^{-\bullet} \qquad (2\text{-}1)$$

Dismutation of superoxide produces hydrogen peroxide (H_2O_2),

$$2H^+ + O_2^{-\bullet} + O_2^{-\bullet} \longrightarrow H_2O_2 + O_2 \qquad (2\text{-}2)$$

Hydrogen peroxide in turn may be partially reduced to hydroxyl radical ($OH^{\bullet}$) by Fenton reaction that is catalyzed by transition metals such as Fe^{2+}, Cu^{2+} and Ni [57]

$$H_2O_2 + Fe^{2+} \longrightarrow OH^- + OH^{\bullet} + Fe^{3+} \qquad (2\text{-}3)$$

It can also be fully reduced to water [58],

$$H_2O_2 + H_2O_2 \longrightarrow H_2O + H_2O + O_2 \qquad (2\text{-}4)$$

Hydrogen peroxide, a precursor of hydroxyl radical, can diffuse through the nucleus and reach DNA. This makes the DNA vulnerable to hydroxyl radical damage. *ROS* induced DNA damage can result in single- or double-strand breakage, base modifications, deoxyribose modification, and DNA cross-linking. Cell death, DNA mutation, replication errors, and genomic instability can occur if the oxidative DNA damage is not repaired prior to DNA replication.

The most extensively studied and the most abundant oxidative DNA lesion produced is 8-hydroxydeoxy guanosine(8-OHdG) which is mutagenic in bacterial and mammalian cells. Numerous studies have demonstrated that 8-OHdG levels are elevated in various human cancers. Thus, it has been widely used as a biomarker of oxidative DNA damage, and measurement of 8-OHdG level is applied to evaluate the load of oxidative stress.

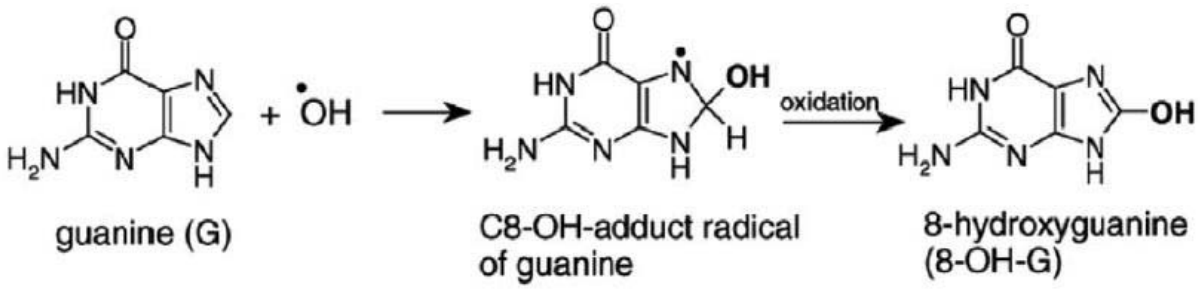

Figure (2-16) Hydroxyl radical reacting with guanine [57]

ROS may attack the lipids in the cell membrane in a process called lipid peroxidation. This initiates a self-propagating chain reaction resulting in the destruction of membrane lipids. This compromises the viability of cells and tissues [59].

Furthermore, *ROS* are used by the cells as part of their defense against pathogens. Superoxide anion is produced by *NADPH* oxidases from O_2 and *NADPH*. These enzymes were originally described in phagocytes where they were shown to kill engulfed pathogens by creating high levels of local oxidative stress. In normal conditions *ROS* serve a controlled function in cells rather than simply acting as toxic byproducts [60].

However, uncontrolled levels of oxidative stress prove to be detrimental. For example, mitochondria directly hit by ionizing radiation are subjected to a transition in their permeability. Ca^{2+}ions are released to be taken up by adjacent mitochondria which then

depolarize, leading to a subsequent increase in *ROS* production. The Ca^{2+} ion could act as a signaling molecule in a chain reaction among the mitochondria after irradiation, leading to the propagation and amplification of the *ROS* signal. This chain reaction would then reach and impact the nucleus. Such imbalance in mitochondrial *ROS* might form a positive feedback mechanism for more depolarization and greater *ROS* production leading to further cell damage [1].

In addition, highly damaged mitochondria will cause cytochrome *c* to leak from their inner membrane to the cytoplasm initiating apoptotic pathways.

To overcome the destructive action of *ROS*, cells developed natural antioxidant defense mechanisms. Enzymes such as catalase and superoxide dismutase are found in the cell to react with *ROS* and limit their action. Vitamins A and E are non-enzymatic natural antioxidants which can also counteract the effects of *ROS*.

High levels of oxidative stress have been monitored in many diseases such as the neurodegenerative conditions of Alzheimer's disease, Huntigton's disease, and Parkinson's disease. Although levels of oxidative DNA damage are not specifically elevated, the major significance for the pathogenesis of these diseases has been placed on lipid and protein oxidation.

There is also a growing evidence for the involvement of *ROS* in atherosclerotic plaque development in cardiovascular disease. Oxidative stress is believed to contribute to aging as well. The free radical theory of aging described by Harman suggests that aging occurs through the gradual accumulation of free radical damage to biomolecules. The failure of antioxidant defenses to scavenge all radical species, evident from the increasing background levels of damage with age, will result in the accumulation of damage and gradual loss of function [61].

2.7.4 **DNA Repair mechanisms**

DNA integrity and stability is crucial in maintaining a correct cell behavior. Damage to DNA can interfere with essential cellular processes such as transcription and replication and can compromise the viability of the cell. Specific DNA damages or lesions induce mutations resulting in cancer and other diseases. Consequently, cells have evolved a network of DNA repair mechanisms to fix different types of DNA damage. DNA damage response is a highly coordinated cascade of events that senses the damage, signals its presence and initiates its repair.

Upon sensing damage the cell cycle is arrested allowing efficient DNA damage repair prior to replication of mitosis. If the damage proves to be persistent or irreparable, apoptotic pathways are then signaled to prevent the damage from spreading to future cell generations and inflicting cancer or disease.

To compensate for the many types of DNA damage that occur, cells have developed multiple repair mechanisms where each corrects a different type of lesions. At minimum, mammalian cells utilize five major DNA repair mechanisms [51] :

- **Base Excision Repair**: the damaged, deformed or lost bases are detected and cleaved. New bases are then introduced using the other strand as a complementary template.
- **Mismatch Repair**: responsible for post-replication repair of mis-incorporated bases that have escaped proofreading activity of replication polymerases
- **Nucleotide Excision Repair**: removes a wide variety of bulky helix-distorting lesions such as inter- and intra-strand crosslinks
- **Homologous Recombination**: repairs double strand breaks. It uses the genetic information contained in the undamaged sister chromatid as a template and thus is an error-free mechanism.
- **Non-Homologous End-Joining**: repairs double strand breaks. It is an error-prone mechanism and involves elimination of DSBs by direct ligation of the broken ends, which is the covalent linking of the two ends of DNA by DNA ligase.

The deregulation of DNA repair mechanisms contributes to the initiation and progression of cancer. The unrepaired DNA eventually turns the cell cancerous. Moreover, disorders such as *Ataxia-telangiectasia*, *Fanconi anemia* and *Xeroderma pigmentosum* are caused by DNA repair deficiencies [62].

2.8 Conclusion

The health and vitality of the cell is mainly controlled by the integrity of the DNA molecules stored in the nucleus in the form of chromosomes. When the genome is intact the cell goes through its regular cycle of growth and duplication also known as interphase and mitosis. However, when errors occur in the DNA structure the cycle is arrested for repairs. In case the repairs are incorrect or inapplicable, the cell goes through apoptosis. If for some reason, apoptosis was not triggered, the deformed DNA produces mutant genes that dictate changes in the cell's replications that might potentially lead to cancer.

Mitochondria play an important role in the cell's life. In addition of providing energy for the cell to produce proteins, grow and replicate they also control apoptosis. Therefore, mitochondrial damage or dysfunction is related to many neurodegenerative diseases as well as cancer.

Ionizing radiation affects biological material directly by ionization and excitation of the atoms or molecules of the medium. Its indirect effects rise from the *ROS* produced by the free electrons originally released by the ionization process. The direct and indirect

interactions with the DNA molecule induce damages in its structure leading to catastrophic consequences if these damages are not correctly repaired.

After exposure to ionizing radiation, mitochondria are affected as well. Mitochondrial DNA will be subjected to damage and mutations. Oxidative phosphorylation will be inhibited reducing ATP production. In addition, the potential damage to the inner membrane will release cytochrome *c* into the cytoplasm initiating apoptosis. The uncontrolled increase in *ROS* after radiation exposure affects the chemical balance of the cell and puts it under oxidative stress leading to many diseases.

Although they are subjected to many environmental factors risking their health and existence, cells have developed very efficient damage repair mechanisms. DNA damages are sensed and their repair is carried out after arresting the cell cycle to prevent the progression into future generations. *ROS* over production is also controlled by producing enzymes such as catalase and using the antioxidant properties of vitamins A and E.

1. *Wikipedia the Free Encyclopedia*. Available from: https://en.wikipedia.org.
2. *Eukaryotic Cell Structure*. Available from: http://www.thinglink.com/scene/322015525372690433?buttonSource=userPage.
3. Fang, F., et al., *Mitochondrial modulation of apoptosis induced by low-dose radiation in mouse testicular cells.* Biomedical and Environmental Scineces, 2013. **26**: p. 820-830,.
4. Alberts, B., et al., *Essential Cell Biology: An Introduction to the Molecular Biology of the Cell*. 1998, Garland Publishing.
5. Kam, W.W.Y., et al., *Predicted ionization in mitochondria and observed acute changes in the mitochondrial transcriptome after gamma irradiation: a Monte Carlo simulation and quantitative PCR study.* Mitochondrion, 2013. **13**(6): p. 736-742.
6. Pfeiffer, R.F., Z.K. Wszolek, and M. Ebadi, *Parkinson's Disease*. 2012, CRC Press.
7. Jakobs, S. *Structure and Dynamics of Mitochondria*. Available from: www.mpibpc.mpg.de/jakobs.
8. *United Mitochondrial Disease Foundation*. Available from: https://www.umdf.org/what-is-mitochondrial-disease/.
9. *Science Learning*. 2011; Available from: http://sciencelearn.org.nz/Contexts/Uniquely-Me/Science-Ideas-and-Concepts/DNA-chromosomes-and-gene-expression.
10. *Structure of the double helix*. Available from: https://geneed.nlm.nih.gov/.
11. *Science Learning Hub*. Available from: https://www.sciencelearn.org.nz/images/198-cell-chromosomes-and-dna.
12. Anderson, S., et al., *Sequence and organization of the human mitochondrial genome.* Nature, 1981. **290**: p. 457 - 465.

13. Montier, L.L.C., J. Deng, and Y. Bai, *Number matters: control of mammalian mitochondrial DNA.* Journal of Genetics and Genomics, 2009. **36**: p. 125-131.
14. Moura, M.B.d., L.S.d. Santos, and B.V. Houten, *Mitochondrial dysfunction in neurodegenerative diseases and cancer.* Environmental and Molecular Mutagenesis, 2010. **51**: p. 391-405.
15. *University of Leicester*. Available from: http://www2.le.ac.uk/departments/genetics/vgec/schoolscolleges/topics/cellcycle-mitosis-meiosis.
16. Morgan, D.O., *The Cell Cycle: Principles of Control*. 2007: New Science Press.
17. Novak, B., J.C. Sible, and J.J. Tyson, *Checkpoints in the Cell Cycle.* Encyclopedia of Life Sciences, 2002.
18. *The cell cycle*. Available from: https://www.studyblue.com.
19. Lengauer, C., K.W. Kinzler, and B. Vogelstein, *Genetic instabilities in human cancers.* Nature, 1998. **396**: p. 643-649.
20. Castedo, M., et al., *Cell death by mitotic catastrophe: a molecular definition.* Oncogene, 2004. **23**: p. 2825–2837.
21. Majno, G. and I. Joris, *Apoptosis, Oncosis, and Necrosis: An overview of cell death.* American Journal of Pathology, 1995. **146**(1).
22. Elmore, S., *Apoptosis: A Review of Programmed Cell Death.* Toxicologic Pathology, 2007. **35**: p. 495-516.
23. *Programmed cell death apoptosis*. Available from: https://medicinembbs.blogspot.com/2011/03/programmed-cell-death-apoptosis.html.
24. Cai, J., J. Yang, and D.P. Jones, *Mitochondria control of apoptosis: The role of cytochrome c.* Biochimia et Biophysics Acta, 1998. **1336**: p. 139-149.
25. Cadet, J., et al., *Oxidative damage to DNA: formation, measurement, and biological significance.* Reviews of Physiology Biochemistry and Pharmachology, 1997. **131**: p. 1-87.
26. Tubiana, M., J. Dutreix, and A. Wambersie, *Introduction to Radiobiology*. 1990.
27. Mathews, L.A., S.M. Cabarcas, and E.H. E., *DNA Repair of Cancer Stem Cells*. Vol. VIII. 2013: Springer.
28. *Encyclopaedia of Occupational Health and Safety*. Available from: http://www.iloencyclopaedia.org/part-iv-66769/toxicology-57951/mechanisms-of-toxicity.
29. Pientenpol, J.A. and Z.A. Stewart, *Cell cycle checkpoint signaling: cell cycle arrest versus apoptosis.* Toxicology, 2002. **181-182**: p. 475-481.
30. Kam, W.W.-Y. and R.B. Banati, *Effects of ionizing radiation on mitochondria.* Free Radical Biology and Medicine, 2013. **65**: p. 607-619.
31. *Study.com*. Available from: http://study.com/academy/lesson/mitochondrial-christae-definition-function-quiz.html.
32. Daya, D., et al., *Mitochodrial Complex II dysfunction can contribute significantly to genomic instability after exposure to ionizing radiation.* Radiation Research Society, 2009. **172**(6): p. 737-745.
33. Nogueira, V. and N. Hay, *Molecular Pathways: reactive oxygen species homeostasis in cancer cells and impications for cancer therapy.* Clinical Cancer Research, 2013. **19**(16): p. 4309-4314.

34. Klaunig, J.E., L.M. Kamendulis, and B.A. Hocevar, *Oxidative stress and oxidative damage in carcinogenesis.* Toxicologic Pathology, 2010. **38**: p. 96-109.
35. Turrens, J.F., *Mitochondrial formation of reactive oxygen species.* Journal of Physiology, 2003. **552**(2): p. 335-344.
36. Mylonas, C. and D. Kouretas, *Lipid peroxidation and tissue damage.* In Vivo, 1999. **13**(3): p. 295-309.
37. Sullivan, L.L. and N.S. Candel, *Mitochondrial reactive oxygen species and cancer.* Cancer and Metabolism, 2014. **2**(17).
38. Cooke, M.S., et al., *Oxidative DNA damage: mechanisms, mutation, and disease.* The FASEB Journal, 2003. **17**.
39. McKinnon, P.J., *DNA repair deficiency and neurological disease.* Nature Reviews Neuroscience 2009. **10**(2): p. 100-112.

3 Ionizing Radiation and Biological Matter

Ionizing radiation are all forms of radiation that removes bound electrons from the orbitals of atoms of the material they interact with resulting in ionizing these atoms. There are two types of ionizing radiation: neutral and charged. Neutral ionizing radiation consists of electromagnetic radiation and neutrons, while charged ionizing radiation consists of a large range of charged particles such as electrons, positrons, protons, alpha particles and many other ions that can be accelerated into beams through cyclotrons and synchrotrons.

For medical applications, X-rays are mostly used. They are commonly used in radiography, CT scanning and radiotherapy of cancer. Other particle beams are recently used for cancer therapy such as electron beams, protons beams, and alpha particle beams. For example, hadron therapy use charged particles such as protons, alpha particles and other heavy ions such as carbon ions in cancer treatment. Hadron therapy is believed to be a more efficient cancer treatment since these heavy particles deliver their energy in a more precise location than x-rays and they traverse the biological medium in a straight path. Therefore, they dump most of their energy in the tumor site preventing the surrounding healthy area from their damaging effect.

3.1 Interaction with Biological Matter

When irradiating biological material with some kind of ionizing radiation, interaction takes place at different phases in time.

- The first phase is the *physical phase* which takes place directly after irradiation.
- Then the *physio-chemical* phase takes place followed by the *chemical phase*.
- And the last phase is the *biological phase* where the long-term effects of radiation start to manifest.

3.1.1 Direct Effects

Directly after irradiation, the physical effects start to take place. As the radiation traverses the material it interacts elastically and in-elastically with its atoms and molecules. The radiation particles will collide with the atoms and the molecules. The elastic collisions will conserve the kinetic energy of the incident particles changing only their direction of propagation. However, the inelastic collisions will transfer some of the incident particle's energy to the target particles causing the incident particles to gradually lose their energy and eventually stop inside the material. The energy transferred to the target material will result in ionizations and excitations of its atoms and molecules.

The electrons of the atoms and the molecules will absorb the energy transferred to them by the incident ionizing particle. The electrons will get excited to a higher energy level after

which they relax to lower states ejecting a photon or an electron. In figure (3-1) atomic excitation and de-excitation are represented. The atom absorbs energy by photo-absorption such that the photon loses all its energy to a bound electron in the atom. The electron having more energy will transfer to a higher orbital in the atom and the atom is said to be excited. The excited atom then relaxes to its ground state by relaxing the electron to its initial level emitting a photon with the excess energy.

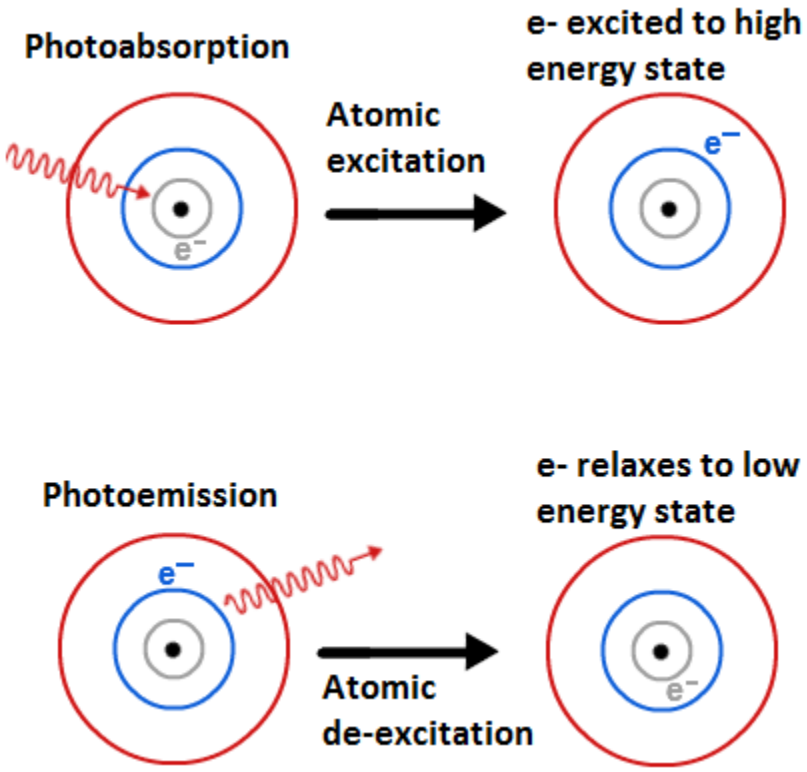

Figure (3-1) Excitation and Relaxation of an Electron after Irradiation, figure adapted from reference [1]

Sometimes the energy absorbed by target electrons is not enough to induce electronic excitations to higher levels. In this case the atoms and molecules undergo vibrational excitations.

If the energy transferred to the electrons is enough to overcome the electromagnetic pull of the nucleus, also known as the binding energy, they will be ejected outside the atom resulting in an ionized atom and a free electron. Figure (3-2) illustrates the ionization of an atom by ejecting one of its electrons away.

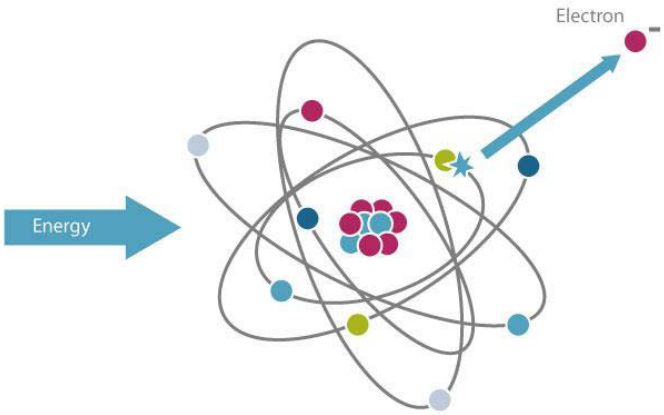

Figure (3-2) Electron Ejection by Ionization, from reference [2]

3.1.2 Indirect Effects

After $10^{-15}s$ from irradiation, the physico-chemical phase begins. The excitations and ionizations create free electrons and positively charged holes. The holes correspond to the ionized molecules lacking an electron. These electrons and holes are very likely to interact with the surrounding bound molecules breaking their chemical bonds and turning them into free radicals.

At $10^{-12}s$ the chemical phase takes place. The electrons and holes of the previous stage will have interacted with the surrounding molecules leaving the medium with a high concentration of highly interacting free radicals. These free radicals diffuse in the medium interacting with sensitive molecules such as DNA [3], breaking their bonds and damaging their structure.

At $10^{-6}s$ the biological phase begins resulting from the damage caused by both physical and chemical phases to the cell as a whole and particularly the DNA. The cells start to detect the damages in their structure and repair mechanisms are activated. If the damages are not fully or correctly repaired, mutations of DNA will occur and the cell may become cancerous or die. The biological effects take place over a long period of time ranging from few minutes, till hours or even several years.

3.1.3 Water Radiolysis

The human cell consists approximately of 70% water [4], so the biological material can be considered equivalent to liquid water. The water molecule has five ionization states and five excitation states. After ionization takes place, a free electron is ejected to the surrounding medium causing further ionizations and excitations, leaving an ionized molecule with high ability to interact with other bound molecules. This is the beginning of a chain of chemical reactions generally known as water radiolysis [5, 6].

The interaction of ionizing radiation with water results in alteration of the structure of water molecules through a process called water radiolysis. The bound molecules of water are broken into highly reactive radicals called reactive oxygen species. The term radical is used to describe an atom or a group of atoms containing an unpaired electron which results in great chemical reactivity. Radicals are represented by adding a dot to the chemical symbol. A radical can be neutral or charged (radical ion). For example, radicals like $HO^{\bullet}$ and $H^{\bullet}$ are produced in the course of water radiolysis and are very reactive. They are distinguished from the ions OH^- and H^+ formed in the spontaneous ionic dissociation of water which do not have unpaired electrons and are chemically unreactive [7].

Figure (3-3) summarizes the stages of radiation interaction in water starting from the physical stage of ionization and excitation, going through the physico-chemical stage and ending at the chemical stage. The final results of water radiolysis process are the reactive oxygen species that wreak havoc on the cells and tissues of an organism. Some of these radicals recombine with each other to form water molecules directly after they are produced. The rest diffuse rapidly away from their production position and interact with molecules of the medium especially the DNA molecule causing mutations.

The hydroxyl radical $HO^{\bullet}$ is extremely reactive and immediately removes electrons from any molecule in its path, turning that molecule into a free radical thus propagating a chain reaction. On the other hand, hydrogen peroxide H_2O_2 has lower reactivity than the hydroxyl radical. This provides enough time for H_2O_2 to diffuse into sensitive sites such the cell's nucleus and reach the DNA molecule which makes it more damaging to DNA than the hydroxyl radical.

Hydrogen peroxide H_2O_2 can partially reduce to hydroxyl radical $HO^{\bullet}$ or fully reduce to water [8].

$$H_2O_2 \longrightarrow HO^{\bullet} + HO^{\bullet} \qquad (3\text{-}1)$$

$$H_2O_2 + H_2O_2 \longrightarrow H_2O + H_2O + O_2 \qquad (3\text{-}2)$$

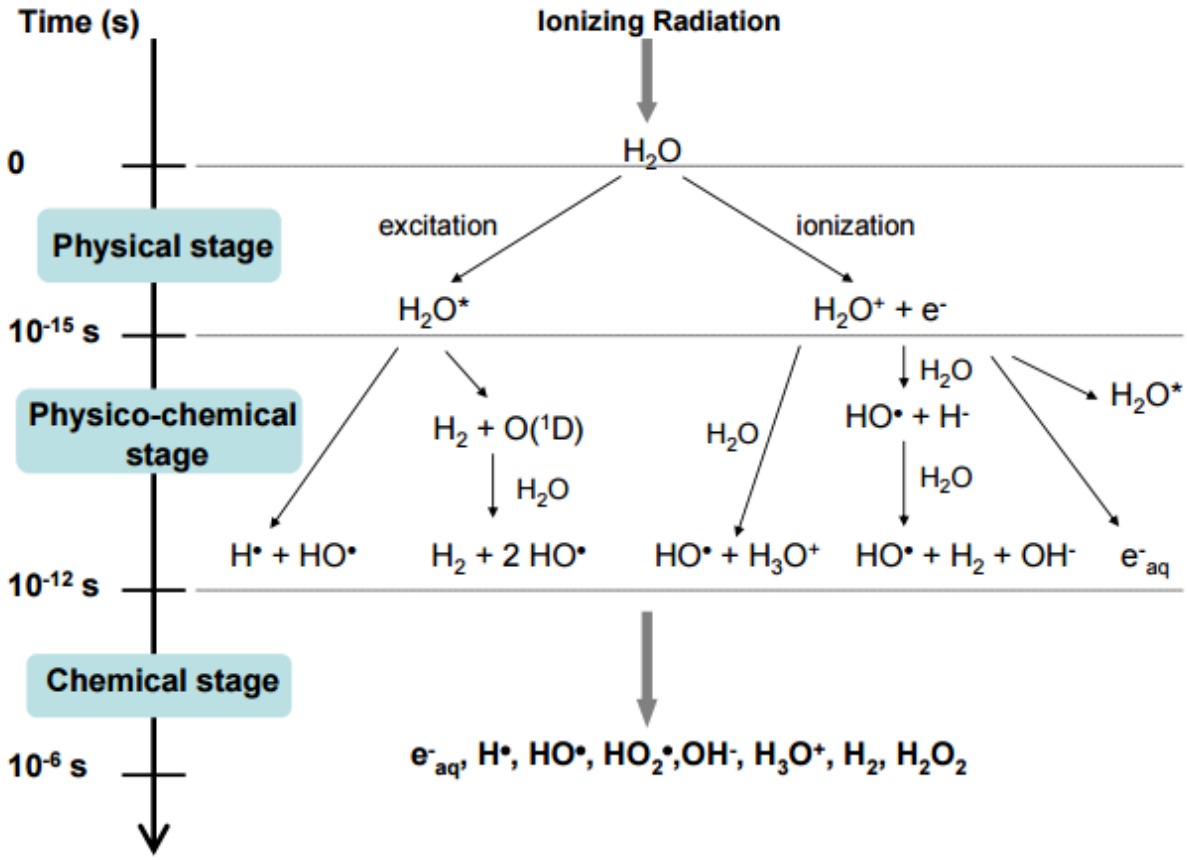

Figure (3-3) Water Radiolysis, from reference [5]

3.2 Interaction of photons with matter

Photons are electromagnetic radiation with no mass or charge and a constant speed $c{\sim}2.998 \times 10^8\ m/s$ in vacuum. When travelling through matter, they do not steadily lose energy via Coulomb interaction since they are electrically neutral. They usually travel some considerable distance through the material before interaction happens leading to partial or total transfer of their energy to electrons of the medium. Photons are considered more penetrating than charged particles of similar energy. Photon interactions include elastic interactions such as Rayleigh scattering and inelastic interactions such as photoelectric effect, Compton scattering and pair production [9]. These inelastic interactions produce secondary electrons capable of further interactions in the medium called "delta rays".

3.2.1 Photoelectric effect

Also called photoemission, is an inelastic phenomenon. The photon transfers all its energy to the electrons of the medium. The energy transferred to the electron exceeds its binding energy to the atom. Therefore, the electron has enough energy to leave the atom and move freely in the medium with a kinetic energy $T_e = h\nu - W$, where W is the binding energy of

the electron to the atom, h is Planck's constant and ν is the frequency of the photon. In the case of gamma-rays with energies more than a few hundred keV, the photoelectron carries off the majority of the original photon energy. And since they have sufficient energy, the photoelectrons will most probably be extracted from the most tightly binding K shell.

As figure (3-4) shows, a vacancy created by the ejection of an electron from an inner shell is filled by an outer electron falling into it, also called de-excitation. This creates an excess of energy in the atom that is emitted as either a fluorescent X-ray or an Auger electron.

The fluorescent X-ray photon will be emitted with energy equals to the difference between the two energy shells, the previously vacant shell and the outer shell of which the falling electron used to occupy. In case of Auger electron, the excess energy is transferred to an outer shell electron that will then be ejected from the atom.

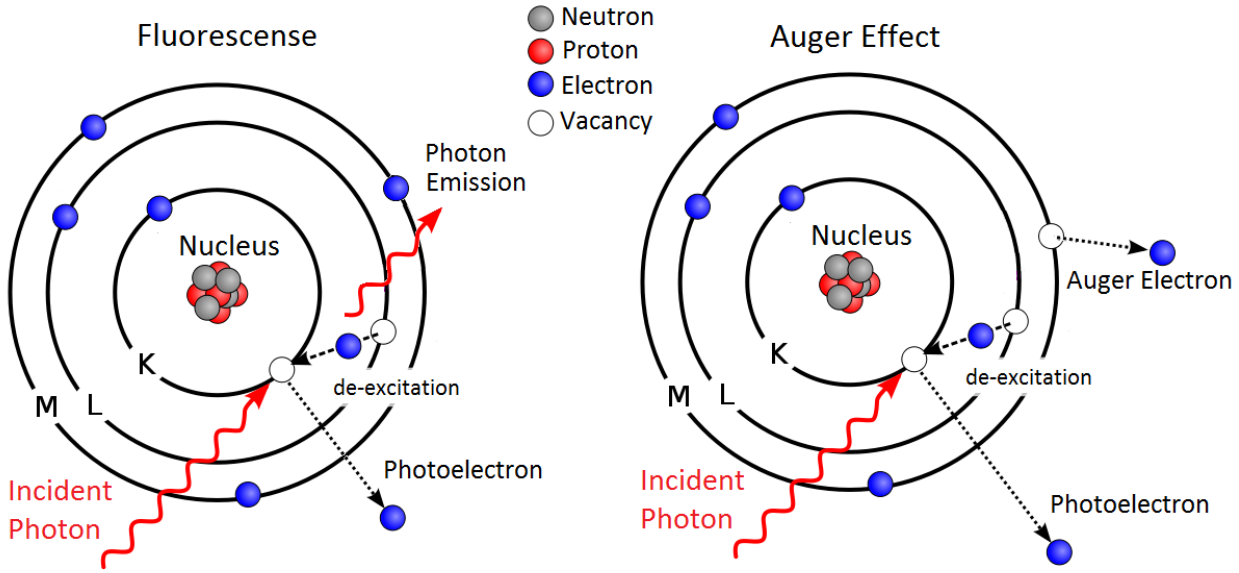

Figure (3-4) Relaxation processes after the photoelectric effect

3.2.2 Compton effect

The Compton scattering interaction is the inelastic scattering of a photon by a charged particle, usually an electron, thus creating a scattered photon and a recoil electron. The photon is then deflected by an angle θ with respect to its initial direction. This deflection results in a decrease in energy of the photon (decrease in photon's frequency) called the Compton Effect. The photon transfers a portion of its energy to the recoil electron. The energy of the recoil electron is defined as T such that

$$T = h\nu - \frac{h\nu}{1 + \frac{h\nu}{m_e c^2}(1 - \cos\theta)} \qquad (3\text{-}3)$$

Where $h\nu$ is the energy of the incident photon of wavelength λ, m_e is the mass of the electron, and θ is the angle of the scattered photon. The scattered photon will carry a wavelength λ' such that

$$\lambda' - \lambda = \frac{h}{m_e c}(1 - \cos\theta) \qquad (3\text{-}4)$$

See figure (3-5) for illustration.

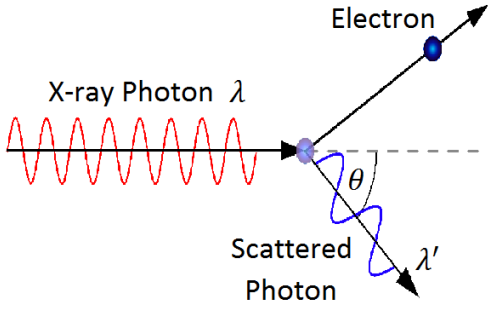

Figure (3-5) Compton scattering

3.2.3 Pair production

Pair production occurs when a high energy photon is in the intense influence of the electric field near the nuclei of the absorbing material. The photon may disappear as a photon and reappear as an electron-positron pair. The photon should have a minimum energy of $2m_e c^2$ that is the rest mass energy of the electron-positron pair in order for this process to occur. Thus $E_{e+} + E_{e-} = h\nu - 2m_e c^2$, where E_{e+} is the positron energy, E_{e-} is the electron energy, and $h\nu$ is the incident photon energy as shown in figure (3-6).

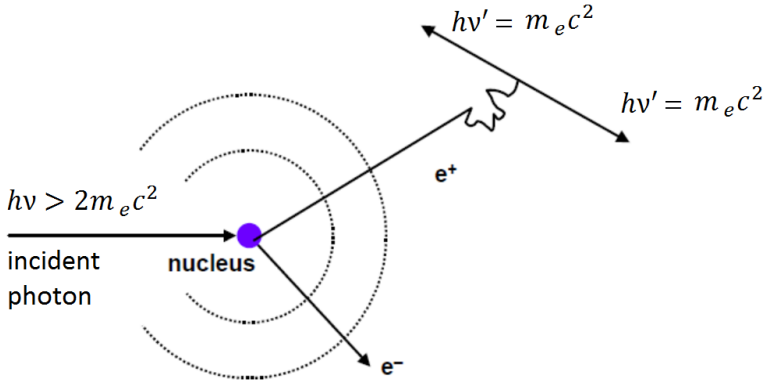

Figure (3-6) Electron-positron pair production followed by the positron annihilation into 2 photons, from reference [10]

This is a very complicated process due to the fact that a positron is not stable. It will annihilate when it comes into contact with an electron, which are very abundant. Upon annihilation, two 0.511 MeV photons will be released back into the system. This process will happen quite quickly and will appear to be in coincidence with the original pair production.

The photon interaction probability with matter depends on the photon energy and the atomic number of the material. As can be seen from figure (3-7) the photoelectric effect is dominant for low energy photons and high Z materials. Pair production is dominant for high energy photons and high Z materials. Compton scattering is dominant for moderate energies. The total cross-section of photon interactions with an atom σ_{total} is equal to the sum of all partial cross-sections of the possible interactions.

$$\sigma_{total} = \sigma_f + \sigma_C + \sigma_P \qquad (3\text{-}5)$$

Where σ_f is the photoelectric cross-section, σ_C is the Compton scattering cross-section and σ_P is the pair production cross-section.

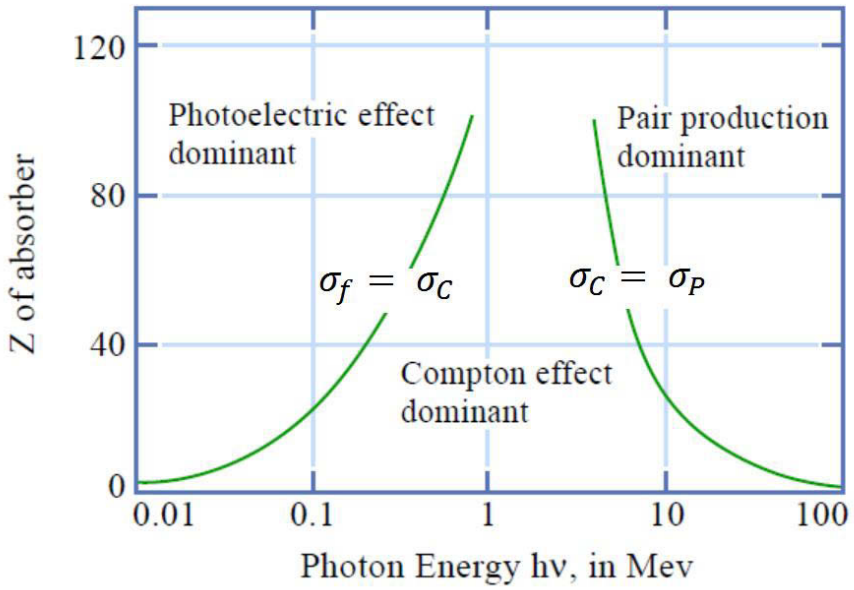

Figure (3-7) Photon interaction probabilities according to photon energy and the atomic number of the absorber material, from reference [11]

3.2.4 Attenuation

The interactions of a photon with matter in the form of photoelectric effect, Compton scattering or pair production results in the complete removal of this photon from the incident beam. Consequently, the photon beam gradually loses some of its photons as it passes through the material. This means that the photon beam crossing the medium is not degraded in energy but is only attenuated in intensity. This attenuation is governed by an exponential law:

$$I = I_0 e^{-(\mu/\rho)(\rho x)} \qquad (3\text{-}6)$$

Where, I_0 is the incident beam intensity, I is the attenuated beam intensity, μ is the linear attenuation coefficient of the material, ρ is the density of the material and x is the thickness of the material crossed by the beam. The linear attenuation coefficient increases with the increase of absorber atomic number and decreases as the incident photon energy increases.

The average distance traveled by a photon between two successive interactions is called the mean free path l and can be calculated from the linear attenuation coefficient by the relation $l = 1/\mu$.

The mass attenuation coefficient is defined as the ratio of the linear attenuation coefficient and the absorber density, noted as μ/ρ and measured in $cm^2.g^{-1}$. The values of mass attenuation coefficients depend on the absorption and scattering of the incident radiation.

The mass attenuation coefficient is in direct relation with the interaction cross-section such that

$$\frac{\mu}{\rho} = \frac{\sigma N_A}{uA} \qquad (3\text{-}7)$$

Where σ is the interaction cross-section or the probability that the incident photon makes an interaction in the target material, $N_A = 6.023 \times 10^{23}\ mol^{-1}$ is Avogadro's number, ρ is the material density, u is the atomic mass unit and A is the atomic mass of the target material.

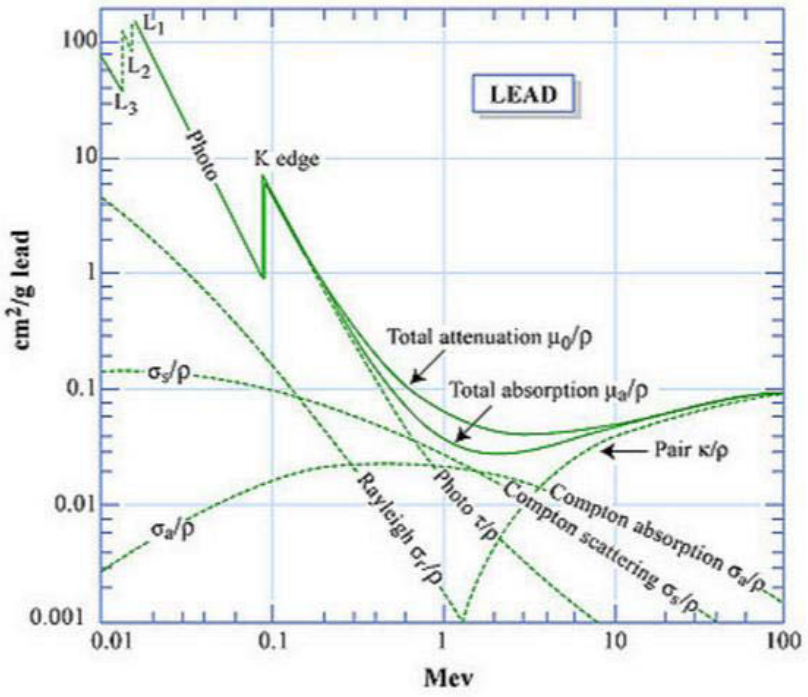

Figure (3-8) Mass attenuation coefficients of photons in Lead, from reference [11]

Figure (3-8) shows the attenuation coefficients of photon energies in lead. The total attenuation contains the contributions of all photon interactions in lead, the photoelectric interactions, Compton interactions, pair production and Rayleigh scattering. The discontinuities in the photoelectric curve are due to the absorption edges. These edges correspond to the binding energies of electrons from the atom's bound shells (*K, L, M*…).

There is a sudden increase in the attenuation coefficient of photons occurring just above the binding energy of the bound shell electron of the atom. This sudden increase in attenuation is due to photoelectric absorption of the photons. For this interaction to occur, the photons must have more energy than the binding energy of shell electron. A photon having energy just above the binding energy is more likely to be absorbed than a photon having energy just below this binding energy.

3.3 Interaction of charged particles with matter

Charged particles such as electrons, protons and ions are considered as directly ionizing radiation. Since they are charged they are under the direct influence of Coulomb forces, and mainly interact with the electrons of the medium they traverse resulting in a series of ionizations and excitations along their tracks. These interactions lead to slowing down of the incident charged particles.

The Coulomb interaction occurring between the incident particle and the electrons of the medium results in a transfer of energy Q to the electrons of the medium that is acquired from the incident particle's kinetic energy T [7]. The maximum energy transfer to an electron of mass m in a single head-on collision by the incident particle of mass M is Q_{max} such that:

$$Q_{max} = \frac{4mM}{(m+M)^2}T \qquad (3\text{-}8)$$

- If the incident particle is an electron ($M = m$), then $Q_{max} = T$. In this case all energy is transferred to the target electron;
- However, if the incident particle is of mass M very much greater than the mass m of the electron ($M \gg m$), then $Q_{max} = 4Tm/M$: for example, a proton cannot transfer to an electron more than 0.2% of its kinetic energy.

For distant collisions, the energy transfer Q depends on the speed v and the charge z of the incident particle and on the distance a between the electron and the trajectory of the incident particle by the following relation.

$$Q = K\frac{1}{a^2}\frac{z^2}{v^2} \qquad (3\text{-}9)$$

This relation shows that as the distance between the incident particle and the target electron increases, the Coulomb interaction is less likely to happen, so less energy is transferred.

However, as the speed of the incident particles increases, interactions become sparse over the area they traverse since they can overcome to a certain extent the Coulombic influence.

Highly charged particles such as alpha particles transfer more energy to the medium than a proton or an electron. They are more likely to interact since the Coulomb force is directly proportional to charge.

Charged particles interact with matter in two main processes ionization and excitation. If the energy transfer is higher than the binding energy of the electron of the medium, that electron is ejected from the atom in an ionization incident. These ejected electrons usually have enough energy to cause further interactions in the medium also known as delta rays. In contrast, if the energy transferred is less than the binding energy, the electron is excited to a higher level in the atom followed by a relaxation releasing a fluorescent photon or an Auger electron to the medium.

The slowing down of heavy charged particles is carried out over the course of very large number of interactions of small energy transfers and their trajectories can be considered as rectilinear. For protons, deviations caused by collisions are very small; the track is straight and its length does not vary between one proton and another as figure (3-9-b) shows. For an electron, distant collisions cause only very small deviations, but the rare close collisions involve large deviations. As figure (3-9-a) shows the track is composed of straight segments with sharp changes in direction; the end of the track is very convoluted. Close collisions involve large losses of energy which vary from one electron to another and the length of the track shows important fluctuations.

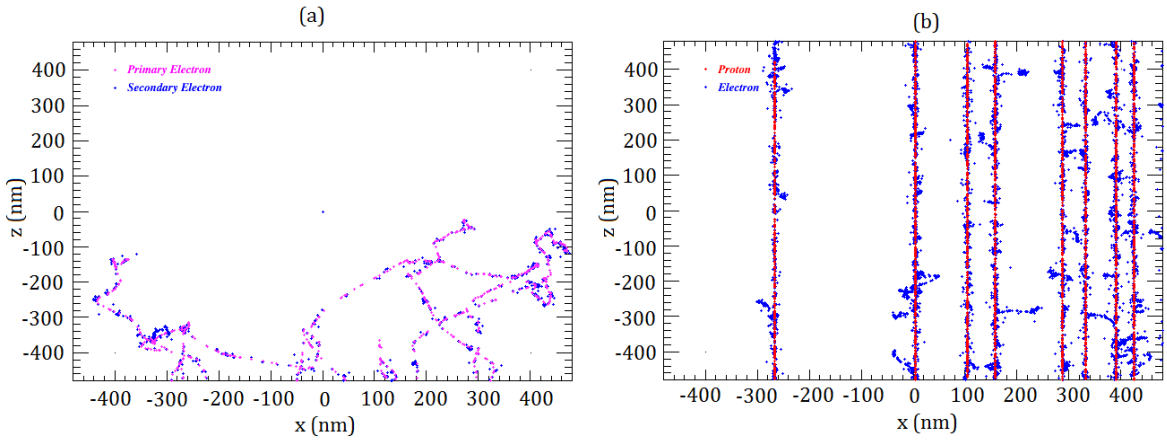

Figure (3-9) Simulated particle tracks in a water cube of edge 1 µm by Geant4 toolkit using the Geant4-DNA electromagnetic processes: (a) shows tracks of 8 electrons of energy 5 keV shot in the positive z direction, primary electrons are in pink and secondary electrons are in blue; (b) Tracks of 8 protons of 1 MeV energy sent in the positive z direction, protons are in red, secondary electrons are in blue.

3.3.1 Bremsstrahlung

Bremsstrahlung, a German term meaning breaking radiation, is electromagnetic radiation produced by the slowing down or deflection of charged particles, especially electrons, passing through matter in the vicinity of the strong electric fields of atomic nuclei (See figure (3-10)). As an electron moves in the influence of the nuclear electric field of an atom, it loses kinetic energy, which is converted into a photon satisfying the law of conservation of energy.

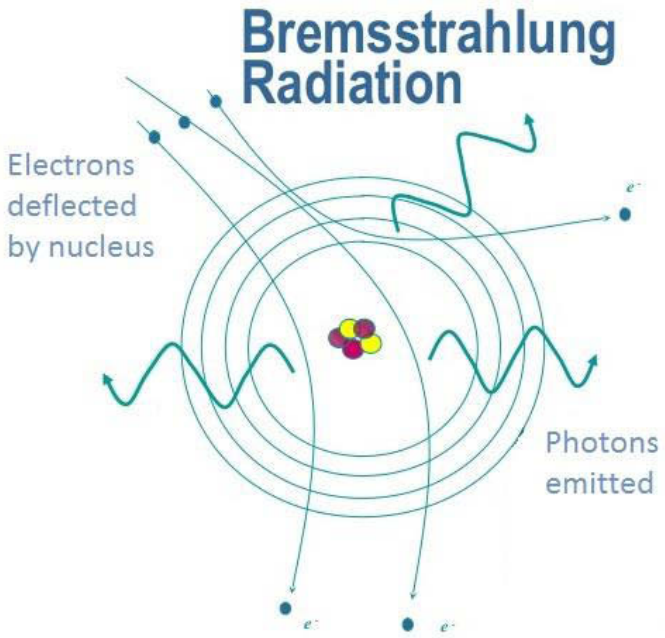

Figure (3-10) Electrons are slowed down and deflected by the electric field of the nucleus, adapted from reference [12]

This type of radiation is commonly seen in the X-ray production. X-ray production typically involves bombarding a metal target in an X-ray tube with high speed electrons which have been accelerated by tens to hundreds of kilovolts of potential. The bombarding electrons can eject electrons from the inner shells of the target atoms leaving vacancies in these inner shells. Those vacancies will be quickly filled by electrons dropping down from higher levels, emitting X-rays with sharply defined frequencies associated with the difference between the atomic energy levels of the target atoms. These are called the characteristic X-rays shown as sharp peaks in figure (3-11).

However, the majority of the spectrum is continuous due to the Bremsstrahlung radiation. When an incoming electron makes a head-on collision with a nucleus, its energy is

completely converted into radiation of maximum energy. Other incoming electrons from the same beam come to rest after being deflected many times by the positively charged nuclei. Each deflection gives rise to a photon of less than maximum energy [13]. Figure (3-11) shows the emission spectrum of X-rays by Bremsstrahlung as a smooth curve. The peak intensity shifts towards higher frequencies as the accelerated electrons energy increases.

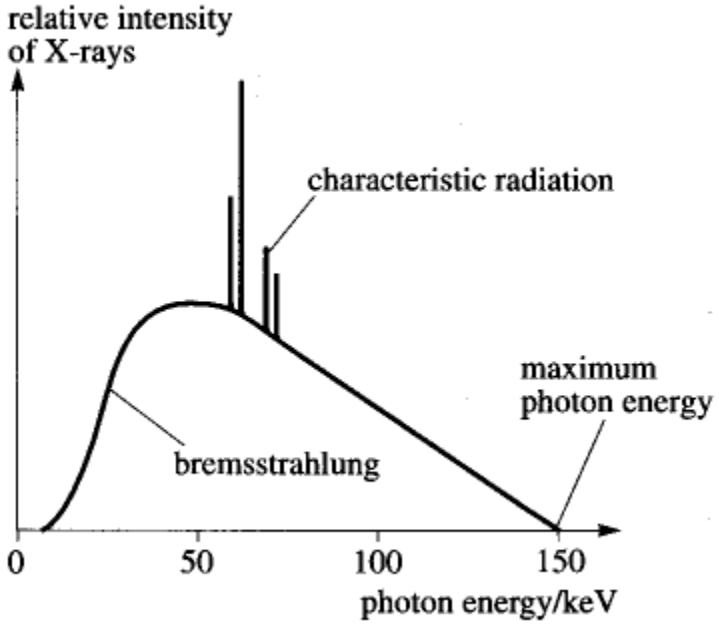

Figure (3-11) A typical X-ray energy spectra, from reference [14]

3.4 The Radiosensitizing Effect of Gold Nanoparticles

For many years, it has been a challenge to target tumors by radiotherapy without inflicting unwanted damage on healthy tissues. Beam delivery methods are refined continually to improve the quality of dose delivery to malignant tissues. To improve the discrimination between tumors and healthy tissues in radiotherapy is an important issue which is being investigated using nanoparticles. Nanoparticles are microscopic particles ranging from 1 to 100 nm in dimensions. They have been used in medical applications as contrast agents in imaging, drug delivery capsules and as cancer radiotherapy enhancers.

Heavy elements have higher mass energy absorption coefficients than tissues. If they can be preferentially delivered to tumors, the dose delivered to tumors is potentially higher than that delivered to the surrounding healthy tissues optimizing the radiotherapy. Nanoparticles, having small sizes, easily enter the tumor tissues by the enhanced permeability and retention (EPR) effect [15]. Tumor tissues differ from healthy tissues by having non-normal vasculature. Malignant tissues have high vascular density with

increased permeability and defective lymphatic draining leading to high retention of absorbed particles [16].

Gold nanoparticles are particularly interesting contrast agents since they have a high mass attenuation coefficient and are considered biocompatible because of their low cytotoxicity. A study by Hainfeld *et al.* [17] showed that gold nanoparticles are preferentially taken up into mouse mammary subcutaneous tumors leading to tumor control enhancement after radiotherapy administration. The dose was enhanced by 200% when the animals were injected with 1.9 nm diameter gold nanoparticles and irradiated with 250 kVp photons leading to 86% one year survival in comparison to 20% survival with radiotherapy alone.

Another study conducted by Chang *et al.* [18] on melanoma bearing mice used 13 nm diameter gold nanoparticles in conjunction with a single dose of 25 Gy of 6 MeV electron beam. The tumor volume was significantly reduced compared to a control group and the number of apoptotic cells in the presence of gold nanoparticles was two times higher than in their absence.

The improvement of deposited dose when cells are injected with GNP results from the enhanced photoelectric cross-section of this high atomic number (Z=79) element compared to tissues. Figure (3-12-a) shows the mass energy absorption coefficients of photons in gold and in soft tissues. In the kilovoltage region, gold has an absorption coefficient greater than that of soft tissues by two orders of magnitude or more. So, a small concentration of gold has the potential to increase the amount of deposited dose in the tumor.

However, this radio-sensitizing effect of gold becomes negligible when the energy of photons is in the MeV region where there is no significant difference in the absorption coefficients between gold and soft tissues. Although some experimental studies [19, 20] have shown that the enhancement effect can be seen also with MeV range photons. In higher energies, the photon interaction with matter produces Compton electrons with a spectrum of energy which have higher absorption coefficient with GNP compared to the surrounding biological matter.

Figure (3-12-b) presents the variation of relative mass energy absorption coefficient of gold to water. The data was derived from National Institute of Standards and Technology (NIST) [21]. The greatest ratio between the absorption coefficient of gold and that of soft tissue is in the region of 40-50 keV, where gold has an absorption coefficient over 150 times higher than that of soft tissue as seen figure (3-12-b). However, the use of such energies for treatment is not suitable since they have low penetration and rapid drop-off of absorbed dose with depth (the half-length of 40 keV photons is roughly 25 mm). This situation can be improved by targeting a more energetic region, specifically in the region of the gold K-edge (80.7 keV), where there is an increase in absorption because the photons have enough energy to excite even the most bound electrons.

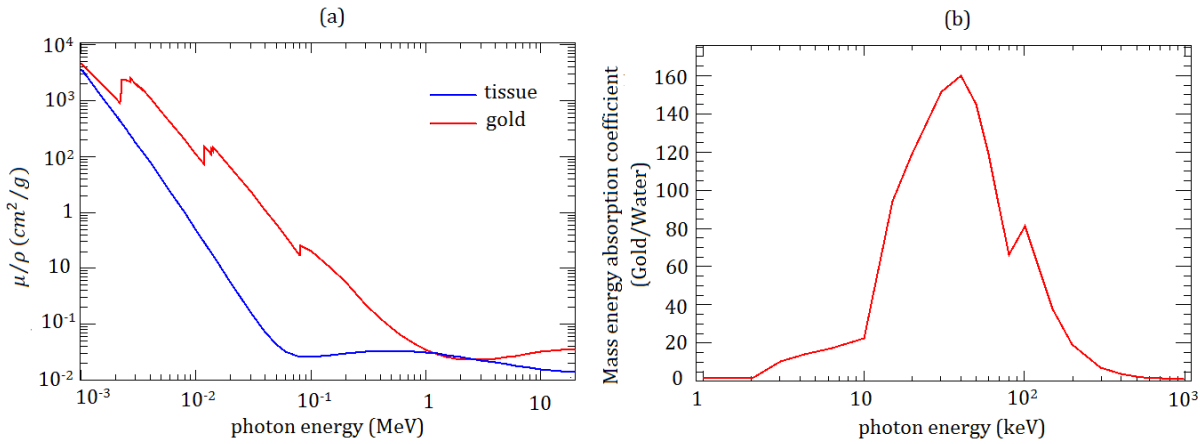

Figure (3-3) (a)Mass absorption coefficients of x-rays in gold and soft tissue, (b) the variation of relative mass absorption coefficient of gold to water with photon energy. (Data from NIST [21])

Interaction of X-rays with GNP for energies less than 500 keV is mainly photoelectric, releasing photoelectrons. This results in a vacancy in a *K*, *L* or *M* shell of the gold atom. In attempt to refill this vacancy a de-excitation event occurs producing either a characteristic X-ray or Auger electron emission. For photons above 500 keV, Compton effect is observed. The Compton scattering will result in atom re-excitation and production of Compton electrons which leads to subsequent photoelectric effect [22].

So, after an ionizing event in gold, several low-energy secondary electrons are produced including the photo- or Compton electron with relatively high energy, followed by a shower of Auger electrons with much lower energies (< 10 keV) which are emitted as electrons of the now ionized gold atom re-organize to fill the vacancy created by the initial ionizing event. The range of these Auger electrons is very short compared to photo- and Compton electrons and they are responsible for much of the additional energy deposited in the proximity of the GNP.

Figure (3-13) shows the average energy deposit in the vicinity of a 20 nm gold nanoparticle after a single ionizing event by a 40 keV photon. This figure is produced by a Monte Carlo study carried out by McMahon *et al.* [23] where energy depositions are scored in concentric shells of water around the nanoparticle. Near the GNP, the highest energy is deposited due to the Auger electrons. As the distance from the nanoparticle increases, energy deposition drops rapidly as low-energy electrons are stopped leaving only the contribution of the energetic *L*-shell electrons beyond 200 nm.

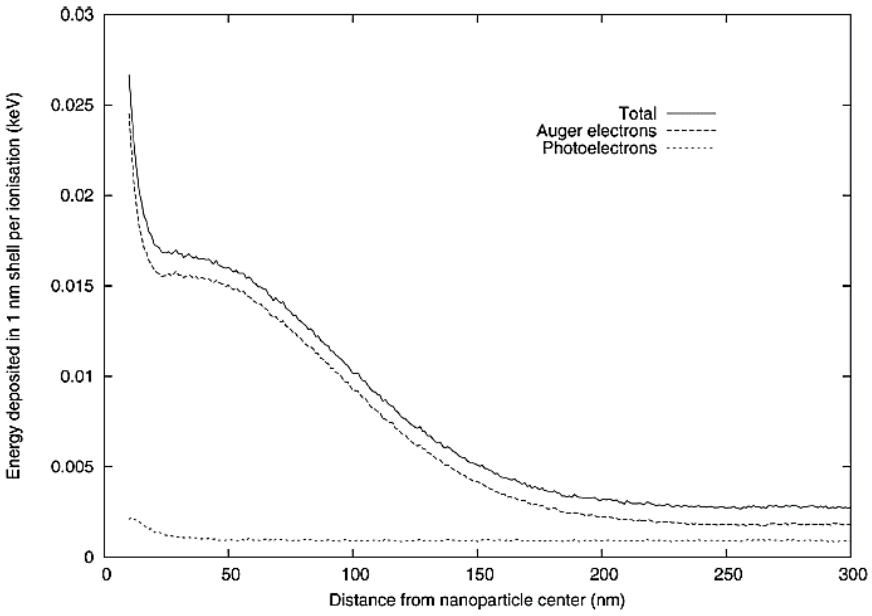

Figure (3-4) Radial energy deposits around a 20 nm gold nanoparticle induced by a single event of 40 keV X-ray; the contribution of photoelectrons and Auger electrons is shown. From reference [23]

GNP enter the cells via endocytosis where they are encapsulated by vesicles. These vesicles travel inside the cell where they merge into endosomes and then into lysosomes [24, 25]. The waste disposal mechanism of the cell then spits them out. In another study by Wang *et al.* [26] gold nanorods were colocalized with the mitochondria. However, as far as we know there has not been any reports claiming any colocalization of GNP with the nucleus.

The maximum uptake of GNP inside one cell varies according to the cell type and the GNP's size and coating properties. The work of Chithrani *et al.* [27] for example shows that 50 nm GNP have the maximum uptake inside human cervix carcinoma cells (HeLa) reaching 6000 in number per cell compared to 3000 for the 14 nm size and 4000 for the 74 nm size.

Another study by Chithrani *et al.* [28] on breast cancer cells (MCF-7) shows that 14 nm uncoated GNP has maximum uptake of about 2000 per cell, and when coated with bovine serum albumin the 14 nm particles reached only 1000 per cell. In Chithrani's work GNP are detected inside vesicles ranging from 300-500 nm in diameter.

Small GNP deposit more dose in their local area than large ones due to the greater relative contribution from the outer layer of the nanoparticle. GNP with larger diameter have a larger ability to reabsorb the Auger electrons, the low energy electrons responsible for enhancing the local dose, in their bulk rather than releasing them to the surrounding [23]. The optimum uptake of GNP is for 50 nm diameter which is not very efficient in enhancing

the local dose compared to smaller sizes. Burger *et al.* [29] introduced a new method to increase the uptake of 10 nm GNP by linking them to DNA and transferring them into HeLa cells by transient transfection. The uptake in this case reached about 14000 GNP per cell and the treated cells were significantly more sensitive to irradiation with 6 MV X-rays than cells treated with unmodified nanoparticles.

3.5 Conclusion

Ionizing radiation passes through many phases after the first impact with the biological material. The physical phase is when ionization and excitation of the atoms and molecules of the biological target take place. These are known as the direct effects of radiation. The physico-chemical phase comes next followed by the chemical phase. These two phases are mostly described by water radiolysis producing *ROS* that cause the indirect effects of radiation. The sensitive biomolecules are attacked by these *ROS* damaging their structure and function. The final phase is the biological phase when the damage is sensed and its repair is carried out. The unrepaired damages leave the cell vulnerable to cancerization or death.

Photons interact in-elastically with the material they traverse losing their intensity by three main processes: photoelectric effect, Compton scattering and pair production. These processes result in secondary electrons released inside the medium. These electrons will then interact further with the material until they lose their newly acquired energy by ionizations and excitations of the atoms surrounding them.

Charged particles such as electrons, protons and ions directly cause ionizations and excitations of the target medium they traverse due to the Coulomb force. As a result delta electrons are produced that move freely and induce further interactions. Fluorescence and Bremsstrahlung also occur due to the passage of the charged particle inside the medium.

Gold nanoparticles are used as radio-sensitizing agents for radiotherapy enhancement. The high mass energy absorption coefficient of gold compared to tissue allows the enhancement of the administered dose to the tumors when GNP are preferentially taken up by tumor cells. In addition, the high rate of Auger electrons produced by the GNP enhances the local dose resulting in higher dose at the tumor site. The uptake of GNP into cells vary by the cell type, the size of GNP and their coating properties. They could be located near the mitochondria, or they could be concentrated inside endosomes and lysosomes.

1. *Neils Bohr Atomic Theory*. Available from: http://chemistry.tutorvista.com/inorganic-chemistry/niel-bohr-atomic-theory.html.
2. *How does NASA deal with static electricity buildup*. Available from: https://sites.google.com/a/lansinglions.org/astronautmegashock/how-does-nasa-deal-with-static-electricity-buildup.
3. Tominaga, H., et al., *Involvement of reactive oxygen species (ROS) in the induction of genomic instability by radiation.* J. Radiat. Res., 2004. **45**: p. 181-188.
4. Alberts, B., et al., *Essential Cell Biology: An Introduction to the Molecular Biology of the Cell*. 1998: Garland Publishing.
5. Le Caër, S., *Water Radiolysis: Influence of Oxide Surfaces on H2 Production under Ionizing Radiation.* Water, 2011. **3**: p. 235-253.
6. Riley, P.A., *Free radicals in biology: oxidative stressand the effects ofionizing radiation.* Int. J. Radiat.Biol., 1994. **65**: p. 27-33.
7. Tubiana, M., J. Dutreix, and A. Wambersie, *Introduction to Radiobiology*. 1990.
8. Turrens, J.F., *Mitochondrial formation of reactive oxygen species.* Journal of Physiology, 2003. **552**(2): p. 335-344.
9. Alpen, E., *Radiation Biophysics*. 2 ed. 1997, San Diego, CA: Academic Press.
10. *Electrons: Fine structure constant and quantum physics*. Available from: http://www.twinkletoesengineering.info/electrons.htm.
11. Coderre, J. *Interaction of photons with matter*. 2004; Available from: https://ocw.mit.edu/courses/nuclear-engineering/22-55j-principles-of-radiation-interactions-fall-2004/lecture-notes/ener_depo_photon.pdf.
12. *The nature of radiation*. Available from: https://www.slideshare.net/erletshaqe1/lecture-1-30005220.
13. *Encyclopaedia Brittanica*. Available from: http://www.britannica.com/science/bremsstrahlung.
14. *Physics in medicine lectures*. Available from: https://koukalaka.wordpress.com/tag/electron-beams/.
15. Maeda, H. and Y. Matsumura, *Timoritropic and lymphotropic principles of macromolecular drugs.* Critical Reviews in Theraputic Drug Carrier Systems, 1989. **6**: p. 193-210.
16. Noguchi, Y., et al., *Early phase tumor accumulation of macromolecules: a great difference in clearance rate between tumor and normal tissues.* Japanese Journal of Cancer Research, 1998. **89**: p. 307-314.
17. Hainfeld, J.F., D.N. Slatkin, and H.M. Smilowitz, *The use of gold nanoparticles to enhance radiotherapy in mice.* Physics in Medicine and Biology, 2004. **49**(18): p. 309-315.
18. Chang, M.Y., et al., *Increased apoptotic potential and dose-enhancing effect of gold nanoparticles in combination with single-dose clinical electron beams on tumor-bearing mice.* Cancer Science, 2008. **99**(7): p. 1479-1484.
19. Chithrani, D., et al., *Gold nanoparticles as radiation sensitizers in cancer therapy.* Radiation Research, 2010. **173**: p. 719-728.
20. Jain, S., et al., *Cell-specific radiosensitization by gold nanoparticles at megavoltage radiation energies.* International Journal of Radiation Oncology Biology Physics, 2011. **79**(2): p. 531-539.

21. *National Institute of Standards and Technology*. Available from: https://www.nist.gov/pml.
22. Mesbahi, A., *A review on gold nanoparticles radiosensitization effects in radiation therapy of cancer.* Reports of Practical Oncology and Radiotherapy, 2010. **15**: p. 176-180.
23. McMahon, S.J., et al., *Biological consequences of nanoscale energy deposition near irradiated heavy atom nanoparticles.* Scientific Reports, 2011. **1**(18).
24. Chithrani, D., *Intracellular uptake, transport, and processing of gold nanostructures.* Molecular Membrane Biology, 2010. **27**: p. 299-311.
25. Shukla, R., et al., *Biocompatibility of gold nanoparticles and their endocytotic fate inside the cellular compartment: a microscopic overview.* Langmuir, 2005. **21**(23): p. 10644-10654.
26. Wang, L., et al., *Selective targeting of gold nanorods at the mitochondria of cancer cells: implications for cancer therapy.* Nano Letters, 2010. **11**(2): p. 772-780.
27. Chithrani, D., A.A. Ghazani, and W.C. Chan, *Determining the size and shape dependence of gold nanoparticle uptake into cammalian cells.* Nano Letters, 2006. **6**(4): p. 662-668.
28. Chithrani, D., et al., *Intracellular uptake, transport, and processing of nanostructures in cancer cells.* Nanomedicine: Nanotechnology, Biology, and Medicine, 2009. **5**: p. 118-127.
29. Burger, N., et al., *A method for the efficient cellular uptake and retention of small modified gold nanoparticles for the radiosensitization of cells.* Nanomedicine: Nanotechnology, Biology, and Medicine, 2014. **10**: p. 1365–1373.

4 Methods for Analyzing Radiation Effects

When passing through a biological medium, ionizing radiation have certain effects on its cells: starting from ionization and excitation of the atoms and molecules constituting the cells, then initiating reactive chemical species and ending in long term damages to the DNA causing cancer or cell death.

In radiobiology, the damaging capacity of a certain radiation type is measured by the dose it deposits inside the medium. The absorbed dose is a statistical average of all deposited energies in the medium disregarding their stochastic nature. The microdosimetry formalism is used to take into consideration this stochastic nature of energy deposition. In our study we use microdosimetric quantities to describe the behavior of radiation in biological material at the micrometric scale. We also study how the energy depositions are clustered since it is a common assumption that the biological effect of a group of damage points or a cluster depends on the density of its energy deposition.

4.1 Dosimetry

The dose at a point represents the density of energy absorbed at that point:

$$D = \Delta\epsilon/\Delta m \qquad (4\text{-}1)$$

In practice $\Delta\epsilon$ represents the energy which appears in the form of ionization, excitation and thermal transfers produced in Δm the mass of the target under study. The unit of dose is the gray (Gy) where $1\ Gy = 1\ J.kg^{-1}$.[1]

Because of the discontinuous nature of the events which lead to the absorption of energy, dose is meaningful only when the mass Δm is large enough that there is neither an appreciable statistical fluctuation in the number of particles traversing such a mass during the irradiation nor in the energy which they deposit. Therefore, the absorbed dose is not a good indicator of the likely biological effect. For example, 1 Gy of alpha radiation would be much more biologically damaging than 1 Gy of photon radiation. Alpha particles leave the cells with clustered damages that are hard to repair, whereas photons leave dispersed damages that are more likely to get repaired.

This brings us to another radiological quality of ionizing radiation, the linear energy transfer (LET). LET describes how much energy an ionizing particle transfers to the material traversed per unit length. It is a measure of average ionization density along the radiation trajectory. It depends on the type and energy of the incident radiation and on the nature of the traversed medium.

$$LET = dE/dl \qquad (4\text{-}2)$$

dE is the average energy locally transferred to the medium by a charged particle along an element dl of its trajectory. The typical unit of LET is ($keV/\mu m$) [2].

LET accounts for the amount of energy transferred to the local environment in the form of ionizations and excitations. Thus, LET indicates the potential for biologically important damage from radiation. The density of ionizations along a given path relates inversely to kinetic energy of the incident particle. Thus, a decelerating particle produces the greatest number of ionizations just before coming to rest. As figure (4-1) shows, particles with low kinetic energy have higher LET. Electrons are generally sparsely ionizing while protons are, at moderate energies, densely ionizing. Note that very energetic protons, as they occur in altitudes relevant to aviation and in space, are sufficiently fast to be sparsely ionizing.

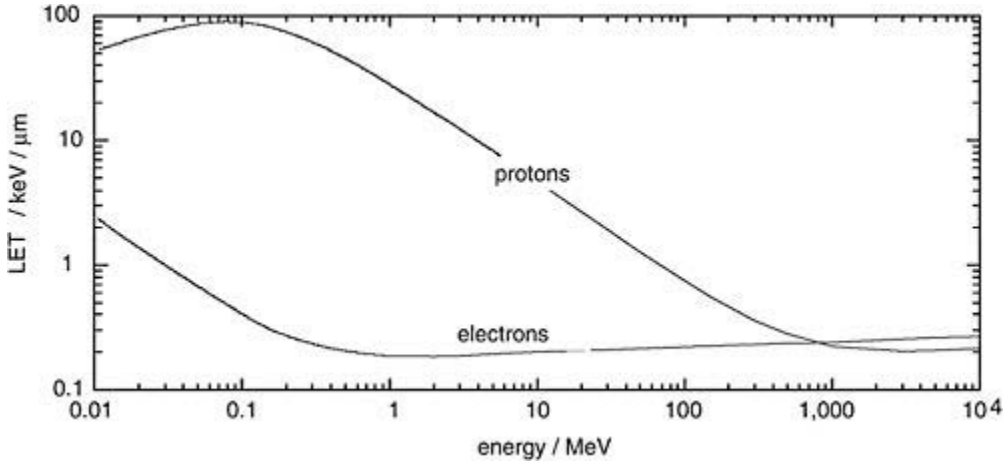

Figure (4-1) Linear energy transfer values for protons and electrons in water [2]

Particles with low LET such as electrons leave sparse energy deposits along their tracks in comparison with high LET particles such as protons and ions. Protons having high LET are densely ionizing causing more interactions along their trajectories as the illustration in figure (4-2) shows. The high concentration of deposited energy can cause more severe damage to any microscopic structures near the particle track.

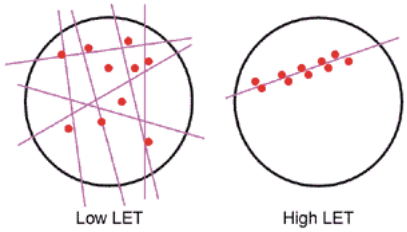

Figure (4-2) Both radiations induce the same number of ionizations in the medium representing the same dose, however different effects result in each case. High *LET* radiation cause closly clustered ionizations along its track, while low *LET* radiation cause dispersed ionizations in the medium [3].

Charged particles passing through matter ionize and thus lose energy in many steps until their energy is (almost) zero. The distance to this point is called the range of the particle. The range depends on the type of particle, its initial energy and on the material through which it passes. This is not to be confused by the mean free path that is the average distance travelled by a moving particle between successive impacts (collisions) which modify its direction or energy or other of its properties.

Large angle scattering is rare for positive ions, so a range may be well defined for that radiation depending on its energy, charge as well as the ionization energy of the stopping medium. Since the nature of such interaction is statistical, the number of collisions required to bring a radiation particle to rest within the medium will vary slightly with each particle (i.e. some travel further and undergo less collisions than others). Hence, there will be a small variation in the range known as straggling.

Due to the statistical nature of electronic stopping power a number of identical particles starting out under identical conditions will have a distribution of different energy deposits as they pass a given depth and a distribution of path lengths traversed before they stop. The phenomenon of unequal energy losses under identical conditions is called energy straggling and the existence of different path lengths is referred to as range straggling. Straggling is not only a longitudinal process but also a transverse process leading to a blow up of the beam-size [4].

The energy loss per unit distance and hence the density of ionization increases while the particle slows down. Shortly before the end, the energy loss passes through a maximum, the Bragg peak, and then drops to zero as described by the Bragg curve.

The behavior of ions presents a specificity which is good in treatment of extremely well localized tumors. So, they destroy with effectiveness the tumor cells without injuring healthy cells. In figure (4-3) we notice that the deposited dose presents a plateau then increases rapidly to reach the Bragg peak after which it decreases rapidly as well. The time of interaction between the projectile and the molecular electrons depends on the speed

between the target and the projectile. The slowing down of the projectile is increased by energy transfer of ionization and excitation. At a low speed the charged projectile captures electrons from the target so its charge decreases until its speed cancels.

In case of ions the curve continues after the Bragg peak due to straggling or fluctuation in energy deposit caused by secondary electrons and fragments of nuclear products in the medium. The residual dose deposited after the Bragg peak is a function of the mass of incident nucleus. So, the usage of carbon ion represents a good compromising between the presence of a Bragg peak and the residual dose beyond it.

Figure (4-3) clearly shows the difference in depth dose deposits for different types of radiation. Photons and electrons build up a peak shortly after penetrating the medium after which the curve decreases. In case of photons the highest intensity attenuation occurs at the peak where interactions with the medium are decreased steadily for a considerable depth in the medium. This shows that photons deposit energy along their path in a medium. Electrons are more readily reactive with the medium where they deposit most of their energy shortly after entering the medium. In contrast, protons and ions deposit almost all their energy at a certain depth in the medium after which they are halted. These properties of protons and ions make them good candidates in hadron therapy of cancer where these heavy charged particles target the tumors leaving surrounding healthy tissues with negligible damage.

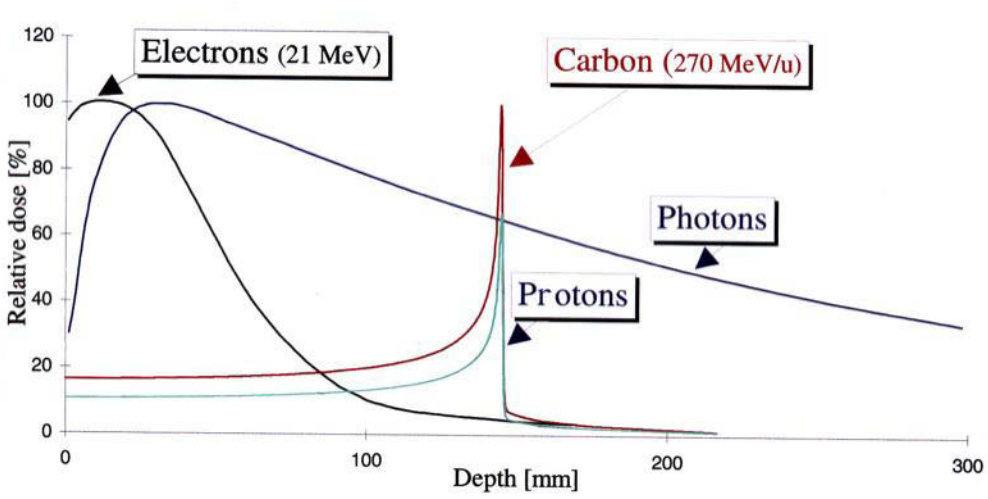

Figure (4-3) Bragg curves of different particles as they penetrate matter such as human tissue. Protons and carbon ions deposit most of their energy at a specific depth, whereas photons used in conventional X-rays tend to leave energy all along their path, damaging healthy tissues [5].

4.2 **Microdosimetry**

On a very small scale on the order of μm the absorbed energy is not distributed in a uniform way because on one hand it is localized close to the tracks of the ionizing particles and on the other the transfer of energy takes place in a discontinuous manner, in discrete amounts, during the course of random collisions between the ionizing particles and the electrons of the medium. Dose is a statistical quantity and does not express these characteristics. It gives a global value determined in mass of matter sufficiently large that the statistical fluctuation is insignificant. *LET* also represents a statistical quantity which does not take into account the discontinuous character of energy transfers.

In fact the biological effect results from the absorption of energy by cellular structures of very small dimensions for which the non-uniform and discontinuous absorption of energy is important. Therefore, it is necessary to add an indication of the microscopic distribution of ionizations or of the absorbed energy. So microdosimetry was introduced by Rossi [6, 7] as an alternative method to overcome the inadequacies of dose and *LET* representations. Figure (4-4) shows that at microscopic scale radiation behaves in a discrete and random manner therefore requiring a different way of study from the continuous approach of macroscopic dosimetry.

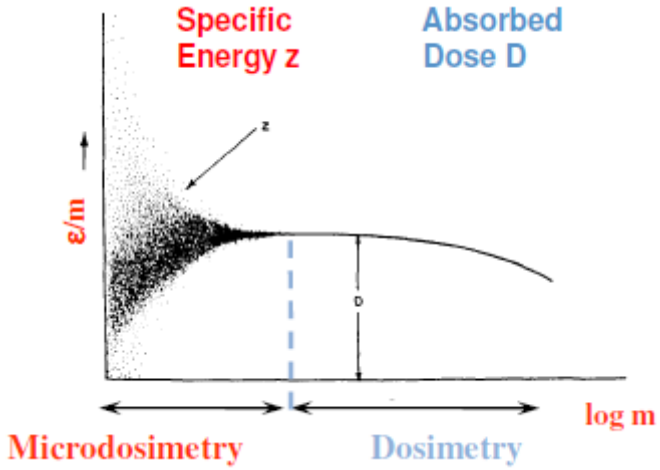

Figure (4-4) The stochastic and discrete behavior of radiation at micrometric scale is described by microdosimetry while the dose describes an averaged continuous behavior on macrometric scale [8]

At the micrometric level sampling is performed in order to determine the probability densities of absorbed energies. There are two types of sampling that can be performed: equiprobable sampling and dose weighted sampling [9]. When the radiation interacts with the medium, energy is transferred at certain positions. These positions are called *transfer points* T_i. The spatial distribution of these transfer points is called the i*nchoate distribution* where at each transfer point certain ionization or excitation energy is deposited. From this

distribution, sampling is performed by choosing a certain volume, a sphere or a cylinder, called *sensitive volume* that engulfs a certain amount of transfer points inside it. This is represented by the following figure (4-5):

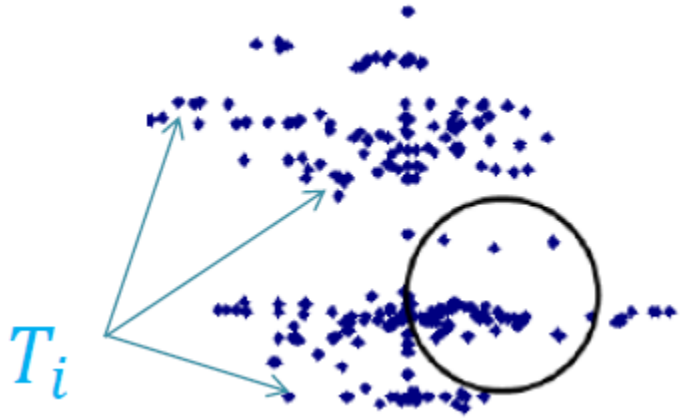

Figure (4-5): Energy Transfer Points (in dark blue) and a sensitive sphere as sampling sphere

The two different methods of sampling produce two types of distributions:

- Frequency distribution: In this case all the sensitive volumes have the same probability to be chosen,
- Dose distribution: In this case the sensitive volumes are chosen relative to the energy deposited inside them, the probability to choose a sensitive volume is proportional to the deposited energy inside it;

Equivalent to dosimetry, in microdosimetry, specific energy z and lineal energy y are calculated instead of absorbed dose and *LET* [10].

The lineal energy y is defined as the energy imparted in one event ϵ divided by the mean chord length $\bar{l}$ [11, 12] that results from the random interception of the site by a straight line:

$$y = \frac{\epsilon}{\bar{l}} \qquad (4\text{-}3)$$

The imparted energy ϵ is the sum of all energy depositions inside the chosen sensitive volume.

- The mean chord length of a sphere is $\bar{l} = 2d/3$, where d is the diameter of the sphere.
- The mean chord length of a cylinder is $\bar{l} = 2dh/(d + 2h)$, where d is the diameter of the cylinder and h is the height of the cylinder.

Applying this formalism, the lineal energy distributions and the mean lineal energies are defined as follows:

- Frequency distribution of lineal energy:

$$f(y) = \frac{dF(y)}{dy} \tag{4-4}$$

where $F(y) = P\left(\underline{y} < y \middle| \nu = 1\right)$ is the sum distribution of y i.e. the distribution function is equal to the probability that the random variable $\underline{y}$ does not exceed y such that one event has taken place.

On a logarithmic scale the densities are transformed; one must plot the dimensionless quantity $\frac{dF(y)}{d\ln y} = y.f(y)$

- Frequency mean lineal energy:

$$\bar{y}_F = \int y f(y)\, dy \tag{4-5}$$

- Dose distribution of lineal energy is:

$$d(y) = \frac{y f(y)}{\bar{y}_F} \tag{4-6}$$

- Dose mean lineal energy:

$$\bar{y}_D = \int y d(y)\, dy = \int \frac{y^2 f(y)\, dy}{\bar{y}_F} = \frac{\overline{y_F^2}}{\bar{y}_F} \tag{4-7}$$

Figure (4-6) shows the frequency distribution of lineal energy in water induced by proton tracks of different incident energies from 47 MeV till 93 MeV. The sensitive volume used in this study is a sphere of diameter 3 µm. This study performed by Francis *et al.* [13] uses Geant4 Monte Carlo track structure simulations to find the energy depositions in water and perform the microdosimetric methods. The obtained results show that beams with high *LET* (protons of lower energies) have higher values of lineal energy and higher peak lineal energy values. This is expected for high *LET* radiation deposits more energy in the targeted medium.

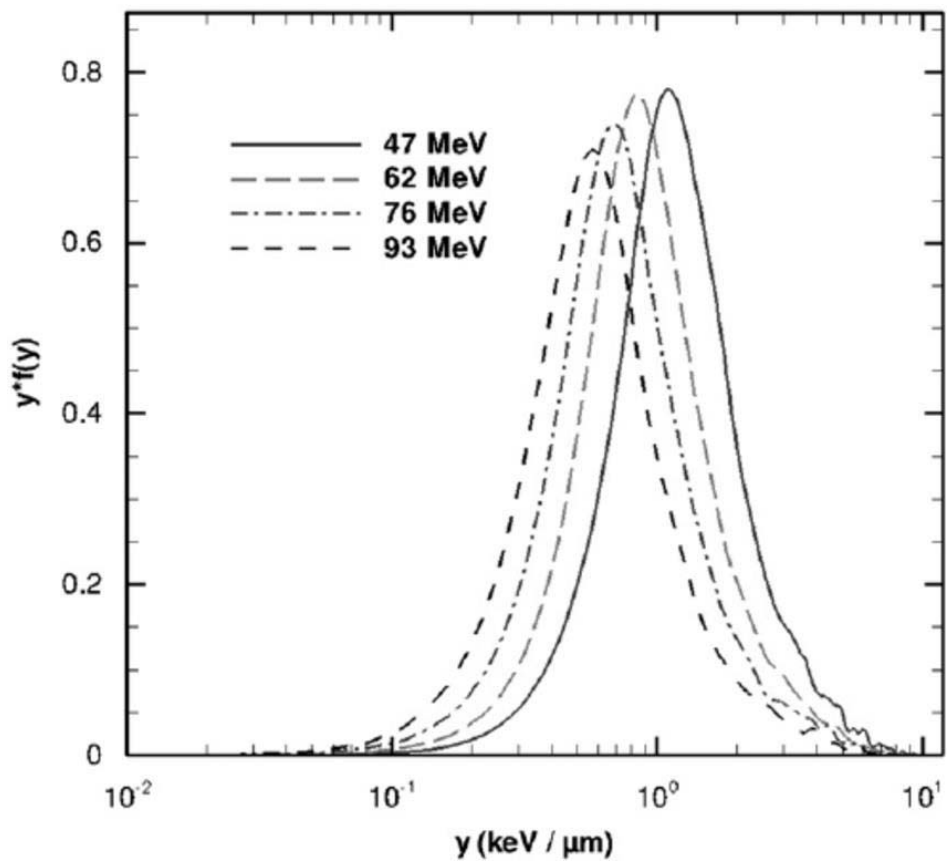

Figure (4-6) Lineal energy frequency distributions for protons of energies (47, 62, 76, 93 MeV) in liquid water through a spherical volume of diameter 3µm obtained by Geant4 simulations [13]

Specific energy z is used in microdosimetry equivalent to absorbed dose and defined as the imparted energy in a certain volume usually a sphere or a cylinder divided by the mass of this volume. Specific energy is calculated according to the following equation:

$$z = \frac{\epsilon}{m} \qquad (4\text{-}8)$$

where ϵ is the total energy imparted inside the sampling volume and m is the mass of the sampling volume. Using the same formalism specific energy distributions and the mean specific energies are defined as follows:

Single event frequency distribution of specific energy:

$$f(z) = \frac{dF(z)}{dz} \qquad (4\text{-}9)$$

where $F(z) = P(\underline{z} < z | \nu = 1)$ is the sum distribution of z i.e. the distribution function is equal to the probability that the random variable $\underline{z}$ does not exceed z such that one event has taken place.

Frequency mean specific energy:

$$\overline{z}_F = \int z f(z)\, dz \tag{4-10}$$

Dose distribution of specific energy is:

$$d(z) = \frac{z f(z)}{\overline{z}_F} \tag{4-11}$$

Dose mean lineal energy:

$$\overline{z}_D = \int z d(z)\, dz = \int \frac{z^2 f(z)\, dz}{\overline{z}_F} = \frac{\overline{z_F^2}}{\overline{z}_F} \tag{4-12}$$

The frequency mean specific energy $\overline{z}_F$ can be related to absorbed dose D by the relation $D = \overline{z}_F \bar{n}$ where $\bar{n}$ is the mean number of events.

The frequency mean variables include the effect of all energy depositions no matter how small they are. However, dose mean variables show the averages of the concentrated energy depositions. The higher concentrations of energy depositions are supposed to be more damaging and thus the dose mean variables show some sort of effectiveness of high density interactions.

4.3 DBSCAN Clustering

DBSCAN "Density Based Spatial Clustering of Applications with Noise" algorithm is a density based algorithm designed to discover clusters of arbitrary shapes and requires basically two input parameters: the radius ε of the neighborhood area and the minimum amount of points ($minPts$) to form a cluster [14]. The algorithm is based on the following quantities:

- Density means the number of points within a specific radius ε.

- A point is considered a *core point* if it has at least a certain specified number of points ($minPts - 1$) surrounding it within the radius ε, so the *core point* is in the interior of a cluster.
- A *border point* has fewer than $minPts - 1$ surrounding it within the radius ε, but it is in the neighborhood of a core point. So the *border point* is considered within the cluster.
- A *noise point* is any point that is neither a *core point* nor a *border point*.

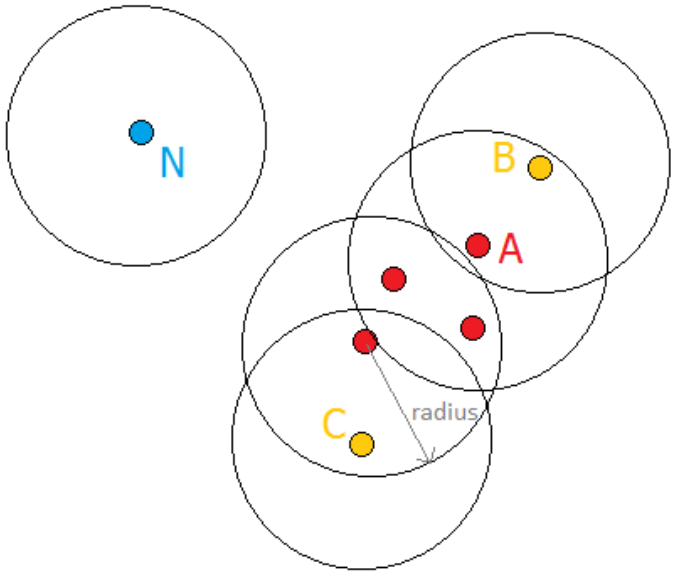

Figure (4-7) Illustrating DBSCAN clustering

Figure (4-7) represents a set of data points. The DBSCAN is performed on this data by choosing the $minPts$ equal to 3. The radius ε is represented by the radius of the circles in the figure. Following the DBSCAN algorithm, the point A and all the red points are considered as core points since each one of them is surrounded by at least 2 points within the radius ε.

The yellow points B and C are considered border points since they are reachable by the core, meaning that the distance separating them from a core point is less than or equal to the radius ε. Thus, the border points B and C are considered part of the cluster. Point N is considered a noise point since it is far away from the core points and the border points, so it does not belong to the cluster.

In short, the clusters are defined as areas of higher density than the remainder of the data set. An example of such clusters is shown in the figure (4-8) below: the points in red and in blue are considered as clusters since the points lye closely together forming a dense region,

where the gray points are scattered away from the majority of the points and are considered as noise outside the clusters.

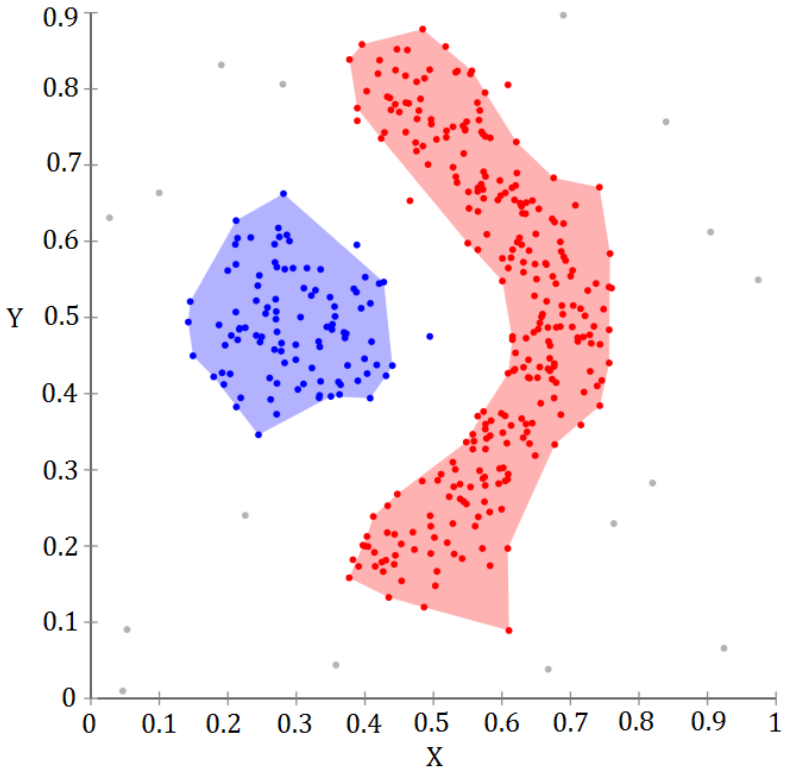

Figure (4-8) Two clusters are shown in red and in blue while the noise points are shown in gray, units are arbitrary [15].

DBSCAN clustering method can be applied to energy deposits in biological material to specify the densely damaged regions from the less damaged ones. Francis *et al.* [16] used the DBSCAN clustering algorithm to study the clustering of single and double strand breaks of DNA molecule induced by proton beams.

They used Geant4-DNA [17] to simulate the proton tracks and the spatial distribution of energy deposits. The particles in this case are tracked to very low energies taking into consideration the details of the damages at a nanometric scale. The algorithm was adapted to the biological nature of the DNA strand breaks where the $minPts$ was set to 2 accounting for two strand breaks forming a clustered damage and the radius ε was set to 3.2 nm accounting for the minimum distance between two single strand breaks to form a double strand break.

The probability of energy deposits to cause damage is related to the presumption that all deposits below 5 eV do not cause strand breakage. The probability of energy deposition damaging ability increases linearly to reach 100% at 37.5 eV above which the damage is

certain to occur. The sensitive parts in the biological medium represented as DNA are considered to be dispersed inside the nucleus occupying 16% of its volume. Therefore, energy deposits in the vicinity of the sensitive parts cause potential damage to the DNA structure. The algorithm runs over all energy deposition points, if their energy value lies within the probability range of causing damage and they lie in a sensitive area they are considered as potential single strand breaks (SSB). These SSBs are then tested for clustering. If at least two SSBs lie at a distance 3.2 nm from each other, they are considered as a cluster. Figure (4-9) shows the yields of simple and clustered SSBs and DSBs induced by proton beams of different energies. The figure shows that clustered damages and DSBs have higher yields with higher *LET* proton radiations.

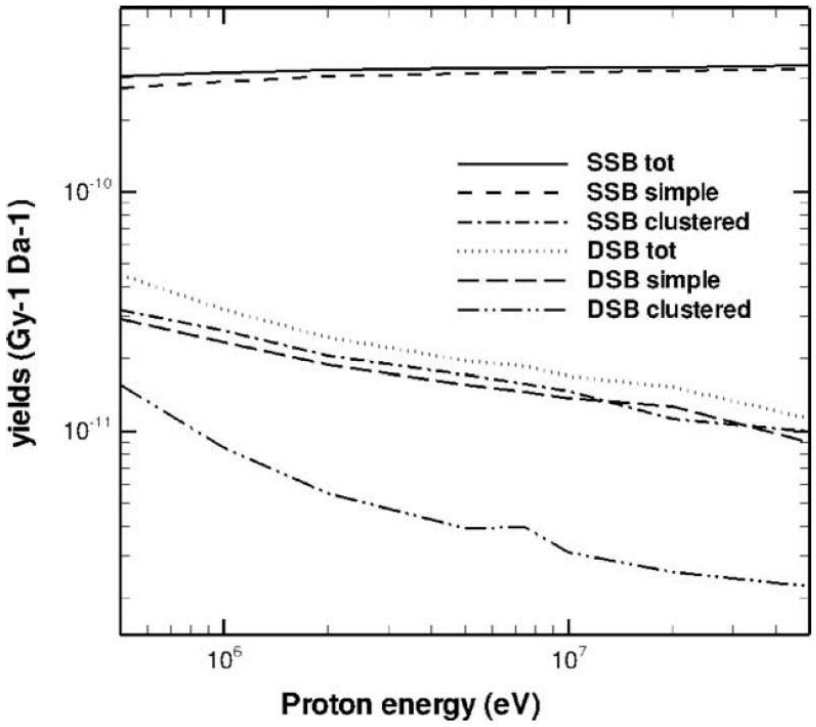

Figure (4-9) Simple and clustered SSBs and DSBs yields comparison for different proton energies [16]

Dos Santos *et al.* [18, 19] and Bueno *et al.* [20] also used the DBSCAN algorithm to estimate clustered damages of DNA for proton and alpha particles with different LET. They used a detailed structure of DNA in the form of nucleosomes and chromatin fibers as their targets filled with water to score the energy depositions.

Clustered damages have a severe effect on the cell's survival since the repair is difficult and prone to errors. DSBs and clustered DSBs are the most difficult types of damage to repair.

Therefore clustering algorithms prove to be beneficial in assessing the damaging effects of ionizing radiation. In our study, we will use DBSCAN algorithm to estimate the clustering densities of energy depositions and reactive oxygen species on mitochondria.

4.4 Conclusion

On large scales, calculating the dose helps quantifying the radiation effect. However, it doesn't take into consideration the stochastic nature of interactions that occur on the microscopic scale. Therefore, microdosimetry provides suitable formalism that take into account the fluctuating nature of energy depositions.

The cell is well equipped with damage repair mechanisms, but when a large number of damages is concentrated in a certain part of the cell repairs take longer time and errors may occur. That is why clustered damages in a small volume are considered harder to repair than single disperse damages. DBSCAN clustering is a simple algorithm that can be used to estimate the radiation induced damage clusters.

1. *ICRU Report 33 Radiation Quantities and Units*. 1980.
2. *ICRU Report 16 Linear Energy Transfer*. 1970.
3. *Radiation Effects Research Foundation*. Available from: www.rerf.jp/radefx/basickno_e/radcell.htm.
4. Tubiana, M., J. Dutreix, and A. Wambersie, *Introduction to Radiobiology*. 1990.
5. *Bragg Peak* Available from: http://www.quantumdiaries.org/2012/02/15/the-hidden-face-of-cern/bragg-peak-3/.
6. Rossi, H.H., *Specification of radiation quality.* Radiation Research, 1959. **10**: p. 522-531.
7. Rossi, H.H., *Spatial distribution of energy deposition by ionizing radiation.* Radiation Research Supplement, 1960. **2**: p. 290-299.
8. Rossi, H.H., *Microscopic energy distribution in irradiated matter*. Radiation Dosimetry, ed. F.H.A.a.W.C. Roesch. Vol. 1. 1968: Academic Press New York.
9. Kellerer, A.M. and D. Chmelevsky, *Concepts of Microdosimetry I.* Radiation and Environmental Biophysics, 1975. **12**: p. 61-69.
10. *ICRU Report 36 Microdosimetry*. 1983.
11. Kellerer, A.M., *Fundamentals of Microdosimetry.* The Dosimetry of Ionizing Radiation, 1985. **1**: p. 78-161.
12. Kellerer, A.M. and D. Chmelevsky, *Concepts of Microdosimetry II.* Radiation and Environmental Biophysics, 1975. **12**: p. 205-216.
13. Francis, Z., et al., *Molecular scale track structure simulations in liquid water using the Geant4-DNA Monte-Carlo processes.* Applied Radiation and Isotops, 2011. **69**(220-226).

14. Ester, M., H.P. Kreigel, and X.X. Sander. *A density-based algorithm for dicovering clusters in large spatial databases with noise*. in *Second International Conference of Knowledge Discovery and Data Mining*. 1996.
15. *Wikipedia the Free Encyclopedia*. Available from: https://en.wikipedia.org.
16. Francis, Z., C. Villagrasa, and I. Clairand, *Simulation of DNA damage clustering after proton irradiation using an adapted DBSCAN algorithm.* Computer Methods and Programs in Biomedicine, 2011(101): p. 265-270.
17. Incerti, S., et al., *The Geant4-DNA Project.* International Journal of Modeling, Simulation and Scientific Computing, 2010. **1**(2): p. 157-178.
18. Dos Santos, M., et al., *Influence of chromatin condensation on the number of direct DSB damages induced by ions studied using a Monte Carlo code*. Radiation Protection Dosimetry, 2014. **161**(1-4): p. 469-473.
19. Dos Santos, M., et al., *Influence of the chromatin density on the number of direct clustered damages calculated for proton and alpha irradiations using a Monte Carlo code*. Progress in Nuclear Science and Technology, 2014. **4**: p 449-453.
20. Bueno, M., et al. *Influence of the geometrical detail in the description of DNA and the scoring method of ionization clustering on nanodosimetric parameters of track structure: a Monte Carlo study using Geant4-DNA*. Phys. Med. Biol., 2015. **60**: p. 8583-8599.

5 Tools to Study the Radiation Effects on Matter

The accurate modeling of ionizing radiation interactions with biological matter remains a challenge in radiobiology. Monte Carlo track structure programs that simulate the interactions of the incoming beam inside the material can provide a good modeling. The Geant4 [1] Monte Carlo simulation toolkit, an open source set of libraries developed for modeling the passage of particles through matter, covers a large variety of application domains, ranging from high energy physics to space and medical applications. It is an object oriented programming toolkit in C++ developed by CERN freely available from the project website [2].

5.1 Basic Principles of Geant4

Geant4 is a software specialized to model interactions of particles and photons in matter. It permits to cover a wide range of physical phenomena studying a variety of applications from medical physics to nuclear astrophysics. Geant4 is designed to be used on a simple PC, where multithreading can be enabled.

Geant4 toolkit provides all the aspects of simulation process to accurately simulate the passage of particles in matter. These aspects include:

- The geometry of the system covering the size, shape, position and material type of the target (known as detector)
- The generation of primary events in the form of fundamental particles specifying their position, direction and energy
- The physics processes governing the particle interactions such as electromagnetic and nuclear interaction processes
- The tracking of particles through materials and electromagnetic fields and the storage of events and tracks
- The capture and analysis of simulation data at different levels of detail and refinement
- The visualization of the detector and particle trajectories

Since it is an object-oriented platform based on C++, there is flexibility for users to construct stand-alone applications or applications built upon another object-oriented framework.

Users can simulate the experiment in the way they want creating the geometry of their system in any way suitable for their study.

Users can simulate physical interactions by specifying to Geant4 the list of physics "processes" and "models" for all particles involved in the simulation. A physics "process" describes a physical interaction such as ionization, multiple scattering etc. and can evoke several physics "models" (which can be fully theoretical, semi-empirical …). Such models compute the physical interaction total cross-section and fully describe the final state of the colliding system, including the production of secondary particles, energy loss and emission angles.

An event is the complete tracking of a primary particle with all its produced secondaries from its production till its absorption.

The particle and its secondaries are tracked step by step along their trajectories taking into account all the physical processes they undergo in the target material.

The properties of the particle and its secondaries such as kinetic energy, position, etc. can be accessed and stored all the way from the point of production to the point of absorption or the point they leave the target. The data can be analyzed afterwards.

5.2 Simple Application in Geant4

A typical Geant4 simulation requires a minimum of three classes classified as three header files and three source files called by a main function. These three class types of information provided by the user are usually called "Detector Construction", "Primary Generator Action" and "Physics List". They describe the basics of simulation as follows:

In **Detector Construction** class the users can describe the geometrical structure of the experiment they intend to simulate. This includes the target of radiation also called the detector, the shielding, the electric and magnetic fields etc. There are geometry classes allowing to construct all elementary shapes such as parallelepipeds, spheres, cones, etc. that can be modified and resized by the users. Users can also define complex geometries such as parametrized volumes and tessellated volumes of non-uniform shapes. Materials are also defined in this class. Users can use predefined materials or they can define compounds according to their needs.

In **Primary Generator Action** class the particle source is defined. The source can be a point source or can have complex geometric form. Its position can be fixed in a precise location but it can also vary during the simulation. The generated particles' direction and their energies can be defined according to the needs of the user. For example, it is possible to generate many particles according to a defined energy spectrum.

In **Physics List** class, all the particles pertaining to the simulation including the secondary particles that may be produced by the primary particles interactions are defined. All the physical processes attributed to each particle in the simulation are also defined. In case of

photons for example, all their properties are defined. All the processes such as photoelectric effect, Compton effect and pair production are included in the class. Users can include physics lists already available with the toolkit or they can define their own physics lists including the particles and processes they need in their simulations.

The user can have access to all the variables (energy deposits, positions, etc.) calculated during the simulation using "Action classes".

- The **Stepping Action** class gives us access to the deposited energy and position of the generated particle as well as other variables at the end of each step.
- A **step** is the distance crossed by the particle between two successive interactions.
- In addition, the **Tracking Action** class gives us access to variables at the beginning and end of each trajectory of a particle.

5.3 CADMesh: Importing Complex Geometry to Geant4

In Geant4, geometry definition can be realized using classes inherited from the *G4VSolid* class defining a certain solid.

These classes include *G4Box* for defining rectangular prisms, *G4Orbs* for defining orbs, *G4Tube* for defining cones among many other classes of regular shapes. Geant4 also allows the user to define parametrizations in order to represent multiple copies or replicas of the same volume. Complex and irregular solids can be defined by a surface mesh created by *G4TessellatedSolid* class.

By definition, tessellation is a shape being repeated over and over again covering a plane, or area leaving no gaps or overlapping. It is performed through many operations like rotation, translation, and reflection. In computer graphics, tessellation is used to create meshes of triangular faces arranged in a precise way to represent 3D objects. Computer aided design models are representations of continuous boundaries of 3D bodies constructed by faces, edges and vertices.

Figure (5-1) shows three different surface meshes of the same 3D human head. As illustrated in the figure, the tessellated representation gets closer to reality as the number of faces increases.

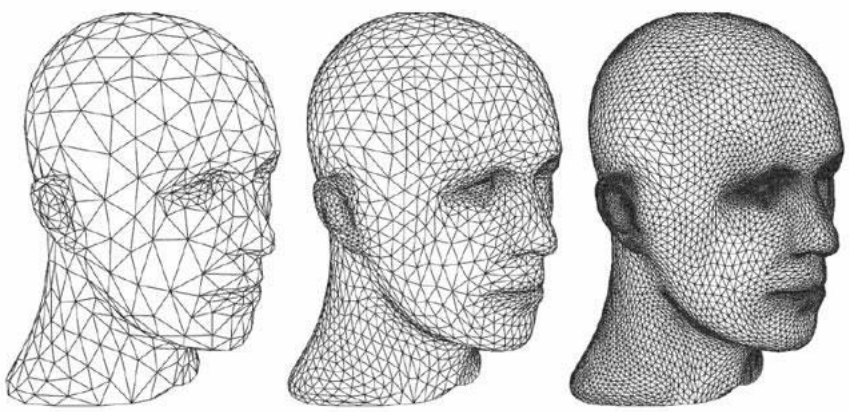

Figure (5-1) Three different meshes modeling a human head with increasing number of vertices and triangular faces [3]

Loading computer aided design (CAD) models as geometry in Geant4 simulations is particularly useful in cases where the geometry is difficult to define with arrangement of primitive solids such as metallic implants of hip prosthesis and anatomical structures derived from x-ray CT scans.

In these cases CAD based geometries provide more accurate representations. The CAD models are triangular or quadrangular boundary representation meshes or surface meshes usually produced in stereo-lithography format (STL)[4] or Stanford polygon file format (PLY)[5].

In order to use these files, intermediate methods of converting these CAD files into GDML [6] formats supported by Geant4 are required. GDML is based on extensible mark-up language (XML) allowing for persistence of many aspects of the Geant4 geometry hierarchy. This conversion into GDML is performed by commercial software such as FastRad [7] and Instep Solveering [8] which may be expensive for most users. In addition, the conversion itself may sometimes produce geometrical errors. Therefore, a direct import of CAD files into Geant4 is more efficient and can be carried out using the freely available CADMesh [9] class written in C++.

The freely available templated C++ library VCGLIB (Visual Computing Laboratory, Italy) offers advanced mesh manipulation functionality and point cloud surface reconstruction algorithms. It also offers an import/export interface for many common CAD file formats along with mesh refinement tools. VCGLIB classes provide the user with access to the CAD file mesh and its encoded elements such as vertices, edges and faces.

The CADMesh interface class is simply a mapping between the VCGLIB derived **CADTriMesh** class composed of faces and vertices, and Geant4 *G4TessellatedSolid* class [10].

Upon creating an instance of CADMesh and supplying it with the file name and type of the target CAD file, an instance of **CADTriMesh** is populated with a mesh described in the CAD file. A VCGLIB import wrapper is used to perform this action.

Now that **CADTriMesh** instance is populated with vertices and faces describing a mesh, **CADTriMesh::FaceIterator** iterator is used to iteratively instantiate a Geant4 *G4TriangularFacet* for each face.

Subsequently, these faces are added to the tessellated solid using the *G4TessellatedSolid::AddFacet* method. Once the iterator has looped over all the faces, the *G4TessellatedSolid::SetSolidClosed* method is called, preventing further faces from being added to the volume.

The user can access the CADMesh interface functionalities by including the *CADMesh.hh* header file in the user detector construction. Instantiation of a CADMesh object and a call to the *CADMesh::TessellatedMesh* method generates and returns a *G4TessellatedSolid* suitable for inclusion in the user geometry in the same manner as with any typical *G4VSolid* object.

The user can then continue the geometry hierarchy of assigning materials and positions to the solid by defining *G4LogicalVolume* and *G4VPhysicalvolume*. The following shows a brief description of the code in the user defined detector construction class for using the CADMesh interface:

```
CADMesh * mesh = new CADMesh("CADFile.ply");

G4TessellatedSolid * cad_solid = mesh->TessellatedMesh();
G4LogicalVolume* cad_logical = new G4LogicalVolume(cad_solid,H2O,"cad_logical",0,0,0);
G4VPhysicalVolume * cad_physical = new G4PVPlacement(rot, G4ThreeVector(0,0,0),
                                  cad_logical,"cad_physical",
                                   mother_logical, false, 0);
```

In order to compile and use the CADMesh interface, it is necessary to have a working installation of Geant4 in addition to the source code for VCGLIB which is freely available on the internet [11].

Using surface meshes on micrometric scale results in navigation errors. Geant4 navigator has problems identifying the position of the tracked particles during simulations. This results in a confusion assigning the positions of the particles whether they are inside or outside the tessellated volume.

CADMesh interface gives an alternative method to avoid these types of errors. This method defines the tessellated solids as tetrahedral meshes in Geant4 [12]. Figure (5-2) shows two tetrahedral meshes.

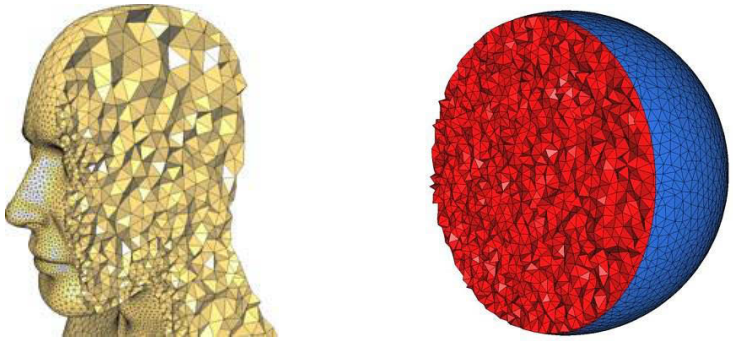

Figure (5-2) Tetrahedral meshes showing a human head [13] and a sphere [14]

To perform tetrahedral meshing, CADMesh uses the freely available C++ quality tetrahedral meshing generator, TETGEN [15]. Using TETGEN library, an input and an output meshes are initialized. The input mesh is populated with a tessellated triangular facet surface mesh described in the CAD file of an STL or PLY format by a load method. The output mesh is then populated with a constrained Delaunay tetrahedralisation of the input mesh using the TETGEN tetrahedralize function. The constrained Delaunay tetrahedralisation configuration preserves the mesh surface described by the input mesh.

Access to individual tetrahedra in the output mesh is available via the **output.tetrahedronlist** vector where every four elements indicate the vertex index numbers of the current tetrahedron. The coordinates of each vertex can then be retrieved from the **out.pointlist** vector. Iterating over the **output.tetrahedronlist** vector, a *G4Tet* solid is then initialized along with a *G4LogicalVolume* for each tetrahedron, where material properties are also assigned. Subsequently each logical volume is added to a *G4AssemblyVolume* allowing for all tetrahedrons to be positioned (including translation, rotation, and reflection operations) within the user detector geometry as a single entity using the *G4AssemblyVolume::MakeImprint* class method. Below is a short illustration of the code in the user defined detector construction class for using the CADMesh interface to produce a tetrahedral mesh from PLY file:

```
CADMesh * tet_mesh = new CADMesh("CADFile.ply", "PLY");
tet_mesh->SetMaterial(H2O);

G4AssemblyVolume * cad_assembly = tet_mesh->TetrahedralMesh();

  G4Translate3D translation(0, 0, 0);
  G4Transform3D rotation = G4Rotate3D(*rot);
  G4Transform3D transform = translation*rotation;

cad_assembly->MakeImprint(World_log, transform, 0, 0);
```

5.4 Step Length

In Geant4, there are different ways to simulate electromagnetic interactions using “standard processes”, “low energy processes” and “DNA processes”. We are interested in

the Geant4-DNA processes and this paragraph summarizes the step length calculation for these processes. As for the standard and low energy processes other parameters play a role in the step length calculation and further description could be found in the thesis of Djamel Dabli [16].

Geant4-DNA simulation of particle transport is performed step by step. A true step length for a next physics interaction is randomly sampled using the mean free path of the interaction.

At the beginning of a step, a random draw from different cross sections of possible processes is done enabling to choose the process type taking place during the step.

Computation of mean free path of a particle in a medium is performed in Geant4 using cross section of a particular physics process and density of atoms.

The mean free path of a process, λ, also called the interaction length, can be given in terms of the total cross section:

$$\lambda(E) = \left(\sum_i [n_i \cdot \sigma(Z_i, E)] \right)^{-1} \quad (5\text{-}1)$$

Where $\sigma(Z, E)$ is the total cross section per atom of the process and the summation runs over all elements composing the material. n_i is the number of atoms per volume in the i^{th} element of a compound material. Z is the atomic number of the material.

$\sum_i [n_i \cdot \sigma(Z_i, E)]$ is also called the macroscopic cross section. The mean free path is the inverse of the macroscopic cross section and represents the step length.

5.5 Sampling Procedure in Geant4

The interaction of particles in matter is a random phenomenon and random variables sampling techniques are required to simulate such behavior. Geant4 toolkit uses a combination of the composition and rejection Monte Carlo methods [17] This combination is advantageous in saving calculation time. In brief, sampling of random numbers goes as follows.

Suppose we wish to sample a variable x in the interval $[x_1, x_2]$ from the distribution $f(x)$, where the normalized probability density function can be written as:

$$f(x) = \sum_{i=1}^{n} N_i h_i(x) g_i(x) \quad (5\text{-}2)$$

Such that $N_i > 0$, $h_i(x)$ are normalized density functions on $[x_1, x_2]$, and $0 \leq g_i(x) \leq 1$.

According to this method, x can be sampled in the following way:

1. Select a random integer $i \in \{1,2, \cdots n\}$ with probability proportional to N_i
2. Select a value x_0 from the distribution $h_i(x)$
3. Calculate $g_i(x_0)$ and accept $x = x_0$ with probability $g_i(x_0)$;
4. If x_0 is rejected restart from step 1.

The average number of tries necessary to accept a value of x is $\sum_i N_i$.

In practice, a good sampling method from the distribution $f(x)$ has the following properties:

- All the sub-distributions $h_i(x)$ can be sampled easily;
- The rejection functions $g_i(x)$ can be evaluated easily/quickly;
- The mean number of tries is not too large.

5.6 Physical Processes and Models

In nature, each particle undergoes certain number of interactions with matter depending on the particle's type and energy and on the type and conditions of the material. These interactions are dealt with as processes in Geant4. These processes are called in the Physics List class.

One process can be based on many different physical models whether they are theoretical or empirical. For example, the photoelectric effect of a photon is defined as a process in Geant4. The user can choose a model among many available models. For one electromagnetic process, table (5-1) shows 4 different models to choose from depending on the user's needs.

Table (5-1) Many models implemented for one physics process, the photoelectric effect in Geant4

EM process	EM model
G4PhotoElectricEffect	G4PEEffectFlouModel G4LivermorePhotoElectricModel G4LivermorePolarizedPhotoElectricModel G4PenelopePhotoElectricModel

Each model has its own interaction cross section data that governs the particles' interactions during a certain simulation.

Geant4 provides different models of interactions since for some types of interactions there is no single model to describe the overall particle's behavior on all energy scales. For example, in the Geant4-DNA extension protons with energy higher than 500 keV are described by the theory of first Born approximation model for ionizations and excitations. However, this model is inapplicable for energies lower than 500 keV and semi-empirical models are used instead. Ionization is modeled by Rudd's model and excitation is modeled by Miller and Green's model [18].

5.7 Livermore Physics List Processes

Geant4 provides many sets of processes and models to various types of interactions. The standard electromagnetic processes do not include interactions at low energies. So the toolkit is extended to cover interactions at lower energies.

These processes are included in the Livermore low energy processes. The current implementation of low energy processes is valid for energies down to 10 eV and can be used up to approximately 100 GeV for gamma processes. For electron processes upper limit is significantly below. It covers elements with atomic number between 1 and 99.

At low energies atomic shell structure is important and the low energy processes make direct use of shell cross section data. The low energy processes include the photoelectric effect, Compton scattering, Rayleigh scattering, gamma conversion, bremsstrahlung and ionization. Fluorescence of excited atoms is also considered.

All processes involve two distinct phases:

- The calculation and use of total cross sections, and
- The generation of the final state.

Both phases are based on the theoretical models and on exploitation of evaluated data. The data used for the determination of cross sections and for sampling of the final state are extracted from a set of publicly distributed evaluated data libraries:

- EPDL97(Evaluated Photons Data Library)[19]
- EEDL (Evaluated Electrons Data Library)[20]
- EADL (Evaluated Atomic Data Library)[21]
- Binding energy values based on data of Scofield.[22]

Evaluated data sets are produced through the process of critical comparison, selection, renormalization and averaging of the available experimental data, normally complemented by model calculations. These libraries provide the following data relevant for the simulation of Geant4 low energy processes:

- Total cross sections for photoelectric effect, Compton scattering, Rayleigh scattering, pair production and bremsstrahlung
- Subshell integrated cross sections for photoelectric effect and ionization
- Energy spectra of the secondaries for electron processes
- Scattering functions for electrons for all subshells
- Transition probabilities between subshells for fluorescence and the Auger effect

The energy range covered by the data libraries extends from 100 GeV down to 1 eV for Rayleigh and Compton effects, down to the lowest binding energy for each element for photoelectric effect and ionization and down to 10eV for bremsstrahlung.

The energy dependence of the total cross section is derived for each process from the evaluated data libraries. For ionization, bremsstrahlung and Compton scattering the total cross section at a given energy E is obtained by interpolation according to the formula:

$$\log\big(\sigma(E)\big) = \frac{\log(\sigma_1)\log(E_2/E) + \log(\sigma_2)\log(E/E_1)}{\log(E_2/E_1)} \qquad (5\text{-}3)$$

Where E_1 and E_2 are the closest lower and higher energy points respectively for which data σ_1 and σ_2 are available.

5.8 Atomic Relaxation

Ionization processes leaves the atoms with a vacancy in their electronic shells. This is considered as a type of excitation to the atom and induces atomic relaxation.

Atomic relaxation occurs when an electron from a high energy level relaxes to a lower level to fill the vacancy created by ionization. This relaxation results in the production of a fluorescent photon or an Auger electron.

In Geant4, processes inducing atomic relaxation are photoelectric effect, Compton effect and ionization.

For this, Geant4 uses the Livermore Evaluation Atomic Data Library EADL [21] that contains data to describe the relaxation of atoms back to neutrality after they are ionized. This data includes the radiative and non-radiative transition probabilities for each sub-shell of each element with atomic numbers from Z=1 to 100. Since an ionization process ejects an electron from a sub-shell of a bound atom leaving a vacancy in that subshell, the EADL data are used to calculate the complete radiative and non-radiative spectrum of X-rays and electrons emitted when the atom relaxes back to neutrality.

The radiative relaxation is represented by fluorescence process and simulated in Geant4 by the following procedure:

1. If the vacancy shell is not included in the data, energy equal to the binding energy of the shell is deposited locally
2. If the vacancy subshell is included in the data, an outer subshell is randomly selected taking into account the relative transition probabilities for all possible outer subshells
3. In the case where the energy corresponding to the selected transition is larger than a user defined cut value (equal to zero by default), a photon particle is created and emitted in a random direction in 4π with an energy equal to the transition energy provided by EADL
4. The procedure is repeated from step 1 for the new vacancy subshell

The final local energy deposit is the difference between the binding energy of the initial vacancy subshell and the sum of all transition energies which were taken by fluorescence photons. The atom is assumed to be initially ionized with an electric charge of $+1e$.

The non-radiative relaxation process is represented by Auger effect which is complimentary to fluorescence. Therefore, for Auger processes the same simulation procedure is followed, with the exception that two random shells are selected: one for the transition electron that fills the original vacancy, and the other for selecting the shell generating the Auger electron.

Subshell data in EADL tables are provided for Z > 5, so fluorescence and Auger processes are considered for atoms of atomic number from 6 to 100. In case of Z <5 the simulation ends with a local deposit corresponding to the electron binding energy of the ionized subshell.

Note that the fluorescence and Auger processes are not turned on by default and can be included in the simulation by shell commands or macro file commands. Below is an example of how to turn on these processes in the Geant4 simulations:

```
/process/em/fluo true
/process/em/auger true
```

5.9 Geant4-DNA

Geant4 has been extended to microdosimetry applications in liquid water at very low energies and sub-micrometer scale in the framework of the Geant4-DNA project [23, 24]. As a component of Geant4 electromagnetic physics, Geant4-DNA simulates the dominant physical interactions of electrons, protons and other ions in liquid water down to very low energies reaching to the eV scale [25, 26]. It is applied in the medical domain such as

particle therapy to study radiation effects at the cellular level. It is also of interest for possible manned space exploration programs to evaluate the effects of cosmic radiation on astronauts.

The recent versions of Geant4-DNA, starting from the geant4.10.1 version, contains libraries simulating the physico-chemical and chemical phases of radiation effects [27]. These libraries help simulate the radiolytic species production, their diffusion and their mutual interactions in liquid water after the physical phase ends.

In Geant4-DNA, photon interactions (also called gamma interactions) are based on the Geant4 Livermore models and are included by default in the G4EmDNAPhysics constructor. This constructor is a built-in class available to the users just by calling it from the Physics List of their applications.

In our study we will list the electron interaction models of Geant4-DNA summarized in table (5-2). These models are implemented based on theoretical and semi-empirical studies.

Table (5-2) Geant4-DNA models of electron physics processes

Interaction	Process Class	Model Class	Min energy	Max energy
Elastic scattering	G4DNAElastic	G4DNAChampionElasticModel	0eV	1MeV
Elastic scattering	G4DNAElastic	G4DNAScreenedRutherfordElasticModel	0eV	1MeV
Electronic excitation	G4DNAExcitation	G4DNABornExcitationModel	9eV	1MeV
Electronic excitation	G4DNAExcitation	G4DNAEmfietzoglouExcitationModel	8eV	10keV
Ionization	G4DNAIonisation	G4DNABornIonisationModel	11eV	1MeV
Ionization	G4DNAIonisation	G4DNAEmfietzoglouIonisationModel	10eV	10keV
Vibrational excitation	G4DNAVibExcitation	G4DNASancheExcitationModel	2eV	100eV
Attachment	G4DNAAttachment	G4DNAMeltonAttachmentModel	4eV	13eV

5.9.1 **Ionization and Excitation**

Ionization and excitation inelastic cross sections in liquid water are calculated using the Plane-Wave First Born Approximation (FBA) method detailed by Landau and Lifshitz [28] and Bethe [29, 30].

5 ionization states and 5 excitation states of water molecule are considered using the dispersion model of Emfietzoglou *et al.* [31, 32]. The dielectric response function (DRF) of the target molecule is used to calculate the interaction cross sections for incident particles. According to the FBA, energy and momentum transfers are related to the energy loss function (ELF) $Im[-1/\varepsilon(E,q)]$, where ε is the complex DRF characterizing the target molecule. The Born double differential inverse mean free path (IMFP) is given in terms of energy loss E and momentum transfer q by [33]:

$$\frac{d^2\Sigma(T,E,q)}{dE.dq} = \frac{1}{\pi\alpha_0 Tq} Im\left[\frac{-1}{\varepsilon(E,q)}\right]\theta[q - q_-(E,T)]\theta[q_+(E,T) - q] \quad (5\text{-}4)$$

Where α_0 is the Bohr radius, T is the kinetic energy of the incident electron, θ is the Heaviside step function and $\varepsilon = \varepsilon_1 + \varepsilon_2$ represents the complex dielectric response function of the target material.

The momentum transfer limits are given as follows:

$$q_\pm = \sqrt{2M}\left(\sqrt{T} \pm \sqrt{T - E}\right) \quad (5\text{-}5)$$

M is the mass of the incident particle.

The single differential cross section and the integrated IMFP can be obtained simply by the following expressions:

$$\frac{d\Sigma(T,E)}{dE} = \int \frac{d^2\Sigma(T,E,q)}{dE.dq} dq \quad (5\text{-}6)$$

$$\Sigma(T) = \int dE \int \frac{d^2\Sigma(T,E,q)}{dE.dq} dq \quad (5\text{-}7)$$

Note that the inverse mean free path is proportional to the total cross section of a certain process.

The K-shell electrons have a relatively high kinetic energy (~800 eV), therefore their orbiting speed becomes comparable with that of the incident projectile. In this case, the implemented model is the one proposed in ICRU report 55 [34, 35]:

$$\frac{d\Sigma_{K-shell}}{dE} = n\frac{4\pi\alpha_0^2 R^2 N}{T + B + U} \times \left\{\left[\frac{1}{E^2} - \frac{1}{E(T - E + B)} + \frac{1}{(T - E + B)^2}\right] + \frac{4U}{3}\left[\frac{1}{E^3} + \frac{1}{(T - E + B)^3}\right]\right\} \quad (5\text{-}8)$$

Where B is the binding energy of the K-shell (~539.7 eV), n is the total number of electrons in that shell, α_0 the Bohr radius, R the Rydberg constant, T the kinetic energy of the projectile, U the kinetic energy of the electrons in the K-shell and N the molecular density.

For very low electron energies (<1 keV) the FBA fails and to take into account the perturbation effects caused by the kinetic energies of the target's electrons, several correction terms are available in the literature.

To account for the potential energy gained by the incident electron in the field of the target molecule a classic Coulomb-field correction is used. Therefore, the calculated cross-section for an electron with kinetic energy T is calculated with energy $T' = T + B_j + U_j$ for ionizations, where B_j and U_j are the j^{th} shell binding energy and the shell's electron kinetic energy, and $T' = T + 2E_j$ for excitations, where E_j is the j^{th} excitation energy.

At low energies, the exchange correction term from [36] is taken into account:

$$\frac{d\Sigma^j_{exchange}}{dE}(E,T) = \frac{d\Sigma^j}{dW}(T + E_j - E, T) - \left(1 - \sqrt{\frac{E_j}{T}}\right) \times \left(\frac{d\Sigma^j}{dE}(E,T)\frac{d\Sigma^j}{dE}(T + E_j - E, T)\right)^{1/2} \quad (5\text{-}9)$$

Thus,

$$\frac{d\Sigma^j(T,E)}{dE} = \frac{d\Sigma^j(E,T')}{dE} + \frac{d\Sigma^j_{exchange}}{dE}(E,T) \quad (5\text{-}10)$$

In case of high kinetic energy incident electrons, other corrections are applied. For electrons exceeding 10 keV, the transverse interaction becomes more significant where relativistic assumptions are considered. The transverse interaction term is calculated from the following equation [37] with $\beta = v/c$:

$$\Sigma_j^T = \frac{1}{\pi\alpha_0\beta^2 Tmc^2}\left\{\int_{E_{min}}^{E_{max}} Im\left[\frac{-1}{\varepsilon(E,0)}\right]_j dE\right\} \times \left[\ln\left(\frac{1}{1-\beta^2(T)}\right) - \beta^2(T)\right] \quad (5\text{-}11)$$

Where E_{min} is the binding energy of each shell and $E_{max} = (T + B_j)/2$.

5.9.2 **Electron Elastic Collisions**

At low energies elastic collisions are the dominant interaction process for electrons. In this case kinetic energy is conserved and electrons change their direction with each collision. Therefore, it is important to take into account elastic scattering in order to calculate the whole track structure. Two different models are implemented in Geant4-DNA and they are independently available for users:

1. The screened Rutherford model [38] for electrons with energy >0.2 keV and Brenner and Zaider formula [39] for electrons with energy <0.2 keV,
2. The Champion *et al.* model [40] applicable to electrons and positrons in liquid and gaseous water.

The screened Rutherford model for elastic scattering of electrons with energies >0.2 keV is implemented according to the Rutherford differential cross section including a term to account for screening effects that agree well with experiments:

$$\frac{d\sigma_{el}}{d\Omega} \propto \frac{Z(Z+1)e^4/4T^2}{\left[1+2\frac{(\alpha_1+\beta_1\ln T)KZ^{2/3}}{(T/mc^2)(2+T/mc^2)}-\cos\theta\right]^2} \quad (5\text{-}12)$$

Where $d\Omega$ is the solid angle element in the scattering direction θ, Z is the atomic number of the target and constants have the following values, $\alpha_1 = 1.64$, $\beta_1 = 0.0825$ and $K = 1.7 \times 10^{-5}$.[41].

The Brenner and Zaider formula for electron elastic scattering differential cross section is:

$$\frac{d\sigma_{el}}{d\Omega} \propto \frac{1}{[1+2\gamma(T)-\cos\theta]^2} + \frac{\beta(T)}{[1+2\delta(T)-\cos\theta]^2} \quad (5\text{-}13)$$

Where $\beta(T)$, $\gamma(T)$ and $\delta(T)$ are parametric functions established by fitting experimental data and their analytic expression can be found in [39].

5.9.3 **Scattering Directions for Primary and Secondary Electrons**

The direction of primary electron scattering by inelastic collisions was processed with the Grosswendt and Waibel model [41].

So the scattering polar angle θ of the primary particle is calculated by the following relations depending on the final kinetic energy W of the secondary electron:

- For $W > 100\ eV$

$$sin^2\theta = \frac{W/T}{\left(1-\frac{W}{T}\right)\left(\frac{T}{2mc^2}\right)+1} \quad (5\text{-}14)$$

Note that T is the initial kinetic energy of the primary electron.

- For $W \leq 100\ eV$

$$\theta \in \left[0, \frac{\pi}{4}\right] \quad (5\text{-}15)$$

The ejection angle θ' of the secondary electrons was obtained by the following:

- For $W > 200\ eV$

$$sin^2\theta' = \frac{1 - W/T}{1 + W/2mc^2} \quad (5\text{-}16)$$

- For $50\ eV \leq W \leq 200\ eV$

$$90\%\theta' \in \left[\frac{\pi}{4}, \frac{\pi}{2}\right] \quad (5\text{-}17)$$

$$10\%\theta' \in [0, \pi] \quad (5\text{-}18)$$

- For$W < 50\ eV$

$$\theta' \in [0, \pi] \quad (5\text{-}19)$$

The azimuthal angle of the primary electron Φ is assumed to be uniformly distributed between 0 and 2π while the secondary electron angle is taken as $\Phi' = \Phi - \pi$.

For low energy electrons $W < 50\ eV$ the electrons direction is isotropic in space and the behavior of the direction change is not well known for scattering in liquid water, besides the direction change over this energy domain is mainly governed by elastic scattering angles.

5.9.4 **Sub-excitation Electrons**

Sub-excitation electrons are electrons with energies below 8.22 eV and do not have enough energy to undergo ionization or excitation interactions with the medium. However, they can undergo vibrational excitations, elastic scattering and electron attachment.

Cross sections for sub-excitation electron scattering are not available for liquid water, but some measurements are done with experiments on amorphous ice films described by Michaud *et al.* [42].

These measurements take into account 9 excitation phonon modes; 2 translational, 2 vibrational, bending, stretching, asymmetrical stretching, stretching-vibrational combination and an overtone of the stretching modes. In condensed water phase cross sections are expected to be higher than for ice, so cross sections on ice films are multiplied by a factor of 2 to account for differences between solid and liquid phases. This factor is

deduced somehow empirically by analyzing the expected results after comparing the difference between the gas phase data [43] and the solid phase data [42, 44], and also because it leads to a reasonable range and energy loss rate for sub-excitation electrons. Vibrational excitations are available up to 100 eV and neglected above this energy due to the lack of data. Below 1.7 eV which is the lowest energy provided by the experiment, a uniform extrapolation down to 0 eV is applied. Angular deflection of the electron's direction after such excitations are neglected to simplify the computing task and usually it is dominated by the elastic scattering process at these energies.

5.10 Conclusion

Geant4 is a Monte Carlo simulation toolkit designed to track particles inside different types of target materials. It is used to simulate experiments with different types of beams and a variety of targets with simple or complex shapes. Elementary shapes like boxes and spheres can be defined as well as complex tessellated meshes. The CADMesh library helps the users to import CAD designs of complex shapes into Geant4 in the form of tessellated and tetrahedral meshes.

Interactions of the particles in Geant4 are carried out by physics processes that are described by theoretical and empirical models. Each model has its own data set of interaction cross-sections.

The Livermore physics list describes the electromagnetic interactions of photons and electrons. Ionizations, excitations and Bremsstrahlung of electrons as well as photoelectric effect, Compton effect and pair production of photons are available. Atomic de-excitation in the form of Fluorescence and Auger electrons can also be activated.

Geant4-DNA physics list provides models of electromagnetic interactions of charged particles for very low energies up to few eV. These models are applied to liquid water targets only. These libraries are used for medical applications since the biological media contain about 70% water.

1. Agostinelli, S., et al., *Geant4-a simulation toolkit.* Nuclear Instruments and Methods in Physics Research A, 2003. **506**: p. 250-303.
2. *Geant4*. Available from: http://www.geant4.org/geant4/.
3. Kobbelt, L., J. Vorsatz, and H.-P. Seidel, *Multiresolution Hierarchies on Unstructured Triangle Meshes.* Computational Geometry Journal: Theory and Applications, 1999. **14**: p. 5-24.
4. *Stereolithography Interface Specification*. 1989, 3D Systems Inc

5. *PLY - Polygon File Format. Computer software and file format description.* . 2012; Available from: http://local.wasp.uwa.edu.au/~pbourke/Dataformats/ply/
6. Chytracek, R., et al., *Geometry description markup language for physics simulation and analysis applications.* IEEE Transactions on Nuclear Science, 2006. **53**(5): p. 2892-2896.
7. Beutier, T., et al. *Fastrad new tool for radiation prediction*. in *Proceedings of the 7th European Conference on Radiation and Its Effects on Components and Systems*. 2003.
8. *Solveering LLC*. Available from: https://www.solveering.com/instep.htm.
9. Poole, C.M. *CADMESH*. Available from: https://github.com/christopherpoole/CADMesh.
10. Poole, C.M., et al., *A CAD interface for Geant4.* Australian Phys Eng Sci Med, 2012. **53**(3): p. 329-334.
11. *VCG Library*. Available from: http://vcg.isti.cnr.it/vcglib/.
12. Poole, C.M., et al., *Fast Tessellated Solid Navigation in Geant4.* IEEE Transactions on Nuclear Science, 2012. **59**(4): p. 1695 - 1701.
13. Alliez, P., et al. *Variational Tetrahedral Meshing*. in *SIGGRAPH*. 2005. ACM.
14. Alliez, P., et al. *CGAL 4.10 - 3D Mesh Generation User Manual* Available from: http://doc.cgal.org/latest/Mesh_3/index.html.
15. *Tetgen: a quality tetrahedral mesh generator and a 3D Delaunay triangulator*. Available from: http://wias-berlin.de/software/tetgen/.
16. Dabli, D., *Utilisation d'un modèle microdosimétrique (MKM) pour l'interprétation d'irradiations cellulaires dans le cadre de l'hadronthérapie*. 2010, Université Blaise Pascal Clermont Ferrand II.
17. *Geant4 Physics Reference Manual*. Vol. version geant4 10.1. 2014.
18. Francis, Z., et al., *Molecular scale track structure simulations in liquid water using the Geant4-DNA Monte-Carlo processes.* Applied Radiation and Isotops, 2011. **69**(220-226).
19. Cullen, D., J.H. Hubbell, and L. Kissel, *EPDL97: the Evaluated Photon Data Library, '97 version.* UCRL–50400, 1997. **6**(5).
20. Perkins, S.T., D.E. Cullen, and S.M. Seltzer, *Tables and Graphs of Electron-Interaction Cross-Sections from 10 eV to 100 GeV Derived from the LLNL Evaluated Electron Data Library (EEDL), Z=1-100.* UCRL-50400, 1991. **31**.
21. Perkins, S.T., et al., *Tables and Graphs of Atomic Subshell and Relaxation Data Derived from the LLNL Evaluated Atomic Data Library (EADL), Z=1-100.* UCRL-50400. **30**.
22. Scofield, J.H., *Radiative Transitions*, in *Atomic inner-shell processes*. 1975, Crasemann, B. (ed.); Academic Press, Inc; : New York. p. 265-292.
23. Incerti, S., et al., *The Geant4-DNA Project.* International Journal of Modeling, Simulation and Scientific Computing, 2010. **1**(2): p. 157-178.
24. Incerti, S., et al., *Energy deposition in small-scale targets of liquid water using the very low energy electromagnetic physics processes of the Geant4 toolkit.* Nuclear Instruments and Methods in Physics Research A, 2013. **306**: p. 158-164.
25. Incerti, S., et al., *Comparison of GEANT4 very low energy cross section models with experimental data in water.* Medical Physics, 2010. **37**: p. 4692-4708.
26. Tran, H.N., et al., *Modeling proton and alpha elastic scattering in liquid water in Geant4-DNA.* Nuclear Instruments and Methods in Physics Research, 2015. **A**(343): p. 132-137.

27. Karamitros, M., et al., *Modeling Radiation Chemistry in the Geant4 Toolkit.* Progress in Nuclear Science and Technology, 2011. **2**: p. 503-508.
28. Landau, L.D. and E.M. Lifshitz, *Electrodynamics of continuous media*. 1970, Pergamon Press.
29. Bethe, H., Annalen der Physik, 1930. **397**(3): p. 325-400.
30. Bethe, H., *Handbuch der Physik*, H.Geiger and K.Scheel, Editors. 1933, Springer: Berlin. p. 273.
31. Emfietzoglou, D., *Semi-empirical inelastic cross-sections for electron transport in liquid water.* Radiation Protection Dosimetry, 2002. **99**: p. 39-46.
32. Emfietzoglou, D. and M. M, *Inelastic collision characteristics of electrons in liquid water.* Nuclear Instruments and Methods, 2002. **B**(193): p. 71-78.
33. Francis, Z., et al., *Stopping power and ranges of electrons, protons and alpha particles in liquid water using the Geant4-DNA package.* Nuclear Instruments and Methods in Physics Research, 2011. **B**(269): p. 2307-2311.
34. *ICRU Report 55: Secondary Electron Spectra from Charged Particle Interactions*. 1996.
35. Villagrasa, C., Z. Francis, and S. Incerti, *Physical models implemented in the Geant4-DNA extension of the Geant4 toolkit for calculating initial radiation damage at the molecular level.* Radiation Protection Dosimetry, 2011. **143**(2-4): p. 214-218.
36. Dingfelder, M., et al., *Electron inelastic-scattering cross-sections in liquid water.* Radiation Physics and Chemistry, 1998. **53**: p. 1-18.
37. Bousis, C., et al., *Electron ionization cross-section calculations for liquid water at high impact energies.* Nuclear Instruments and Methods, 2008. **B**(266): p. 1185-1192.
38. Emfietzoglou, D., et al., *A Monte-Carlo track structure code for electrons (~10eV-10keV) and protons (~0.3-10MeV) in water partitioning of energy and collision events.* Physics in Medicine and Biology, 2000. **45**: p. 3171-3194.
39. Brenner, D.J. and M. Zaider, *A computationally convenient parametrisation of experimental angular distributions of low energy electrons elastically scattered off water vapour.* Physics in Medicine and Biology, 1983. **29**(4): p. 443-447.
40. Champion, C., et al., *A free-parameter theoretical model for describing the electron elastic scattering in water in the Geant4 toolkit.* Radiation Physics and Chemistry, 2009. **78**: p. 745-750.
41. Grosswendt, B. and E. Waibel, *Transport of low energy electrons in nitrogen and air.* Nuclear Instruments and Methods, 1978. **B**(155): p. 145-156.
42. Michaud, M., A. Wen, and L. Sanche, *Elastic and inelastic cross-sections for low-energy (1-100 eV) electron scattering in amorphous ice.* Radiation Research, 2003. **159**: p. 3-22.
43. Banna, M.S., et al., *The photoelectron spectrum of water in the 30–140 eV photon energy range.* Journal of Chemistry and Physics, 1986. **84**: p. 4739-4744.
44. Michaud, M. and L. Sanche, *Total cross-section for slow electrons (1–20eV) scattering in solid H2O.* Phsical Review, 1987. **A**(36): p. 4672-4683.

6 A Realistic Mitochondria Phantom

In mammalian cells, mitochondria take on a wide variety of shapes ranging from long interconnected tubules to individual small spheres [1]. In cultured fibroblasts the mitochondrial population consists mostly of short and long tubules which constantly migrate along their axes along the microtubule tracks [2]. Mitochondria usually replicate or fuse with each other changing their number according to the energy needs of the cell [3].

Since the mitochondria are crucial to the cell's functioning and overall vitality, it is important to study the ionizing radiation effects on them. Monte Carlo simulation of particle tracks is a good tool to study these effects by dose deposits calculation in individual cells. Monte Carlo Geant4 toolkit is a powerful tool that is able to mimic the stochastic nature of elementary particle interaction with matter. This calculation had been performed up to now by assuming simple cell geometries based on the combination of simple mathematical volumes such as spheres, cylinders, and ellipsoids containing liquid water, the main component of biological tissue [4, 5].

These approximations do not take into account the variety and complexity of the organelle geometries encountered in a typical cell. Therefore, we aim to create a mitochondria phantom to model the physical shape of the mitochondrial network taking into account the complexity of these structures inside the cell. To do so, microscopic images of fibroblast cells were imaged at the Mitolab Laboratory in Angers University Hospital [6].

6.1 Cell Culture Preparation and Imaging

6.1.1 Primary fibroblasts cultures

Fibroblast cell cultures were derived from skin biopsies from healthy and mitochondrial disease affected subjects at Angers University Hospital, after obtaining written consent [1].

Control fibroblasts were cultured in 2/3 Dulbecco's modified Eagle's medium (DMEM) with 25 mM glucose and 1/3 Amniomax, supplemented with 10% foetal bovine serum (FBS), uridine (50 µg/ml, Sigma) and pyruvate (100 µg/ml, Sigma). All cell cultures were established and grown at $37^{\circ}C$ in a humidified atmosphere of 5% CO_2, and no antibiotic was used in the following protocols.

[1] This work was approved by the Ethical Committee of the University Hospital of Angers (*Comité de Protection des Personnes CPP Ouest II – Angers, France*; identification number CPP CB 2014/02; Declaration number DC-2011-1467 and Authorization number AC-2012-1507)

6.1.2 **Micropatterned coverslips**

The complexity of mitochondrial imaging arises from the fact that the mitochondrial network undergoes continuous remodelling, with cycles of fission and fusion giving rise to various shapes of mitochondrial reticulum, ranging from groups of sacks or cisternae to extensive, interconnected tubules [7, 8]. Conventionally prepared for microscopy, cells spread on slides present images of considerable heterogeneity [9]. Thus, cells may appear to be narrow or wide, with irregular cytoplasmic extensions spreading over neighbouring cells, leading to misinterpretation. These apparent variations of cell morphology have greatly impeded the analysis of mitochondrial network architecture.

The recently developed Cytoo® micropatterned coverslips allow standardization of the size and shape of cultured cells [10]. Cells were seeded on Cytoo® micropatterned coverslips (cytoo.com) at least 4 hours prior to image acquisition, in DMEM-F12, 1% FBS, in a humidified atmosphere (95% air, 5% CO2) at 37°C [6].

6.1.3 **Microscopy, deconvolution, and mitochondrial network analysis**

Mitochondria of the cultured cells were stained using Mitotracker® Green (Molecular Probes). Images were acquired with an inverted wide-field Nikon Ti-E microscope equipped with an Andor NEOsCMOS camera controlled by NIS Element software. Each image was obtained with a 100x oil objective (Nikon Plan Apo100x, N.A. 1.45). The size of the pixel of the Andor NEOsCMOS camera is 6.5 µm x 6.5 µm. Combined with the 100x oil objective, final pixel size of the recorded images is 65 nm x 65 nm in *x* and *y*.

The high precision *z*-axis nanopositioners Piezo MCL Nano Z100-N Ti allowed faster *z*-step movements, keeping the sample immobile while shifting objective lens. Stacks of 2D images were acquired along the *z*-axis with 0.2µm increments. Measurements were performed at room temperature (20 C) to reduce mitochondrial movement. For fluorescent imaging, well-spread triangular cells were selected.

Microscopy images are always degraded by blurring and noise. The blurring is largely due to diffraction limited imaging by the instrument. Preliminary to any processing, images had been so subjected to deconvolution using Huygens software [11] (Scientific Volume Imaging) with adapted Point Spread Function (PSF). Huygens Essential deconvolution software computes a theoretical PSF based on a model of the microscope and known microscopic parameters. In our case, we adapted the PSF to the experimental conditions (widefield microscope type, 1.45 numerical aperture, 1.51 oil lens immersion, 488 nm excitation wavelength of the Mitotracker® Green probe, 520 nm emission wavelength, (100 nm, 100 nm, 200 nm) xyz sampling intervals, CMLE algorithm, 50 maximum interactions, signal to noise ratio is 40, and the quality threshold is 0.01). We used point-spread function (PSF)-Speck microspheres (Invitrogen) to test the system's optical stability.

Mitochondria form a network of filaments within the cytoplasm, generally surrounding the cell's nucleus. On the right of figure (6-1) the image of the mitochondrial network of a human fibroblast cell acquired with an inverted wide-field microscope, after staining with Mitotracker® Green (Molecular Probes) is shown. On the left, the same cell is shown in phase contrast microscopy indicating the location of the nucleus. The global shape could also be fragmented when the cell is affected by diseases. As an example, Figure (6-2) shows two configurations of fibroblasts' mitochondria chemically affected by mitochondrial inhibitors (antimycin 18 µM, 6 h).

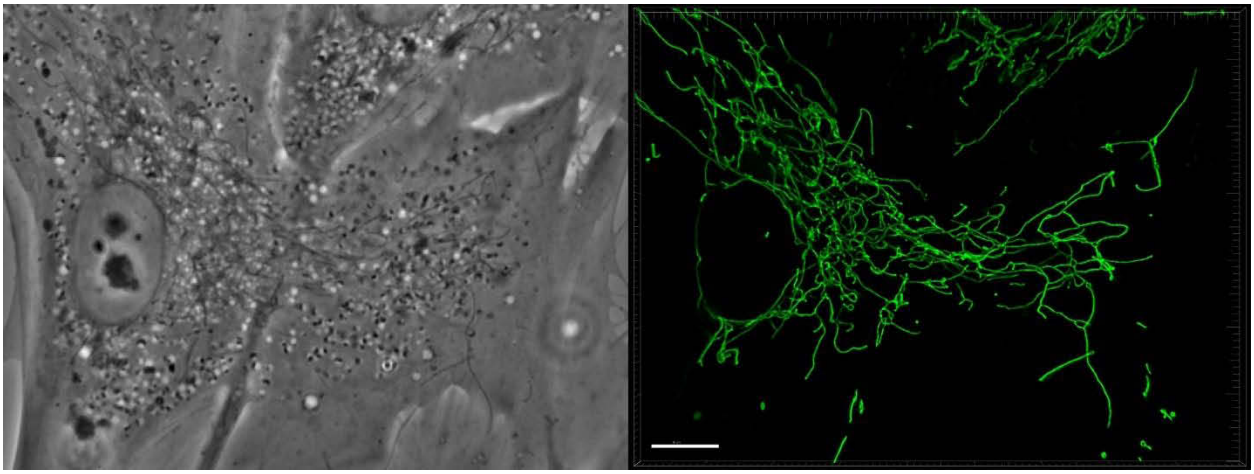

Figure (6-1) Right: image of the mitochondrial network of a human fibroblast cell, acquired with an inverted wide-field microscopy, after staining with Mitotracker® Green. Left: the same cell in phase contrast microscopy showing the nucleus in the cell. Scale bar 10 µm shown in white.

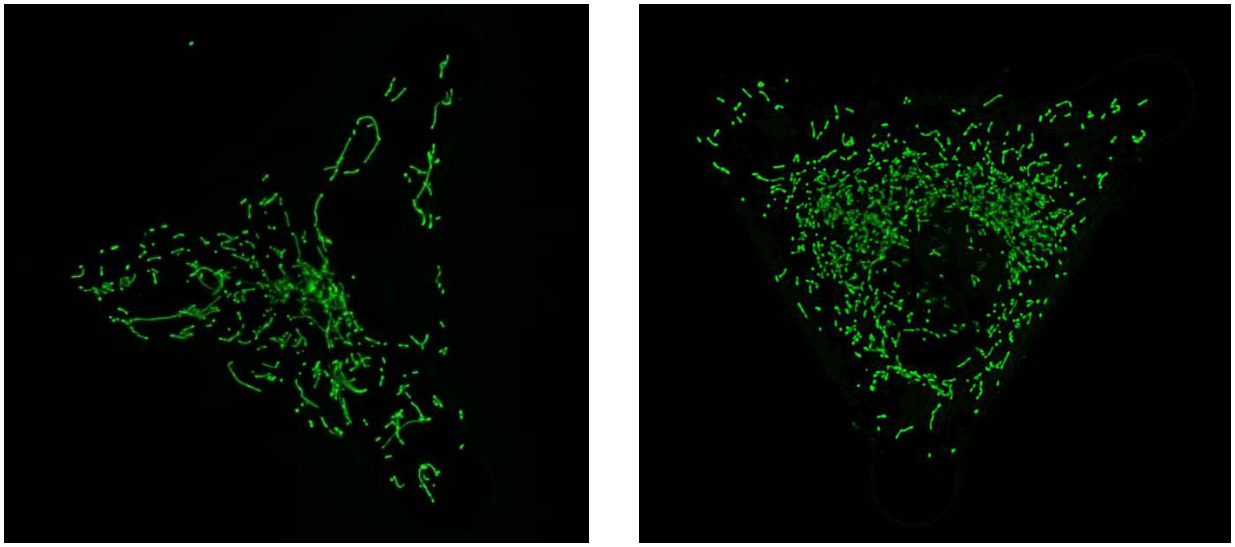

Figure (6-2): Representative images of mitochondrial networks, chemically affected by mitochondrial inhibitors (antimycin 18 µM, 6h) in fibroblasts.

Figure (6-3) shows four fluorescent images of mitochondria networks in healthy fibroblast cells stained with Mitotracker Green using maximum intensity projection (MIP). All the slices belonging to the same stack are projected on top of each other, and the total intensity of all slices is shown in one picture. The image on the top right of figure (6-3) is chosen as a first prototype to develop the method of 3D phantom creation. These images consist of 2D slices in the *x*-*y* plane stacked over each other along the *z*-axis. The slices are separated by 0.2 μm distance in the *z* direction. The mitochondrial network we chose is a stack consisting of 29 slices. Figure (6-4) presents some of the 2D slices of the stack after Huygens deconvolution. These slices chosen are separated by 400 nm starting from the central slice to show significant difference in the topology of each slice.

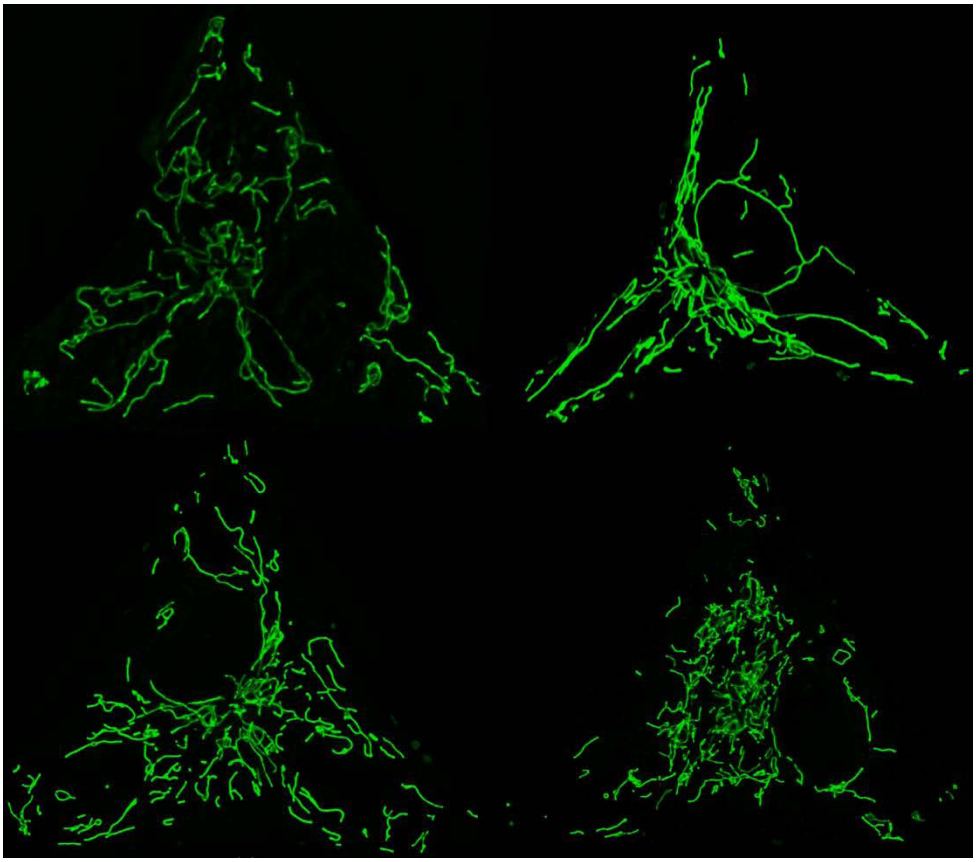

Figure (6-3) Four different images of fluorescent stains of mitochondria network in healthy fibroblast cells, using Mitotracker Green. For this representation, a maximum intensity projection (MIP) was used.

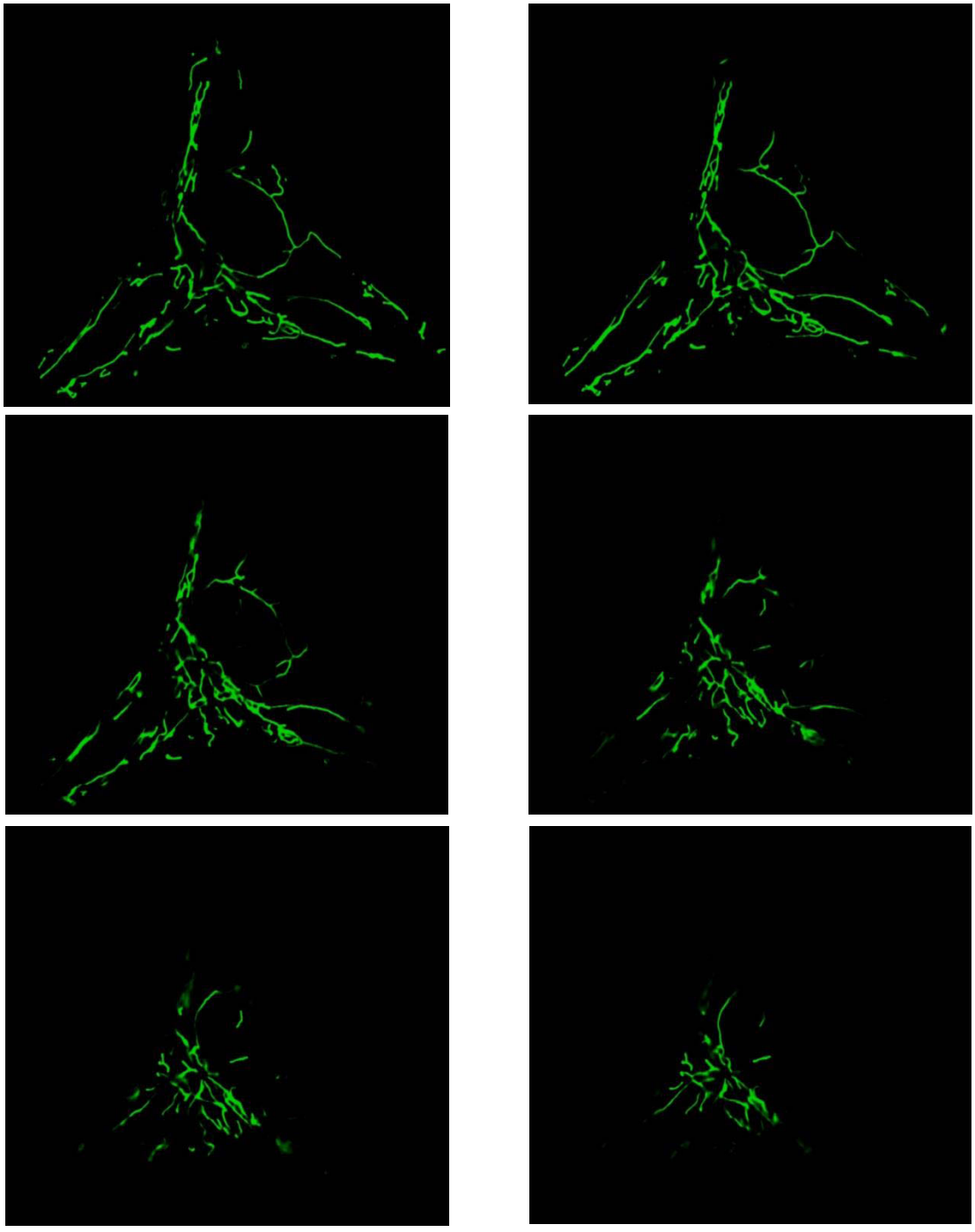

Figure (6-4) Six of the central 2D slices of the stack shown in figure ((6-3) top-right). The increment between each of the slices is 400 nm along the *z*-axis, starting from the central slice. The images had been deconvoluted using Huygens software

6.2 **Realization of a voxellized phantom from 2D stack**

To produce our phantom we try using the voxellization method introduced by S. Incerti *et al.* [12] described in the Geant4 microbeam advanced example of the official Geant4 releases [13]. This method models a human keratinocyte (HaCaT) single cell geometry (nucleus and cytoplam) obtained from high resolution confocal microscopy. The cell's chemical composition was measured experimentally by ion beam analysis (IBA) at the micrometric scale. The cell was then irradiated with 3 MeV incident alpha particles.

This approach taken by Incerti *et al.* allowed to build realistic three-dimensional geometries with a voxellised architecture. A single cell can be modeled in simulations by a phantom made up of a large number of parallelepiped voxels (up to 512 x 512 x 512 voxels). Each individual voxel contains information about its absolute position within the whole cellular phantom as well as the local chemical composition and density. The cell nucleus and cytoplasm could be extracted into individual files that were merged into a single phantom file. This phantom could then be imported directly into the Geant4-based simulation using the specific Geant4 *G4PVParameterised* class.

The widefield fluorescent image of the fibroblast mitochondria consists of a stack of 2D images pertaining to the fluorescent positions of the Mitotracker® Green (emission wavelength at 516 nm). This stack is in *.ics* format.

After deconvolution with SVI Huygens software, we can extract each 2D image in *.tiff* format. Each of these 2D images is pixellized in *x* and *y* directions, with a total number of 1058x953 pixels. The intensity of the pixels, as well as their positions are accessible using ImageJ.1.50f software. So for each of the 29 images, we can extract from ImageJ a text file with x and y pixel coordinates along with the corresponding intensity pixel.

The resulting 29 text files are then combined into one file with *x*, *y*, and *z* voxel coordinates along with the pixel intensity. The spatial 3D distribution of the points in the final text after noise elimination is shown in the figure (6-5a). Figure (6-5b) shows the *x*-*y* distribution of all points of the file giving a nice and clean picture of the mitochondria.

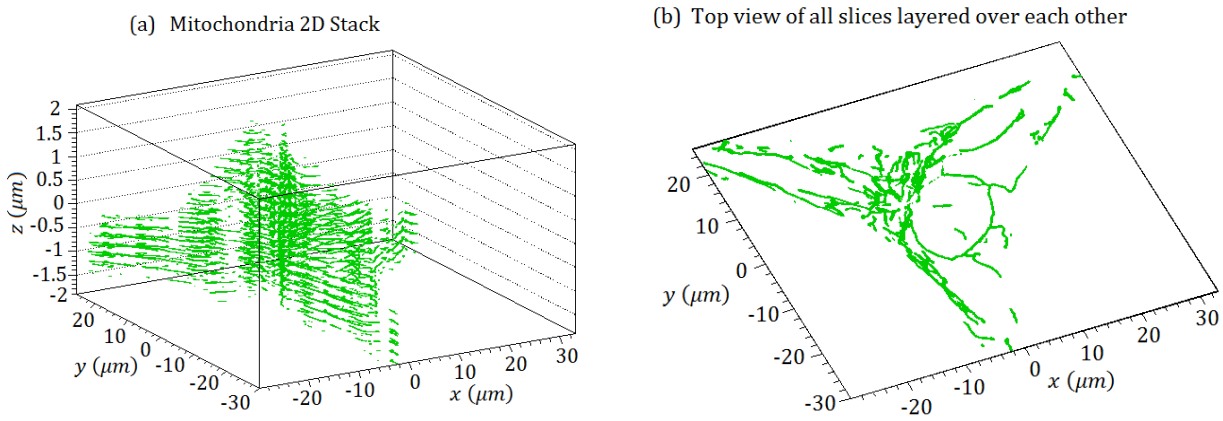

Figure (6-5) Spatial distributions of text file points extracted by ImageJ: (a) Side view of the stacks in 3 dimensions, (b) Top *x-y* view of the stacks layered over each other.

To reduce the noise, we set a threshold in voxel intensity by excluding all voxels with intensity less than 20. This text file finally provides a voxelized phantom made of 167273 voxels. These voxels are chosen to be parallelepipeds of dimensions 65nm x65nm x200nm. These dimensions are chosen according to the original pixel dimensions of the confocal image described in table (6-1). The center of each box is positioned at a certain point from the phantom file resulting in 167273 boxes each representing a voxel.

The parametrization function of the *G4PVParameterised* class is then used inside the detector construction class of the Geant4 application with each voxel filled with liquid water. The whole set of all these voxels is treated as one volume inside Geant4.

Nevertheless, this method is affected by two difficulties:

i.) First, such a voxelization cannot take into account the complexity of the mitochondria structure in cells. Then, the surface is not smoothed enough since the voxels are too large in comparison to the mitochondria scale.

ii.) Finally, the phantom is also dependent on the choice of the threshold used to clean the original pictures. That is why, we then produce a more realistic simulation of the mitochondrial network and this is obtained by changing the 3D image into a tessellated mesh.

Table (6-1) Image properties: total number of pixels in x, y, and z directions and their sizes.

Cartesian Direction	Size of a Pixel	Number of Pixels
x	65 nm	1058
y	65 nm	953
z	200 nm	29

6.3 3D Object Production from Bitplane

The deconvoluted original stack of 2D images is imported into Imaris v8.0.1 software for image reconstruction. Imaris v8.0.1 is a Bitplane's (Andor Technology, Belfast, Northern Ireland) software module that provides all the necessary functionalities for data management, visualization, analysis, and segmentation of 2D and 3D microscopy datasets [14]. The *FilamentTracer* option in Imaris was originally developed to analyze neuron morphology. It was especially designed to automatically map areas of fluorescence on confocal images and construct 3D dendritic models [15]. The mitochondrial network of the fibroblast cell in our case is similar in shape to the tree like structure of neuronal dendrites, axons and spines. Therefore, we can take advantage of the *FilamentTracer* option to reconstruct the mitochondrial network into a filamentous 3D object.

The *FilamentTracer* module can be operated through a sequence of steps where some parameters can be adjusted by the operator. This approach has the advantage of providing a set of measurements of the branched structures of the mitochondrial network. These measurements include segment properties (length, cross-sectional diameter, …), angles between the branches and the number of endpoints. This method allows us to manually optimize all the *FilamentTracer* parameters. Once defined, these parameters can be grouped and saved together in a single macro file to be applied for reprocessing of other images.

The processing steps with Imaris software summarized in figure (6-6) go as follows:

i.) The parameters of *FilamentTracer* module are optimized in a step by step processing of the deconvoluted stack of 2D images. All the defined parameters can then be stored in a macro file for global processing of other stacks.

ii.) The *FilamentTracer* module extracts isolated segments and filaments foreground and connects them to build the mitochondrial network. A skeleton is thus created, despite the non-neuronal appearance of the original structure. *FilamentTracer* produces a 3D object built from all the filaments of the mitochondrial network.

iii.) Launching the "Surfaces" tool from the Imaris menubar allows creating a "Surface" object using the set of 3D filament objects previously produced. When this process is completed, we can highlight the isosurfaces corresponding to the 3D reconstruction of the whole set of mitochondrial fibers.

iv.) The selected "surface" object is exported with "Obj Export Surfaces", a specific Imaris macro. An *.OBJ* ASCII file is thus created.

v.) This *.OBJ* ASCII file could then be imported to MeshLab [16] tool, which is a system for processing and editing unstructured 3D triangular meshes, to produce a

stereo-lethography (*STL*) file that defines the whole surface object as a tessellated mesh with triangular facets. *STL* is a file format created by 3D systems and widely used for rapid prototyping, 3D printing and computer-aided manufacturing.

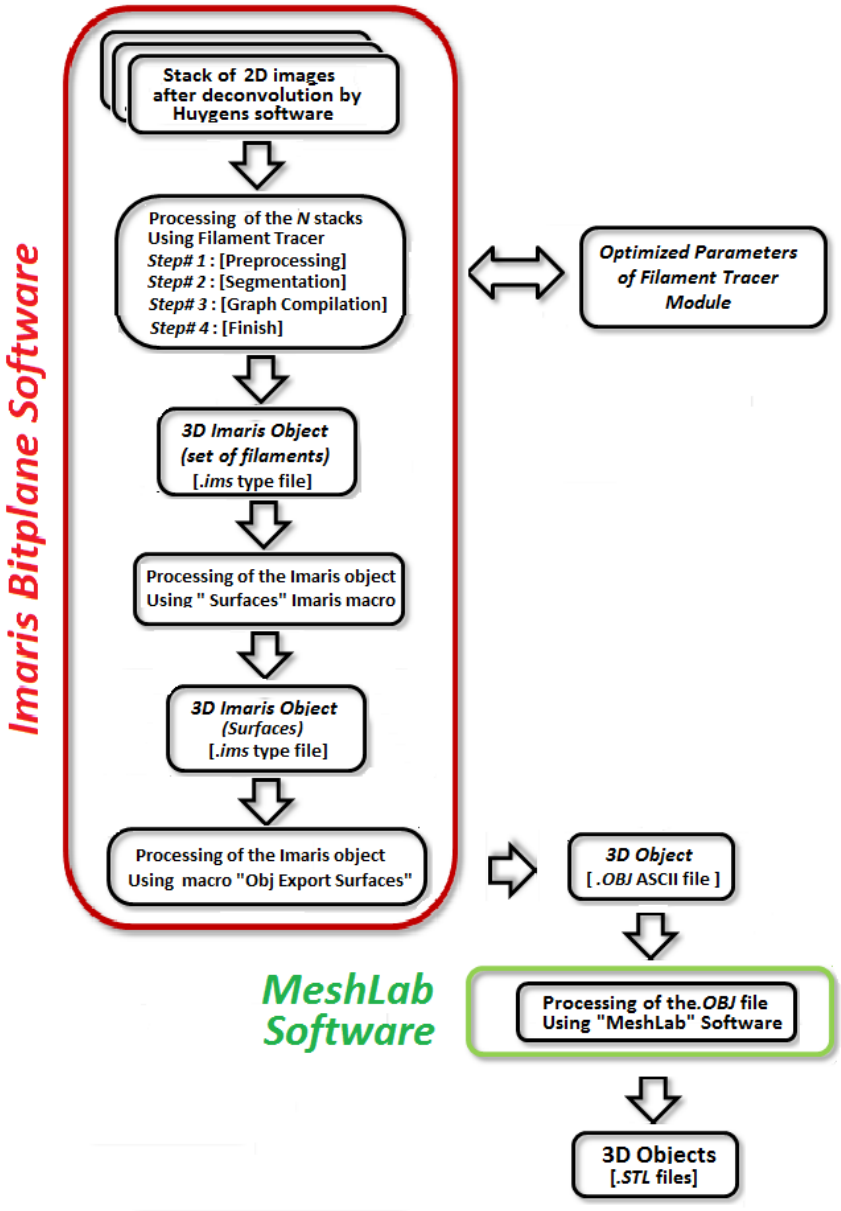

Figure (6-6) Processing of the initial stacks of 2D files to produce the *.STL* file, using Imaris *FilamentTracer* tool and MeshLab.

6.4 Tessellated Mesh in GDML Format

The reconstructed 3D image which is converted into a *STL* file can be transformed into *GDML* using the limited time trial of Instep Solveering software [17].

GDML is a comprehensive geometry description format using XML (Extensible Mark-up Language) and developed by CERN that can provide a geometry data exchange format for applications of Geant4 and ROOT [18]. Simple solid geometries such as boxes, spheres and cylinders as well as tessellated objects and materials can be described in a *GDML* file [19].

When in *GDML* format, the reconstructed 3D image of mitochondrial network is uploaded as tessellated tubules into Geant4. Instead of dealing with small parallelepipeds arranged next to each other according to the initial image of fluorescent dots positions, we now have a smooth volume of tube like structures giving a better representation of the initial image and closer to the real form of the mitochondrial network.

In the case of tessellated geometry, *GDML* files are easier to deal with at run time since they do not take up much of the memory compared to tessellated solids directly defined in Geant4 classes. Since this tessellated volume has micrometric scale, navigation problems occur when using physics processes with nanometer cutoff such as the low energy Livermore physics processes and the DNA physics processes of Geant4. After some investigation, the Geant4 navigator cannot determine whether the propagating particles are inside or outside our complex tessellated volume when the production cutoff is of the same scale as the tessellation dimensions.

6.5 Tetrahedral Mesh

When changing the tessellated mesh into a tetrahedral mesh the particles will propagate through an assembly of tetrahedra closely packed beside each other in the volume of the tessellated mesh. In this case navigation errors are resolved even with nanometric cutoffs since Geant4 can determine easily the positions of the particles inside primitive volumes. The *STL* file is imported into Geant4 using CadMesh library [20-22]. This library can transform tessellated meshes into tetrahedral meshes. So, this option is used to transform the phantom into a tetrahedral mesh that is imported directly as geometry into Geant4 classes.

Figure(6-7) represents two of the phantoms in *STL* format to be imported in Geant4. The left one corresponds to mitochondrion network in healthy fibroblast cells shown in top-right of Figure(6-3). The right one corresponds to chemically affected mitochondrion network shown in right of Figure(6-2).

Figure (6-8) shows a summary of all steps taken to produce the phantom.

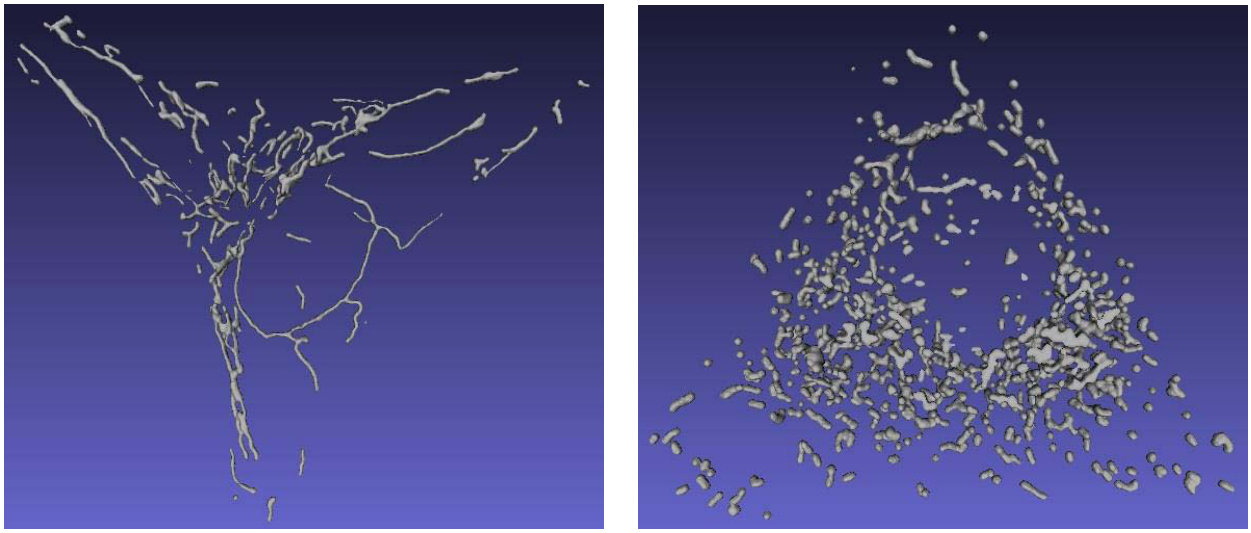

Figure (6-7) STL files of mitochondrial networks produced by MeshLab to be imported directly as geometry into Geant4. Left: healthy fibroblast cells shown in top-right part of Figure (6-3). Right: mitochondrial network chemically affected by mitochondrial inhibitors (antimycin 18 μM, 6 h) shown in right part of Figure (6-2)

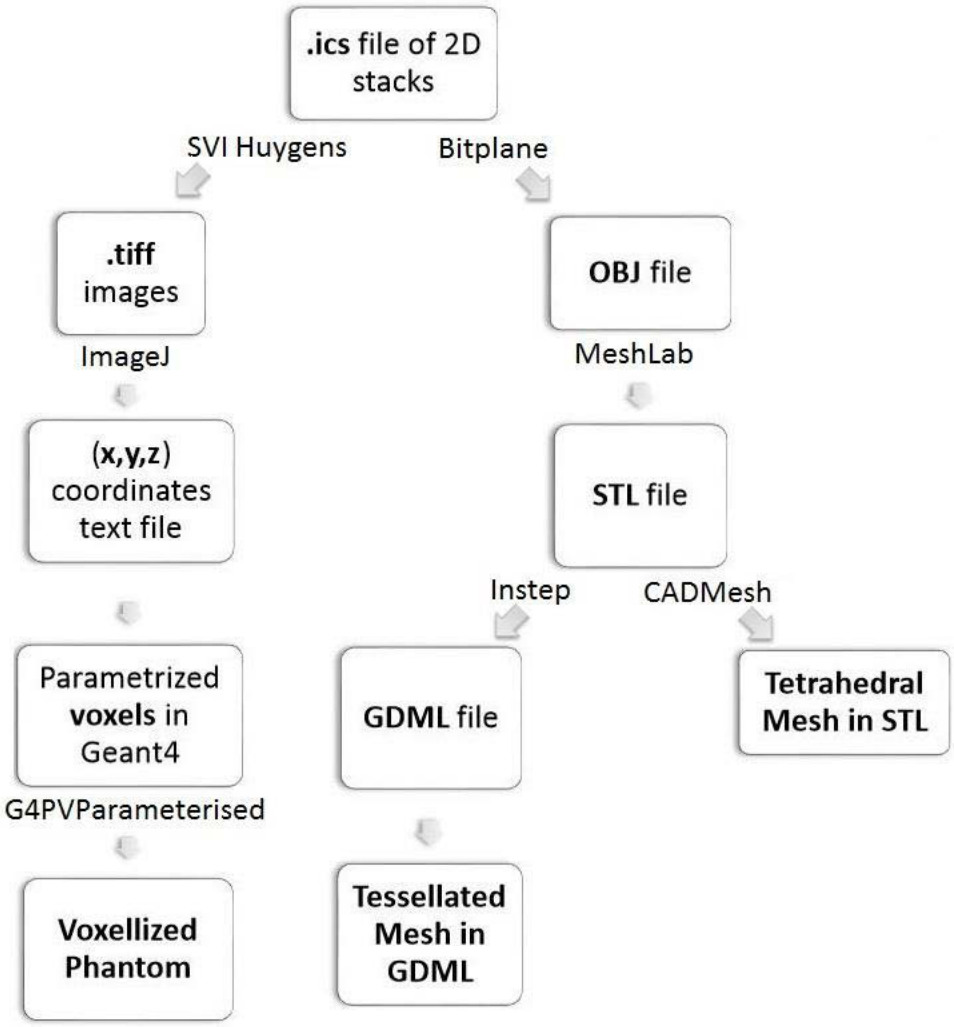

Figure (6-8) Complete synoptic for the production of the different phantom types of the mitochondria network

6.6 Conclusion

A method for constructing mitochondria phantoms from microscopic images is introduced. The microscopic images are obtained by an inverted wide-field microscope after staining fibroblast cells with Mitotracker® Green. The images are then deconvoluted to remove noise. The final images are in the form of stacks of 2D slices. Each slice contains the x-y positions of detected mitochondria.

The 2D slices are then reconstructed into 3D objects in *.STL* format by the software Imaris. The *.STL* files are imported into Geant4 as tessellated meshes that are then converted into tetrahedral meshes by the CadMesh library. This is the best procedure that we found adequate to perform our simulations without navigation errors.

Other approaches to produce the phantoms were studied. The stacks were directly converted into parallelepiped voxels inside Geant4. This method does represent the complexity of the mitochondria. Another way is use *the .STL* file as a tessellated mesh by transforming it into a *.GDML* file. This method produced errors in the results due to a navigation problem with Geant4 for tessellated objects at microscopic scales.

In the end, we stick with the method that produces the phantom as a tetrahedral mesh inside Geant4.

1. Bereiter-Hahn, J. and M. Voth, *Dynamics of mitochondria in living cells: shape changes, dislocations, fusion, and fission of mitochondria.* Microscopy Research and Technique, 1994. **27**: p. 198–219.
2. Chen, H. and D.C. Chan, *Mitochondrial dynamics in mammals.* Current Topics in Developmental Biology, 2004. **59**: p. 119–44.
3. Kam, W.W.Y., et al., *Predicted ionization in mitochondria and observed acute changes in the mitochondrial transcriptome after gamma irradiation: a Monte Carlo simulation and quantitative PCR study.* Mitochondrion, 2013. **13**(6): p. 736-742.
4. Alard, J., et al., *Simulation of neutron interactions at the single-cell level.* Radiation Research, 2002. **158**: p. 650-656.
5. Tung, C., et al., *Calculations of cellular microdosimetry parameters for alpha particles and electrons.* Applied Radiation and Isotops, 2004. **61**: p. 739-743.
6. Chevrollier, A., et al., *Standardized mitochondrial analysis gives new insights into mitochondrial dynamics and OPA1 function.* The International Journal of Biochemistry & Cell Biology, 2012. **44**: p. 980–988.
7. Benard, G. and R. Rossignol, *Ultrastructure of the mitochondrion and its bearing on function and bioenergetics.* Antioxidants and Redox Signaling, 2008. **10**: p. 1313-1342.
8. Twig, G., et al., *Biophysical properties of mitochondrial fusion events in pancreatic beta-cells and cardiac cells unravel potential control mechanisms of its selectivity.* Am J Physiol Cell Physiol, 2010. **299**: p. C477-C487.
9. Kuznetsov, A., et al., *The cell-type specificity of mitochondrial dynamics.* Int J Biochem Cell Biol, 2009. **41**: p. 1928-1939.
10. Thery, M., et al., *Anisotropy of cell adhesive microenvironment governs cell internal organization and orientation of polarity.* Proc Natl Acad Sci USA, 2006. **103**: p. 19771-19776.
11. *Scientific Volume Imaging*. Available from: https://svi.nl/HuygensEssential.
12. Incerti, S., et al., *Monte Carlo dosimetry for targeted irradiation of individual cells using a microbeam facility.* Radiation Protection Dosimetry, 2009. **133**(1): p. 2-11.
13. *Microbean Example Geant4*. Available from: https://twiki.cern.ch/twiki/bin/view/Geant4/AdvancedExamplesMicrobeam.
14. *Bitpalne Oxford Instruments*. Available from: http://www.bitplane.com/imaris/imaris.

15. Sugawara, Y., et al., *The Three-Dimensional Morphometry and Cell–Cell Communication of the Osteocyte Network in Chick and Mouse Embryonic Calvaria.* Calcified Tissue International, 2011. **88**: p. 416-424.
16. *MeshLab*. Available from: http://meshlab.sourceforge.net/.
17. *Solveering LLC*. Available from: https://www.solveering.com/instep.htm.
18. *Geometry Description Markup Language*. Available from: http://gdml.web.cern.ch/GDML/.
19. *Geometry Discription Markup Language Manual*. Available from: http://gdml.web.cern.ch/GDML/doc/GDMLmanual.pdf.
20. Poole, C.M., et al., *A CAD interface for Geant4.* Australian Phys Eng Sci Med, 2012. **53**(3): p. 329-334.
21. Poole, C.M., et al., *Fast Tessellated Solid Navigation in Geant4.* IEEE Transactions on Nuclear Science, 2012. **59**(4): p. 1695 - 1701.
22. Poole, C.M. *CADMESH*. Available from: https://github.com/christopherpoole/CADMesh.

7 Energy Depositions Inside the Mitochondria Phantom

A method has been developed to build phantoms of microscopic structures starting from 2D stacks of microscopic images obtained from an inverted wide-field microscope after staining. Out of many images, we choose three different cells to produce three different phantoms with three different configurations of the mitochondrial network.

First, a healthy cell is chosen where mitochondria are stained and their image is taken. The method of producing a phantom in the form of a tetrahedral mesh is tested. A healthy fibroblast cell has interconnected mitochondria in the form of filament-like network as shown in the figure (7-1-a). This phantom will be called phantom F1.

After producing the tessellated mesh in *.STL* format (see paragraphs 6.3 and 6.5), the file is imported into Geant4 and with the help of CADMesh library, the tessellated mesh is transformed into a tetrahedral mesh. This mesh is filled with liquid water, the most abundant compound in biological material. It is positioned inside a container with trapezoidal face to reduce the time and CPU memory usage of simulations where this container is filled with water as well. Figure (7-1-b) illustrates the dimensions of the trapezoidal faced container and how the tetrahedral mesh is placed inside it.

(a) 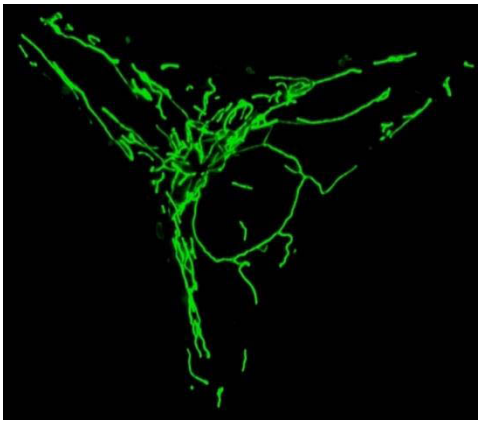 (b) 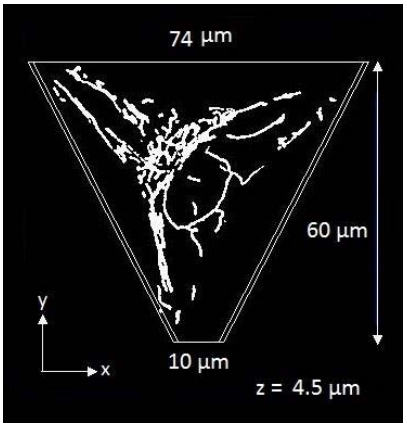

Figure (7-1) (a) The filamented network of mitochondria as shown by the inverted wide-field microscope, (b) The tetrahedral mesh positioned inside a box with trapezoidal face

Interactions of 250 keV photons with the phantoms are studied using the Livermore low energy physics processes. The source is placed 3 cm below the container where photons are shot randomly on the x-y face of the container and in parallel to the positive z-direction. Photons at this energy are sparsely interactive with water, mainly governed by the photoelectric effect and Compton scattering. The number of interactions produced by such a simulation with water container is summarized in the table (7-1) for different number of

photon events. This means that a large number of photon events is needed to produce good statistics of energy depositions.

Table (7-1) Secondary electrons produced mainly by photoelectric and Compton scattering of 250 keV photons in water for different number of initial photon events, simulations performed on a duo core Pentium computer

Number of photon events	Number of interactions (Secondary electrons)	Simulation time (sec)
10^5	9	21
10^7	528	2240
10^8	5771	24648

The secondary electrons produced by the photon interactions with water are the ones responsible for the energy depositions inside the phantom. Therefore, Geant4-DNA libraries are chosen to simulate the electromagnetic interactions of these secondary electrons at micrometric and nanometric scales up to very low energies. In order to reduce the simulation time and use the Geant4-DNA processes to describe the interactions of the secondary electrons, a resampling technique is applied to optimize the simulation.

7.1 Resampling Methods of Electron Energy Spectra

Since the mitochondria have micrometric dimensions and the photons in the keV range do not interact heavily with water, a high number of events are needed to collect the data of energy depositions. To avoid this time-consuming process an alternative method of energy resampling is performed. Photons interact with water by Compton scattering and photoelectric effect releasing secondary electrons. The energy spectrum of these secondary electrons is calculated. In a second simulation, instead of producing a high number of photons, secondary electrons with energies chosen from the calculated energy spectrum are produced. And since electrons are more reactive than photons, this insures that every produced secondary electron will interact with the medium. This method divides our simulation into two consecutive calculation phases, the first phase simulates the monoenergetic photons to produce the first generation of secondary electrons with a wide range of energies. In the second phase, the number of regenerated electrons can be increased in order to improve the statistical quality of the results.

Resampling goes as follows, in Geant4 a water box of dimensions 20x20x5 cm^3 is irradiated with 250 keV photons. A large water box is used to get a good number of photon interactions. The mono-energetic photon beam is directed towards the upper x-y face of the box as shown in the figure (7-2). The Livermore physics list is used to perform the simulation. These photons will interact mainly by Compton scattering inside water releasing secondary electrons. The kinetic energies of the first generated secondary

electrons are measured and a spectrum of the first-generation secondary electrons energy is created as shown in figure (7-3). The deposited dose to produce this spectrum is 31.46 mGy in the water box.

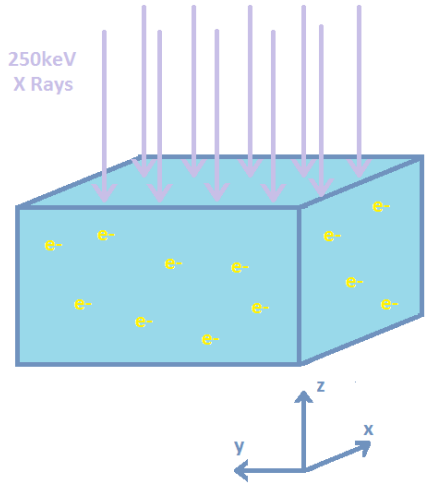

Figure (7-2) Shooting mono-energetic photons on the upper face of a water box to produce secondary electrons

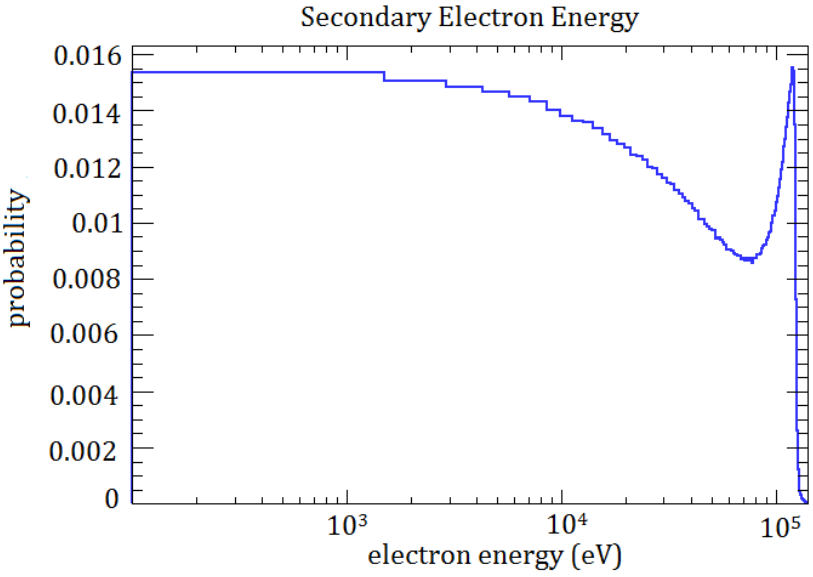

Figure (7-3) First generation secondary electrons energy spectrum produced from 250 keV photons in the water box

After obtaining the first generation of secondary electrons induced by photon interactions with water, we can use the energy spectrum in other simulations of smaller targets producing electrons instead of simulating primary photons. So when studying the effects on mitochondria phantom we generate secondary electrons randomly in the box containing the phantom assigning them energies from the distribution calculated by resampling

shown in figure (7-3). To perform microdosimetric calculations, we use the Geant4-DNA physics processes for the resampled electrons.

As figure (7-3) shows, the produced secondary electrons by photon interactions with water have a wide range of energies from 1 keV to 120 keV. The range of electrons in water increases with energy. 1keV electrons have 423.5 nm range in water, 10 keV electrons have 2.5 μm range, and 120 keV electrons have 220 μm [1]. The maximum range of secondary electrons produced reaches about 220 μm in water at most. This means that a good number of secondary electrons will be able to cross the micrometric dimensions of the mitochondria phantom and its container.

7.2 Mean Chord Length Calculation

The mean chord length of the phantom is calculated by the proton tracks intercepting with the whole tetrahedral volume. For this a simple Geant4 simulation is performed to calculate the length of proton tracks as they cross the mitochondria phantom. The phantom as a tetrahedral mesh is placed inside a sphere of radius 40 μm, and both are filled with water. Protons of energy 90 MeV are produced in the lower dome of the sphere and are directed randomly upward towards the central x-y plane of the sphere (as shown in figures 7-4 and 7-5). Since protons at this energy have straight tracks in water, they will not deviate enabling us to create straight tracks (chords) intercepting the volume of the phantom. We calculate the coordinates of the entry point and the leaving point of the proton tracks as they cross the phantom. From this we can calculate the lengths of the proton tracks crossing the phantom. In the end the average of these track lengths is calculated obtaining the mean chord length of mitochondria.

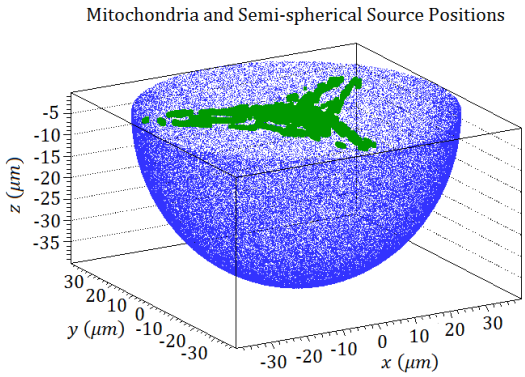

Figure (7-4) Mitochondria phantom and the proton source positioned at the lower dome of the sphere

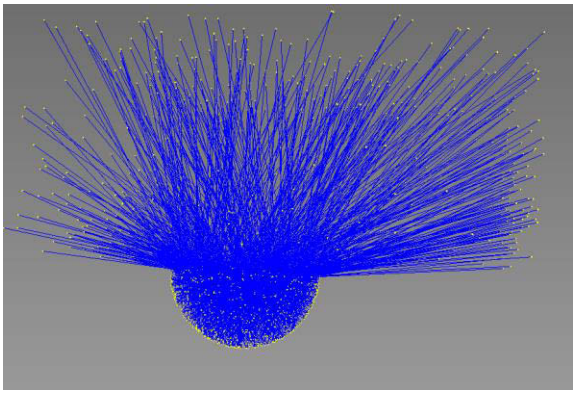

Figure (7-5) Proton tracks created in lower dome of the sphere directed upward towards the central xy plane of the sphere

The distribution of the chord length values intercepting the phantom is shown in the figure (7-6). The mean chord length of mitochondria $\bar{l} = 462.036$ nm is obtained by calculating

the average of the distribution of figure (7-6). The range of 1 keV electrons is 423.5 nm which is very close to calculated mean chord length of the phantom. As discussed earlier, the range of electrons increases with electron energy. Therefore, electrons with values larger than 1 keV will have ranges with values starting with hundreds of nm reaching till hundreds of μm in length. The electron energy values we are using in our simulations shown in figure (7-3) are suitable to perform lineal energy calculations since the value of the mean chord length of the sensitive volume, which is the phantom, is smaller than most of the ranges of electrons used.

The simulation of protons that is used in this case is aimed to produce a geometrical length and the physical interactions are of no importance. In fact, the secondary interactions are ignored and the non-deviated trajectories of protons take our only attention. Protons of 90 MeV energy have a relatively large range of about few centimeters with a low stopping power enabling them to cross the volume of the water sphere with straight line trajectories and little interactions. Protons with lower energies, in the keV region for example, will have very short ranges of few μm or less preventing them from crossing the 80 μm diameter sphere [2]. Note that if electrons are used instead we will not get the intended result since electrons do not exhibit straight tracks and are highly interactive and have shorter ranges.

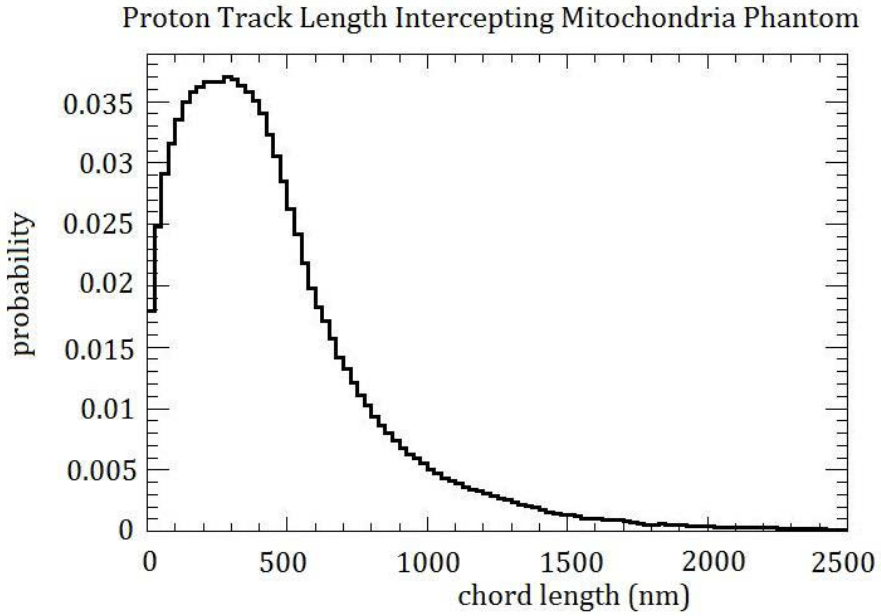

Figure (7-6) Probability distribution of chord lengths corresponding to the proton tracks intercepting the mitochondria phantom.

7.3 Determining the Dose

Our approach is to find the suitable number of electron events depositing the medically accepted absorbed dose inside the total volume of the mitochondria container. Therefore, electrons are released randomly in the volume of the trapezoidal box with energies taken from the electron energy spectra of figure (7-3) and the absorbed dose in the whole container box is calculated. Table (7-2) shows the absorbed dose produced by different numbers of electron events.

Table (7-2) Absorbed dose inside the trapezoidal face container of the mitochondria phantom induced by different numbers of electron events. Simulations performed on a duo core Pentium computer

Number of electron events	Absorbed Dose in (mGy)	Simulation time (sec)
100	5.81	23
500	30.19	83
1000	61.47	263
10000	581.91	3158
20000	1193.87	5702

Note that the masses of both the mitochondria phantom and its container can be calculated by Geant4 with the function `GetMass()`. These solids are filled with water in the simulations and their masses are summarized in table (7-3). Therefore, the absorbed doses are calculated according to the equation $D = E/m$ where E is the total energy deposition per run and m is the mass of the phantom (or the trapezoidal box).

Table (7-3) Masses in kg of the mitochondria phantom and its container both filled with water

Target	Mitochondria (F1)	Trapezoidal box
Mass (kg)	1.59×10^{-13}	1.134×10^{-11}

7.4 Comparing three simulation approaches

To check which electron event number is the most suitable for producing microdosimetric statistics and DBSCAN clustering analysis three simulation approaches are considered and their results are compared.

Therefore three steps are followed:

1. First, one simulation is carried out where $2x10^4$ electron events are shot randomly depositing about 1.19 Gy inside the phantom container.

2. Then, 10 simulations are performed, each running $2x10^4$ electron events and delivering 1.19 Gy separately. The total delivered dose of these 10 simulations is 11.9 Gy inside the phantom's container. The average of these 10 simulations is considered for calculations.
3. Finally, one simulaton is carried out where $2x10^5$ electron events are shot randomly depositing 11.89 Gy total dose inside the container.

Each of these steps result in a spatial distribution of energy depositions inside the phantom that enables us to calculate the absorbed doses, the imparted energy and the DBSCAN analysis. Note that the values of the deposited doses in the trapezoidal box are in the range of dose of cell survival irradiation experiments in radiobiology. These three different simulations are performed to see if the 1.19 Gy dose can be generalized to predict how the microdosimetric quantities would differ with different values of deposited dose.

This also tests if the imparted energies show a significant difference when the deposited dose is deliverd gradually in separate simulations of 1.19 Gy eventually summing up to 11.91 Gy than in the case of one single simulation of 11.89 Gy dose.

The total energy depositions and the absorbed dose inside the phantom and its container are summarized in the table (7-4) for different event number of electrons. The total energy deposition and the deposited dose inside the mitochondria phantom and in the total volume of its container (including the volume of the phantom) increase by a factor of 10 when the total number of electron events increases from $2x10^4$ to $2x10^5$. Therefore, the relation between the number of electron events and the absorbed dose is linear.

Table (7-4) Absorbed dose inside the mitochondria phantom and inside its container

Event Number	Total Energy in Mitochondria (MeV)	Absorbed Dose in Mitochondria (Gy)	Total Energy in Container box (MeV)	Absorbed Dose in Container box (Gy)
2×10^4	1.29777	1.30276	84.6019	1.19368
2×10^5	13.8122	13.8653	843.015	11.8944

Imparted energy is the sum of energy deposited inside the volume of mitochondria per event. This energy is calculated for a single application of 1.19 Gy ($2x10^4$ electron events), for the averaged 10 applications of 1.19 Gy ($2x10^4$ electron events 10 times), and for the single application of 11.9 Gy ($2x10^5$ electron events). The mean values of imparted energy in each of the three cases are shown in table (7-5).

Figure (7-7-a) shows the imparted energy distribution inside the phantom when a total dose of 1.19Gy is delivered by $2x10^4$ electron events as simulation (1.) explains. Figure (7-7-b) shows the averaged imparted energy distribution inside the phantom when 10

separate simulations of 1.19Gy dose delivered by $2x10^4$ electron events are performed as explained by simulation (2.). The imparted energy distribution inside the phantom produced by $2x10^5$ electron events delivering 11.9Gy dose is shown in figure (7-7-c) as explained by simulation (3.).

Table (7-5) Mean values of the imparted energy for different simulations done on a duo core pentium computer

	1 simulation of $2x10^4$ events (1.19Gy)	10 simulations of $2x10^4$ events (1.19Gy)	1 simulation of $2x10^5$ events (11.9Gy)
Mean imparted energy (eV)	677.688	694.004	721.981
Simulation time (hours)	3.08	18.4	7.65

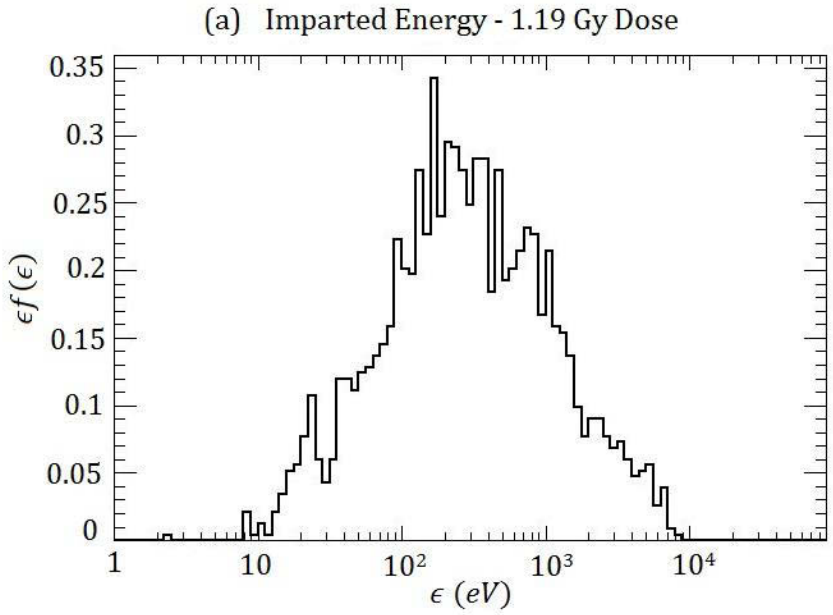

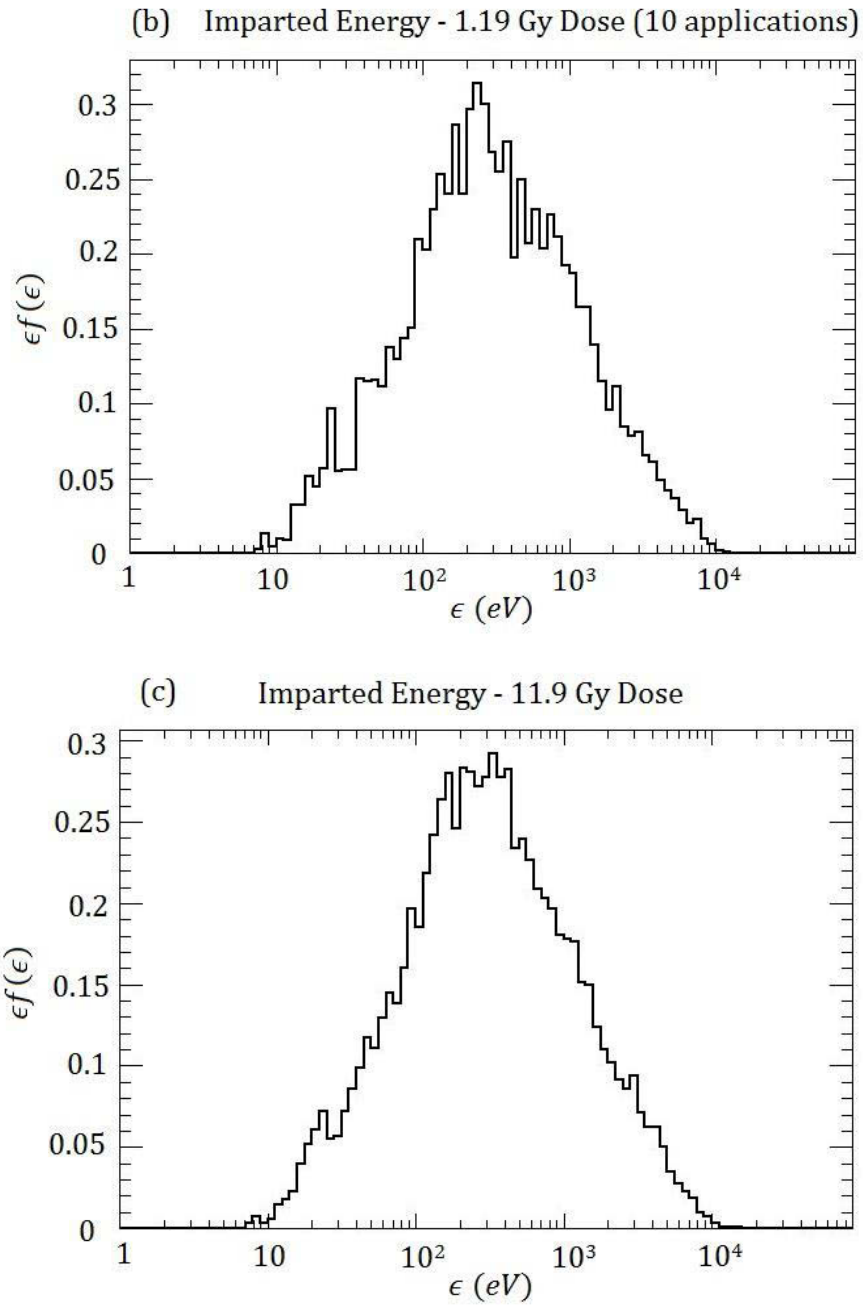

Figure (7-7) Imparted energy inside the mitochondria phantom: (a) Simulation run once for 1.19 Gy dose, (b) simulation run 10 times for 1.19 Gy dose and then averaged over 10, (c) simulation run once for 11.9 Gy dose

As table (7-5) and figures (7-7) show, on the microdosimetric level, there are no significant differences in the energy imparted inside the mitochondria. Figure (7-7-a) shows a poorly constructed curve due to the low number of interacting electron events with the mitochondria phantom. In figure (7-7-b) the curve is better configured although some fluctuations occur resulting in some roughness in the curvature. Figure (7-7-c) is the

smoothest and thus is the best of all three figures in showing the distribution of imparted energy. Therefore, the simulation of 11.9 Gy dose is most efficient in producing good distribution curves and is considered best representative of microdosimetric statistics.

Notice that the microdosimetric mean quantities converge to a certain value as the number of events increase whereas the absorbed dose increase with the increase of event number. This shows the difference between the dosimetry and microdosimetry formalisms. Microdosimetric quantities vary from event to event due to the fluctuation of the energy depositions but their average is almost consistant. The absorbed dose depends on the total exposure to radiation.

The frequency and dose weighted lineal energy distributions are constructed in figure (7-8) based on the energy depositions inside the phantom by $2x10^5$ electron events depositing 11.9 Gy dose in the container box. In this case the frequency mean lineal energy $\bar{y}_F$ is 1.32 keV/μm and dose mean lineal energy $\bar{y}_D$ is 4.98 keV/μm. Distributions and mean values of lineal energy show that the dose weighted values tend to be larger than frequency weighted values. This is in agreement with the literature since frequency weighted sampling that results in the frequency distributions gives equal oportunities for the imparted energy inside the sensitive volume to be chosen. In comparison, the dose weighted sampling gives the higher values of imparted energy a better chance to be chosen [3, 4]. This gives the high imparted energy values a larger probability to influence the dose weighted distribution.

We can see that the curve $yf(y)$ peaks at 0.7 keV/μm. In contrast, the curve $yd(y)$ peaks at much higher values 7 keV/μm and 9 keV/μm. The low lineal energy values from 0.019 keV/μm till about 1.7 keV/μm have lower probabilities with $yd(y)$ than with $yf(y)$, and all the other values higher than 1.7 keV/μm have higher probabilities with $yd(y)$ indicating that low imparted energy values are less likely to be included in the sampling. The $yd(y)$ curve starts to fluctuate after the lineal energy exceeds 2.9 keV/μm showing that the high values of imparted energy are not that frequent and the height of the curve is influenced by the high values of energy rather than the frequency of their occurence. Altough the high values of imparted energies diminishe in number, the dose weighted sampling gives them high importance which explains the larger probabilities of $yd(y)$ on the right side of the curve and lower probabilities on its left side.

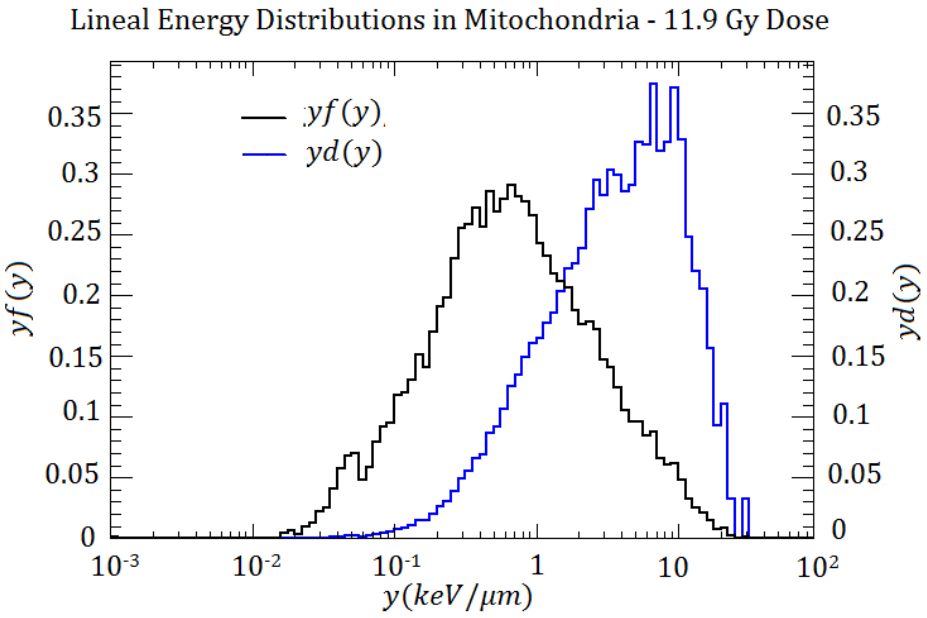

Figure (7-8) Frequency and dose weighted distributions of lineal energy inside the phantom F1 in the case of 11.9 Gy absorbed dose

7.5 DBSCAN Analysis inside the phantom

After the biological media are exposed to radiation, the cells undergo many phases of change starting from the physical interactions of ionization and excitation of biomolecules going through the chemical phase of free radical production and propagation and ending in the biological phase where damage repair processes take place. Simple damages are easy to repair compared to complex damages consisting of two or more damages lying very close to each other. The closer the damages are to each other the harder they are to repair. So the distance between two damage points is important. Therefore, two or more damage points lying within a certain distance are considered a cluster of damages.

Recently, a new model has been described by Fernanda Villegas *et al.* [5-7] to explore the use of the frequency of the energy deposition clusters of different sizes (cluster order) as a surrogate (instead of, e.g., *LET*) classification of the physical characteristics of ionizing radiation at a nanometer scale, to construct a framework for the calculation of relative biological effectiveness (*RBE*) with cell survival as endpoint. In their model, the frequency of cluster order is calculated by sorting the energy deposit points generated with the Monte Carlo track structure code into clusters based on a single parameter called the cluster distance being the maximum allowed distance between two neighboring energy deposit points belonging to a cluster.

Published cell survival data parameterized with the linear-quadratic (LQ) model for V79 cells exposed to 15 different radiation qualities (including brachytherapy sources, proton, and carbon ions) were used as input to a fitting procedure, designed to determine a weighting function that describes the capacity of a cluster to damage the cell's sensitive volume. The proposed framework allows to construct surrogate based functions for the LQ parameters alpha and beta from which *RBE* values can be derived.

The DBSCAN clustering algorithm calculates the distances between energy deposit points and groups the points lying within a certain maximum neighboring distance *d* into clusters. All energy deposit points are included in the algorithm.

To our knowledge, there is not enough information about the suitable value of *d* less than which the damages are considered complex and hard to repair inside mitochondria. For this reason, we investigate three values of *d* to perform the clustering analysis inside the volume of the mitochondria phantom.

We are still using the energy deposit spatial distribution obtained from irradiating the mitochondria phantom (F1) of figure (7-1-a) with $2x10^5$ electron events as in the previous paragraph.

Clusters are produced according to three maximum neighboring distances *d* = 1 nm, 2 nm and 3 nm. The clusters obtained in each case have different and irregular shapes. One way to distinguish the shape of such clusters is by calculating the root mean square radius (*RMSR*) which is the square root of the sum of the squared distance between the points forming the cluster and its center. The *RMSR* gives an approximate representation of the physical radius of the cluster.

Figure (7-9) shows the probability distribution of the *RMSR* of clusters for the three different values of *d*.

- When *d* = 1 nm the *RMSR* values range from 0 to 2 nm where the curve peaks at 0.45 nm.
- For *d* = 2 nm the *RMSR* values range from 0 to 5 nm where the curve peaks at 0.9 nm.
- For 3 nm neighboring distance the *RMSR* values range from 0 to 7 nm where the curve peaks at 1.2 nm.

Clusters of smaller *d* values have smaller sizes as the curve of 1 nm has sharper peak than the 2 nm and the 3 nm curves. This is expected because most of the clusters formed by smaller neighboring distances should be more isolated and contain fewer energy transfer points than clusters of higher neighboring distances.

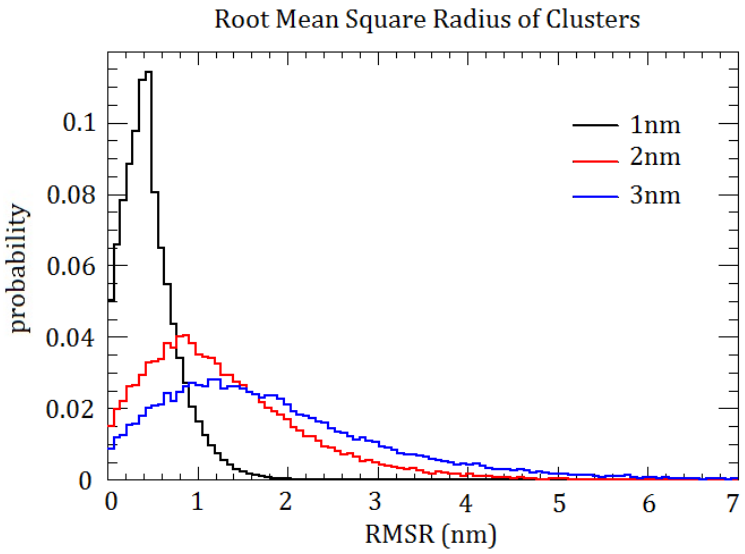

Figure (7-9) Root mean square radius distributions for *d* = 1 nm, 2 nm and 3 nm

The cluster size is the total number of energy transfer points inside a cluster separated at most by the distance *d*. These energy transfer points represent potential damages on the molecular level. These damages that are considered a part of a cluster become harder to repair as they increase in number. So a cluster with a large size is considered potentially more damaging than smaller clusters. Figure (7-10) shows the distributions of cluster sizes for the three different values of *d*. The curves peak at very small values of cluster size and decrease gradually showing the low probability of large clusters.

Very small clusters of size less than 10 energy transfer points are most probable for *d* = 1 nm where we get the highest peak. These cluster sizes are less probable for *d* = 2 nm and 3 nm respectively. In contrast, when the cluster size is larger than 20 energy transfer points *d* = 3 nm curve becomes the most probable followed by 2 nm and 1 nm respectively. This shows that we have a high probability of complex damages.

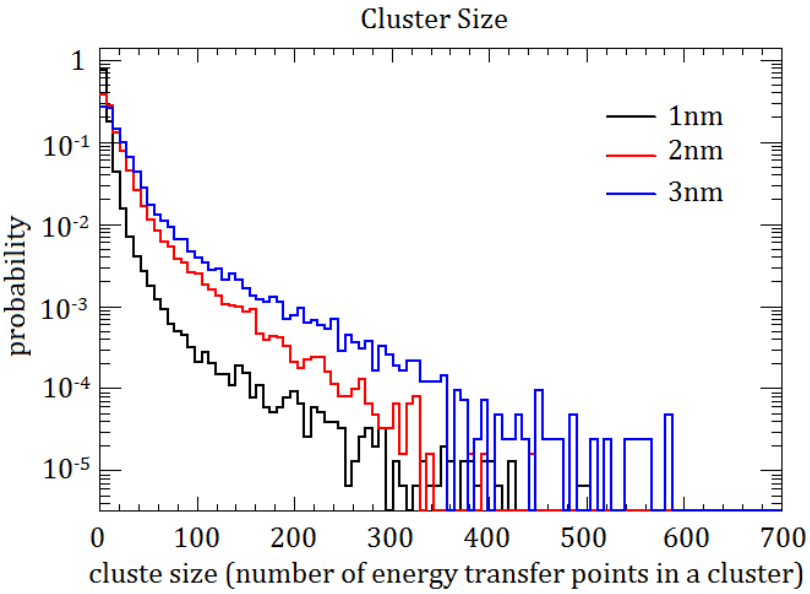

Figure (7-10) Cluster size probability distribution for *d* = 1 nm, 2 nm, and 3 nm

Clustering the energy transfer points means concentrating the energy deposited inside the cluster. For each event pertaining to a single photon interaction inside the mitochondria phantom the total energy inside each cluster of three different clustering configurations can be measured. So, the probability distribution of total energy per cluster is shown in figure (7-11).

We notice that the 1 nm curve has the highest peak followed by the peaks of 2 nm and 3 nm curves. These peaks correspond to the lowest cluster energies below about 20 eV. So the least energetic clusters are the most probable and clustering with small values of *d* produces isolated small clusters with low energies.

The curve with *d* = 3 nm becomes the highest in probability for values greater than 20 eV meaning that these clusters are the most energetic where curves of *d* = 2 nm and 1 nm have lower probabilities respectively and thus less energetic.

The three curves peak at energies less than 50 eV and decrease smoothly till they form another peak at about 539.7 eV. This signifies a *K*-shell ionization point within the clusters although these are less probable to occur. The curves continue to decrease afterwards.

Above the value of about 700 eV, fluctuations occur in the three curves indicating some noise in our calculations. Clustering with high values of *d* produces more energetic clusters but these are less probable and their damages are considered less complex since the complexity of damages depend on the distance between the damages.

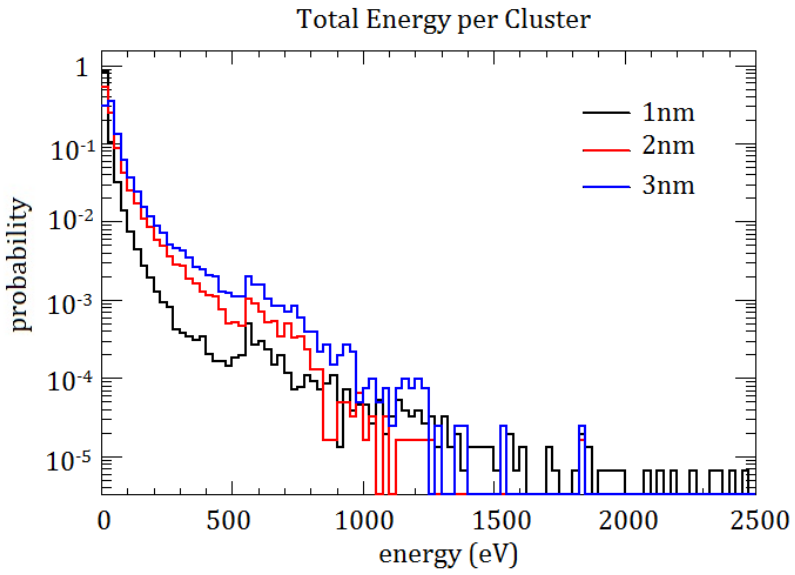

Figure (7-11) Total energy per cluster for three different values of *d* = 1 nm, 2 nm and 3 nm

Figure (7-12) shows the frequency distributions of cluster density for the three clustering configurations. The cluster density is the total number of energy transfer points in each cluster divided by the *RMSR* of the cluster.

The 1nm curve has the highest frequency followed by the 2 nm and 3 nm curves respectively. This indicates that 1 nm neighboring distance clusters have more closer energy points and thus denser than 2 nm and 3 nm neighboring distance clusters respectively. This also shows that the number of clusters decreases as the maximum neighboring distance increases. This is in agreement with results of table (7-6) that shows the total number of clusters in each case.

We conclude that smaller values of *d* result in a high density of energy transfer points that could be considered as potential damages. However, an energy transfer point is more damaging if it is more energetic and small values of *d* do not result in high probability of energetic clusters. In contrast, large values of *d* result in lower densities of energy transfer points but these clusters are more likely to be damaging. We need to collect more information about the repair mechanisms inside the mitochondria in order to specify which values of *d* are the most convenient.

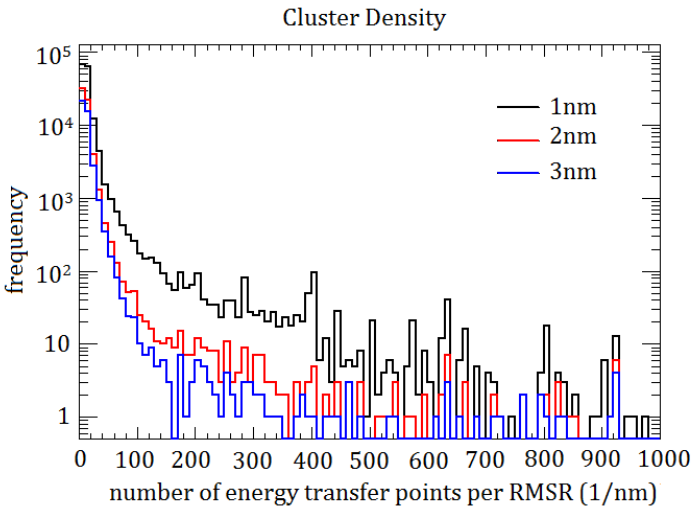

Figure (7-12) Cluster density distribution for *d* = 1 nm, 2 nm and 3 nm

Table (7-6) Total number of clusters for three different values of maximum neighboring distance *d*

d (nm)	1	2	3
Number of clusters	154571	61959	42062

7.6 Filamented and Fragmented Phantoms

In the fibroblast cells mitochondria form a network of filaments. When the cell is affected by diseases, the structure of mitochondria changes and apoptosis is induced. Mitochondria become fragmented and the network loses its connectivity. The microscopic image of a healthy fibroblast mitochondria in figure (7-13-a) shows the intact connections of the filamented network. However, in figure (7-13-b) the fibroblast mitochondria network is clearly fragmented. This is due to the chemical effect of mitochondrial inhibitors. The cell in this case is treated with 18 μM of Antimycin for 6 hours prior to image production. Antimycin inhibits ATP synthesis and leads to pre-apoptotic mitochondrial fragmentation.

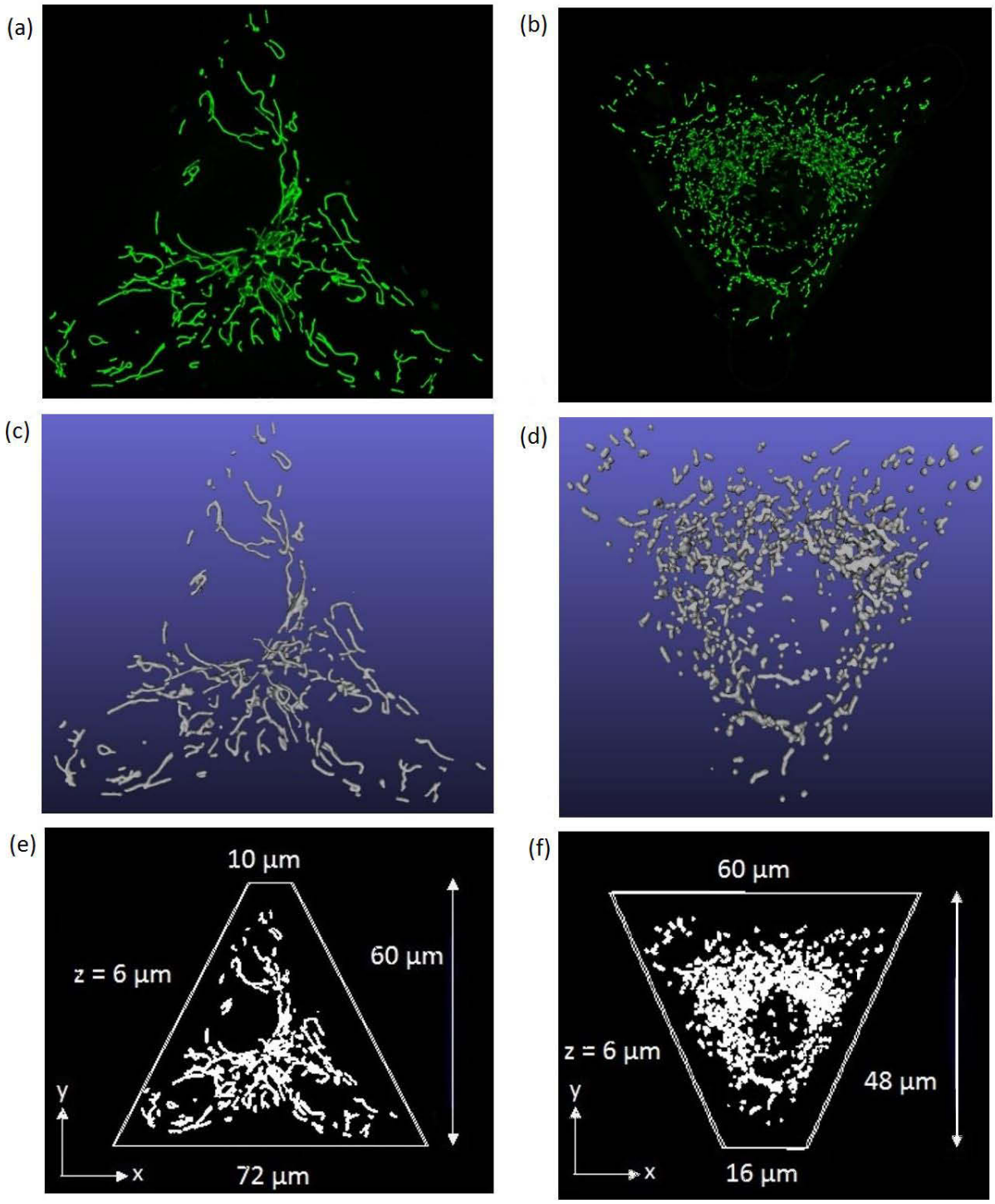

Figure (7-13) Microscopic images of mitochondria: (a) Healthy mitochondria, (b) inhibitor affected mitochondria, (c)Tessellated mesh of healthy mitochondria, (d) Tessellated mesh of fragmented mitochondria, (e) placing the healthy phantom in a trapezoidal faced container, (f) placing the fragmented phantom in a trapezoidal faced container

Similar to the image of figure (7-1-a), images (7-13-a) and (7-13-b) are also used to produce phantoms. These images are transformed into tessellated meshes of the *.STL* formats using the same method described in paragraphs 6.3 and 6.5 of the previous chapter 6. The produced *.STL* files are respectively shown in figures (7-13-c) and (7-13-d). These files are uploaded into Geant4 by CADMesh to be treated as tetrahedral meshes as previously done with the initial phantom of figure (7-1-a). We will use the notation F1, F2 and F3 to refer to the phantoms of figure (7-1-a), figure (7-13-a) and figure (7-13-b) respectively. Therefore, phantoms F1 and F2 have filamented structures and phantom F3 is fragmented.

Phantoms F2 and F3 now treated as tetrahedral meshes are filled with liquid water and are also placed in water filled containers having trapezoidal faces to optimize the simulations as shown in figures (7-13-e) and (7-13-f). Electrons with energies derived from the electron spectra of figure (7-3) are randomly shot inside the container boxes where the spatial distribution of the energy deposits inside the phantoms are registered. The Geant4-DNA processes are used at this point.

Table (7-7) shows the properties of each of the three phantoms filled with water. The masses of the phantoms are obtained using the function `GetMass()` of Geant4. The mean chord length of each phantom is calculated separately using the method introduced in paragraph 7.2.

The filamented phantom F1 has the smallest mass and thus the smallest volume and the smallest mean chord length. The filamented phantom F2 has slightly larger mass and larger mean chord length. Whereas the phantom F3 has the largest mass and thus the largest volume but it has the smallest mean chord length. F3 is fragmented and has smaller individual structures compared to the longer filaments which explains the smaller value of mean chord length.

Table (7-7) Properties of the three different phantoms extracted from Geant4

Phantom	Mass (kg)	Mean chord length $\bar{l}$ (nm)
F1 (filamented)	1.59×10^{-13}	462.04
F2 (filamented)	2.06×10^{-13}	473.56
F3 (fragmented)	2.82×10^{-13}	458.14

In what follows, we show a comparison of the lineal energy distributions, mean lineal energies and DBSCAN analysis for the three phantoms.

Microdosimetric quantities are calculated inside the phantoms. Figure (7-14) shows the imparted energy distributions inside each of the three phantoms after shooting $2x10^5$ electron events. We notice that the curve of F3 is slightly shifted to the right showing the largest values of imparted energy. Curves F2 and F1 have lower values of imparted energies respectively. Notice that the three curves have a small peak at 23 eV due to the contributions of electronic excitations and vibrational excitations in water.

Figure (7-15) shows similar results for the frequency distributions of lineal energy inside the three phantoms. Table (7-8) lists the mean values of imparted energy and the frequency and dose weighted mean lineal energies. The table shows compatible results with the microdosimetric distributions.

Phantom F1 has the smallest mass and therefore the least imparted energy and lineal energies. Phantom F2 has larger mass and thus larger microdosimetric mean values. Phantom F3 has the largest mass and thus the largest mean values of the imparted and lineal energies. Absorbed doses do not follow the same trend as microdosimetric quantities such that F2 scores a smaller dose than F1. Even though the total energy deposited in F2 is larger than F1, absorbed dose is inversely proportional to the phantom's mass and this results in a smaller dose for F2 with the larger mass. F3 has the largest mass but it scores the highest dose meaning that the total deposited energy is very large compared to the cases of F1 and F2.

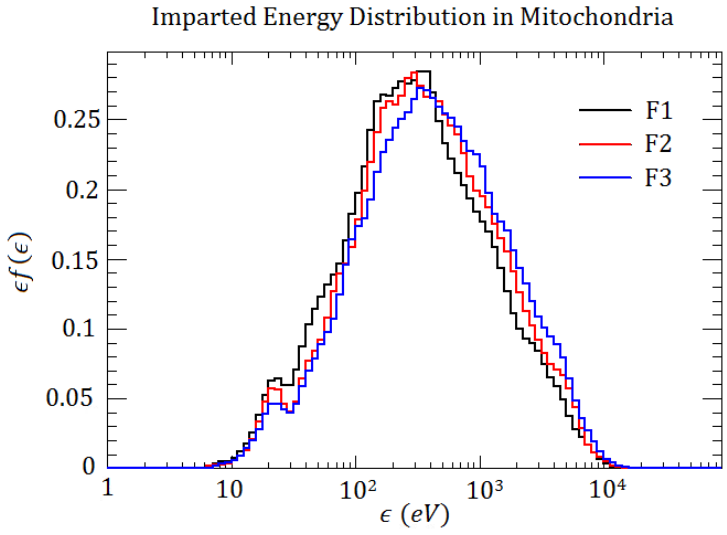

Figure (7-14) Comparison of imparted energy inside the three phantoms

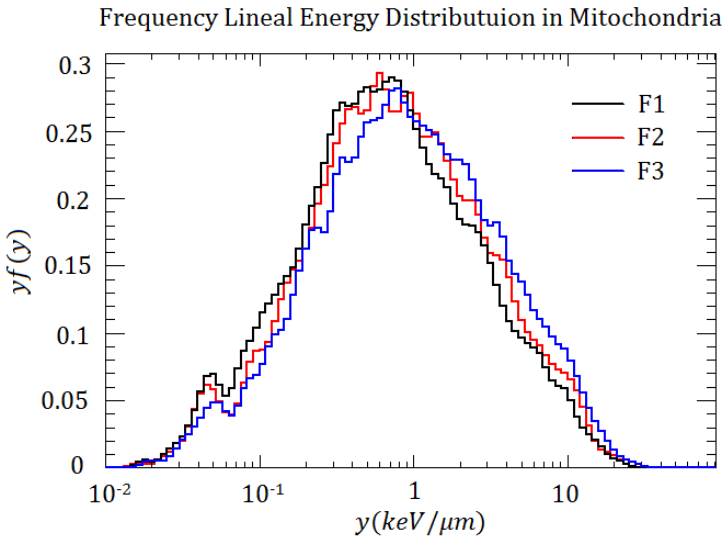

Figure (7-15) Frequency lineal energy distributions inside the three different phantoms

Table (7-8) Number of events, absorbed dose and the microdosimetric mean values inside the phantoms

Phantom	Event N°	Dose(Gy)	ε (eV)	$\bar{y}_F$ ($keV/\mu m$)	$\bar{y}_D$ ($keV/\mu m$)
F1(filamented)	2x10^5	13.87	611.95	1.32	4.98
F2(filamented)	2x10^5	12.82	818.42	1.73	5.63
F3(fragmented)	2x10^5	16.56	953.08	2.08	6.70

DBSCAN clustering analysis is performed for the phantoms F2 and F3 using the same three values of maximum neighboring distance *d*: 1 nm, 2 nm and 3 nm. The frequency distributions of RMSR, cluster sizes, total energy per cluster and cluster densities are plotted.

Figure (7-16) is a chart showing the total number of clusters in each phantom for the three different values of *d*. Phantom F3 has the highest number of clusters followed respectively by F2 and F1 in all clustering configurations. So as the total volume of the phantom increases, the number of clustered damages increases as well.

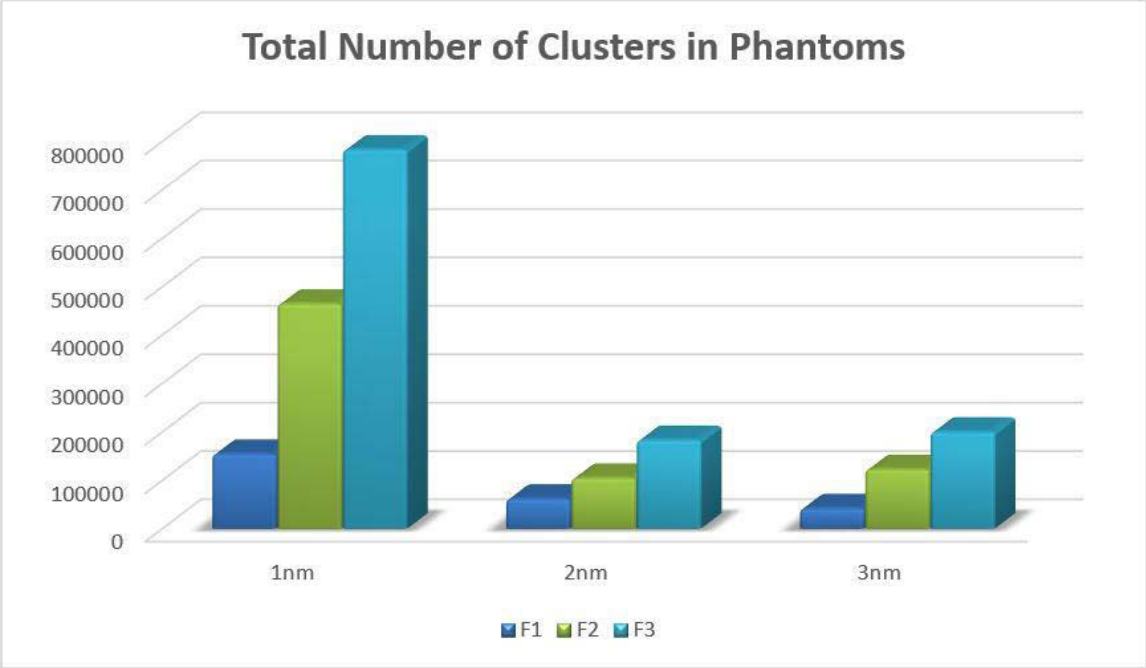

Figure (7-16) Total number of clusters inside the three phantoms with different values of *d*: 1 nm, 2 nm and 3 nm

Figures (7-17), (7-18), (7-19) and (7-20) show the clustering analysis inside the three phantoms for three different values of maximum neighboring distance *d*. All the figures are in agreement with the previous microdosimetric results.

Phantom F3 shows the highest frequencies for all clustering quantities followed respectively by the frequencies of F2 and F1 for all three values of *d*. This is expected since F3 scored the highest energy depositions followed by F2 then F1. Since all of these phantoms are filled with water and the same energy source is used, we see that all these curves have almost the same shape peaking at about the same values differing only in the frequencies. Therefore, the shape and volume of the target affects the severity of the potential clustered damages.

When clustering with d = 1 nm, small sized clusters are the most frequent and their energy is small as well. However, when clustering with d = 3 nm, the sizes and energies of clusters become large. This is observed in all cases of the three phantoms. The value of *d* used in the DBSCAN algorithm affects the total number of clusters produced and their sizes which consequently affects the energetic density of these clusters.

The simulations give us a primary idea about the potential damages taking into account the spatial distributions and energy depositions of the interaction points with water. In reality, things might be a little different. Mitochondria have two membranes, and the internal membrane is considered the most sensitive part since it constitutes of proteins in charge of

energy production for the cell. In addition, the release of cytochrome *c* (a protein in the internal mitochondrial membrane) from the internal membrane and into the cytoplasm initiates apoptosis. Therefore, internal membrane damages would affect the overall vitality of the cell. It would be interesting if we knew the best value of *d* that causes two or more damage points to form a cluster from the biological observations. However, this information is not available at the moment.

In our simulations, we used two healthy mitochondria phantoms and one fragmented phantom. We used the same algorithm for all three to produce the clusters. In reality, the fragmented mitochondria might undergo apoptosis. Therefore, they might not need a large dose to get damaged.

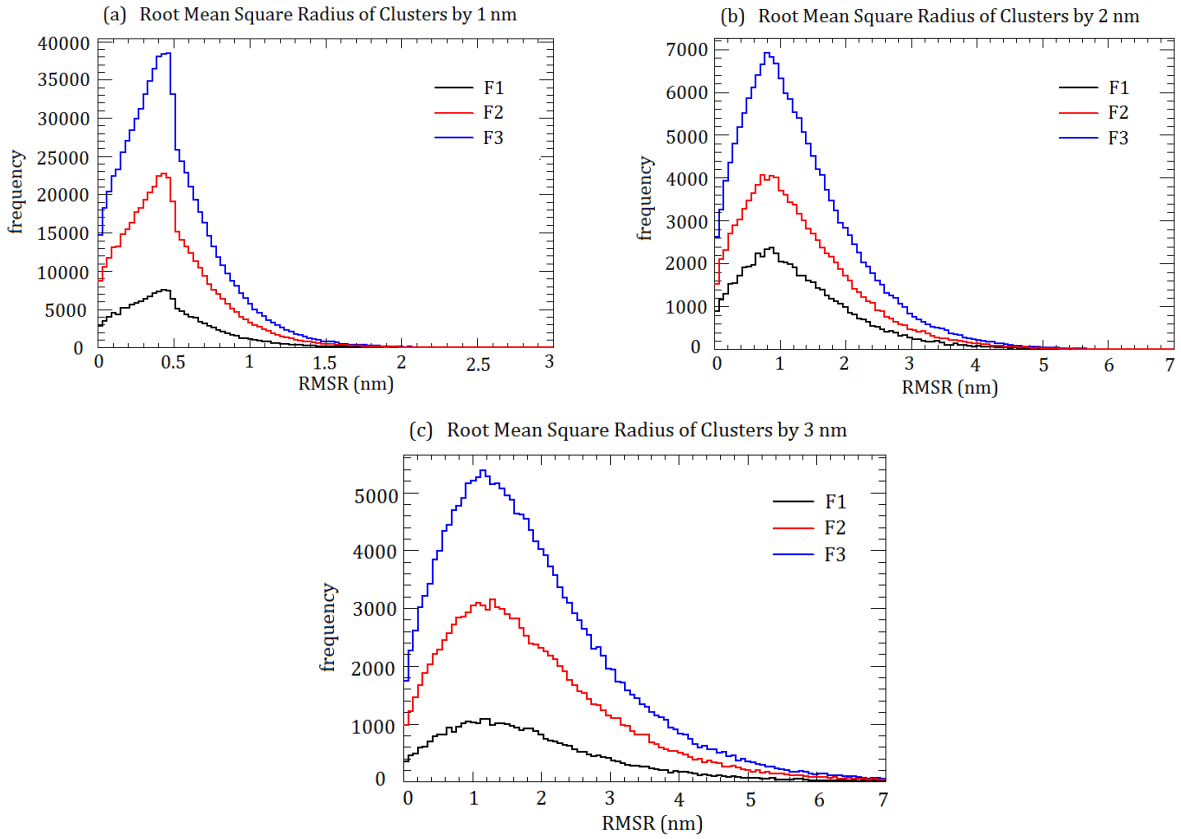

Figure (7-17) RMSR distributions for three different phantoms: (a) clustering with *d* = 1 nm, (b)clustering with *d* = 2 nm, (c) clustering with *d* = 3 nm

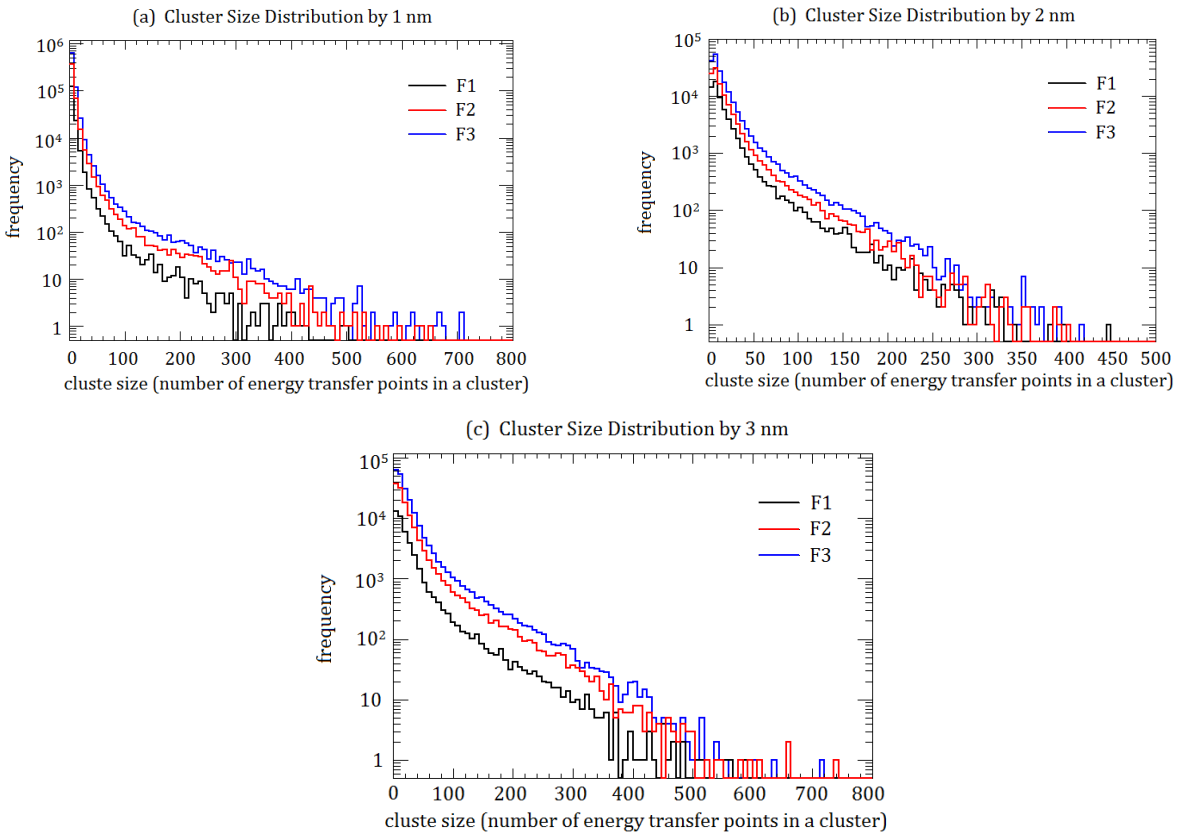

Figure (7-18) Cluster size distributions for three different phantoms: (a) clustering with *d* = 1 nm, (b)clustering with *d* = 2 nm, (c) clustering with *d* = 3 nm

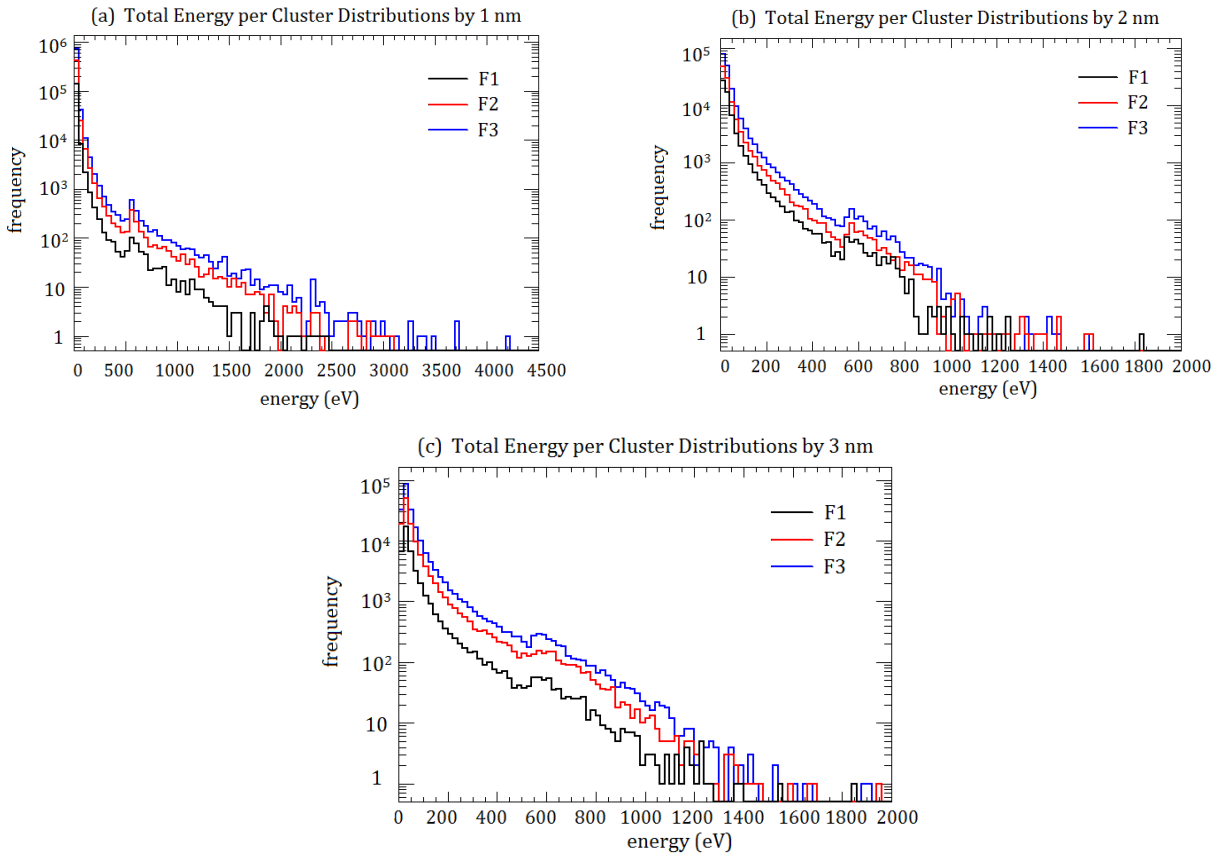

Figure (7-19) Total energy per cluster distributions for three different phantoms: (a) clustering with *d* = 1 nm, (b)clustering with *d* = 2 nm, (c) clustering with *d* = 3 nm

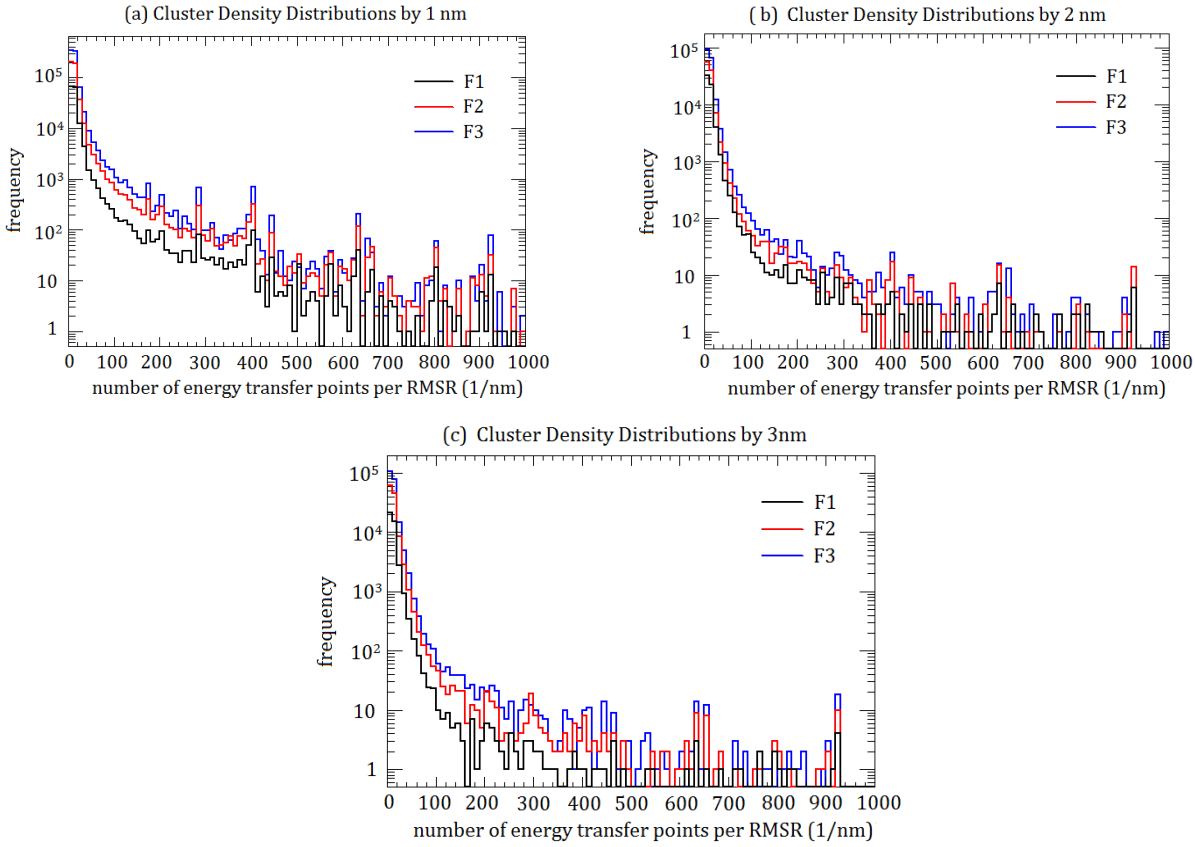

Figure (7-20) Cluster density distributions for three different phantoms: (a) clustering with *d* = 1 nm, (b)clustering with *d* = 2 nm, (c) clustering with *d* = 3 nm

7.7 Conclusion

A resampling method is used to account for the interaction of 250 keV photons with water by reproducing electrons with energies ranging from 1keV to about 120 keV. This method is used to save calculation time since 0.006% of the primary photons will interact wasting a huge flux of the incident beam.

Mean chord lengths of all three phantoms are calculated using the proton track interception mean chord length method exploiting the straight trajectories and large ranges of 90 MeV protons.

Each of the three phantoms is irradiated with $2x10^5$ electron events and the total absorbed dose is calculated. The imparted energy and the frequency lineal energy distributions are produced for each phantom. The mean values of lineal energies and imparted energies are also calculated for the three different phantoms. These calculations show that the shape and size of the phantom directly affects the number and spatial distribution of energy depositions. We conclude that as the volume of the target increases, more energy

depositions are likely to be produced inside and this increases the chance for higher imparted energies and lineal energies.

DBSCAN clustering analysis is performed for the three phantoms by three different values of maximum distance *d*. Small values of *d* produce isolated small clusters with low energies, while large values of *d* produce larger clusters with larger energies. Moreover, targets with large volumes are exposed to a high number of interactions that produce a high number of energy depositions. These will increase the number of produced clusters.

Note that the simulations done in this chapter were carried out with Geant4.10.01.p02 version, except for phantoms F2 and F3 irradiations that were carried out with Geant4.10.02 version.

1. *ICRU Report 90: Key Data for Ionizing-Radiation Dosimetry: Measurement Standards and Applications*. 2016.
2. *National Institute of Standards and Technology*. Available from: https://www.nist.gov/pml.
3. Kellerer, A.M. and D. Chmelevsky, *Concepts of Microdosimetry I.* Radiation and Evironmental Biophysics, 1975. **12**: p. 61-69.
4. Kellerer, A.M., *Fundamentals of Microdosimetry.* The Dosimetry of Ionizing Radiation, 1985. **1**: p. 78-161.
5. Villegas, F., et al., *Cluster pattern analysis of energy deposition sites for the brachytherapy sources 103Pd, 125I, 192Ir, 137Cs, and 60Co.* Physics in Medicine and Biology, 2014. **59**(18): p. 5531-5543.
6. Villegas, F., et al., *Corrigendum: Cluster pattern analysis of energy deposition sites for the brachytherapy sources 103Pd, 125I, 192Ir, 137Cs and 60Co (2014 Phys. Med. Biol. 59 5531–43).* Physics in Medicine and Biology, 2016. **61**(15).
7. Villegas, F. and e. al., *Energy deposition clustering for modelling RBE* Medical Physics, 2016. **43**(12).

8 Gold Nanoparticles Effect on Mitochondria

In this chapter, we are investigating the effects of gold nanoparticles (GNP) on mitochondria after 250keV photon irradiation. Geant4-DNA libraries simulate the electromagnetic interactions only in liquid water. To take into account the effects of GNP at the microscopic scales we are using a resampling method of electron energies leaving the surface of GNP similar to the method used in chapter 7 paragraph 7.1 to resample the secondary electron energies induced by the primary photon interaction in liquid water.

In the present versions of Geant4, the implemented Geant4-DNA processes are available for interactions with water. Therefore, we cannot use these processes in gold. Instead, the standard Livermore electromagnetic processes are used for photon interactions with gold and the energies of the secondary electrons leaving the surface of the GNP are calculated.

To simplify things, the electrons leaving the GNP surface are called **gold electrons** and the first generation of secondary electrons induced by photon interactions with water are called **water electrons**.

Two configurations will be tested hereafter with two different sizes of GNP:

- First, GNP are considered as spheres of diameter 10 nm. Half of these GNP are attached to the surface of the phantom and the other half are suspended randomly in the container box that is considered as the cytoplasm.
- Then, GNP are considered as spheres of diameter 13 nm that are attached to the surface of the mitochondria phantom similar to the work of Kirkby and Ghasroddashti[1].

Throughout this chapter, the phantom used is the filamented phantom F1 produced from the microscopic image shown in figure (7-1), and simulations are performed with Geant4.10.01.p02 version. The production of **gold electrons** only were carried out with Geant4.10.03 version.

8.1 Case #1: 10 nm GNP

8.1.1 GNP positions

In the work of Chitrani *et al.* [2] the maximum uptake of GNP of 50 nm diameter after 8 hour incubation is 6000 per cell. After consulting with our biology colleagues, we decided to test 5000 GNP of 10 nm diameter with our mitochondria phantom. We assume that half the number of GNP are attached to the mitochondrial membrane. Thus, 2500 gold spheres of diameter 10 nm are placed near the surface of mitochondria phantom where the

distance from the phantom's surface to the center of the gold spheres is 15 nm accounting for 10 nm thickness of a supposed GNP coating and 5 nm for the GNP radius.

To find the positions of the centers of gold spheres, rescaling the mitochondria phantom is performed. In *DetectorConstruction* class, after creating an instance of CADMesh, the scale of the phantom's tessellated mesh is set to 1.015 μm. This produces a new surface mesh that is slightly larger than the original mesh where the distance between the new surface points and the original surface mesh points is 15 nm.

This way a new surface mesh is produced enveloping the original one where the thickness separating the two surfaces equals 15 nm. In Figure (8-1) we see an illustration of this rescaling procedure showing a spherical mesh that is rescaled 1.5 times its size. Suppose the original radius of the sphere of red color is 1cm, the rescaled sphere of white color enveloping the original red one has a radius of 1.5 cm.

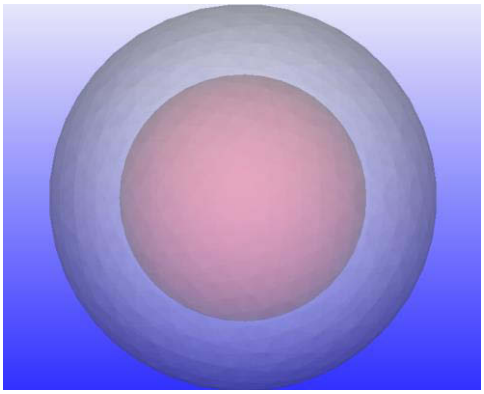

Figure (8-1) A spherical surface mesh rescaled to 1.5 its original size. The original mesh is in red and the rescaled is in white enveloping the original.

After rescaling, the vertices of the rescaled tessellated mesh are considered as potential positions of the gold spheres. It is possible to increase the number of surface points by performing subdivisions in MeshLab [3].

This way we can have more than one configuration of the surface points to place the nanoparticles. These different configurations allow studying different densities of gold nanoparticles attached to the surface of mitochondria.

As an example, figure (8-2) shows a tessellated sphere that is subdivided twice to increase the number of vertices on its surface. The sphere in figure (8-2-a) is the original sphere introduced into MeshLab with 642 vertices. Applying the subdivision option once increases the number of vertices to 1922 as shown in figure (8-2-b). Applying the subdivision option twice increases the number of vertices to 7680 as figure (8-2-c) shows.

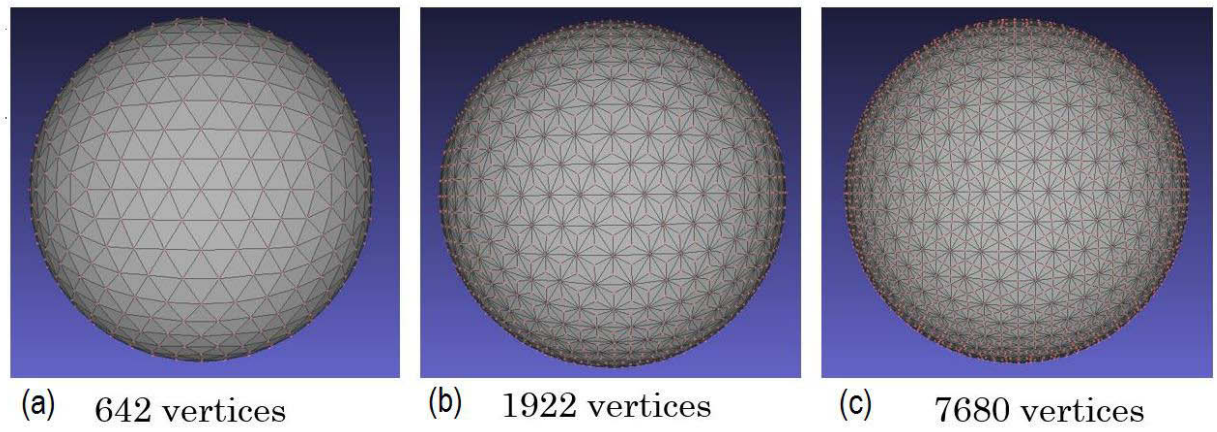

Figure (8-2) Performing subdivisions on a tessellated sphere in MeshLab

Using this rescaling method, the vertices of this inflated tessellated mesh are extracted out of which a random 2500 are chosen for the GNP surface positions. The remaining 2500 GNP are spread randomly in the container box outside the phantom supposedly roaming in the cell's cytoplasm.

Figure (8-3-a) shows positions of the GNP surrounding the phantom and spread in the cytoplasm in a 3D view. Figure (8-3-b) shows the x-y view of the GNP positions where the central area is kept empty accounting for the cell nucleus since GNP are not absorbed inside the nucleus.

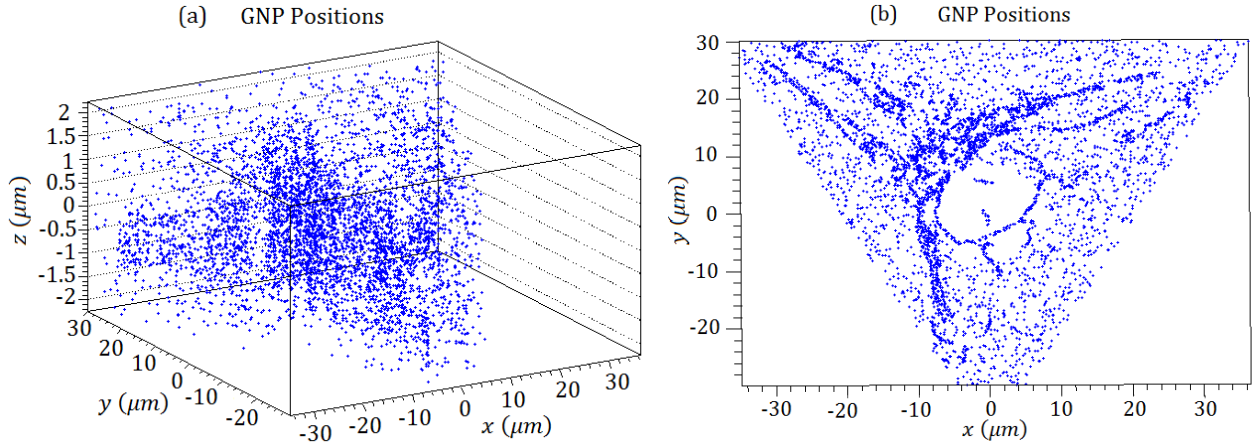

Figure (8-3): (a) 3D Positions of GNP, (b) upper view of 2D positions of GNP

250 keV photons are launched randomly on the upper x-y face of the box containing the mitochondria phantom and the assembly of GNP where the box and the phantom are filled with water. The photon source is placed at -10mm in the z-direction and the Livermore physics processes are used for photon interactions with gold and water. Auger processes

are activated for this simulation. $2x10^9$ photon events are launched in parallel towards the box with all that it contains. Only 0.04% of photons actually interact with the box. The first generated secondary electrons (**water electrons**) and the electrons leaving the surface of the GNP (**gold electrons**) are registered. We find that 0.002% of the produced electrons exit the GNP volume through the spherical surfaces while the rest are absorbed inside the nanoparticles. The total number of electrons are summarized in table (8-1).

Table (8-1) Number of electrons produced in box and phantom filled with water and number of electrons leaving the GNP surface when shooting $2x10^9$ 250keV photons

Total photon number	1^{st} generated e^- in water	All e^- Leaving gold spheres
$2x10^9$	827547 (99.998%)	14 (0.002%)

8.1.2 **Gold Electrons Energy Spectrum**

A gold sphere of radius 10 nm is placed inside a box of dimensions 1x1x1 mm^3 filled with water. The 250 keV photon source is placed at -5 nm of the z-axis. Photons are produced randomly from a disc shaped source of radius 5 nm in the x-y plane and directed in parallel towards the positive z-direction. $2x10^9$ photon events are produced where the Livermore physics processes are used and the Auger processes are turned on.

The kinetic energy of all electrons leaving the surface of the gold sphere are recorded and their probability distribution is shown in the figure (8-4). In a later Geant4-DNA simulation the electrons leaving the GNP surface will have energies chosen according to this probability distribution.

The gold sphere is surrounded with water and in this region the Geant4-DNA physics processes are activated. Electrons are tracked in water and energy deposits are recorded. This water volume is then considered as concentric shells of increasing radii and the total energy deposit in each shell is calculated. This will then produce the radial dose surrounding the gold sphere induced by the photon irradiation.

In this case all photon interactions outside the gold sphere are stopped so that we have the radio-induced effect of the gold alone. The radial dose values with respect to distance from the sphere's surface are shown in figure (8-5). The same simulation is repeated for a 10 nm water sphere and the radial dose due to the water sphere is also calculated as the red curve of figure (8-5) shows.

We can see from this figure that electrons produced by GNP have the largest effect on their immediate surroundings depositing the largest doses in the closest area to the GNP after which the dose decreases gradually as the electrons travel away from the sphere. The gold

sphere produces higher radial dose in the surrounding medium than the water sphere. This indicates the dose enhancement of gold after irradiation. On all the radial range there is at least an enhancement of one order of magnitude between the two curves. Effectively the largest effect is produced in the vicinity of the gold sphere.

Figure (8-6) shows the radial distance of all energy transfer points of electron interactions in the water medium surrounding the gold sphere. Most energy transfer events occur near the gold sphere and become less frequent as their distance from the sphere's surface increases. The distance is calculated from the center of the gold sphere for all energy depositions in water excluding the energy depositions inside the sphere.

The energy transfer seizes completely at 500 μm distance from the sphere's surface. We can estimate that the maximum range of electrons leaving the gold sphere's surface to be 500 μm. Fluctuations in the curve start at about 200 nm distance from the center of the sphere where the number of electron interactions drop. This shows that most electrons travel up to 200 nm which could be accounted for Auger electrons.

The curve contains many hills depicting several increases in the number of electron interactions followed by decreases as they travel away from the gold sphere showing an electron buildup. This could be attributed to the three *K*, *L*, and *M* shells of gold releasing three groups of Auger electrons. The least energetic Auger electrons released from the *M* shell interact near the gold sphere till up to 20 nm followed by the *L* shell electrons that interact till about 200 nm and the *K* shell electrons interact further away till about 2μm. The furthest hill which is the least frequency could be attributed to the photoelectrons interactions.

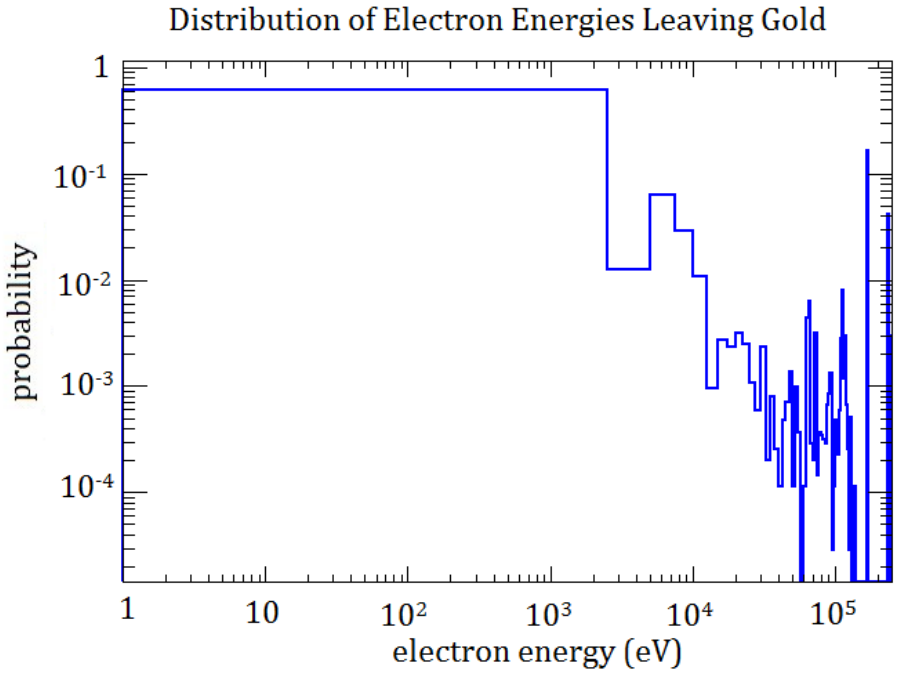

Figure (8-4) Probability distribution of electron energies leaving the surface of a 10 nm gold sphere. 2x10^9 photons are produced randomly from a disc shaped source of radius 5 nm in the x-y plane and directed in parallel towards the positive z-direction. The Livermore physics processes are used and the Auger processes are turned on.

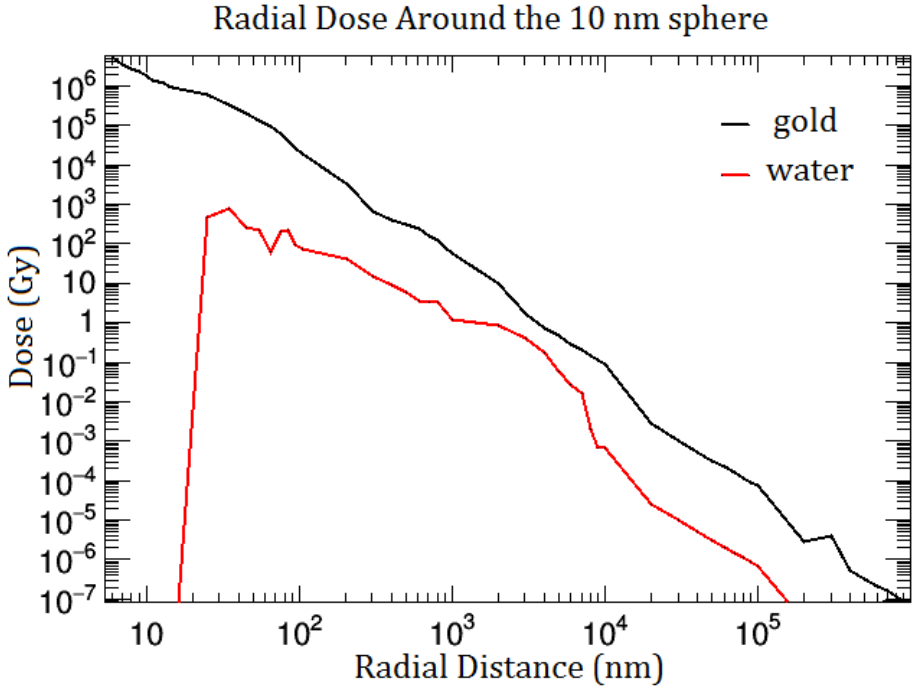

Figure (8-5) Radial dose with respect to radial distance from the surface of the 10nm gold sphere (black) and the 10 nm water sphere (red)

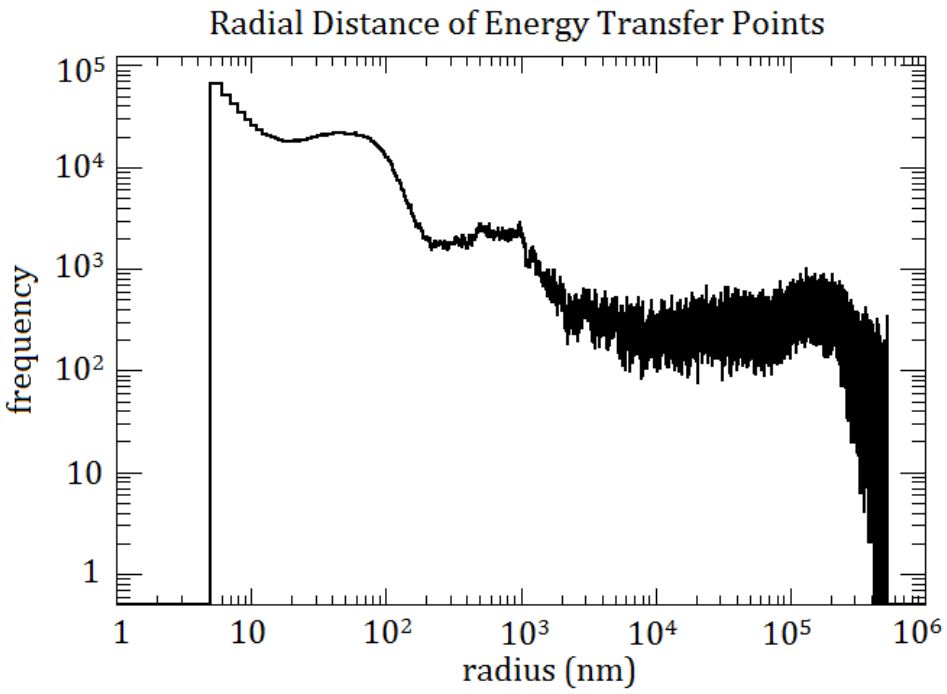

Figure (8-6) The radial distance of energy transfer points in liquid water surrounding the gold sphere calculated relative to the sphere's center.

8.1.3 Geant4-DNA Simulations

We run two simulations using Geant4-DNA processes:

- Simulation with Mitochondria phantom in the water box using **water electrons**
- Simulation with Mitochondria phantom using **water electrons** and **gold electrons**

The first simulation simply shoots $2x10^5$ electrons randomly inside the box containing the mitochondria phantom. The energies of these electrons are **water electrons** taken from the spectrum of figure (7-3). Energy depositions inside the phantom are recorded.

When using Geant-DNA physics processes the used medium is liquid water, so in the second simulation we introduce the GNP by the electrons that leave their surface into the surrounding water medium. These electrons that we will call **gold electrons** take their energies from the energy spectrum of figure (8-4) and their positions from the spatial distributions of GNP as explained in paragraph 8.1.1. As for the electrons produced in the phantom and container box regions (**water electrons**) they take their energy from the water energy spectrum of figure (7-3) introduced in chapter 7. In short, the GNP are not directly inserted in the second simulation, but their effect is taken into consideration.

Only 0.002% of the electrons will be **gold electrons** as explained in paragraph 8.1.1 and the rest will be **water electrons**, see table (8-1). So, if 10^6 electron events are launched in

the total volume of the container box only 20 will be **gold electrons** at most. These **gold electrons** will have random direction pertaining to a 4π solid angle.

The frequency lineal energy distributions inside the mitochondria phantom produced by running $2x10^5$ electron events in the container box of the phantom in the presence and absence of GNP are shown in figure (8-7).

Both curves in this figure do not show any significant difference and thus the presence of GNP in this case did not produce any effect. The lineal energy mean values in each case do not predict any energy deposit enhancement as table (8-2) shows. The absorbed dose values inside the phantom show no difference in both cases either. The number of electrons produced from the surface of the GNP is very small (4 electrons maximum in the case of $2x10^5$ electron events), so it is coherent that no significant effect will be produced in this case.

In order to get a radio sensitizing effect, the number of GNP should be increased. Therefore, more investigations should be done to see how to increase the uptake of GNP into living cells, as well as to know their precise localization inside the cell (close to the mitochondria membrane, spread or clustered in the cytosol). This last point is not precisely clear from the published literature.

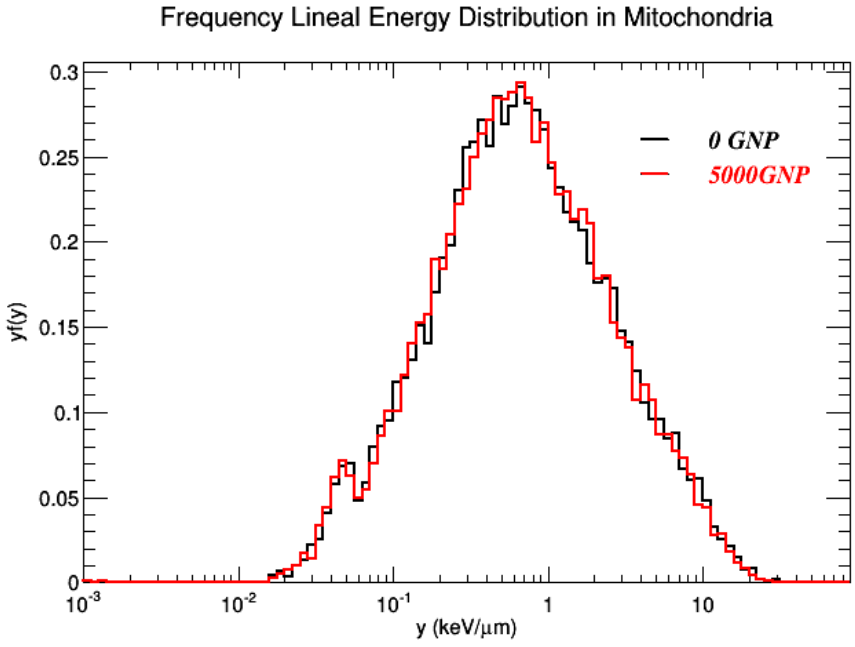

Figure (8-7) Lineal energy frequency distributions of electron events inside the mitochondria phantom in the presence and absence of 5000 10 nm GNP

Table (8-2) Absorbed dose, and mean values of imparted energy, frequency lineal energy and dose lineal energies inside the mitochondria phantom induced by $2x10^5$ electron events

GNP number	Dose inside the phantom (Gy)	$\bar{y}_F$ $(keV/\mu m)$	$\bar{y}_D$ $(keV/\mu m)$
0	13.87	1.56	5.56
5000	13.63	1.51	5.23

8.2 Case #2: 13 nm GNP

8.2.1 Resampling of Electron Energies with Gold Nanoparticles

So far, there is no experimental evidence that GNPs enter the mitochondria but some reports indicate that the GNPs may get localized near the mitochondrial membrane. Taking into account that GNPs are not absorbed into the interior of the mitochondria, in our simulation, we assume that all the nanoparticles are attached to the surface of the mitochondrial membrane. The GNPs are represented as spheres of gold having radius 6.5 nm. Note that the distance between the center of the gold spheres and the mitochondrial surface is taken to be 20 nm accounting for some sort of coating of the nanoparticles.

The positions of GNPs are determined using the rescaling method introduced in paragraph (8.1.1) where the tessellated mesh is rescaled to 1.02 μm. The number of vertices is increased by using subdivisions.

The number of GNPs used in this case is 503050 spheres projecting 7% surface area coverage of the mitochondrial membrane. This corresponds to 213.6 μg/ml mass concentration of gold.

Assuming all the nanoparticles are attached to the mitochondrial surface, this concentration is calculated relative to the volume of the 70x70x6 μm^3 water box containing both the mitochondria phantom filled with water and the GNPs.

Figure (8-8) shows how the GNPs are distributed near the surface of the phantom. Note that the size of the spheres is exaggerated for representation purposes. The gold sphere positions are tested before performing the simulations to avoid any potential geometry overlapping.

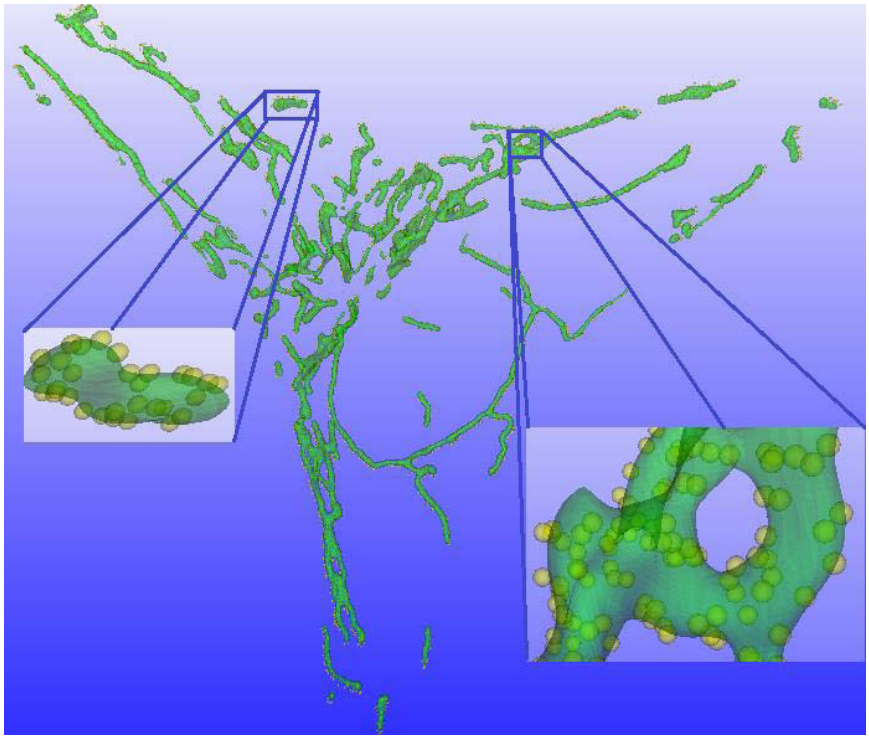

Figure (8-8) GNP spread near the surface of the mitochondria phantom

After placing the gold spheres in their positions surrounding the phantom, 10^8 photon events are randomly shot in parallel on the upper face of the box containing the mitochondrial phantom and the GNP. The Livermore physics processes are used while Auger processes are turned on.

The energies of the first generated secondary electrons in all water regions of the box are registered otherwise known as **water electrons**.

The energies of all electrons leaving the surface of the gold spheres, known as **gold electrons**, are also registered. Since we already calculated the energy spectrum of **water electrons**, we now calculate the energy spectrum of gold electrons shown in figure (8-9).

Contrary to case#1 where the **gold electrons** spectrum is produced from a single gold sphere, figure (8-9) is obtained by irradiating the total 503050 gold spheres while they are suspended around the surface of the phantom. The energy spectrum in this case is different from case #1. In case #1, the energy spectrum is calculated by irradiating a single gold sphere by 250 keV photons and it is produced by the effect of photons alone. However in this case all the spheres are irradiated by 250 keV photons. These photons will produce secondary electrons that leave one sphere and will probably interact with other neighboring spheres that will produce further electrons into the water medium. The kinetic energy of electrons leaving the surface of GNP that are initially induced by photon interactions or by secondary electron interactions from neighboring spheres will be

recorded to produce the spectrum of figure (8-9). Hence the spectrum is affected by the electrons produced by all the spheres not just the primary photons. In the current case #2, Auger electrons are not as dominant as in case #1.

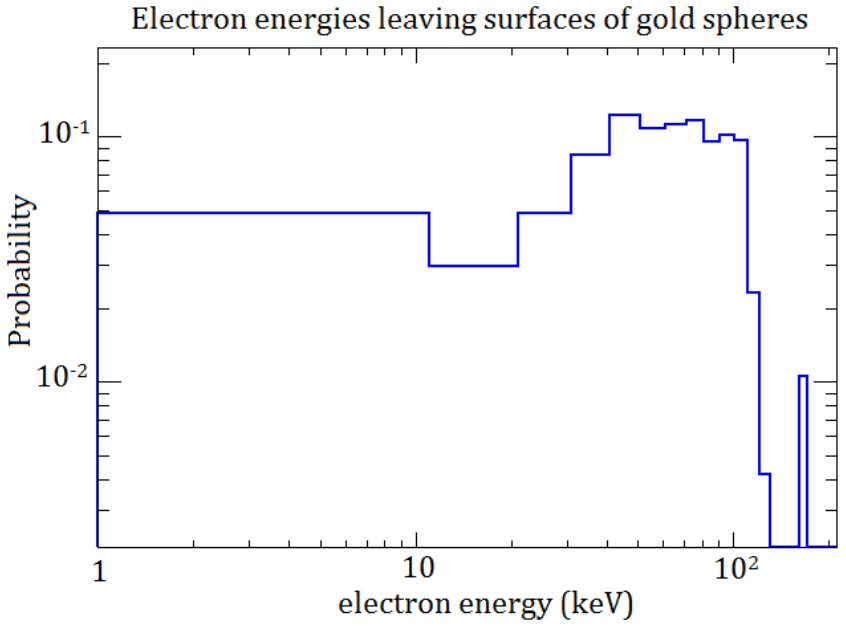

Figure (8-9) Energy spectrum of electrons leaving the surface of gold spheres in case of 7% surface coverage of mitochondrial membrane.

It is important to calculate the percentages of electrons produced in water and electrons leaving the surface of gold spheres. These percentages will be used later in a simulation with Geant4-DNA processes. The percentages are shown in the table (8-3) below:

Table (8-3) Percentages of secondary electrons produced by photon interactions in different parts of the box containing mitochondria and gold nanoparticles

10^8 events	7% gold coverage
1st generated e^- in Box	84.9%
1st generated e^- in Mitochondria	15%
All e^- Leaving gold spheres	0.1%

In this case of 7% coverage of mitochondrial surface area, out of 10^8 photon events 508684 interacted. The electrons of interest are the first generated in the box accounting for 84.9%, the first generated in mitochondria accounting for 15% and all electrons leaving the gold particles accounting for 0.1%.

8.2.2 **Geant4-DNA Simulations**

In order to complete our study we need to run two simulations using Geant4-DNA processes:

- Simulation with Mitochondria phantom in the water box
- Simulation with Mitochondria phantom with 7% GNP surface coverage

The first simulation consists of the mitochondrial phantom as a tetrahedral mesh filled with water and centered in a water box of dimensions 70x70x6 μm^3. Electrons are generated randomly in the whole volume of the box including the volume of the phantom. The primary energies of the electrons are generated according to the probability distribution function of water electrons illustrated by the figure (7-3).

The second simulation consists of the mitochondrial phantom as a tetrahedral mesh filled with water and centered in a water box of dimensions 70x70x6μm^3. Gold spheres are not added to the geometry in *DetectorConstruction*. However, their effect is taken into account by creating electrons at the surface positions of where they are supposed to be and giving these electrons energies according to the probability distribution function of **gold electrons** illustrated in figure (8-9). Electrons generated in the remaining volume, namely the mitochondria and the surrounding volume of the box have energies according to the probability distribution function of **water electrons** illustrated by the figure (7-3).

In the second simulation corresponding to the 7% gold surface coverage, 0.1% of the electrons are produced at the supposed gold spheres surfaces with energies from the **gold electrons** spectrum, figure (8-9). The rest of 99.9% of the electrons are produced randomly in the volume of the box and the phantom with energies from the photon-water interaction spectrum, figure (7-3). (See table 8-3).

Since in Geant4-DNA only interactions in water can be simulated, the resampling energy methods gave us the possibility to create the gold nanoparticle effects without directly simulating them in the geometry. It also reduced the time of calculation.

8.2.3 **Lineal Energy in Mitochondria**

The following are results of Geant4-DNA simulations of 10^6 electron events interactions in the cases of no gold and 7% gold as described earlier in paragraph 8.2.2. Lineal energy frequency distributions in the mitochondria phantom are shown in the figure (8-10).

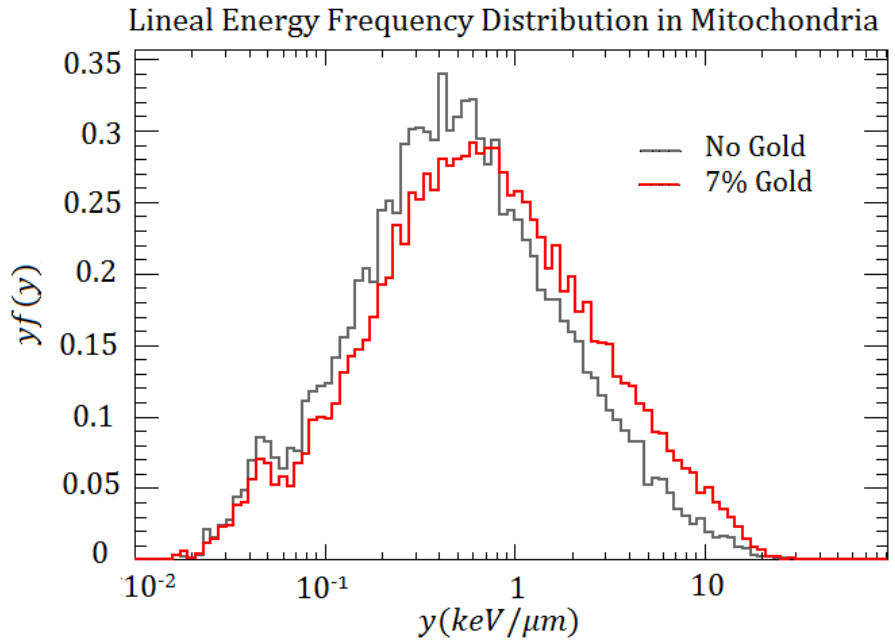

Figure (8-10) Lineal energy frequency distributions inside mitochondria in the presence and absence of gold nanoparticles induced by the 250 keV photons

As figure (8-10) shows the lineal energy frequency distribution curve shifts towards higher values in the presence of gold nanoparticles. This is due to the increase in energy depositions created by the gold nanoparticles after irradiation.

Table (8-4) Absorbed dose and mean values of frequency lineal energy and dose lineal energy inside mitochondria in the presence and absence of gold nanoparticles

Gold percentage	Absorbed Dose (Gy)	$\bar{y}_F$ $(keV/\mu m)$	$\bar{y}_D$ $(keV/\mu m)$
No Gold	13.64	1.11	4.22
7% Gold	25.41	1.54	5.43

The total absorbed dose inside the phantom increases by a ratio of 1.86 when the GNP are introduced in the simulation. Mean values of frequency lineal energy and dose lineal energy recorded in table (8-4) are in agreement with frequency distributions. $\bar{y}_F$ increases by 38.7% and $\bar{y}_D$ increases by 28.6% when GNP are introduced. The mean values in the presence of GNP are slightly higher than the mean values in the absence of GNP. Thus, GNP produce more energy deposits in mitochondria after irradiation.

For 10^6 electron events, 0.1% leave the GNP surface meaning that a maximum of 1000 electrons are accounted for gold energies in the 7% case. The electrons produced from the GNP surface take random direction in space with 4π solid angle. Therefore, not all electrons

leaving the surface of GNP will interact with the mitochondria. This would explain the small increase in lineal energies.

GNP placed in the vicinity of the mitochondria increase the number of energy deposited inside after irradiation with 250 keV photons. The number of GNP used is very large and is not observed with experiments so far. It has not been clear if the GNP attach themselves to the mitochondrial membrane exclusively although they were detected near mitochondria.

8.3 **Conclusion**

Two sizes of GNP are used in simulations with mitochondria to investigate their radio-sensitizing effect after 250 keV photon irradiation.

A resizing method with CadMesh library is introduced to determine the GNP positions surrounding the mitochondria phantom exploiting the tessellated geometry of the phantom using the MeshLab software. The GNP effect is introduced into Geant4-DNA simulations by energy resampling techniques without directly inserting the nanoparticles into the *DetectorConstruction*.

In the first case of 10 nm GNP, a low number is investigated where the GNP are suspended near the mitochondrial outer membrane and randomly throughout the cytoplasm. This configuration simulates what is expected experimentally for GNP uptake. However, the absorbed dose and lineal energies do not show any enhancements. To our knowledge, there are no experimental studies that calculated lineal energies after GNP are included inside the cells. Until now, Monte Carlo simulations are the only way to perform such calculations since it is not possible to calculate the doses experimentally inside mitochondria.

In the second case of 13 nm GNP, a very large number of GNP is used and they are exclusively positioned around the surface of the mitochondria phantom. The electron event number is also increased to 10^6 in order to increase the number of gold electrons interactions. The absorbed dose is indeed enhanced and the lineal energy values show a little improvement.

The GNP study needs more investigation on the biological part to determine the optimal uptake of GNP into the cells. The spatial distribution of GNP is not clear yet. Some experiments show colocalization of GNP with mitochondria [4, 5] while others do not. The total uptake and the distribution inside the cells depends on the types of cells and the methods used for GNP manufacturing. They also depend on the size of GNP.

Some experiments reported enhancements in survival fraction curves with introduction of GNP into the cells [2]. The effect of GNP in cell killing could be attributed to an increase in

ROS production in the cytosol where GNP are more likely to be spread as clusters inside vesicles throughout the cytosol. Although GNP are detected in the vicinity of mitochondria, it is not clear if the increase in cell killing is directly related to their presence near mitochondria.

In short, we can say that the use of GNP as radio-sensitizers for radiotherapy is promising but more experiments are needed in this area of study to determine the optimal conditions for their usage.

1. Kirkby, C. and E. Ghasroddashti, *Targeting mitochondria in cancer cells using gold nanoparticle-enhanced radiotherapy: A Monte Carlo study.* Medical Physics, 2015. **42**(2): p. 1119-1128.
2. Chithrani, D., et al., *Gold nanoparticles as radiation sensitizers in cancer therapy.* Radiation Research, 2010. **173**: p. 719-728.
3. *MeshLab*. Available from: http://meshlab.sourceforge.net/.
4. Karatas, O.F., et al., *Interaction of gold nanoparticles with mitochondria.* Colloids and Surfaces B: Biointerfaces, 2009. **71**: p. 315-318.
5. Wang L., et al. *Selective targeting of gold nanorods at the mitochondria of cancer cells: implications for cancer therapy*. Nano Letters. 2011. **11**: p. 772-80.

9 Chemical Phase Inside the Mitochondria Phantom

New versions of Geant4-DNA contain libraries describing the chemical phase of irradiation in water simulating water radiolysis [1]. The chemical phase starts when the physical phase of ionizations and excitations ends at about 1 ps after first impact with water. The chemical processes are simulated till 1 μs after irradiation. From 1 ps till 1 μs the chemical compounds are created and diffused where they react with each other combining and reproducing further compounds.

In our study, we are trying to simulate the chemical compounds that are most likely to be produced inside the mitochondria phantom when under the influence of 250 keV photon irradiation. The mitochondria phantom used in this case is the filamented phantom F1 created from the microscopic image of figure (7-1).

The source used in this case is the resampled electron energy spectrum produced from the photon-water interaction as explained earlier and illustrated in figure (7-3).

All simulations were performed with Geant4.10.01.p02 version.

9.1 Chemical Species at 1ps After Irradiation

When simulating chemical processes, Geant4 provides two options to stop the simulation after a certain moment in time or a certain step in time by the following functions:

```
G4Scheduler::Instance()->SetEndTime();
```

```
G4Scheduler::Instance()->SetMaxNbSteps();
```

Using these functions, we can stop the simulation at any time we want or after any number of steps in time.

9.1.1 Stopping the chemistry at some time after irradiation

First, we run $2x10^4$ electron events randomly inside the container box of the phantom. The absorbed dose inside the phantom in this case is 1.38 Gy. The simulation is forced to stop 1 ps after irradiation, using `G4Scheduler::Instance()->SetEndTime()` function. For technical reasons that are not yet understood, the simulation is forced to stop at 1.001 ps.[2] The number of various chemicals primarily produced inside the phantom is registered into a file and displayed in the table (9-1) with their percentages. The percentage of each chemical compound produced in this case is shown in the pie chart of figure (9-1-a).

[2] Note that if the simulation is forced to stop at 1 ps we get an error.

Table (9-1) The number and percentages of various chemicals produced inside the mitochondria phantom when irradiated with 2x10⁴ electron events and the chemical processes stopped at 1.001 ps after irradiation, using the `G4Scheduler::Instance()->SetEndTime()` function.

	e^-_{aq}	H_2O^+	H_2O^-	H_2O^*	Total
Number	67910	68525	722	8226	145383
Percentage	46.71%	47.13%	0.50%	5.66%	100%

9.1.2 Stopping the chemistry after 1 step of chemical phase

In this case we force the simulation to stop at the end of the first step in the chemical phase using `G4Scheduler::Instance()->SetMaxNbSteps()` function. We run 2x10⁴ electron events inside the phantom container such that the absorbed dose inside the phantom is 1.44 Gy. The number of the chemical compounds produced is registered and shown in the table 1-2 and the pie chart in figure (9-1-b).

Table 9-2 The number and percentages of various chemicals produced inside the mitochondria phantom when irradiated with 2x10⁴ electron events and the chemical processes stopped at 1st step in time after physical phase ended, using `G4Scheduler::Instance()->SetMaxNbSteps()` function

	e^-_{aq}	H_2O^+	H_2O^-	H_2O^*	Total
Number	65326	65941	683	8061	140011
Percentage	46.65%	47.10%	0.49%	5.76%	100%

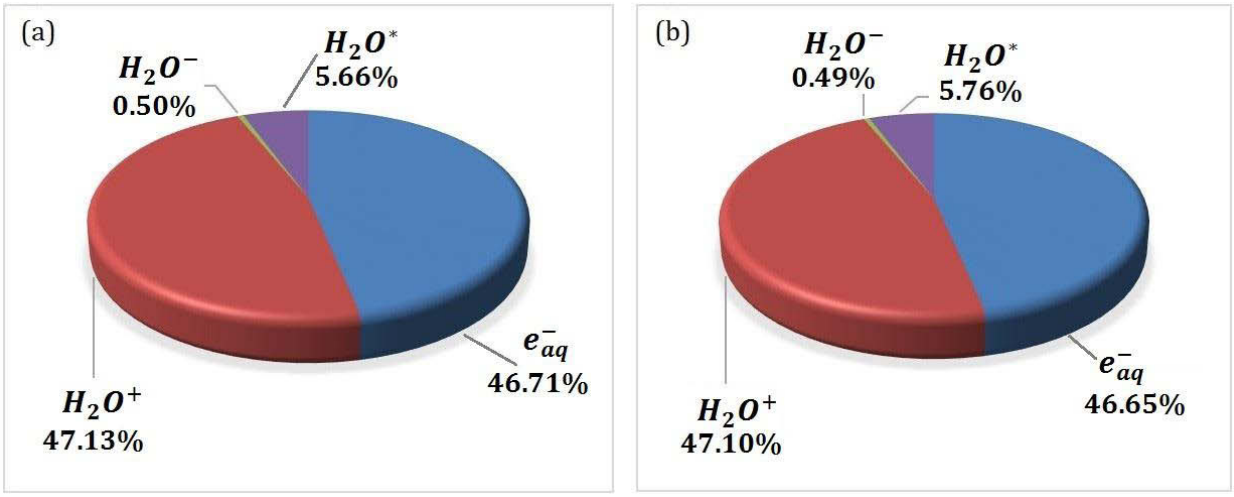

Figure (9-1) Percentages of chemical species produced inside the mitochondria phantom using two methods of forced stop: (a) the simulation is forced to stop at 1.001 ps after irradiation, (b) the simulation is forced to stop after the 1st step in time when the physical phase ended

We notice that there is no difference in the percentage of chemicals, however the number of chemicals produced in the second case is a bit higher. This is due to the number of events that interacted with the phantom which is a bit larger in the second case. This can also be deduced from the absorbed dose which is slightly larger. The number of produced chemicals is directly related to the number of electrons interacted in the physical phase. Therefore, using any of the two functions to stop the simulation at a very early chemical stage produces the same results.

As figures (9-1-a) and (9-1-b) show, the negatively charged water ion H_2O^- is very scarce compared to the abundant positively charged water ion H_2O^+ and the aqueous electrons e_{aq}^-. The number of excitations is not significant compared to the number of ionizations as the low percentage of H_2O^* shows (5.7%).

At this point these compounds are the primarily produced in the chemical phase or what is also called the physico-chemical phase. Note that the distinction between the physico-chemical phase and chemical phase is not well characterized and thus we will consider these compounds to be the primarily produced in the chemical phase. The equations governing their production are [2]:

$$H_2O \xrightarrow{X\ ray} H_2O^+ + e_{aq}^- \quad (9\text{-}1)$$

$$e_{aq}^- + H_2O \rightarrow H_2O^- \quad (9\text{-}2)$$

$$H_2O \xrightarrow{X\ ray} H_2O^* \quad (9\text{-}3)$$

9.2 Chemical Species from 1 ps till 1 μs After Irradiation

A simulation of chemistry processes is performed where the events are allowed to undergo the physical processes followed by the whole range of chemical processes. The incident electrons with energies taken from energy spectra of figure (7-3) are shot randomly inside the box containing the phantom and the chemical phase is activated after the physical phase is completed. Chemical species produced inside the mitochondria phantom during the whole chemical phase are registered.

In this case, the simulation is forced to stop at 1 μs after irradiation which is considered the end of the chemical phase. All the produced chemicals at each time step is registered and their distribution in time is shown in figure (9-2). The total number of electron events released inside the container box of the phantom is 1000 out of which 121 interacted with the phantom depositing 85.06 mGy of absorbed dose. Note that the produced data is very large and tracking 1000 events is enough to produce a reasonable amount of statistics. The

simulation was performed on a duo core machine that took about 22 hours to finish 1000 events.

Figure (9-2-a) shows the number of H_2O^+, H_2O^-, and H_2O^* produced in the first step of the chemical phase at 1 ps. The excited water molecules H_2O^* and the ionized water molecules H_2O^+, and H_2O^- react with the water medium and disappear after 1 ps giving rise to the production and propagation of other chemicals.

Figure (9-2-b) shows the probability of H_2, $H^\bullet$, and OH^- over the whole period of the chemical phase. We can see that the number of these chemicals is somehow stable in the first part of chemical phase till 2 ns. $H^\bullet$ and OH^- will increase in number till they peak at 7ns and H_2 peaks at 10 ns. After 10 ns these three chemicals decrease in number and fluctuations occur in the curves till the end of the chemical phase indicating that their production becomes less probable since they start to get reabsorbed in the medium.

The probability of H_2O_2, e^-_{aq}, H_3O^+ and $OH^\bullet$ produced over the whole chemistry period is shown in figure (9-2-c). We notice that e^-_{aq}, H_3O^+ and $OH^\bullet$ have the same shape starting with a high probability and decreasing gradually till 1 µs. However, H_2O_2 peaks at 10 ns after which it decreases.

All the chemicals produced after 1 ps will react among themselves and with the water medium during which some recombine and produce water molecules explaining the decrease in the curves exhibited by all the chemicals except for H_2O_2 that has a temporary peak at 10 ns similar to H_2, $H^\bullet$, and OH^-.

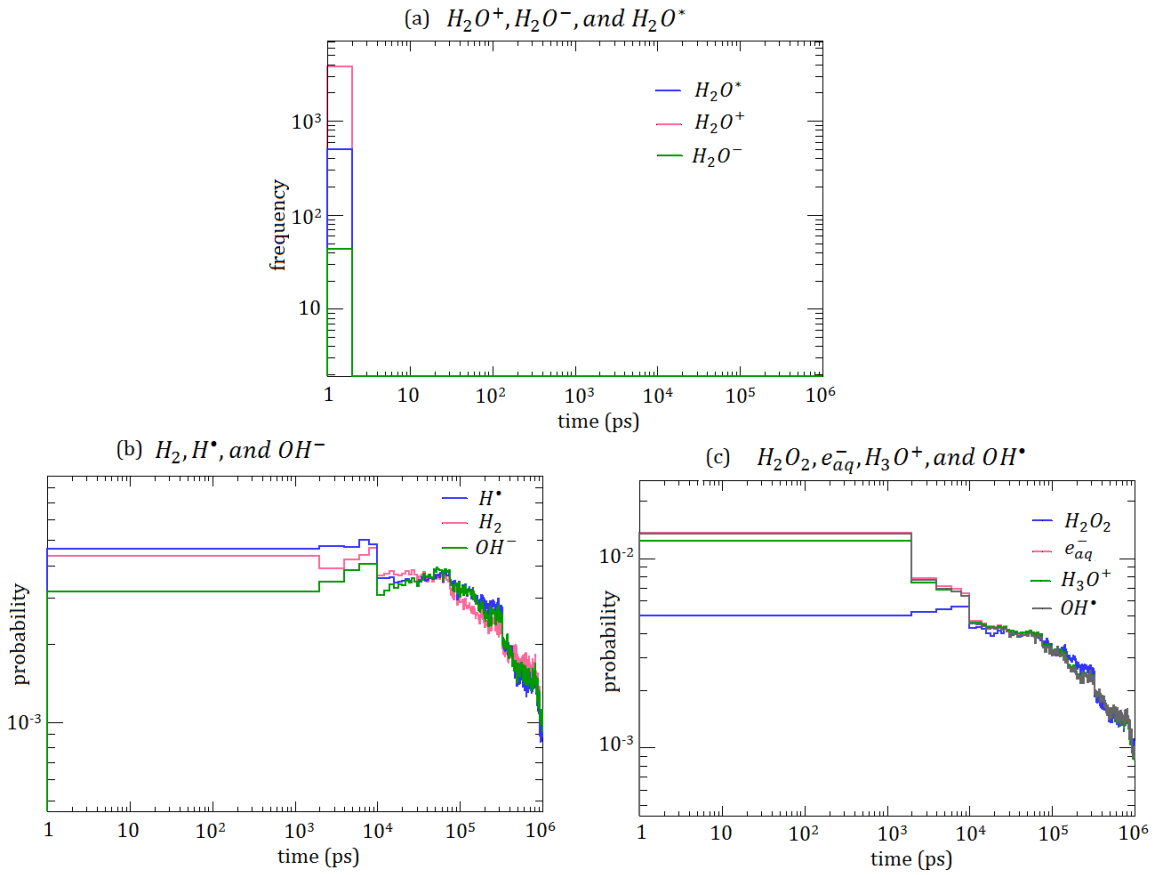

Figure (9-2) Chemical species produced inside the mitochondria phantom over the period extending form 1 ps till 1 μs after irradiation. (a) the probability of H_2O_2, e^-_{aq}, H_3O^+ and $OH^\bullet$; (b) the probability of H_2, $H^\bullet$, and OH^-; (c) the number of H_2O^+, $H_2O^-$and H_2O^*;

We run another simulation of 1000 events with chemistry processes till 1 μs and register the chemicals at certain moments or steps in time. Unlike the previous simulation that registers the chemicals during the whole chemical phase, this simulation runs the chemical processes till 1 μs but registers the chemicals at 7 specific moments in time. Figure (9-3) shows the number of chemicals produced at 7 moments in time during the chemical stage.

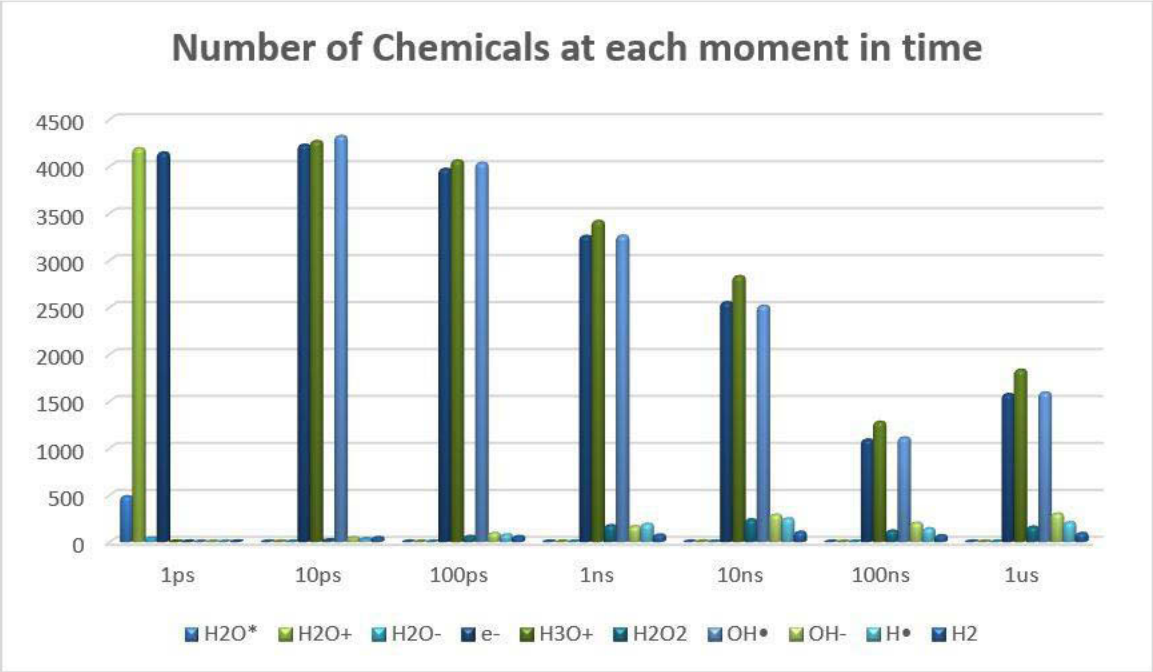

Figure (9-3) Number of chemical species produced at certain moments in time during the whole chemical phase

The concentration of the different 10 chemicals at each of the 7 time steps is shown in figure (9-4). The concentration in our case is the percentage of a certain chemical relative to the total number of chemicals at a certain time step. The figure shows how the concentrations of the chemicals differ in time.

At 1 ps the chemicals e_{aq}^{-}, H_2O^{+}, H_2O^{-}, and H_2O^{*} are exclusively produced. The concentration of H_2O^{+} is the largest followed by the concentration of e_{aq}^{-}. Notice that the concentration of H_2O^{-} is negligible but adding it to the concentration of e_{aq}^{-}, the negative charges equate the positive charges and the charge is conserved. This means that the chemicals in the initial phase are all produced inside the phantom and none has migrated outside yet. Excitations H_2O^{*} are not as frequent as ionizations for 250 keV photon irradiation.

At 10 ps, the excited water molecules will have either de-excited to their neutral state H_2O, or dissociated into $H^{\bullet}$ and $OH^{\bullet}$ radicals. The negatively charged water molecule H_2O^{-} will have dissociated into $H^{\bullet}$ radical and OH^{-} ion, and the positively charged water molecule H_2O^{+} will have dissociated into H_3O^{+} and $OH^{\bullet}$. The electron will combine with H_3O^{+} to produce $H^{\bullet}$ or it will propagate in the water medium as a solvated electron.

Aqueous electrons or solvated electrons, also called hydrated electrons, are the free electrons produced by ionizations after they lose their kinetic energy to 100 eV or less and attract the permanent dipole of several water molecules [2]. These chemicals will undergo

further reactions recombining into water or producing other radicals according to the reactions (9-4) to (9-12) [1].

$$H_3O^+ + e_{aq}^- \rightarrow H_2O + H^\bullet \quad (9\text{-}4)$$
$$H_3O^+ + OH^- \rightarrow 2H_2O \quad (9\text{-}5)$$
$$OH^\bullet + e_{aq}^- \rightarrow OH^- \quad (9\text{-}6)$$
$$OH^\bullet + OH^\bullet \rightarrow H_2O_2 \quad (9\text{-}7)$$
$$OH^\bullet + H^\bullet \rightarrow H_2O \quad (9\text{-}8)$$
$$e_{aq}^- + e_{aq}^- \rightarrow 2OH^- + H_2 \quad (9\text{-}9)$$
$$e_{aq}^- + H^\bullet \rightarrow OH^- + H_2 \quad (9\text{-}10)$$
$$e_{aq}^- + H_2O_2 \rightarrow OH^- + OH^\bullet \quad (9\text{-}11)$$
$$H^\bullet + H^\bullet \rightarrow H_2 \quad (9\text{-}12)$$

These reactions govern the chemical processes of Geant4-DNA chemical phase.

Note that H_3O^+ and OH^- are considered of low importance since they are not that chemically reactive in comparison to the radicals e_{aq}^-, $H^\bullet$ and $OH^\bullet$ [2].

According to figure (9-3), H_2O^+, H_2O^-, and H_2O^* disappear completely at 10 ps and leaving only e_{aq}^- from the previous time step but with lower concentration. H_3O^+ has slightly larger concentration and $OH^\bullet$ has the largest concentration. H_2O_2, H_2, $H^\bullet$, and OH^- have started to form but their concentrations are negligible compared to H_3O^+, e_{aq}^- and $OH^\bullet$.

From 100 ps till 1 μs, H_3O^+ has the highest concentration of 32% and is almost unchangeable. $OH^\bullet$ starts with a high concentration of 33% at 10 ps and decreases slowly till 27% at 1 μs not losing much of its concentration. e_{aq}^- starts with a high concentration of 46% at 1 ps and decreases to a concentration of 27% at 1 μs. These three chemicals decrease in concentration with time since they produce other chemicals. H_2O_2 is produced at 10 ps with 0.15% concentration and reaches almost 3% at 1 μs. Similarly H_2, $H^\bullet$, and OH^- are produced with low concentrations of 0.37%, 0.27% and 0.35% respectively increasing slowly to reach 1.69%, 3.68% and 5.28% respectively at 1 μs. Therefore, e_{aq}^-, H_3O^+, and $OH^\bullet$ are the most abundant throughout the whole chemical phase and H_2O_2, H_2, $H^\bullet$, and OH^- are negligible in comparison.

At the end of the chemical phase considerable amounts of hydroxyl radical, $OH^\bullet$, and aqueous electron, e_{aq}^- are produced. $OH^\bullet$ is highly reactive and ready to react with and change the structure of neighboring sensitive biomolecules. Hydrogen peroxide, H_2O_2, is not produced as abundantly as the hydroxyl radical and is not as highly reactive. Therefore, it has the ability to migrate for longer distances and dissociate into $OH^\bullet$ and OH^-. If this dissociation is in the vicinity of a sensitive molecule, the newly produced $OH^\bullet$ radical will take care of the rest. Although hydrogen peroxide has the ability to migrate to more places

than the hydroxyl radical, they have considerably lower concentrations throughout the chemical phase and therefore have lower ability to produce damages.

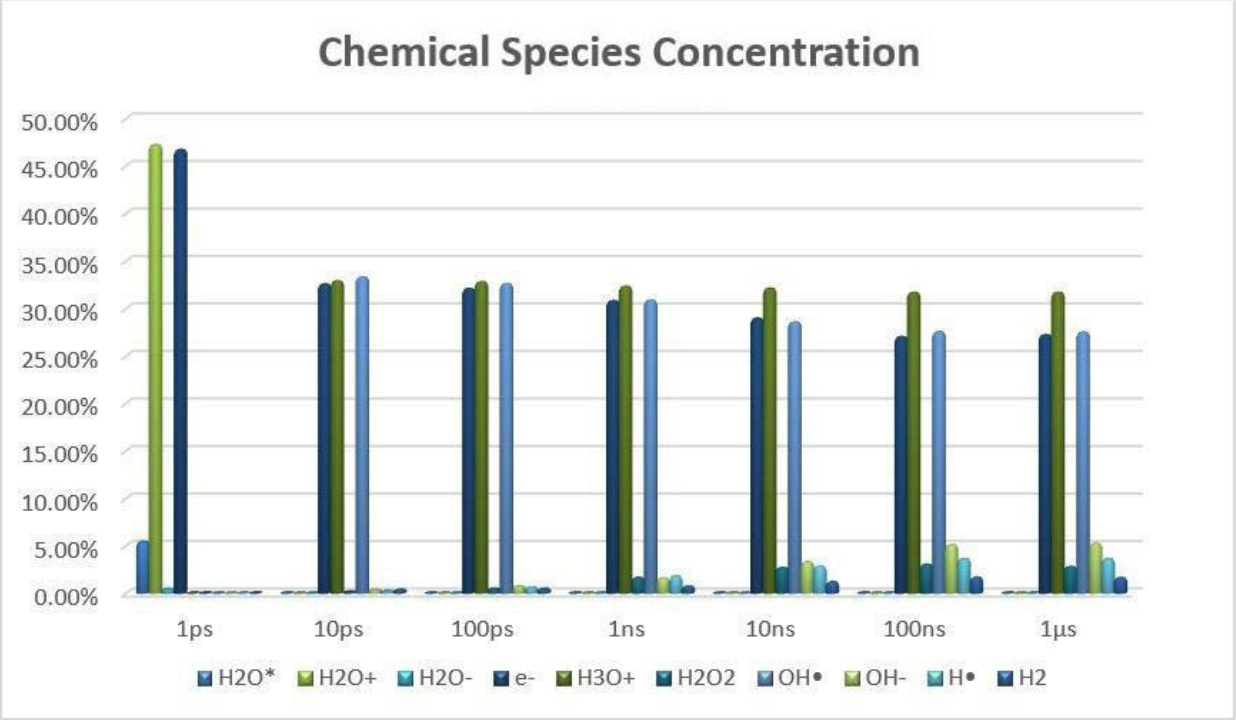

Figure (9-4) Concentration of the produced chemical compounds at various moments of the chemistry simulation; at each moment, the percentages are calculated relative to the total number of chemicals produced at that specific instant in the time of the simulation.

The percentage of each chemical specie as they evolve in time (as a function of time) is shown in the figure (9-5). Here the percentage of each specie is calculated relative to the total number of this specific chemical produced over the total duration of the simulation. In this case, certain moments in time of the simulation are chosen and the number of each specie is recorded as shown in figure (9-3). This shows how the concentration of each chemical compound evolves with time. H_2O^+, H_2O^-, and H_2O^* are excluded from this figure since they disappear after 1 ps as shown earlier.

At 1ps only the aqueous electrons are produced as demonstrated earlier. Their percentage, 20%, is highest at 1 ps and it decreases gradually with time till 100 ns and at 1 µs the percentage rises again to 10%. The other chemicals are registered at 10 ps, 100 ps, 1 ns, 10 ns 100 ns and 1 µs noting that none is created at 1 ps. H_3O^+ and $OH^\bullet$ have their highest percentage at 10 ps after which these percentages drop. On the other hand, H_2O_2, H_2, $H^\bullet$,

and OH^- have their lowest percentages at 10 ps after which the curves increase to reach a peak at 10 ns. Note that all the percentages drop at 100 ns and then rise again at 1 µs.

From these percentages, we notice that as e^-_{aq}, H_3O^+ and $OH^\bullet$ decrease, but H_2O_2, H_2, $H^\bullet$, and OH^- increase indicating that the interactions of the first three among themselves and with the water medium produces the other four as shown earlier for the concentrations in figure (9-4).

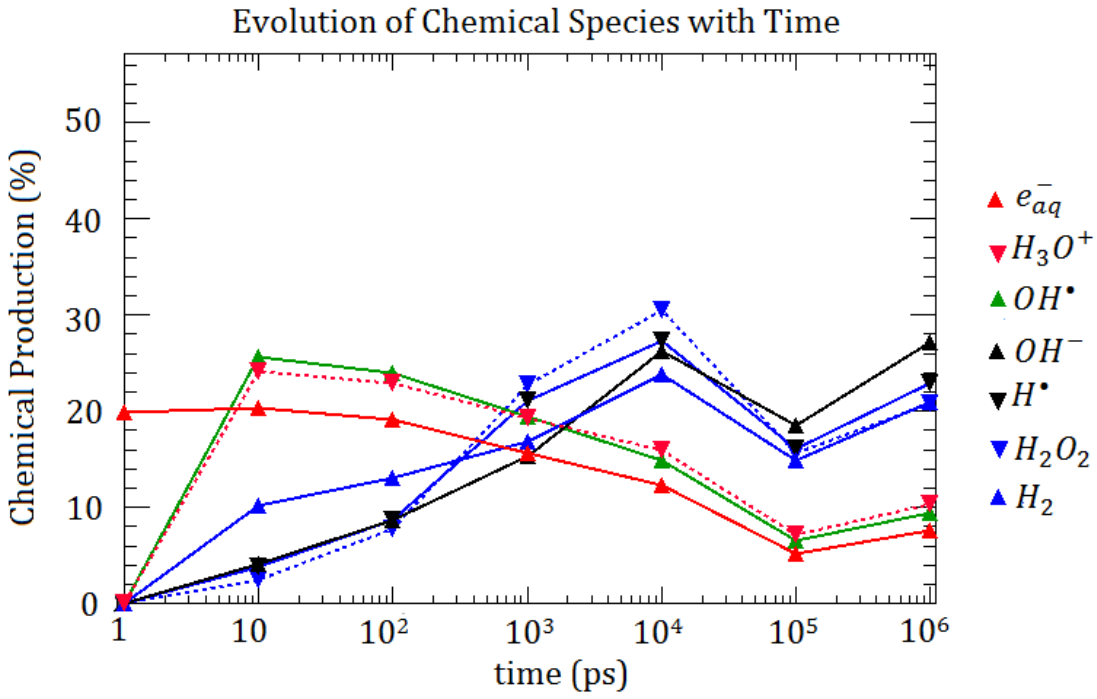

Figure (9-5) Evolution of chemical species with time over the whole period of the chemical phase. The percentage of each chemical is calculated at 7 different moments in time.

9.3 DBSCAN analysis of the primary produced chemicals

DBSCAN analysis is performed with chemicals initially produced at 1ps after irradiation. Distributions of all chemicals together (e^-_{aq}, H_2O^*, H_2O^- and H_2O^+) is analyzed with DBSCAN as well as the distributions of e^-_{aq} and H_2O^+ since they are abundantly produced in addition to the clustering of energy transfer points. As in the previous chapter 7, paragraph 7.5, clustering is performed for three values of *d*, the maximum neighboring distance

between two chemicals or two energy transfer points to produce a cluster. As explained earlier, damages produced very close to each other, otherwise known as complex damages require more effort to repair and sometimes are not properly repaired. Therefore, it is important to identify clusters of chemicals produced after irradiation.

The total number of clusters of energy transfer points, all chemicals (e_{aq}^{-}, H_2O^*, H_2O^- and H_2O^+), and each of e_{aq}^{-} and H_2O^+ are shown in figure (9-6) for three values of *d*.

- Energy transfer points produce the highest number of clusters for three values of *d*. Clustering with *d* = 1 nm produces the largest energy clusters followed by *d* = 2 nm and 3 nm.
- For all chemicals, all three values of *d* produce close number of clusters.
- It is obvious that chemical clusters are produced mainly by the contribution of H_2O^+ since they also produce the highest cluster number of *d* = 2 nm.
- As for e_{aq}^{-}, clustering with *d* = 3 nm produces the largest cluster number and the total number of clusters for the three values of *d* is much lower than those of H_2O^+ clusters.

This shows a difference in the spatial distribution of different chemicals and indicates that aqueous electrons are more diffused in the medium than H_2O^+ at 1 ps. These electrons are dispersed in the medium and are less likely to form clusters and hence do not contribute much to the total clustering of chemicals.

Table (9-4) shows the total number of energy transfer points and the total number of chemicals showing the detailed number of the various chemicals produced at 1 ps.

Inside the mitochondria phantom, energy transfer events are about three times higher than chemical events. e_{aq}^{-} and H_2O^+ are close in number. H_2O^* and H_2O^- have negligible numbers and do not contribute much to the total number of chemicals and thus are excluded from the clustering analysis. This gives us a good idea about the energy and chemistry population inside the phantom. Energy transfer events will have the largest influence on the radiation damages.

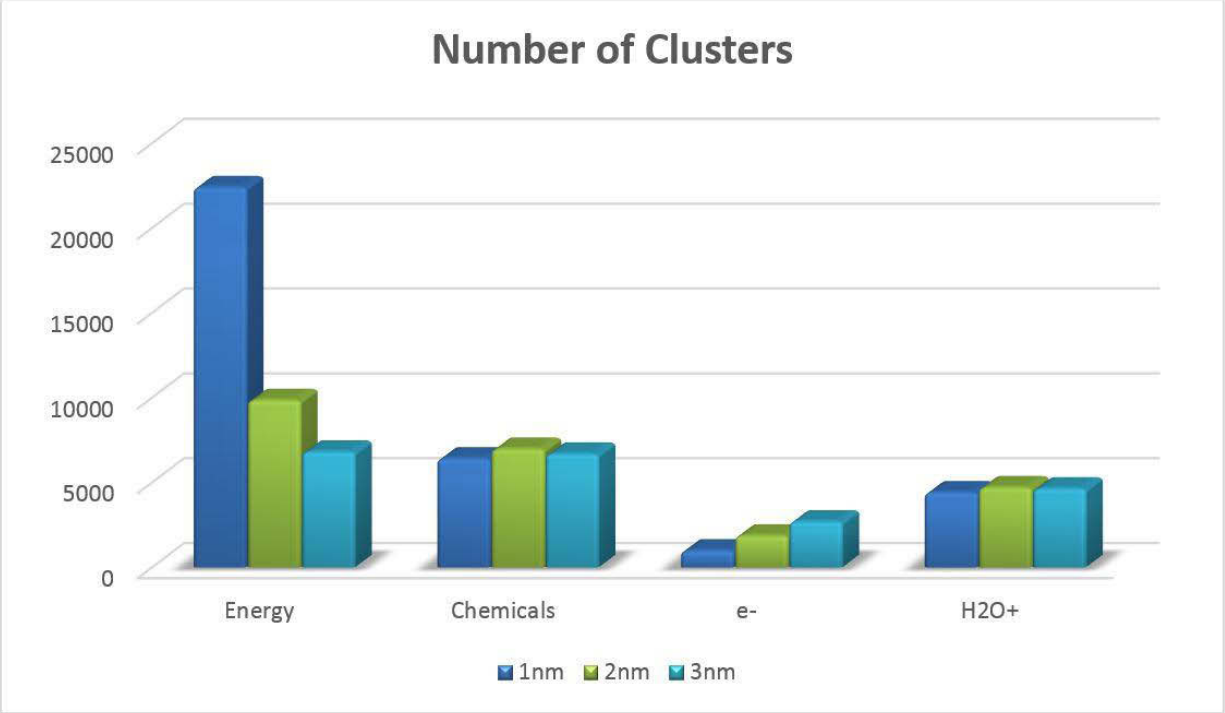

Figure (9-6) Total number of clusters for energy transfer points, all chemicals e_{aq}^{-} and H_2O^+ for three values of *d*, 1 nm, 2 nm and 3 nm.

Table (9-3) Total number of energy and chemistry events

	Number of points
Energy transfer points	302622
All chemicals	101453
e_{aq}^{-}	47277
H_2O^+	47785
H_2O^-	535
H_2O^*	5857

The root mean square radius (*RMSR*) of clusters is calculated for three values of *d*, 1 nm, 2 nm and 3 nm.

Figure (9-7-a) shows the RMSR distributions for clusters of all chemicals. For *d* = 1 nm the curve ranges till 1.5 nm and peaks at 0.45 nm, for *d* = 2 nm it ranges till 3.5 nm and peaks at 1 nm, and for *d* = 3 nm it ranges till 4 nm and peaks at 1.4 nm although the curve is not very smooth in this case and the peak is not sharp.

For energy transfer points as figure (9-7-b) shows, the curves peak at smaller values of 0.4 nm for *d* =1 nm, 0.8 nm for *d* = 2 nm and about 1.2 nm for *d* = 3 nm. The curves have wider ranges for energy transfer points and their peaks have smaller probabilities. This shows

that chemicals at 1 ps form smaller clusters than energy transfer points which implies that chemicals are not produced close to each other as energy transfer points.

Figures (9-7-c) and (9-7-d) show the *RMSR* distributions of e_{aq}^{-} and H_2O^+ respectively. These chemicals are produced with almost the same quantities at 1 ps as figures (9-1-a) and (9-1-b) show. However, they cluster rather differently. e_{aq}^{-} has higher probability of small cluster production than H_2O^+ for the three values of *d*. The three curves of e_{aq}^{-} have sharper peaks showing a preference in cluster production for sizes up to RMSR of 0.45 nm, 0.9 nm and 1.4 nm. Larger clusters are less probable.

On the other hand, H_2O^+exhibits a peak at 0.3 nm for *d* = 1 nm, but for *d* = 2 nm, and 3 nm the curves have a plateau like shape with fluctuations indicating that H_2O^+ have more probability to produce clusters of large sizes and are not confined to small clusters as e_{aq}^{-}. This also shows that e_{aq}^{-} change their position very rapidly and migrate away from the ionization event that initially produced the free electron that when slowed down exhibits the property of chemically reactive aqueous electron. H_2O^+ in comparison are not as actively mobile and therefore do not migrate as much which makes it possible for them to cluster in large sizes.

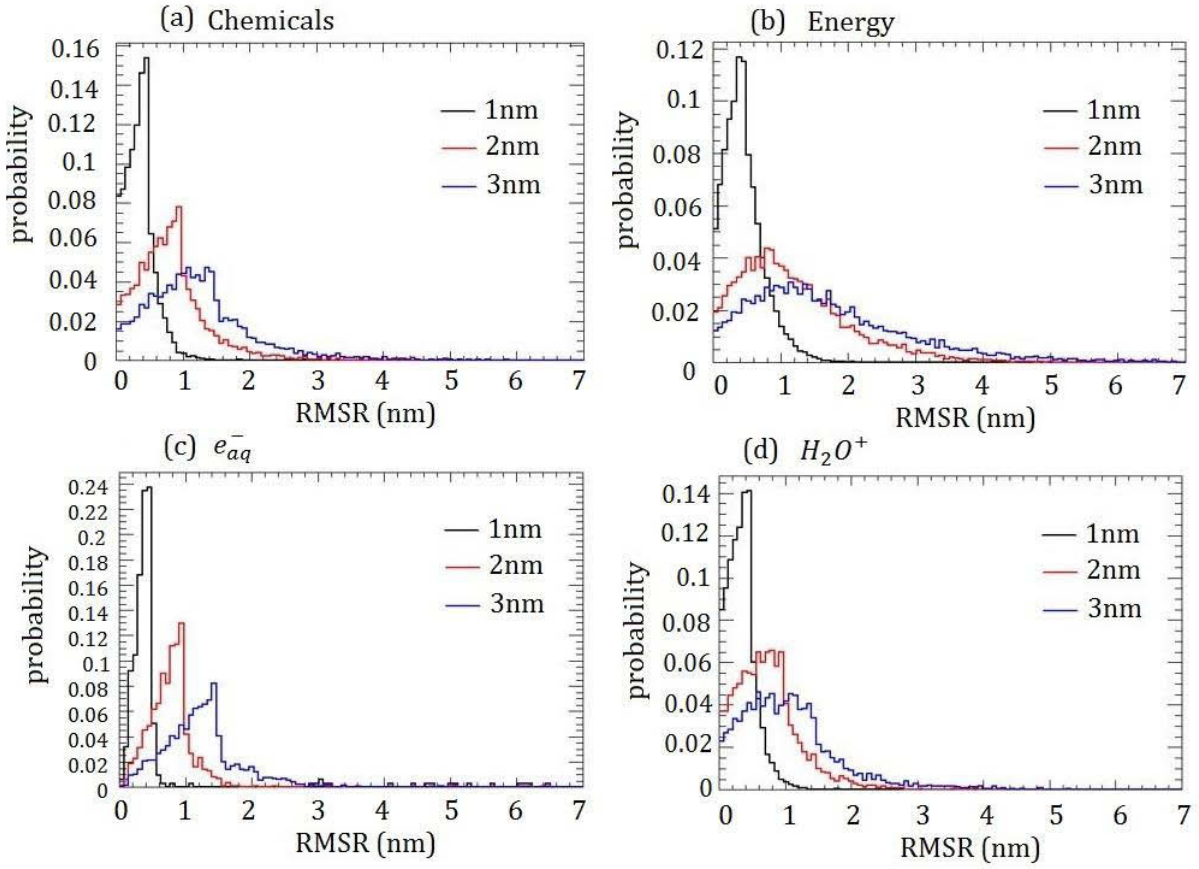

Figure (9-7) Distribution of RMSR of clusters for (a) energy transfer points, (b) all chemical species, (c) e_{aq}^-, and (d) H_2O^+.

Figure (9-8) shows the frequency distributions of cluster sizes of energy transfer points, chemicals (e_{aq}^-, H_2O^*, H_2O^- and H_2O^+), e_{aq}^-, and H_2O^+ when clustering with (a) d = 1 nm, (b) d = 2 nm, and (c) d = 3 nm.

The cluster size is a notation we are using for the total number of chemicals or energy transfer points inside one cluster. Clusters of energy transfer points have the highest frequencies for all three values of d.

All the curves have the same trend starting with high frequency of small size clusters and then decreasing as the cluster size increases showing abundance in small clusters.

In figure (9-8-a), the energy curve lies above the chemistry curves indicating the large number of energy clusters compared to chemistry clusters. This is also shown in the bar graph of figure (9-6). Energy transfer points are about three times more than the chemicals produced later on. This will produce more clusters of energy transfer points.

Figures (9-8-b) and (9-8-c) also show that energy clusters are larger in number for clusters larger than 5 points, but for clusters smaller than 5 in size, chemicals produce more clusters. The height of the energy curve shifts more above the chemicals curve as the value of d increases. This means that as the value of d increases energy transfer points are capable of producing more large clusters than chemicals.

The frequency of H_2O^+ is higher than that of e_{aq}^- for small cluster sizes till about size 25. For sizes larger than 25, e_{aq}^- start to have higher frequencies. For d = 1 nm and 2 nm the curves fluctuate heavily for large sizes. This indicates that clusters containing more than 30 chemicals are less likely to occur. However, for d = 3 nm the curves of e_{aq}^- and H_2O^+ show a clear distinction between the frequencies of large size clusters. e_{aq}^- tend to have more clusters of size greater than 25 and they produce larger clusters for larger values of d. This is clear indication that these electrons are not close to each other.

Clustering with larger values of d produces more large clusters than clustering with lower values of d. However, if the value of d is large the expected damages are less likely to be considered complex. When the cluster size is relatively large with somewhat small neighboring distance d between the chemicals or the energy transfer points, it is more probable to cause complex damages to the cell that are harder to repair. The best value of d could be determined with further studies on dimensions of the sensitive targets of the mitochondria.

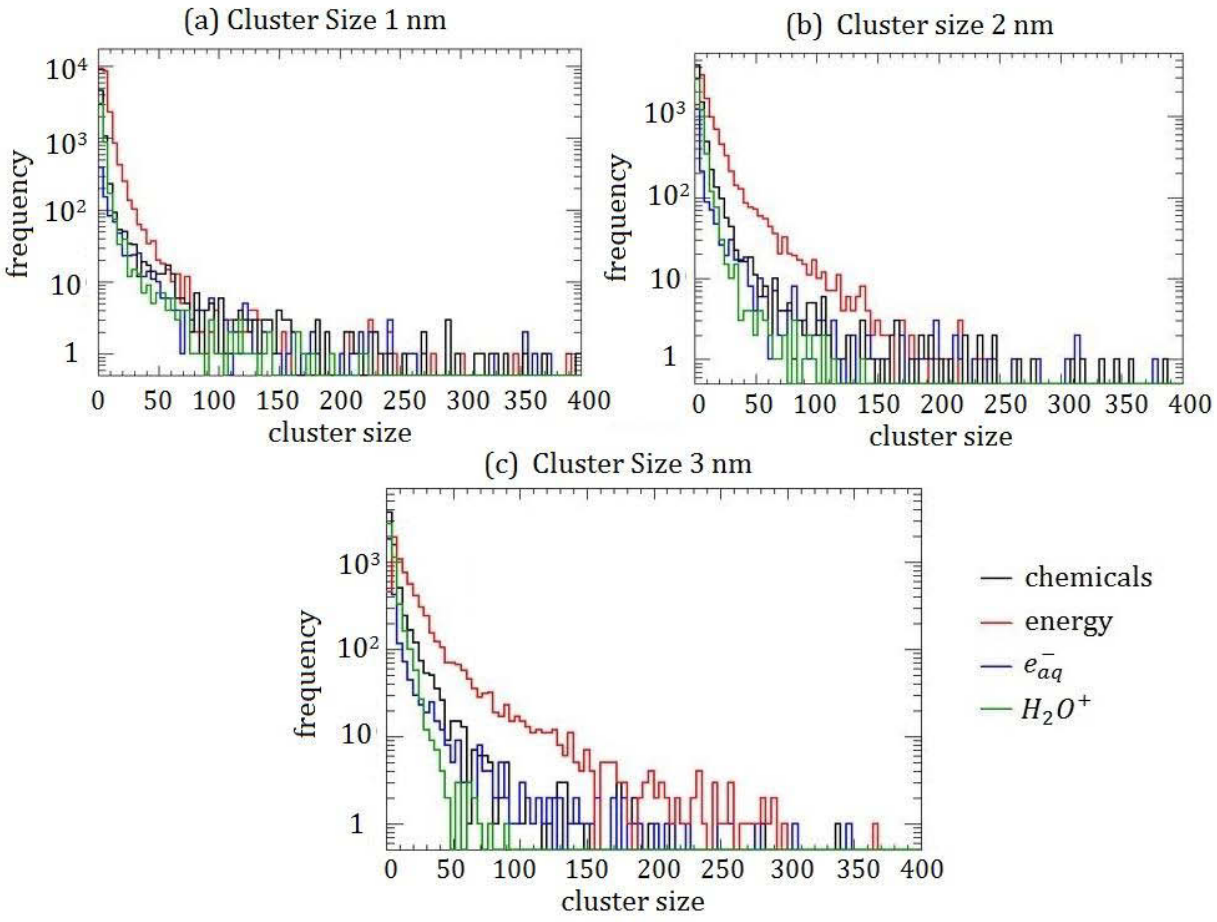

Figure (9-8) Cluster size distributions of energy transfer points, all chemicals, e^-_{aq} and H_2O^+ for (a) d = 1 nm, (b) d = 2 nm, and (c) d = 3 nm. Cluster size is the number of points making up a cluster.

Figure (9-9) shows the distributions of cluster densities for energy transfer points, all chemicals produced at 1 ps in addition to e^-_{aq}, and H_2O^+. The cluster density is the total number of points constituting a cluster divided by the *RMSR* of the cluster. Each cluster has its own unique irregular shape and thus its volume is not easy to calculate. Therefore, this quantity represents a form of density showing how the points are clustered together over a certain distance.

Results of the three values of clustering maximum neighboring distance *d*, 1 nm, 2 nm and 3 nm, are shown in figures (9-9-a), (9-9-b) and (9-9-c) respectively.

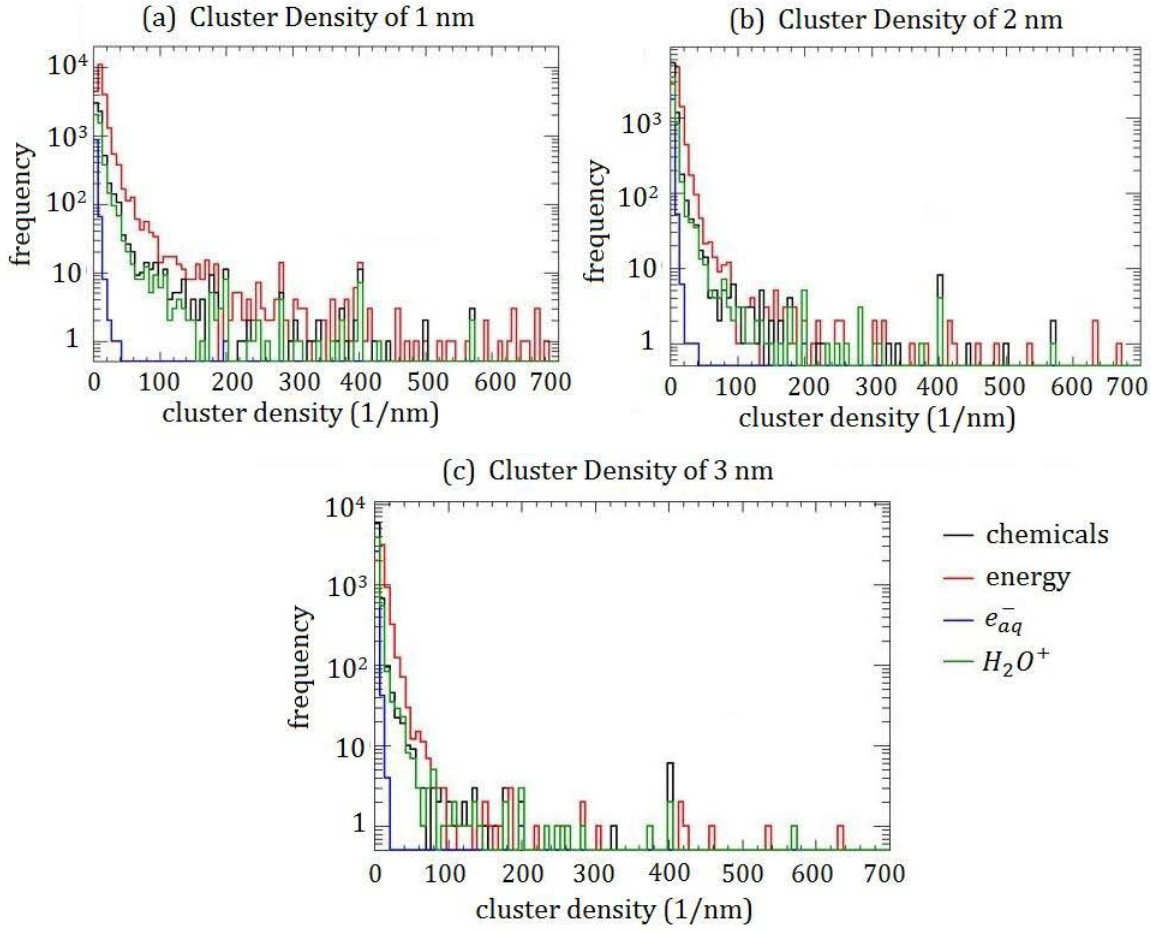

Figure (9-9) Distributions of cluster densities for energy transfer points, chemical species, e^-_{aq}, and H_2O^+. A cluster density is the number of points making up a cluster divided by the RMST of this same cluster. (a) clustering with d = 1 nm, (b) clustering with d = 2 nm, and (c) clustering with d = 3 nm.

The low density of e^-_{aq} clusters in the three figures shows that these electrons migrate away from the ionization location very fast making them less susceptible to form clusters unlike H_2O^+ that diffuse at a slower rate.

Therefore, the chemical clusters are formed mainly by H_2O^+ where e^-_{aq} contribute very little in their formation which is shown by the superposition of the curves of chemicals and H_2O^+ in the three figures.

Energy clusters are denser than chemistry clusters for the three values of d. This is mainly due to the overpopulation of energy transfer points compared to chemicals inside the

phantom. Another reason for this is low clustering probability of e_{aq}^{-} which influences the low density of chemistry clustering.

Chemicals will diffuse even faster away from their primary productions location and will react with more water molecules until they produce the highly reactive $OH^{\bullet}$ radical that alters the molecular structures of sensitive biomolecules if they reach them. H_2O_2 has the ability to diffuse and migrate a considerable distance and may reach sensitive biomolecules like the DNA or the protein complexes responsible for electron transport chain and oxidative phosphorylation.

The H_2O_2 molecules would then produce OH^{-} and $OH^{\bullet}$ in the site of these sensitive targets causing their damage. However, complex damages are less likely to occur in the chemical phase because chemicals diffuse in the medium. Since the primarily produced species have low cluster densities, they are less likely to produce denser clusters in time. In contrast, it is more likely to get single damages rather than complex ones especially since the more damaging chemicals $OH^{\bullet}$ and H_2O_2 are not produced at 1ps. H_2O_2 and $OH^{\bullet}$ are considered most influential of the reactive oxygen species since $OH^{\bullet}$ is considered as the most reactive and H_2O_2 eventually dissociates into the hydroxyl radical [2].

Chemicals will not cluster as frequently as energy transfer points. The number of chemical clusters produced are fewer than energy transfer points clusters. Complex damages are mostly caused by the physical phase of irradiation. Chemical damages are produced later and they are a threat to sensitive biomolecules, but they do not necessarily cause complex damages. Chemicals produced are smaller in number than energy transfer points and many of them would migrate outside the phantom.

9.4 **Conclusion**

The chemical species resulting from water radiolysis are simulated inside the volume of the mitochondria phantom. The evolution of the various chemicals from 1ps to 1μs after irradiation is studied. The concentration of each specie is calculated at specific moments in time during chemical phase.

DBSCAN clustering analysis is performed on the primarily produced chemicals at 1ps after irradiation. The chemistry clusters are compared with the energy deposition clusters. The energy transfer points tend to produce larger and denser clusters than the chemical species. This suggests that the clustered damages are more likely to occur due to energy depositions than due to *ROS*.

1. Karamitros, M., et al., *Modeling Radiation Chemistry in the Geant4 Toolkit.* Progress in Nuclear Science and Technology, 2011. **2**: p. 503-508.
2. Alpen, E.L., *Radiation Biophysics*. 1998: Elsevier.

10Conclusion

Most of the research in radiobiology have been concentrating on nuclear DNA damage by ionizing radiation since DNA is considered the most sensitive part of the cell and its health is important to the cell's vitality. Recently, there is a rising interest in studying radiation effects on mitochondria that are also considered as targets sensitive to radiation. Mitochondria have many vital functions and their integrity dictates the vitality of the cell among which are energy production, reactive oxygen species production and regulation, and apoptosis control. That is why we are interested in studying the ionizing radiation effects on mitochondria.

We were successful in introducing a new method for building phantoms of fibroblast mitochondria starting from microscopic images acquired by an inverted wide-field microscopy. The method is described in detail and three phantoms were built, two of healthy mitochondria networks, and one of chemically affected mitochondria by inhibitors that is clearly fragmented. These phantoms were uploaded to Geant4 as tessellated and tetrahedral meshes where irradiation simulations were performed with Geant4-DNA electromagnetic processes. The sources used in all three cases are electron sources with resampled energies from the interaction of 250 keV with water.

Lineal energies were calculated and DBSCAN clustering analysis was performed. In the end, a comparison of the three phantoms was carried out showing that the structural and geometrical difference between the three phantoms affects the microdosimetric quantities and the clustering of possible damages. Mitochondria with larger volumes would be more affected by radiation and since they occupy a large part of the cell, their damage by radiation is important to identify the overall cell's health.

Gold nanoparticles are considered as radio-sensitizers to enhance the local dose of radiation when they are preferentially delivered in tumor sites. They are supposed to increase the damaging ability of radiation in tumors preventing the healthy tissues from the effects of high doses. Therefore, we investigated two sizes of gold nanoparticles and their effect on one mitochondria phantom when irradiated with 250 keV photons. Lineal energy values showed some enhancement in the case of high concentration of gold nanoparticles that are preferentially absorbed near the surface of the phantom. However, for low concentrations where the gold nanoparticles are not concentrated near the phantom, no significant enhancement was found.

In the last part, simulations of chemical species inside one phantom were performed. The chemical phase of radiation effects on biological material produces reactive oxygen species due to water radiolysis and this is simulated with the help of the new Geant4-DNA

chemistry libraries. The concentrations of the different chemicals at different time steps of the simulations were calculated to show how the free radicals evolve during the chemical phase of radiation. DBSCAN clustering was performed to primarily produced chemicals and the comparison with energy transfer points clustering shows that chemicals do not form clustered damages as much as ionization events.

In this study, mitochondria phantoms were uniformly filled with water. The microdosimetric calculations were performed using the Geant4-DNA libraries which limited the simulations with water interactions. It would be interesting to know the exact constituents of mitochondria. The percentages of different elements making up mitochondria could be inserted into the simulations. This needs a collaboration with biologists who are willing to provide such experimental information.

This is a first step in phantom production for detailed study of mitochondria. Although our phantoms represent the complexity of the geometrical form of mitochondria, they do not take into consideration the details of the interior. The inner membrane of the mitochondria is considered the most sensitive part and it would be interesting to find a way to simulate the radiation damages in the inner membrane and assess the threshold over which the damages become critical. However, such information is still unavailable.

The primary mirodosimetric results due to GNP show some enhancement inside the mitochondria phantom. The research on GNP is still in its infancy and more information is needed to make more precise simulations. The damages from GNP could be linked to increase in *ROS* that migrate to sensitive parts of the cell. In the future, *ROS* production could be studied using Monte Carlo simulations to give a better idea on the cell killing improvement by the radio-sensitizing effect of GNP.

In my opinion, this study could be extended to have a better understanding of the radio-induced damages on mitochondria. The DBSCAN clustering analysis for example could be optimized for energy transfer points lying in the inner membrane of the mitochondria. In the future, I will be investigating the minimum value of energy transfer that causes definite damages to the electron transport chain proteins. This value will give us a clearer idea on clustered damages. The appropriate value of maximum neighboring distance for producing a clustered damage should be determined. We can also try to determine the damages on mitochondrial DNA.

The GNP part can also be extended and studied in more detail. In this study we tried to determine their effect on mitochondria, but the effects on the nucleus and the nuclear DNA is important as well. Later on, we can also take into consideration their effect in the chemical phase.

All in all, I think this study is a stepping point for further research. The production of the realistic mitochondria phantoms is a good start for simulating detailed subcellular structures. In addition, we introduced new methods for energy resampling that helped us optimize the simulation time and include the GNP effects with Geant4-DNA processes.